Title
Modeling, Estimation, and Control of Waste Heat Recovery Systems

Author
Luong, David

Publication Date
2013

Peer reviewed|Thesis/dissertation

University of California
Los Angeles

Modeling, Estimation, and Control of Waste Heat Recovery Systems

A dissertation submitted in partial satisfaction
of the requirements for the degree
Doctor of Philosophy in Mechanical Engineering

by

David Luong

2013

Abstract of the Dissertation

Modeling, Estimation, and Control of Waste Heat Recovery Systems

by

David Luong

Doctor of Philosophy in Mechanical Engineering

University of California, Los Angeles, 2013

Professor Tsu-Chin Tsao, Chair

Energy consumption and efficiency continue to be an area of high interest with the diminishing supply and rising costs of fossil fuels. In the United States, the industrial and transportation sectors consume a significant portion of the resources and total energy, accounting for significant fossil-fuel-related environmental impacts such as greenhouse gas pollution and global warming. It has been estimated that between 20 to 50% of the energy consumed is lost as waste heat in the form of hot exhaust gases, cooling water, and hot equipment surfaces. By converting the heat to a more useful energy form, waste heat recovery (WHR) technologies are capable of creating emission-free, low-cost, and sustainable energy sources. However, WHR systems, if not properly designed and operated, may not be economically and or even feasible, particularly with low-grade and highly-transient heat sources. The aim of this dissertation is to predict WHR performance and feasibility through physics-based static and dynamic Rankine Cycle (RC) modeling for low- and medium-grade transient heat sources. The dynamic models provided are low-order, control-oriented, and suitable for tractable estimation and control methods that improve operational performance and observability of key process

variables. Thermoproperties for water and steam are obtained from equations of state formulations based on Helmholtz and Gibbs free energy. For general fluids and their mixtures, equations of state can be obtaned from a presented least squares property fit routine. This dissertation applies the modeling, estimation, and control methods on a WHR application for heavy-duty diesel powertrain where important RC variables are captured and monitored while satisfying specified design and operating constraints. An organic working fluid mixture of ethanol and water is considered for this organic RC (ORC) application. Estimation and control methods are simulated on a dynamic ORC model of different architectures and actuator configurations. Power load following is also examined. The simulation results indicate improved ORC operation with feedback controls over the open-loop case. Multi-input multi-output controllers that rely on state estimation feedback show better tracking performance than single-input single-output controllers. Finally, a library of static and dynamic component models are provided as a useful aid for designing general WHR systems.

The dissertation of David Luong is approved.

Panagiotis D. Christofides

Adrienne G. Lavine

James S. Gibson

Tsu-Chin Tsao, Committee Chair

University of California, Los Angeles

2013

To my mom and dad

Table of Contents

List of Figures

List of Tables

Acknowledgments

UCLA has given me unbelievable opportunities to find higher truths in the language of mathematics and the context of engineering. It is a select people I have met and interacted with along the way who helped me complete my studies to the best of my capability. To them I am indebted to.

I have immense gratitude for my advisor Professor Tsu-Chin "T-C" Tsao who has stuck with me every bit of the way throughout this journey. He gave me autonomy over an engineering challenge that is now becoming a reality on a fleet of trucks soon to roam the roads more efficiently than ever before. Through the many personal and group meetings we have had, his wealth of knowledge and judgements have no doubt earned my respect and I am grateful to have had the opportunity to learn and apply his gifted engineering ways.

I would like to acknowledge Volvo Powertrain of North America and the Department of Energy for their financial and technical support of waste heat recovery research under contract DE-EE0004232. Specifically, I would like to give special thanks to Thomas Horne for his insightful comments and infinite patience during the many conference calls we engaged in.

My colleagues of the Mechatronics and Controls Laboratory at UCLA deserve many thanks for providing me a relaxed yet stimulating environment to learn about engineering crafts and myself. Yigang, Kevin, Jason, Chris L., Stephen, Herrick, Chris K., Shalom, Yen-Chi, and Kuo-Tai were all positive influences during the many hours we spent in lab together. Thank you all for embracing me and my interests, allowing me to be your "Bike Ninja." Special thanks goes to Herrick for being a loyal go-to guy for just about anything since day one of

graduate school.

I would also like to thank my committee members Steve Gibson, Adrienne Lavine, and Panagiotis Christofides for their support. To Professor Lavine, I will always remember our warm discussions and your willingness to review my equations with care and insight.

Many thanks to Don Browne for the invaluable teaching opportunities that have given me so much reward in front of the classroom.

To the UCLA Cycling Team, thank you for pushing me to my physical potential on the bike. Specifically to Maziar, Nina, Quiros, and Scott, thank you for being trustworthy friends (on and off the bike) with poignant feedback and suggestions for research and in life.

From the early days of graduate school to the present, I am truly grateful for Yao Xu and her family for treating me like family.

I owe gratitude to my brother Richard who has made me value high standards and encouraged me to always reach for them.

Lastly, I cannot thank my parents enough for instilling in me the value of education that has no doubt led me to where I am today.

Vita

2002	High School Diploma, Lowell High School, San Francisco, California.
2004	Teaching Assistant, Data and Chance, Johns Hopkins Center for Talented Youth (CTY), Stanford, California.
2005	Undergraduate Research Intern, Analytical, Research, and Consulting, Bose Corporation, Framingham, Massachusetts.
2006	B.S. (Engineering) and B.A. (Economics), Swarthmore College.
2006	Intern, Air Traffic Strategy and Performance Group, Federal Aviation Administration, Washington, D.C.
2007	Assistant Manager, Strategic and Technical Services, Aramark Corporation Facility Services, Madison, Connecticut.
2008	Graduate Research Intern, Systems Teaching Institute, NASA Ames Research Center and University Affliated Research Center, Moffett Field, California.
2008	M.S. (Mechanical Engineering), UCLA, Los Angeles, California.
2008–2011	Teaching Assistant and Associate, Engineering Department, UCLA. Taught sections of Engineering 183 (Ethics and Society) and 185 (Art of Engineering Endeavors) under the direction of Donald Browne, Gershon Weltman, and Robert Silverstein.

2011–2012	Teaching Fellow, NSF GK-12 Fellowship Program, Culver City High School, UCLA. Assisted in high school physics instruction under the direction of John Bakunin, Professor Terri Hogue, Professor Peter Nonacs, and Janice Daniel.
2013	Teaching Fellow, Department of Mechanical and Aerospace Engineering, UCLA. Taught sections of MAE 157s (Basic Mechanical Aerospace Laboratory) under the direction of Professor Yongho Suntaek Ju.
2013–present	Member of the Technical Staff, Vehicle System Division, Flight Control Department, Aerospace Corporation, El Segundo, California.

Publications

Transient Dynamic Modeling and Control for Waste Heat Recovery of Heavy-Duty Diesel Powertrain: Volvo-UCLA Final Research Report, Collaboration with Volvo Powertrain of North America and University of California, Los Angeles, 2012. Technical documentation of waste heat recovery efforts in Phase I and II under U.S. Department of Energy Contract DE-EE0004232.

D. Luong and T.-C. Tsao, "Nonlinear State Estimation of Moving Boundary Heat Exchanger Models for Organic Rankine Cycle Waste Heat Recovery," in *Proceedings of the 2013 Dynamic Systems and Control Conference*, Oct. 2013, Accepted for Publication, May 2013.

CHAPTER 1

Introduction

1.1 Introduction

Increasing energy demands, diminishing fossil fuel resources, and rising environmental impacts are challenges resulting from how society generates and consume energy. The unwanted byproducts of energy consumpton include production of greenhouse gases from industrial processes that are believed by many to contribute to global warming. Vehicle emissions significantly contribute to air pollution in the form of smog and acid rain. And the use of refrigerants and other ozone-depleting substances in refrigeration and aerosols are steadily shrinking the total volume of ozone layer that prevents most of the harmful ultraviolet light entering Earth's atmosphere. As population continues to grow, the demand for energy and their detrimental environmental impacts will grow as well. Figure 1.1 shows the ever-increasing consumption of energy sources dating back to the formation of the United States.

Petroleum is currently the largest source of energy in the United States with the rising demand for it not showing signs of slowing. The transportation and industrial sectors rely heavily on petroleum-based energy as seen in Figure 1.2. The footnotes can be found [Adm11]. Other fossil fuel resources are heavily dependent as well with renewable energy having a small energy contribution. Coupled with their diminishing supply, the need is growing to switch from an economy heavily

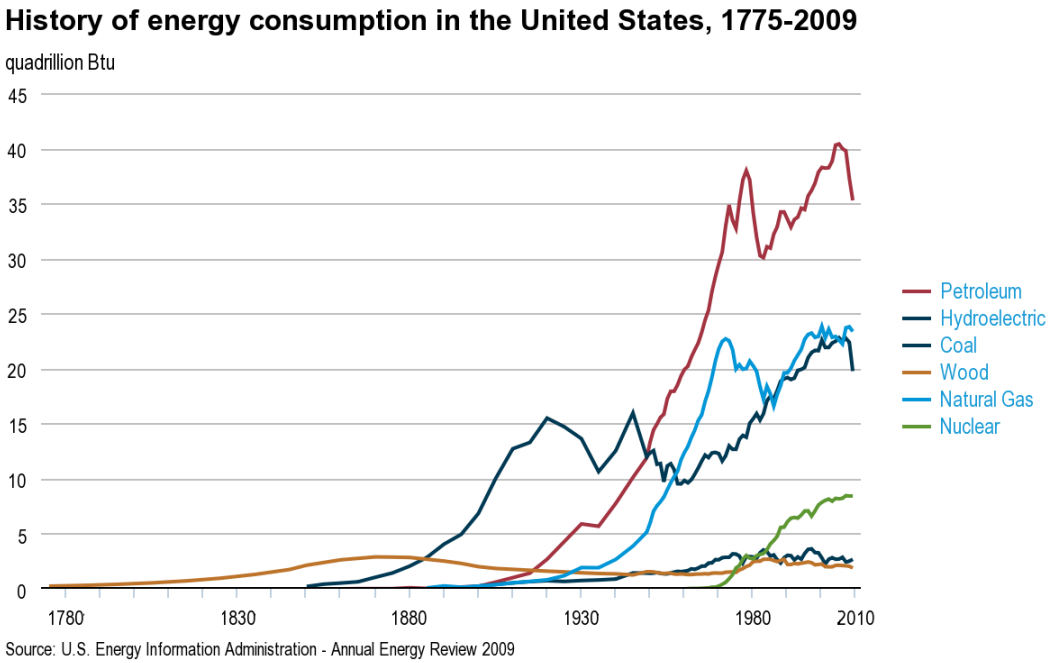

Figure 1.1: Historical Energy Consumption in the United States

dependent on fossil fuels to one relying on other energy sources are economically and environmentally advantageous.

To reduce our energy consumption that is highly dependent on fossil fuel resources, seeking alternative energy sources and improving energy efficiency are becoming increasingly popular solutions. Solar, wind, geothermal, and biomass energy sources are attractive for their sustainability and low generation of detrimental byproducts. Recovering energy from processes generating waste heat has been expected to bring process efficiencies higher thus requiring less energy consumption. To improve existing energy efficiency, recent research endeavors have involved dynamic modeling and controlling energy systems to better understand them in design and performance. Numerous works have been published in power

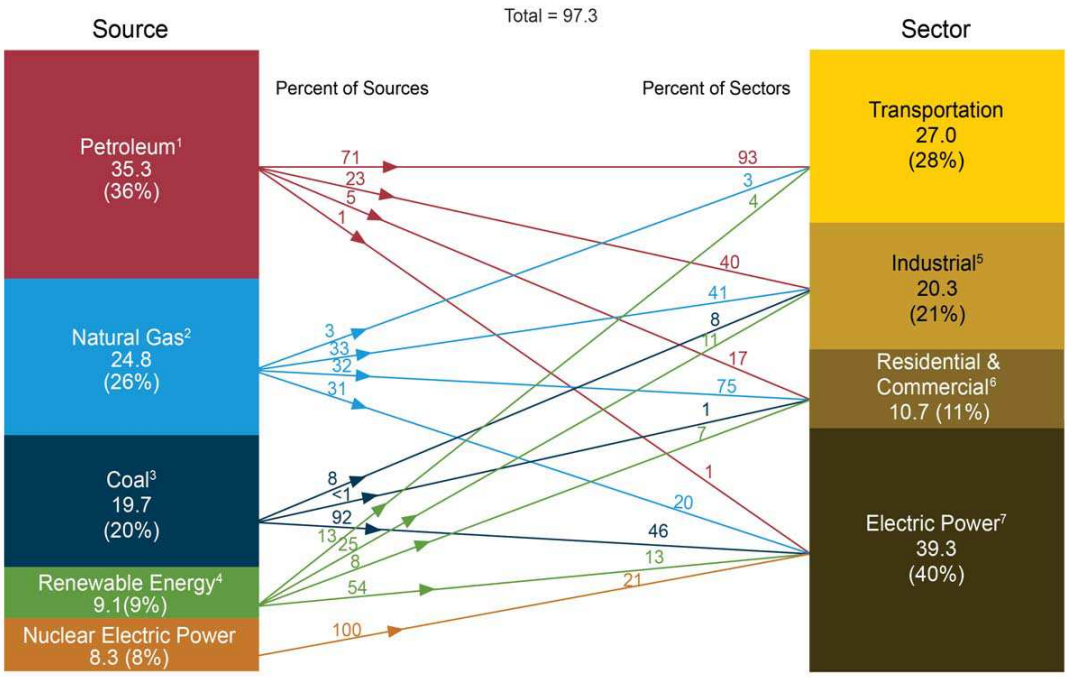

Figure 1.2: Energy Supply and Demand in the United States, 2011 [Adm11]

[WLL90][QLL10] and refrigeration cycles [RA04] to recover energy from a heat source and provide proper space conditioning [QD08][HLA97]. More recently, power generation from heat recovery using the Rankine Cycle, specifically ones operating organic working fluids, has been an active area of research and commercialization for a variety of applications with heat sources.

Rankine cycles (RC) have been receiving increasing attention in the market of power generation, particularly in automotive applications, where there is opportunity in recovering useful energy from engine heat. The RC seeks to recover the waste heat in the form of engine exhaust by producing expansion work that can be converted to mechanical torque for the engine drivetrain or electrical storage to power vehicle accessories.

Although the cycle has been in existence for some time, the RC has been fos-

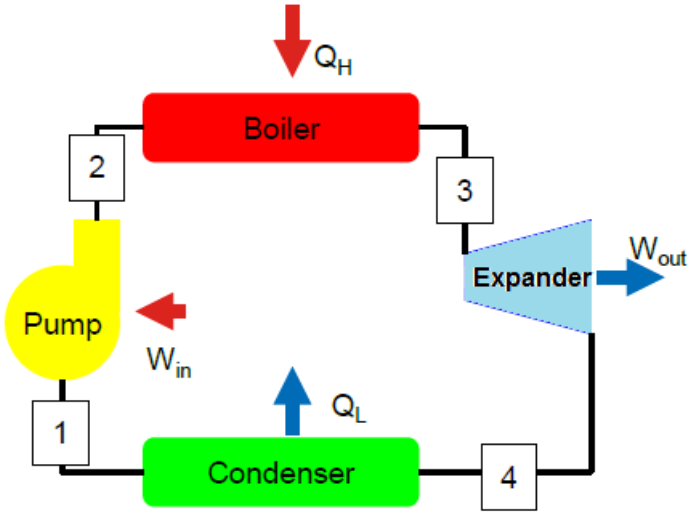

Figure 1.3: Components of the Rankine Cycle

tering renewed interest in small-scale systems characterized with low temperature heat sources. This characteristic makes it ideal in automotive systems where the physical space is limited under the hood and the exhaust used for waste heat recovery is not particularly high in temperature.

In heavy-duty (HD) vehicles, waste heat recovery (WHR) has been identified as a key technology in improving efficiency. The United States Department of Energy established the SuperTruck project to improve long-haul Class 8 vehicle freight efficiency [DOE10]. Among many areas for improvements including aerodynamics of tractor skirts or tire compound technology, reducing heat loss has the most opportunity for efficiency gains [DOE09]. Figure 1.4 highlights the energy distribution in Class 8 trucks for urban and highway driving with combustion dissapating the highest energy.

The advantage of a small-system RC is the ease to manufacture the parts derived from vapour compression systems such as refrigerators. Although such

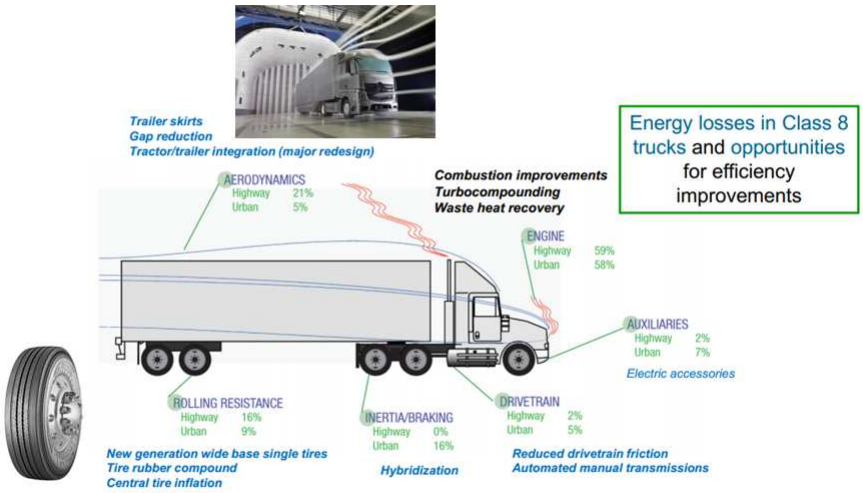

Figure 1.4: Areas for Improving Truck Efficiency [DOE09]

Rankine systems are typically associated with low efficiencies (8-12%) [Ros08], their feasibility in recovering waste heat in automotive engines has demonstrated fruition. Research and prototyping from Honda Motors have shown that in 100 kph (62 miles/hour) constant-speed driving, the use of the Rankine cycle improved the thermal efficiency of the engine by 3.8% [Ros08].

When the heat source is classified as low-grade (60° - 220°C) or medium-grade (220° - 450°C), the choice of working fluid becomes more important to achieve power generation and efficiency. Solar and geothermal applications are increasingly using organic working fluids which are better suited for low-grade heat sources. Typically refrigerants or hydrocarbon working fluids, these organic fluids have lower latent heat of vaporization and pinch points that occur at higher quality so that they can approach the heat sources temperature more closely than water. RCs with organic working fluids are referred to as organic Rankine cycles (ORCs.

Heat sources are often unsteady or transient which can affect power generation feasibility and performance. Depending on the driving terrain, the engine's exhaust can experience large exhaust temperature and flow rate swings. Figure 1.5 shows the exhaust temperature and mass flow rate of a 13 liter heavy-duty diesel engine for a Rolling Hills driving cycle. The transients creates a challenge in operating the WHR as a steady-state cycle and introduces concerns of drying out and flooding components.

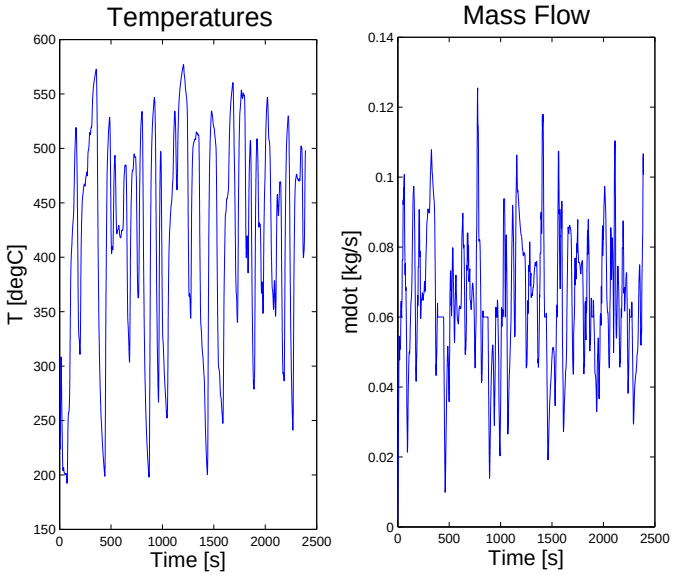

Figure 1.5: Heat Source for Rolling Hills Driving Cycle

Due to the low-grade heat characteristic describing waste heat and other renewable energy sources, there is a need for modeling, controlling, and monitoring ORC WHR systems during unsteady operations. For the given design and equipment operating conditions, the WHR system must be properly controlled to satisfy constraints in the presence of transient heat sources. To do so, a control-oriented ORC model is needed that accurately captures the salient trends of the system. Due to the multiple actuators and process variables found in the ORC, coupling

between them must be accounted for through the control strategy for constrained operation. Furthermore, some process variables are difficult to measure and if possible may add to system complexity and cost. In vehicular applications, the limited space under the engine hood necessitates minimal, automotive grade sensors that can adequately infer the system's current state of health and performance. Pressure, temperature, and mass flow rate sensors are typically available. Other process variables are difficult to measure such as wall temperatures and phase boundaries in two-phase flow. While phase change boundary detectors exist, they are expensive research grade sensors and thus not suitable for commercialization. Practically, this boundary cannot be measured directly in automotive and other applications, but remains an important variable to monitor to avoid flooding and dryout.

In determining the performance of recovering waste heat via such a cycle, it is important to understand the operating viability of the RC during an actual driving cycle and avoid critical conditions with proper control. The amount of available exhaust heat depends on driving style and terrain and has an impact on the performance in recovering waste heat and converting it to power. These are referred to as transient disturbances to the RC. Also important is how they critically affect the operation of the cycle. A critical condition of interest is when the proportion of liquid and vapour in the heat exchangers are outside acceptable ranges, causing stalling or temperature shocks to the components and damaging the system [WLL90]. In Figure 1.6, the interaction of the turbine blade and excessively wet steam caused bending damage. To avoid such critical conditions, property control must ensure an acceptable amount of superheat after the heat exchanger.

Such problems can be addressed at the design stage by a physical, dynamic

Figure 1.6: Turbine Blade Damage from Wet Steam (Source: PTG Advisers, Inc.)

model and simulations. Not only can such a model help size a system, but also forecast the actual system's operating viability under typical driving conditions. In this case, we are interested in how often the cycle can run as well as the power generated. The other advantage of having a control-oriented model is the ability to design and apply control strategies to optimize the cycle's performance in the presence of driving transients. Such optimization includes satisfying the constraints such as positive net power generated and requiring component inlet fluid conditions at the appropriate quality.

The rest of this chapter illustrates past and current work performed for modeling, estimation, and control of ORC WHR systems.

1.2 Dynamic Modeling for Refrigeration and Power Systems

1.2.1 Heat Exchanger Modeling

Physics-based dynamic modeling of heat exchangers can be based on approaches with trade-offs between accuracy and computation as shown in Figure 1.7. The truth model obtained from discretizing partial differential equations (PDEs) describing energy, mass, and momentum conservation offers high accuracy at the expense of significant computational load. The design model that removes spatiality in the PDEs by assuming lumped parameters and properties provides computational ease by trading away accuracy. The Moving Boundary approach results in fairly accurate, low-order, and control-oriented models.

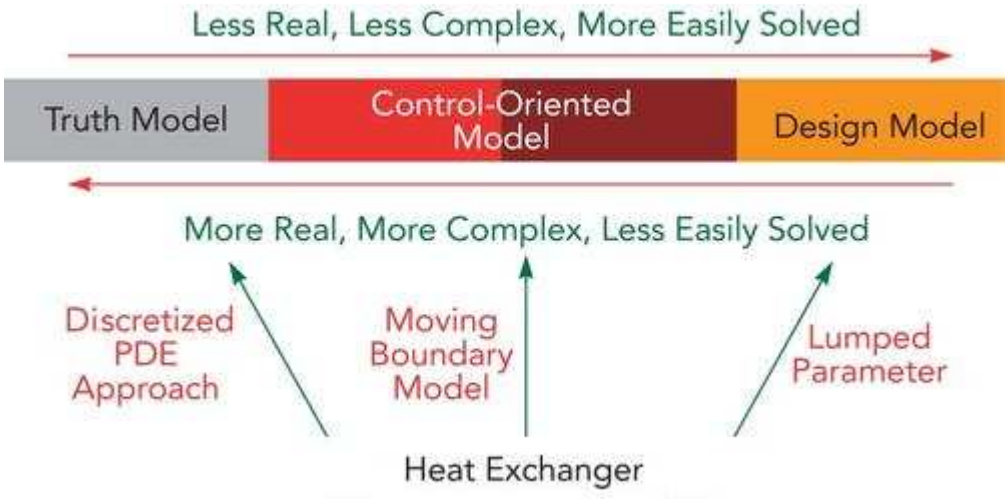

Figure 1.7: Heat Exchanger Modeling Approaches [Cra11]

Moving Boundary models have successfully described heat exchanger dynamics in refrigeration systems. Researchers have developed a control-oriented model for

transcritical vapor compression systems where the gas cooler and evaporator were described by one and two-zone Moving Boundary models, respectively [RA04]. The nonlinear heat exchanger models were linearized around an operating point for linear analysis and model reduction and showed agreement in dynamic trends with both the nonlinear model and experimental results.

Extensive research has focused on the Moving Boundary heat exchanger models in HVAC systems for the purpose of control and monitoring. The aim has been to increase performance and efficiency by exploiting the model's mathematical structure. There have been efforts in multivariable control of vapor compression systems that take advantage of the multi-input multi-output (MIMO) Moving Boundary models [HLI98]. By designing controllers that incorporate the coupling between multiple inputs and outputs, the authors showed that MIMO control could significantly improve the transient behavior of HVAC systems compared to the conventional single-input single-output (SISO) control scheme. Other researchers investigated a power plant utilizing waste heat and achieved transient performance and steady-state energy savings using a LQR with PI controller on a MIMO heat exchanger model [ZZH12].

However, limited research has been conducted on nonlinear Moving Boundary models that are important in describing WHR dynamics. While linear models are effective in reducing simulation and model complexity and conducive for linear control analysis tools, these models only apply to steady-state operating or equilibrium points. Driving cycles, in particular, rarely operate in steady-state conditions, typically with large heat source/sink transients. Linear models are no longer valid in these scenarios. Nonlinear models instead capture a larger state space and can model transients over a range of operations.

This dissertation adopts the Moving Boundary approach for dynamic heat

exchanger modeling. Both the nonlinear and linear models are developed for evaporators and condensers with different number of fluid-phase zones.

1.3 State Estimation

The performance and health of heat exchangers are important in power recovery and refrigeration systems for their ability to move heat effectively from one location to another. Often operated for long durations in a blackbox fashion, the heat exchanger states of health are important to know from available external measurements. Their heat transfer effectiveness degrades over time with chemical deposits and clogging and is known as fouling. Figure 1.8 shows a tube bundle that has been crusted over with chemical deposits and is in need of cleaning and maintenance. Without being able to measure every process variable for fouling checking, model-based estimators are useful mathematical tools to infer unmeasured variables from measured ones.

State estimation for these process variables is discussed in the literature and often required in feedback control and monitoring. Nonlinear observers were applied on a low-order evaporator model based on sensor measurements of evaporating temperature and used to synthesize feedback control [CHA04]. The fixed observer gains were obtained for specified operating points and guaranteed state estimation convergence. An Extended Kalman Filter (EKF) has been applied on a dynamic heat exchanger model to detect fouling [JLP07]. However, the considered working fluid does not undergo a phase change. To the knowledge of the authors, estimation has not been explored for the mathematically richer Moving Boundary heat exchanger models. Furthermore, state estimation performance using particular measurements has received little attention. The availability and cost of these sensors can impact whether feedback control is achievable.

Figure 1.8: Fouled Heat Exchanger Tube Bundles [Ibr12]

This dissertation examines linear and nonlinear state estimation on the Moving Boundary model. The linear state estimator is based on the linear Moving Boundary model while the nonlinear model used an Extended Kalman Filter. Pressure and temperature measurements are assumed available to infer the model states. For the EKF, cases for with and without process/measurement noise are examined. A discussion of relative observability is given for the nonlinear estimator. Finally, estimation performance is examined under the presence of heat exchanger fouling.

1.4 Working Fluid Selection

The selection of working fluids and operation conditions are important to overall WHR system efficiency, operation, and environmental impact[LCW04]. As attention is shifted to designing small WHR systems for low-temperature applications,

the selected working fluid must be chosen accordingly. The amount of heat available for heat transfer to the working fluid primarily dictates this choice. In high temperature applications such as powerplants, these systems typically use water and steam to take advantage of the large latent heat of vaporization to store heat and produce a large expansion during power generation. Low heat sources, however, require a working fluid (typically refrigerants having low flash points) that can easily flash into vapor from low heat with a compromise of a smaller expansion. Depending on the expected heat source grade, a working fluid is chosen between these two extremes.

In terms of operation and environmental impact, the selected working fluid must be compatible with and not cause damage to the system components and the environment in which they operate. In meeting these considerations, organic working fluids are receiving attention as as a favorable replacement for water in low-temperature applications. Some of these working fluids include, but are not limited to, the following in Table 1.1.

Many working fluids for Rankine cycle power systems are possible. The chosen fluid aim to have thermodynamic properties resulting in high efficiency and low cost systems. Desirable characteristics include having low toxicity, explosive tendencies, and controllable flammability behaviors [SM78][PJ77] as well as material compability and fluid stability limits [SM78][NGL78]. To aid in selection, these and other working fluids can be classified intro three different categories based on a metric provided in [LCW04]. As a working fluid undergoes expansion at the turbine or other expansion devices, its entropy can either decrease, increase, or remain roughly the same. While the latter case (isentropic expansion) is typically ideal, working fluids in practice are either wet (entropy decrease) or dry (entropy increase). Dry and isentropic fluids are guaranteed superheated after expansion,

Working fluids	Calculated by	Type
Water	-13.1818	Wet
Ethanol	-5.4299	Wet
R11	-0.3903	Isentropic
R123	0.1202	Isentropic
HFE7100	1.8252	Dry
n-Pentane	1.2335	Dry
Iso-Pentane	1.1801	Dry
Benzene	0.3316	Isentropic
Toluene	1.0600	Dry
p-Xylene	1.539	Dry

Table 1.1: Working Fluid Types [LCW04]

and eliminates the concern of liquid droplets in the expansion device. Hence, dry or isentropic fluids are preferred over wet types. [LCW04] suggests examining the quantity $\xi(=\frac{ds}{dT})$, the slope of the saturated vapor curve on a T-s diagram. Dry type fluids are characterized by $\xi > 0$, wet types by $\xi < 0$, and isentropic types by $\xi \cong 0$ where

$$\xi = \frac{C_P}{T_H} - \frac{\frac{nT_{rH}}{1-T_{rH}} + 1}{T_H^2}\Delta H_H \tag{1.1}$$

T_H is the temperature at the evaporating condition, T_{rH} is T_H normalized to the critical temperature, the exponent n is 0.38 given by [PPO01], and ΔH_H is the enthalpy of vaporization. Table 1.1 provides acceptable agreement between thermodynamic data and the predicted types of the working fluids. Notice that water and ethanol, both with large enthalpies of vaporization, have significant negative ξ values.

Together with knowledge of the working fluid type, a sensible choice of working

fluid can be based on the desired operating condition consistent with the available heat source and heat sink. Knowing the superheat temperature, the selected working fluid should undergo expansion (dry or isentropic) while ensuring sufficient cooling capacity is available to bring the fluid to a subcooled state. This provides insight in sizing the cooling capacity for the system. Because the heat source availability can vary, the working fluid must be appropriately chosen and cooling capacity must be designed for that range of operation.

The efficiency and power generation capability of the Rankine cycle can also be improved by the use of mixtures. Pure fluids are typically azeotropes, that is they exhibit constant boiling temperature. Water is such an azeotropic fluid. When boiling, the transfered heat acts to break the molecular bonds and does nothing to increase the fluid temperature until it reaches superheat. This has a neutral effect on the cycle efficency as the working fluid is not able to converge closer to the heat source temperature as shown in Figure 1.9. Zeotropic fluids, however, have non-constant boiling temperatures and can reach closer to the heat source temperature. This has the effect of increasing both the cycle efficiency and power. Water-ethanol and water-ammonia mixtures are both zeotropic and are popular working fluid choices in waste heat recovery applications.

The working fluid must also have a desirable freeze point in applications encountering freezing ambient conditions. Pure water is not ideal in many areas of the world experiencing freezing conditions, so some anti-freeze protection may be required to lower the freezing point. Water mixtures involving ethanol or ammonia can have a sufficiently low freeze point, and with the help of fluid circulation can deter freezing.

This dissertation uses water and 52% ethanol-48% water mixture as the working fluid.

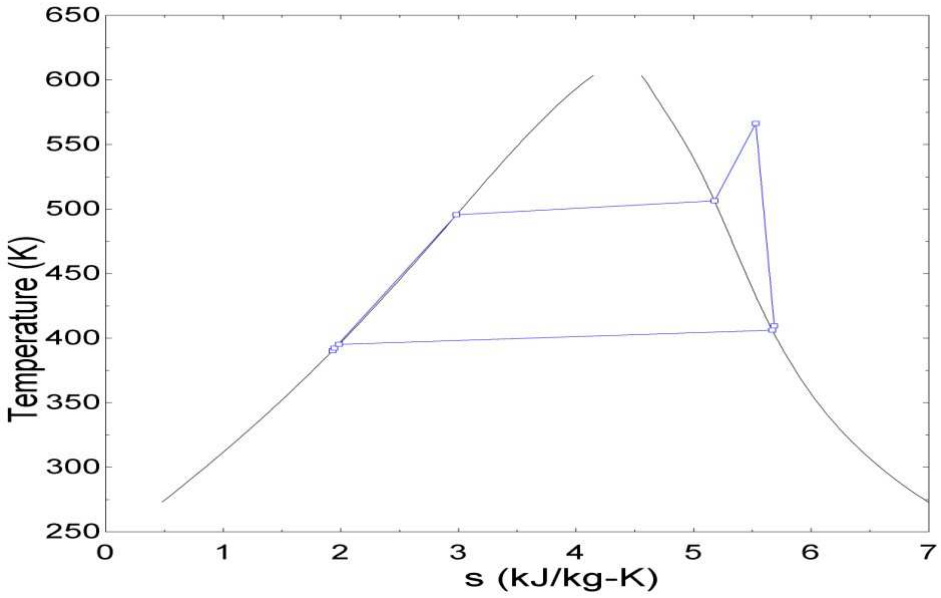

Figure 1.9: Temperature-entropy diagram for Ethanol-Water Mixture (52% Ethanol-48% Water Mixture)

1.5 Thermodynamic and Transport Property Models

In constructing thermodynamic models, obtaining fluid properties for the working fluid can be a challenge needed to solve the RC models. Thermodynamic and transport properties are often available in tables from reference books or property software. For well-studied fluids such as water and steam, equations of state exist and are based on Helmholz and Gibbs free energy principles. However, not every working fluid, including organic working fluids that has been of recent research interest, has easily accessible or available equations of state for the desired operating conditions.

Thermodynamic software are available to retrieve thermodynamic and transport properties given two independent properties. If the thermodynamic software

does not provide communication to the modeling software environment for property retrieval, the properties are often imported and a table look-up scheme is employed. Transport and thermodynamic tables of properties typically exist for many studied fluids. Selected ranges of these property tables can be programmed into the modeling language and 2-D lookup and interpolation methods can be employed to retrieve desired properties defined by two independent properties. The latter method's interpolation may result in significant computational demand over the course of simulations.

This dissertation obtains equations of state by performing an off-line property least squares fit [Lim11]. The equations of states are highly accurate, but less so near the independent properties' range boundaries. The property evaluations are often more computationally efficient than interpolation in table look-up.

1.6 Control of Rankine Cycles

RCs are typically used in power applications where a steady heat source and sink are available. Such cycles operate in steady-state fashion due to the consistent heat source (constant $\dot{Q}_{in}$ for the heater and $\dot{Q}_{out}$ for the cooler) with little concern of highly transient conditions disturbing the cycle from its normal operating condition designed with acceptable margins away from critical conditions. Such include dry-out, flooding, and temperature shocks in heat exchangers. A flow and temperature-entropy (T-s) diagram describing a steam RC is shown in Figure 1.10.

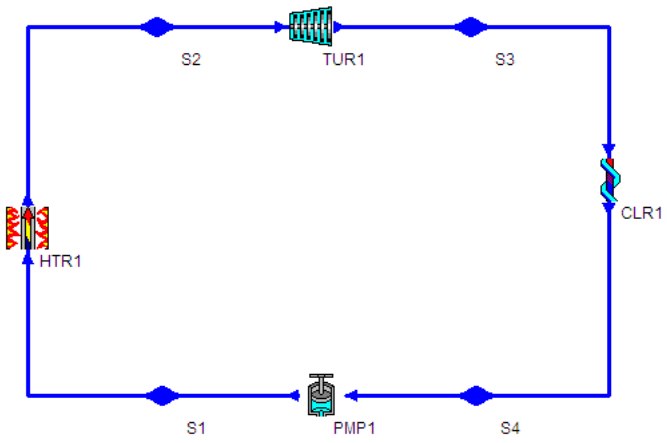

Figure 1.10: RC Schematic

HTR1 and CLR1 in Figure 1.10 are respectively synonymous with the evaporator and condenser terminology used in this dissertation. TUR1 represents a generic expansion device, not necessarily a turbine.

With the known constant or steady heat source and sink, an evaporating and condensing pressure is chosen in accordance with the appropriate mass flow rate to locate the S1-S4 vertices in the correct phase regions *i.e.* liquid at pump inlet, (superheated) vapor at turbine/expander inlet.

Figures 1.11 and 1.12 show cycles with the same evaporating and condensing pressures. The difference is in the heat sources which causes different superheat and expansion conditions. The S2 vertex shifts away from the saturation dome as more heat is added to the evaporator. The S3 vertex falls inside or outside the dome, indicating wet working fluid phase that the expansion device may not be able to tolerate. The quality at S3 may need to be sufficiently high to prevent liquid droplet damaging turbine blades operating at high speeds.

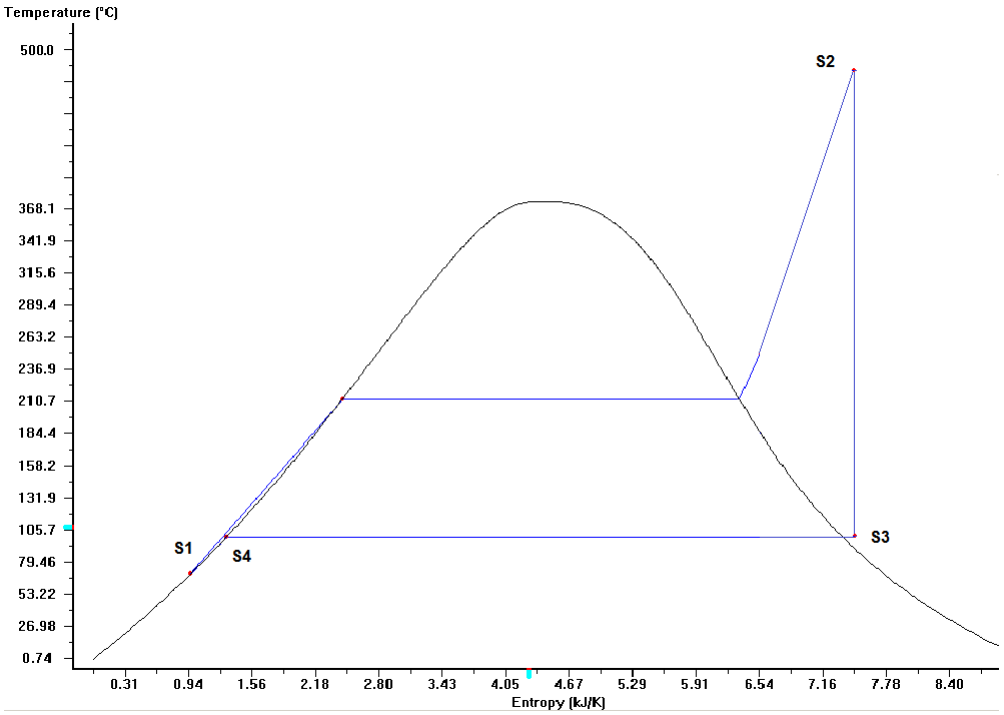

Figure 1.11: RC T-s Diagram (Single Phase Expansion)

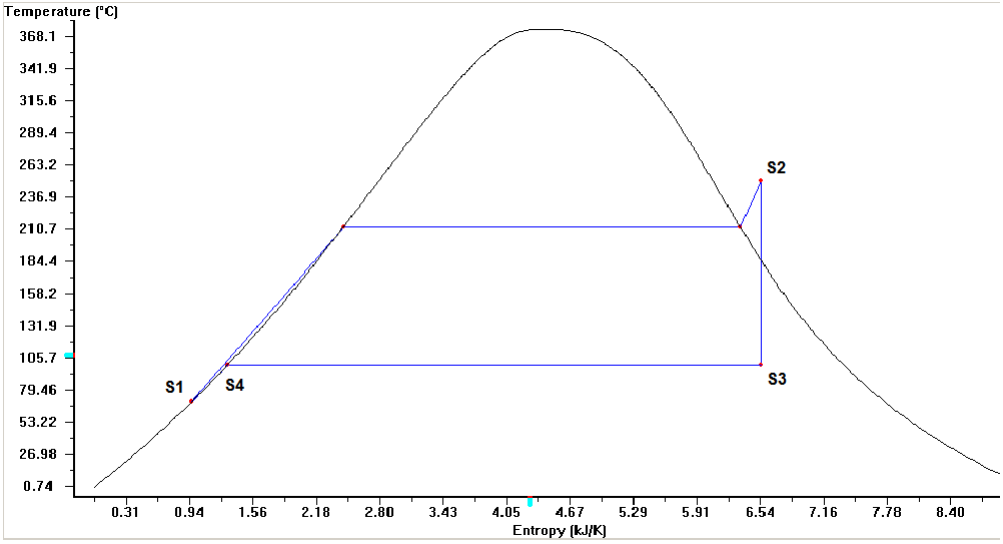

Figure 1.12: RC T-s Diagram (Two-Phase Expansion)

The goal of control is to optimize the working conditions of the Rankine cycle corresponding to the heat source and heat sink. The first step is to assume a static or constant heat source and heat sink defined by average temperature and flow rate. This provides a baseline performance to comparison to the performance of a RC with varying heat source/sink properties. Past control effort for optimal control of a dynamic RC indicated that the following statements should be accounted for [QAG11]:

1. Condensing pressure maintained as low as possible, usually at atmospheric pressure to avoid vacuum conditions
2. Superheating at the evaporator outlet should be kept at an acceptable level to avoid downstream component damage in the expansion device and in general when using organic fluids with high molecular weights
3. Optimal evaporation temperature should result in high heat recovery efficiency

The last statement, however, has undesired effects on the RC system. When increasing the evaporation temperature (from a higher pressure), the following occurs:

1. A higher evaporating temperature results in greater under-expansion losses, which decreases the expansion efficiency
2. The heat recovery efficiency is also less from the heat source cooling down to a higher temperature
3. The expander specific work increases with a higher pressure ratio

These trade-offs are important to quantify when identifying the optimal temperature. The equations to describe these cycle metrics are the following:

$$W_{net} = \int (W_{exp} - W_{pump})dt \tag{1.2}$$

$$\eta_{cycle} = \frac{W_{net}}{\int \dot{Q}_{evap}dt} \tag{1.3}$$

$$\epsilon_{hr} = \frac{\int \dot{Q}_{evap}dt}{\int \dot{m}_{wf}(h_{out} - h_{in})dt} \tag{1.4}$$

For a particular working fluid, the above metrics can be plotted over an operating range of evaporating temperatures. Figure 1.13 below is for the working fluid R245fa where the optimal evaporating temperature is about 117 degree Celcius.

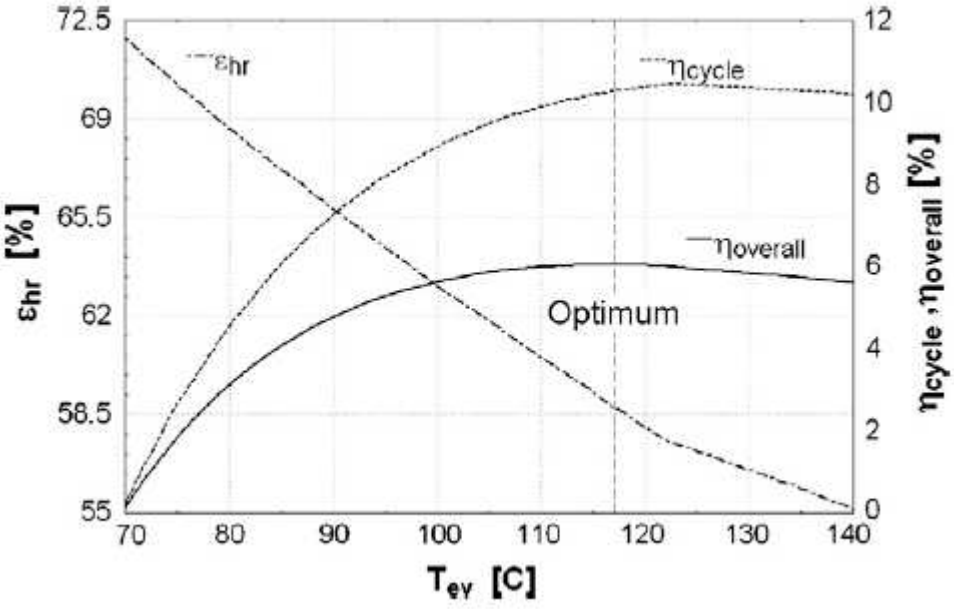

Figure 1.13: WHR Effectiveness, Cycle Efficiency, Overall Efficiency[QAG11]

In the RC, the two degrees of freedom to achieve this optimal point are mass flow rate and pump/expander speed. The pump and expander are controlled in

such a way to affect the working fluid's evaporating temperature and degree of superheat. Throttle valves and their positions set the flow rates in the RC loop.

It should be noted that the mass flow rate and pump/expander speeds have widely different time constants and do not independently affect evaporating temperature and superheat. A change in the pump flow rate changes the evaporating temperature and/or amount of superheat, and experiences a delay from the thermal and fluid dynamics of the heat exchanger [QAG11]. A change in the expander speed, however, produces an almost instantaneous change in the evaporating pressure (and thus temperature). With a constant mass flow rate , the volumetric flow rate is modified through a change in fluid density and vapor pressure.

The authors in [QAG11] decided that evaporating temperature is more of a priority condition to control and uses the faster acting expander speed to affect it. The pump flow rate is used to affect the degree of superheat. The authors apply proportional-integral (PI) control in a feedback manner for three different strategies:

1. Constant evaporating temperature
2. Optimized evaporating temperature depending on actual working conditions
3. Correlated pump speed (for working fluid flow rate as an optimized function of heat source temperature, condensing temperature, and expander speed)

The authors concluded that the best results are obtained with regulation to the optimal evaporating temperature. Finding the optimal evaporating temperature from a steady-state model like in Figure 1.13 is needed a priori for the range of operating temperatures and unsteady heat sources. An offline mapping of some kind is needed for a variety of working conditions. The correlated pump speed

strategy tries to achieve a faster acting pump based on actual working conditions, but was not able to maintain desired superheat in simulation.

The work presented is a step in the direction of Rankine cycle modeling and control for optimal operation. However, there are some shortcomings, specifically with a decoupling of the degrees of freedom in affecting evaporating temperature and superheating. Although the authors mentioned that the time scales is a reason for choosing expander speed to affect superheat and pump flow for evaporating temperature, the simultaneous effects of the actuators are not explored rigorously. Another degree of freedom not mentioned is the inlet enthalpy of the working fluid, which is a function of cooling ability at the condenser and added energy from flowing through the pump.

On a grander scheme, lacking in the Rankine cycle literature is advanced control strategies that takes advantage of multi-input multi-output (MIMO) feature of the entire system. Hindering the advancement of controls is the fact that single-input single-output (SISO) strategies such as the ones presented in [QAG11] do not pay attention to the coupling of the inputs that affect the outputs. While Rankine models exhibit multiple inputs and multiple outputs, they are treated as single inputs affecting single outputs in control design.

The authors in [ZZH12] proposed a linear active disturbance rejection controller for a system identified model of a 100 kW WHR system. The authors in [HLI98] have designed a model-based advanced controller for vapor compression refrigeration systems. Linear Quadratic Gaussian (LQG) strategy was used for both evaporator and condenser to achieve better disturbance rejection and transient response over SISO controllers. However, the literature currently lacks such advanced control efforts and results for ORCs based on the Moving Boundary heat exchanger models. What remains ahead in control design is to shed light on

the benefits of treating the entire system as a multi-input multi-output (MIMO) model and exploring the trade-offs between selected inputs to affect outputs under transient heat source/sink conditions. Multiple time scale behavior of RC components will certainly play an important role in the design. Advanced MIMO controls such as linear quadratic and model predictive control show promise in achieving an operational objectives such as desired superheat and system pressures during transient operation, which this dissertation explores.

CHAPTER 2

Application to Heavy-Duty Diesel Powertrain

2.1 Overview

The application considered has the heat source for the Rankine cycle coming from the exhaust manifold as shown in Figure 2.1. A fraction of the exhaust powers the boost system and turbo-compounding. The remainder of the exhaust flows through the exhaust gas recirculation (EGR) evaporator and serves as the heat source for the Rankine Cycle (RC) before returning to the combustion chamber for nitrogen oxide (NOx) emissions reduction. During driving cycles, the exhaust temperature and mass flow rate exhibit highly transient behavior, thus affecting the $\dot{Q}_{in}$ to the heater *i.e.* evaporator. A similar statement can be made for the condensing side for its cooling medium (passing ambient air or radiator coolant). These transients cause changes of the evaporating and condensing pressures in the heat exchangers, changing the isobars and vertex locations corresponding to working fluid states on the T-s diagram.

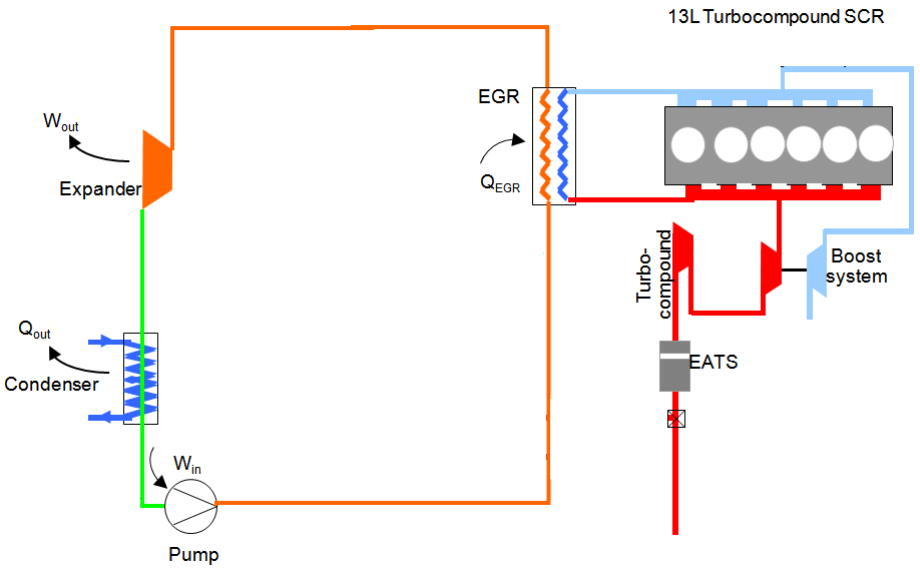

Figure 2.1: Rankine Cycle Architecture (Overview)

2.2 Geometry

The EGR cooler *i.e.* evaporator is shown in Figure 2.2. The overall flow length from inlet to outlet is 0.7 meters distributed in twelve stainless steel tube bundles. The current cooler has a complicated flow arrangement resembling shell and tube with internal flow undergoing multiple passes. The external flow across the tube bundles is a mix of cross, parallel, and counter flow.

Heat Exchanger	(Effective) Length [m]	# Tubes	Tube ID [m]	Shell ID [m]
EGR Evaporator	(2.1) 0.7	12	0.0075	0.009
Condenser	(3.5) 0.7	11	0.02	0.03

The effective length arises from flow in the heat exchangers going through multiple passes that effectively gives a longer length. The effective lengths are used in the modeling.

The wall thickness of the shell and tube is 1 mm for both the evaporator and condenser.

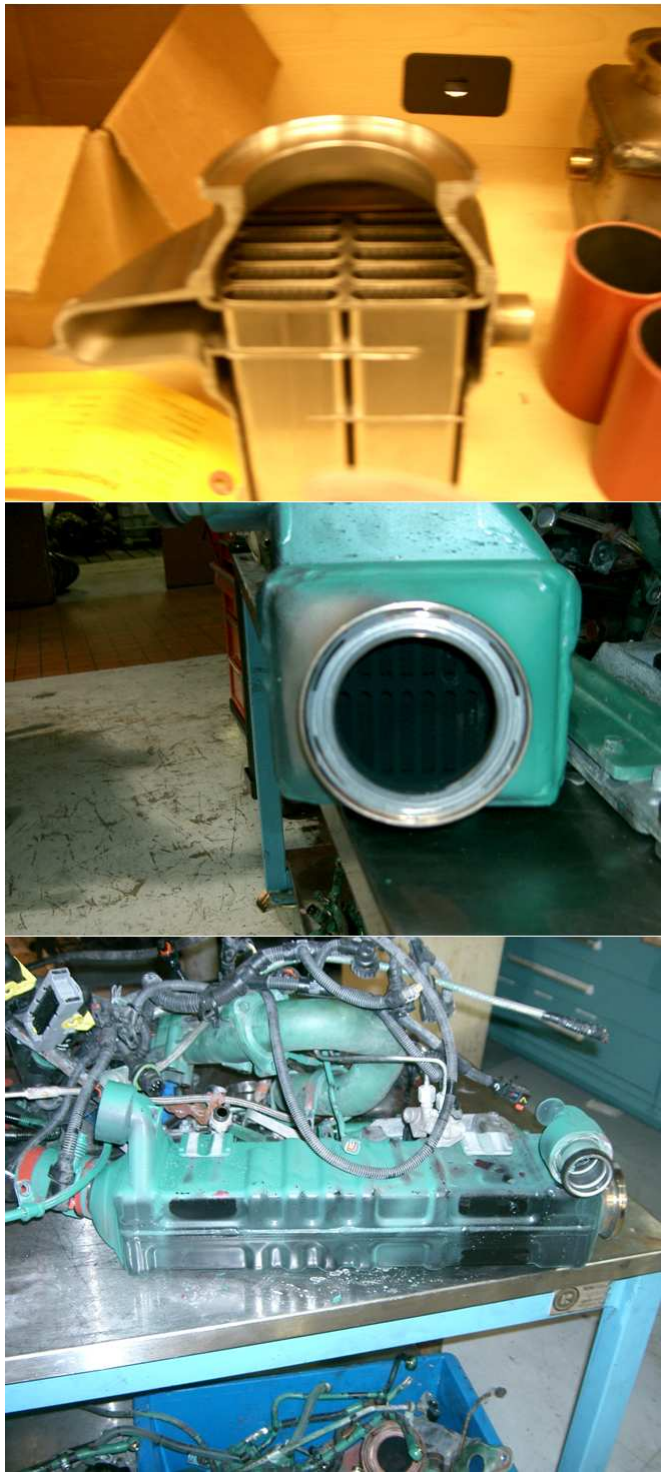

Figure 2.2: Exhaust Gas Recirculation (EGR) Evaporator Cooler

2.3 Working Fluid

The selected working fluid is an organic mixture of ethanol (52%) and water (48%) for its suitability in a vehicular environment. Chemical breakdown of the mixtures occurs around 300 °Celcius, which is an appropriate temperature given the heat source quality (shown later in this chapter). The mixture has inherent resistance to freezing, which can be further aided by fluid circulation.

The Temperature-Entropy diagram for the RC using ethanol-water mixture is shown in Figure 1.9.

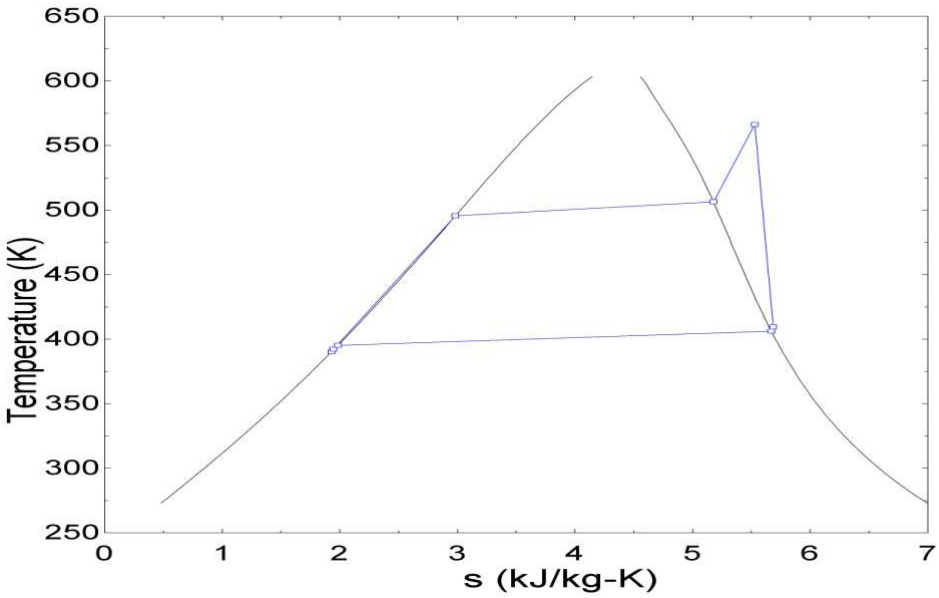

Figure 2.3: Temperature-Entropy Diagram for RC

2.4 Modeling

The RC modeling in this dissertation uses the EGR exhaust stream as the heat addition. The tailpipe exhaust can serve as a pre-heater or parallel heater in other

RC architectures, but is not studied in this dissertation.

The working fluid is 52% ethanol-48% water whose properties are obtained from fitted equations of state (EoS) as outlined in Chapter 3. The exhaust is treated as air whose properties are also obtained from fitted EoS found in [Lim11].

To simplify the dynamic modeling, the evaporator and condenser are assumed tubular heat exchangers with internal working fluid flow through a single circular tube subjected to external exhaust gas flow. The external flow arrangement examined are counter flow in a concentric annulus around the working fluid tube in Chapter 4. Chapter 5 assumes external cross flow across a single cylindrical working fluid tube. Different heat transfer correlations corresponding to these flows are addressed in those chapters. In general, the modeling uses the effective length as the tubular heat exchanger length and assumes an equivalent circular cross-section having the equilvalent flow area as the actual heat exchanger.

The simplification and assumptions reduce the accuracy of the model to the actual heat exchanger and should be noted when reviewing the dissertation's results. For example, the heat transfer coefficients are calculated based on a single tubular geometry and not the more complicated actual geometry that resembles a tube bundle arrangement. Additional improvements can be made in this area in future research efforts.

2.5 Disturbances

Depending on the driving cycle, the heat source can exhibit a variety of conditions. The following figures show these transients for the Flat, Hilly, and Rolling Hills cycle. The two heat sources are from the Exhaust Gas Recirculation (EGR) and tailpipe (TP). For the EGR exhaust, its outlet temperature after heat exchange is

shown to indicate the heat quality of the stream entering the combustion chamber for emissions control.

2.5.1 Heat Source

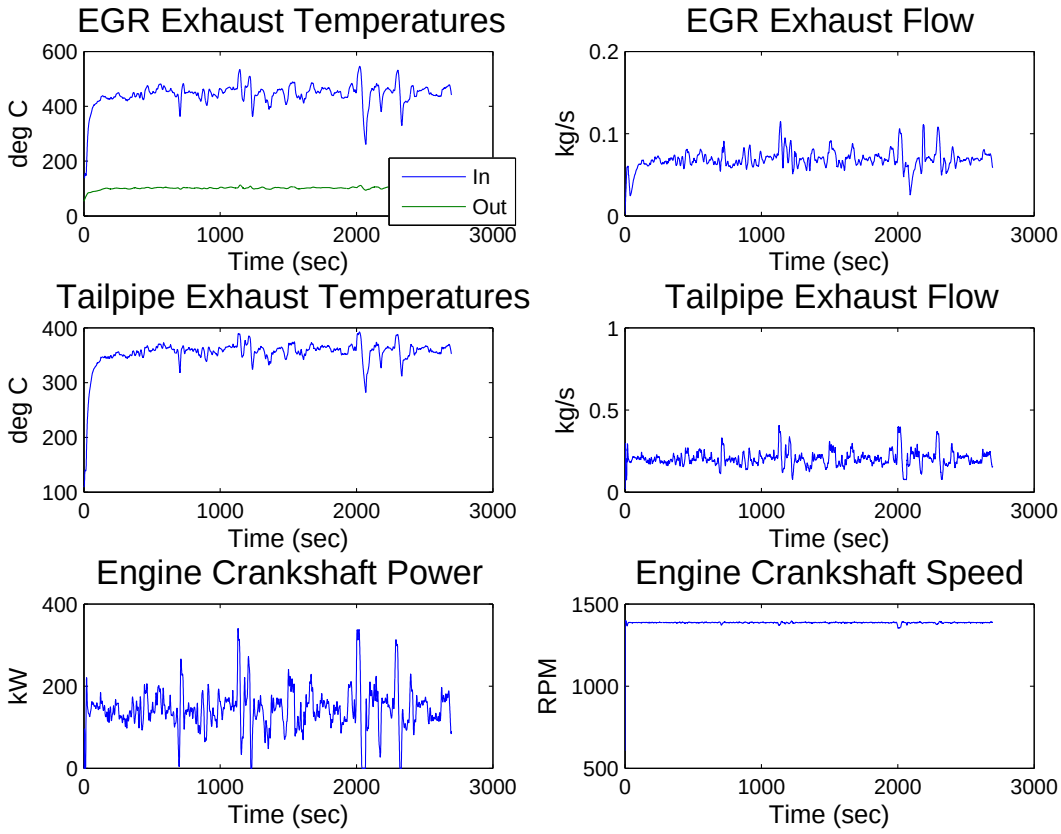

Figure 2.4: Engine Characteristics for Flat Hills Road Cycle

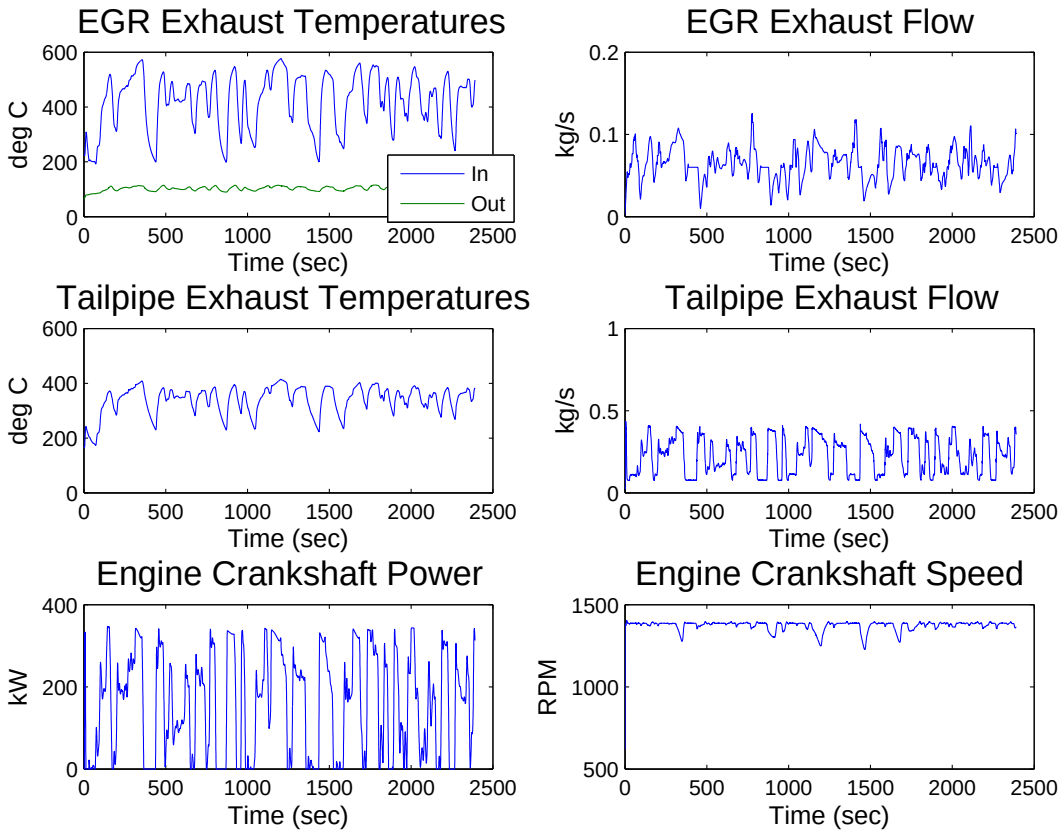

Figure 2.5: Engine Characteristics for Rolling Hills Road Cycle

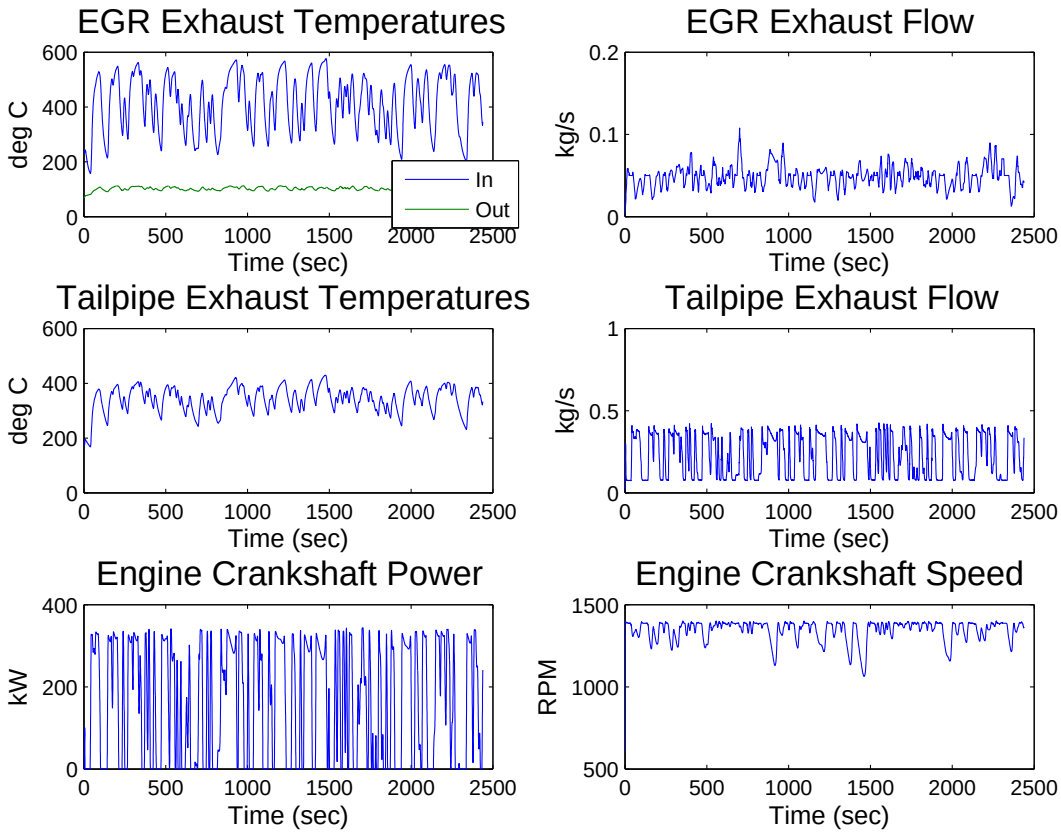

Figure 2.6: Engine Characteristics for Hilly Road Cycle

The average values of each characteristic for the driving cycles are given in Table 2.1.

The other model disturbances are:

1. **Engine Crankshaft**: coupled to the pump and expander shaft in a 1:1 and 1:1.3 (1.3 expander rotations for every crankshaft rotation) ratio, respectively. This translates to disturbance flow rates through these devices. The gear ratio for the expander was as a result of a required gear diameter needed for the expander to mesh with the large gear in the gear train. This

Table 2.1: Averaged Engine Characteristics

Driving Cycle	EGR T (°C)	EGR $\dot{m}$ ($\frac{kg}{s}$)	TP T (°C)	TP $\dot{m}$ ($\frac{kg}{s}$)	Engine Brake Power (kW)	Engine Speed (RPM)
Flat	443	0.0685	354	0.204	143	1386
Rolling	421	0.0647	339	0.225	153	1373
Hilly	415	0.049	342	0.227	153	1344

reason was that the expander was originally designed for a Daimler truck engine, and not a Volvo powertrain.

2. **Heat Sink Temperature**: depends on the current state of radiator coolant (assumed to be water in the modeling). The nominal heat sink temperature and flow rate are 60 °Celcius and 1.5 $\frac{kg}{s}$.

2.6 Desired Operating Conditions

The objectives that control needs to meet are the following:

1. Evaporator outlet temperature for working fluid should not exceed 300 degrees Celcius for long durations to prevent temperature shocks to downstream expander

2. Evaporator pressure should be as high as possible, not to exceed 1.5 MPa to maximize RC work/power

3. Condensing pressure should be as low as possible to maximize RC work/power, not to dip below 0.1 MPa (atmospheric pressure)

4. Condenser outlet temperature for working fluid should not exceed 70 degrees Celcius to avoid excessive and unnecessary subcooling and aid in oil separation in the working fluid

5. Expander throttle valve closes when expander swallowing capacity reached or unavailable engine power

6. Pump throttle valve maintains proper flow into evaporator for pressure and superheat regulation

7. Exhaust gas temperature should be within an appropriate range for EGR emissions reduction

2.7 Control Actuators

The following control 'knobs' for achieving these objectives are:

1. **Pump Throttle Valve**: determines the evaporator outlet (expander inlet) conditions by sending in the proper amount of working fluid. If more/less heat is available, pass more/less working fluid through the evaporator to achieve (superheated) vapor at a high enough pressure.

2. **Heat Sink Cooling Mass Flow Rate** cools the working fluid to the desired liquid condition before travel through the pump. Mass flow rate of the cooling medium is controlled through a valve or fan while temperature is treated as a disturbance.

3. **Expander Throttle Valve**: maintains working fluid flow into expander when engine power is unavailable or maximum swallowing capacity has been reached.

The RC architecture with actuators is shown in Figure 2.7. The heat sink flow rate is actuated by a valve (not shown).

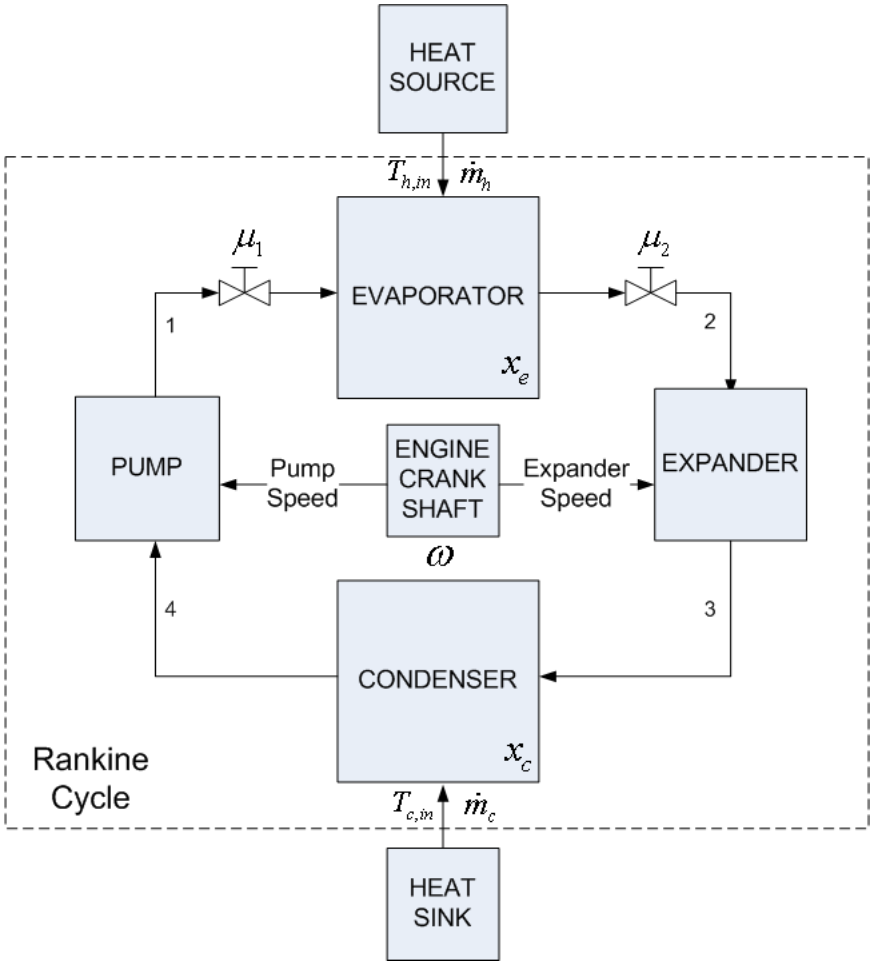

Figure 2.7: RC with Pump and Expander Throttle Valves

CHAPTER 3

Thermodynamic and Transport Property Modeling

This chapter details methods to obtain thermodynamic and transport fluid property needed to model Rankine Cycles (RC). As an alternative to table lookup methods commonly used in analyzing thermodynamic and heat transfer processes, formulations for equations of states are provided for general fluids. The properties are assumed to have the form of a power series as a function of two independent thermodynamic properties. A least squares routine is used to compute a vector of fit coefficients that minimizes the ℓ^2 norm of the estimation error. Fitted properties for an organic working fluid (52%-ethanol, 48% water mixture) is presented. Properties for water and steam are provided based on Helmholtz and Gibbs free energy principles.

3.1 Equations of State for Water

This is based on the International Association for the Properties of Water and Steam (IAPWS) Industrial Formulation (IF97) in [Int07]. The state equations are empirically fitted by sums of products of vector variables and independent thermodynamic variables. The equations are divided into phase regions, of interest are the subcooled, saturated liquid/vapor, and superheated regions. The

coefficient vectors can be found in [Int07].

3.1.1 Saturated Liquid and Vapor

The basic equation for the saturated liquid and vapor phases is a fundamental equation for the Gibbs free energy.

$$\frac{g(P,T)}{RT} = \gamma(\pi,\tau) = \sum_{i=1}^{34} n_i(7.1-\pi)^{I_i}(\tau-1.222)^{J_i} \tag{3.1}$$

where $\pi = \frac{P_{sat}}{P^*}$ and $\tau = \frac{T^*}{T_{sat}}$. Note that the pressure and temperature are at saturated conditions in two-phase flow *i.e.* $T = T_{sat}$ and $P = P_{sat}$. (Obtained from Saturation phase). In saturation, temperature and pressure are not independent *i.e.* $T = f(P)$.

The fundamental equation for the superheated steam phase is given by

$$\frac{g(P,T)}{RT} = \gamma(\pi,\tau) = \gamma^o(\pi,\tau) + \gamma^r(\pi,\tau) \tag{3.2}$$

where $\gamma^o = ln(\pi) + \sum_{i=1}^{9} n_i^o \tau^{J_i^o}$ and $\gamma^r = \sum_{i=1}^{43} n_i \pi^{I_i}(\tau-0.5)^{J_i}$

The familiar thermodynamic properties can be determined by partial differentiation; refer to [Int07]. Recall the following derivative terms are needed for this phase:

$$\frac{d(\rho h)}{dP} \quad \frac{d\rho}{dP} \quad \frac{dh}{dP} \tag{3.3}$$

Special attention is given to the following properties:

$$\frac{d(\rho h)}{dP} = \rho\frac{dh}{dP} + h\frac{d\rho}{dP}$$

3.1.1.1 Saturated Liquid and Vapor

The empirical relation between saturation temperature and pressure is given below.

$$T_{sat} = \frac{n_{10} + D - [(n_{10} + D)^2 - 4(n_9 + n_{10}D)]^{\frac{1}{2}}}{2} T^*, \qquad T^* = 1K$$

$$D = \frac{2G}{-F - (F^2 - 4EG)^{\frac{1}{2}}}$$

$$E = \beta^2 + n_3\beta + n_6$$

$$F = n_1\beta^2 + n_4\beta + n + 7$$

$$G = n_2\beta^2 + n_5\beta + n_8$$

$$\beta = \left(\frac{P_{sat}}{P^*}\right)^{\frac{1}{4}}, \qquad P^* = 1MPa$$

$$\frac{d\rho}{dP} = \frac{d\rho}{d\pi}\frac{d\pi}{dP} + \frac{d\rho}{d\tau}\frac{d\tau}{dP}$$

$$\frac{d\rho}{d\pi} = \frac{-\tau P^* \left(RT^* \sum_{i=1}^{34} n_i I_i (I_i - 1)(7.1 - \pi)^{I_i - 1} (\tau - 1.222)^{J_i} \right)}{\left[RT^* \left(\sum_{i=1}^{34} -n_i I_i (7.1 - \pi)^{I_i - 1} (\tau - 1.222)^{J_i} \right) \right]^2}$$

$$\frac{d\pi}{dP} = \frac{1}{P^*}$$

$$\frac{d\rho}{d\tau} = \frac{A - \tau P^* \left(RT^* \left(\sum_{i=1}^{34} -n_i I_i (7.1 - \pi)^{I_i - 1} J_i (\tau - 1.222)^{J_i - 1} \right) \right)}{\left[RT^* \left(\sum_{i=1}^{34} -n_i I_i (7.1 - \pi)^{I_i - 1} (\tau - 1.222)^{J_i} \right) \right]^2}$$

$$A = \left(RT^* \left(\sum_{i=1}^{34} -n_i I_i (7.1 - \pi)^{I_i - 1} (\tau - 1.222)^{J_i} \right) \right) P$$

$$\frac{d\tau}{dP} = \frac{d\tau}{dT}\frac{dT}{dP} = \left(\frac{-T^*}{T^2} \right) \frac{dT}{dP}$$

$$\frac{dT}{dP} = \frac{T^*}{2} \left[\frac{dD}{dP} - \frac{1}{2} \left((n_{10} + D)^2 - 4 (n_9 + n_{10} D) \right)^{-\frac{1}{2}} 2 (n_{10} + D) \frac{dD}{dP} - 4 n_{10} \frac{dD}{dP} \right]$$

$$\frac{dD}{dP} = \frac{\left[-F - (F^2 - 4EG)^{\frac{1}{2}} 2 \frac{dG}{dP} - B \right]}{\left[-F - (F^2 - 4EG)^{\frac{1}{2}} \right]^2}$$

$$B = 2G \left[-\frac{dF}{dP} - \frac{1}{2} \left(F^2 - 4EG \right)^{-\frac{1}{2}} \left(2F \frac{dF}{dP} - 4 \left(E \frac{dG}{dP} + G \frac{dE}{dP} \right) \right) \right]$$

$$\frac{dE}{dP} = 2\beta \frac{d\beta}{dP} + n_3 \frac{d\beta}{dP}$$

$$\frac{dF}{dP} = 2n_1\beta\frac{d\beta}{dP} + n_4\frac{d\beta}{dP}$$
$$\frac{dG}{dP} = 2n_2\beta\frac{d\beta}{dP} + n_5\frac{d\beta}{dP}$$
$$\frac{d\beta}{dP} = \frac{P^*}{4}\left(\frac{P_{sat}}{P^*}\right)^{\frac{1}{4}} \qquad P^* = 1MPa$$

$$\frac{dh}{dP} = \frac{dh}{d\pi}\frac{d\pi}{dP} + \frac{dh}{d\tau}\frac{d\tau}{dP}$$
$$\frac{dh}{d\pi} = RT^*\sum_{i=1}^{34} -n_i I_i (7.1-\pi)^{I_i-1} J_i (\tau - 1.222)^{J_i-1}$$
$$\frac{dh}{d\tau} = RT^*\sum_{i=1}^{34} n_i (7.1-\pi)^{I_i} J_i (J_i-1)(\tau - 1.222)^{J_i-2}$$

3.1.2 Superheated Steam

The basic equation for the superheated vapor phase is based on a fundamental equation for the Gibbs free energy g, separated into an idea-gas part γ^0 and a residual part γ^r.

$$\frac{g(P,T)}{RT} = \gamma(\pi,\tau) = \gamma^0(\pi\tau) + \gamma^r(\pi,\tau)$$
$$= ln(\pi) + \sum_{i=1}^{9} n_i^o \tau^{J_i^o} + \sum_{i=1}^{43} n_i \pi^{I_i}(\tau - 0.5)^{J_i}$$

where $\pi = \frac{P}{P^*}$ and $\tau = \frac{T^*}{T}$ with $P^* = 1MPa$ and $T^* = 540K$.

The familiar thermodynamic properties can be determined by partial differentiation; refer to [Int07]. Recall the following derivative terms are needed for this phase:

$$\left.\frac{\partial\rho}{\partial P}\right|_h \quad \left.\frac{\partial\rho}{\partial h}\right|_P \tag{3.4}$$

$$\frac{\partial \rho}{\partial P}\Big|_h = \frac{\partial \rho}{\partial \pi}\frac{\partial \pi}{\partial P} + \frac{\partial \rho}{\partial \tau}\frac{\partial \tau}{\partial P}$$

$$\frac{\partial \tau}{\partial P} = \frac{\partial \tau}{\partial T}\frac{\partial T}{\partial P}\Big|_h = -\frac{T^*}{T^2}\frac{\partial \theta(\pi,\eta)}{\partial P}T^*$$

where

$$\frac{T(P,h)}{T^*} = \theta(\pi,\eta) = \sum_1^{34} n_i \pi_i^I (\eta - 2.1)_i^J$$

$$\frac{\partial \theta}{dP} = \frac{\partial \theta}{\partial \pi}\frac{\partial \pi}{\partial P} + \frac{\partial \theta}{\partial \eta}\underbrace{\frac{\partial \eta}{\partial P}}_{0} \text{ due to } \quad (P,h) \quad \text{independence}$$

$$= \sum_1^{34} n_i I_i \pi^{I_i - 1}(\eta - 2.1)^{J_i}\frac{1}{P^*}$$

with

$$\theta = \frac{T}{T^*}$$
$$\pi = \frac{P}{P^*}$$
$$\eta = \frac{h}{h^*}$$
$$T^* = 1K$$
$$P^* = 1MPa$$
$$h^* = 2000\frac{kJ}{kg}$$

$$\frac{\partial \rho}{\partial \tau} = \frac{RT^*(\gamma_\pi^o + \gamma_{pi}^r)P^* - \tau P^*(RT^*(\gamma_{\pi\tau}^o + \gamma_{\pi\tau}^r))}{(RT^*(\gamma_\pi^o + \gamma_\pi^r))^2}$$
$$\frac{\partial \rho}{\partial \pi} = -\frac{\tau P^*(RT^*(\gamma_{\pi\pi}^o + \gamma_{\pi\pi}^r))}{(RT^*(\gamma_\pi^o + \gamma_\pi^r))^2}$$
$$\frac{d\pi}{dP} = \frac{1}{P^*}$$

$$\frac{\partial \rho}{\partial h} = \frac{\partial \rho}{\partial \pi}\frac{\partial \pi}{\partial h} + \frac{\partial \rho}{\partial \tau}\frac{\partial \tau}{\partial h}$$
$$\frac{\partial \pi}{\partial h} = \frac{\partial P}{\partial h} = 0 \quad \text{due to} \quad (P, h) \quad \text{independence.}$$
$$\frac{\partial \tau}{\partial h} = \frac{\partial \tau}{\partial T}\frac{\partial T}{\partial h} = -\frac{T^*}{T^2}\frac{\partial \theta(\pi, \eta)}{\partial h}T^*$$
$$= -\frac{T^*}{T^2}\left(\frac{\partial \theta}{\partial \pi}\underbrace{\frac{\partial \pi}{\partial h}}_{0} + \frac{\partial \theta}{\partial \eta}\frac{\partial \eta}{\partial h}\right)T^*$$
$$= -\left(\frac{T^*}{T}\right)^2\left[\left(\sum_1^{34} n_i \pi^{I_i} J_i(\eta - 2.1)^{J_i - 1}\right)\frac{1}{h^*}\right]$$

3.1.3 Transport Equations of State

The interested properties are viscosity, thermoconductivity, and Prandtl number. [Int08a, Int08b] provide interpolating thermoconductivity and viscosity equations for general and scientific use as a function of temperature, density, and specific heat capacity (constant pressure). An equation for industrial water is also given. The range of validity for the equation is suitable for operating points in this dissertation. The interpolating equation is given by

$$\bar{\lambda} = \bar{\lambda}_0\left(\bar{T}\right) + \bar{\lambda}_1\left(\bar{T}, \bar{\rho}\right) + \bar{\lambda}_2\left(\bar{T}, \bar{\rho}\right) \tag{3.5}$$

where

$$\bar{\lambda}_0 = \frac{\sqrt{\bar{T}}}{\sum_{i=0}^{3}\frac{L_i}{\bar{T}^i}} \tag{3.6}$$

$$\bar{\lambda}_1 = e^{\bar{\rho}\sum_{i=0}^{4}\sum_{j=0}^{5} L_{ij}\left(\frac{1}{\bar{T}}-1\right)^i(\bar{\rho}-1)^j} \tag{3.7}$$

$$\bar{\lambda}_2 = \frac{(55.071)(0.0013848)}{\bar{\mu}_0(\bar{T})\bar{\mu}_1(\bar{T},\bar{\rho})}\left(\frac{\bar{T}}{\bar{\rho}}\right)^2\left(\frac{\partial\bar{\rho}}{\partial\bar{T}}\right)^2_{\bar{\rho}}\bar{\chi}_T^{0.4678}\sqrt{\bar{\rho}}e^{-18.66(\bar{T}-1)^2-(\bar{\rho}-1)^4} \tag{3.8}$$

Refer to [Int08a] for the coefficient values and further details.

[Int08b] derives a formula for (liquid) water visocity as a function of temperature and density:

$$\bar{\mu} = \bar{\mu}_0(\bar{T})\bar{\mu}_1(\bar{T},\bar{\rho})\bar{\mu}_2(\bar{T},\bar{\rho}) \tag{3.9}$$

where

$$\bar{\mu}_0(\bar{T}) = \frac{100\sqrt{\bar{T}}}{\sum_{i=0}^{3}\frac{H_i}{\bar{T}^i}} \tag{3.10}$$

and

$$\bar{\mu}_0(\bar{T},\bar{\rho}) = e^{\rho\sum_{i=0}^{5}\left(\frac{1}{\bar{T}-1}\right)^i\sum_{j=0}^{6}H_{ij}(\bar{\rho}-1)^j} \tag{3.11}$$

$\bar{\mu}_2$ is referred to as the critical enhancement term and is only significant for a small region around the critical point. Refer to [Int08b] for details and coefficients.

3.2 Equations of States for General Fluids

Not every working fluid has easily accessible equations of state, if any exist, for the desired operating conditions. Transport and thermodynamic tables of properties typically exist for many studied fluids. Selected ranges of these property tables can be programmed into software and 2-D lookup and interpolation methods can be employed to retrieve desired properties defined by two independent properties. This method may require significant computation time. Another method is to create a data fit from these property tables which can be completed off-line to reduce computation demand in simulations. This section describes a fluid property database created by the National Institute of Standards and Technology (NIST) and a least squares fitting procedure to generate equations of state for a variety of working fluids and their mixtures. 52% Ethanol and 48% water mixture will be examined.

3.2.1 Reference Fluid Thermodynamic and Transport Properties (REFPROP) Database

The National Institute of Standards and Technology (NIST) created the database for thermodynamic and transport properties. Available properties include the following:

1. Temperature
2. Pressure
3. Density
4. Energy
5. Enthalpy
6. Entropy
7. Cv, Cp
8. Sound Speed
9. Compressibility Factor
10. Joule Thompson Coefficient

11. Quality
12. 2nd and 3rd Virial Coefficients
13. 2nd and 3rd Acoustic Virial Coefficients
14. Helmholtz/Gibbs Energy
15. Heat of Vaporization
16. Fugacity (Coeffiecient)
17. Chemical Potential
18. K value
19. Molar Mass
20. B12
21. Thermal Conductivity
22. Viscosity
23. Kinematic Viscosity
24. Thermal Diffusivity
25. Prandtl Number
26. Surface Tension
27. Dielectric Constant
28. Gross and Net Heating Values
29. Isothermal Compressibility
30. Volume Expansivity
31. Isentropic Coefficient
32. Adiabatic Compressibility
33. Specific Heat Input
34. Exergy
35. Gruneisen
36. Critical Flow Factor
37. Excess Values
38. dp/dr
39. d^2p/dr^2
40. dp/dT
41. dr/dT
42. dr/dp
43. and many others.

This dissertation uses properties from REFPROP Database 23, Version 8.0. [LHM07].

3.2.2 Thermodynamic Toolbox (ThermoBox) for MATLAB

ThermoBox [Lim11], a MATLAB toolbox for modeling of thermodynamic processes, provides a least squares fitting routine. Given a set of dependent property z with independent properties x and y (each being $m \times 1$ vectors), the routine finds the best fit $\hat{z}$ of z by

$$\hat{z} = A(x, y)q \tag{3.12}$$

where A is a $m \times n$ matrix whose rows are sets of functions of x_i and y_i and q is a $n \times 1$ vector of fit coefficients. The ith row of A has the following form

$$\begin{bmatrix} 1 & x_i & y_i & x_i^2 & x_i y_i & y_i^2 \cdots x_i^{N-1} & x_i^{N-2} y_i \cdots x_i y_i^{N-2} & y_i^{N-1} \cdots x_i^N & x_i^{N-1} & y_i^N \end{bmatrix} \tag{3.13}$$

The least squares problem is to find the q that minimizes the ℓ^2 norm of the error between z and $\hat{z}$. That is,

$$\text{minimize} \|z - Aq\| \tag{3.14}$$

The solution is given by

$$q = A^\dagger z \tag{3.15}$$

where $A^\dagger$ is the pseudo-inverse of A.

Note the fit coefficient q is found off-line. The property z is calculated by generating the row vector of functions of x and y with values of the two independent properties and performing a vector multiplication with the column vector q.

The routine performs the property fits to order ten and chooses the fit with the highest R value.

3.2.3 Property Fitting for Ethanol-Water Mixture

The following figures are selected property fits for ethanol-water mixture in the vapor phase. The chosen independent properties are density and temperature, though the user can freely make other choices. Property fits for properties involving enthalpy and pressure as independent properties are also presented since the models in this dissertation make those property choices. The pressure range of the property data is from 0.01 MPa to 10 MPa.

The measure of the closeness of fit is given by R, the coefficient of fit. It is defined as

$$R = 1 - \frac{\left(\sum z - \hat{z}\right)^2}{\left(\sum z - \bar{z}\right)^2} \tag{3.16}$$

The fit coefficient is close to 1 in all of the following properties, though the fitting errors are more pronounced at the low temperature and high density regions.

3.2.3.1 Property Fits for Density and Temperature as Independent Properties

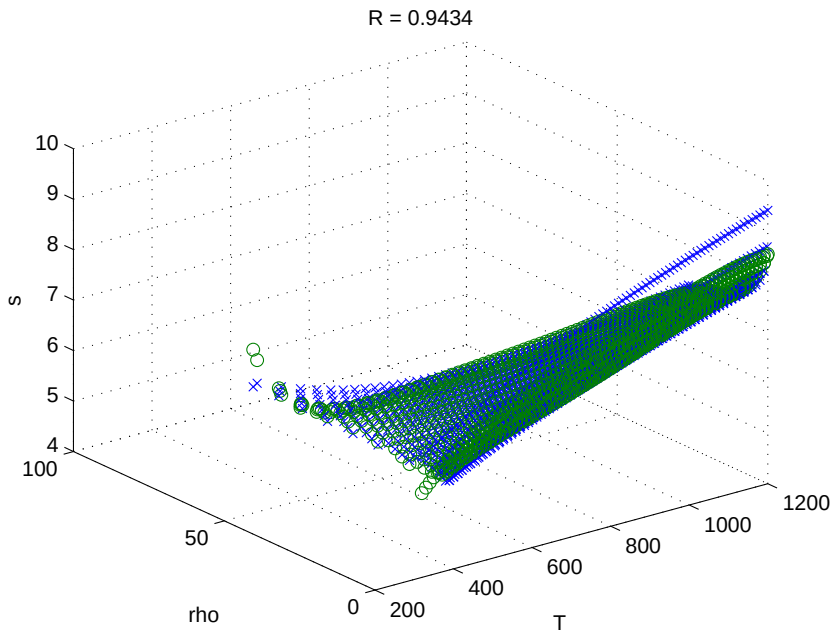

Figure 3.1: ThermoBox Property Fit for Entropy, Ethanol-water (Vapor)

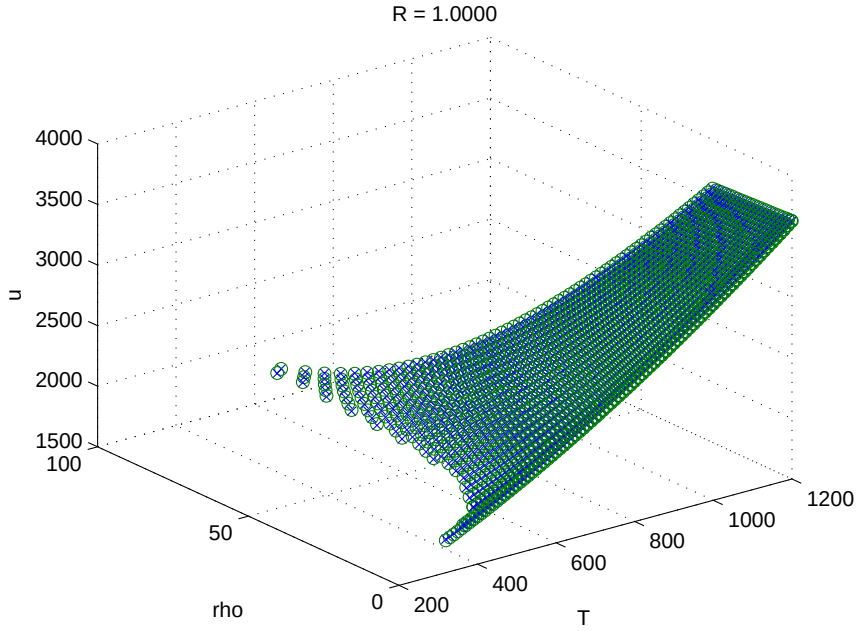

Figure 3.2: ThermoBox Property Fit for Internal Energy, Ethanol-water (Vapor)

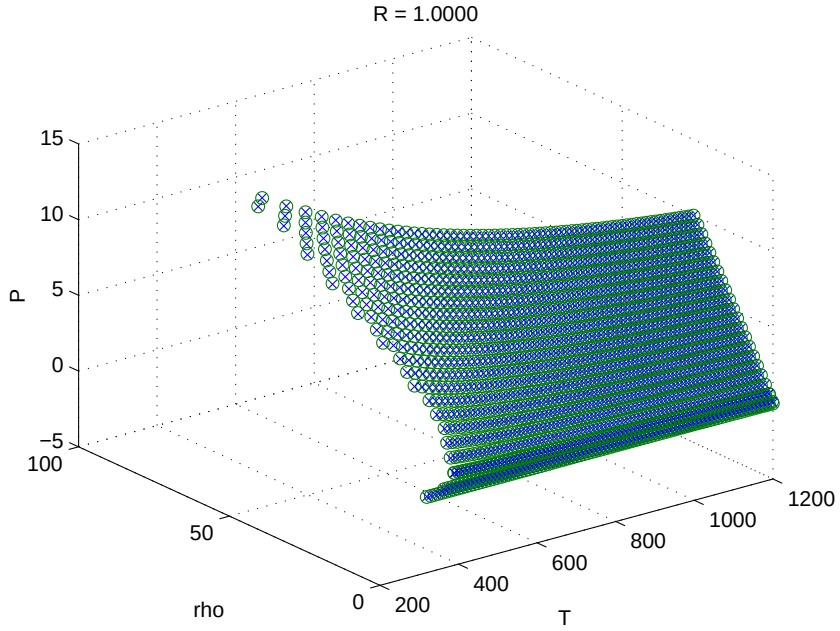

Figure 3.3: ThermoBox Property Fit for Pressure, Ethanol-water (Vapor)

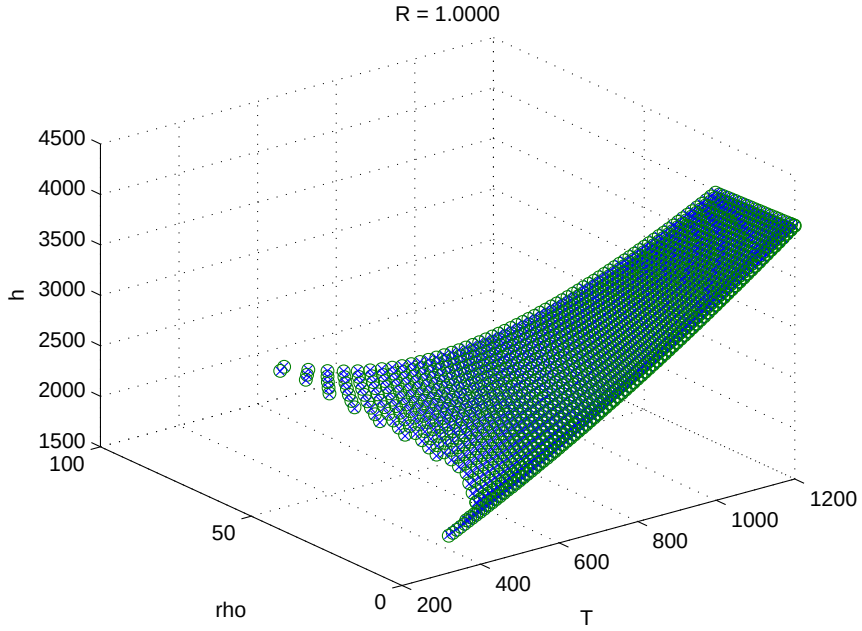

Figure 3.4: ThermoBox Property Fit for Enthalpy, Ethanol-water (Vapor)

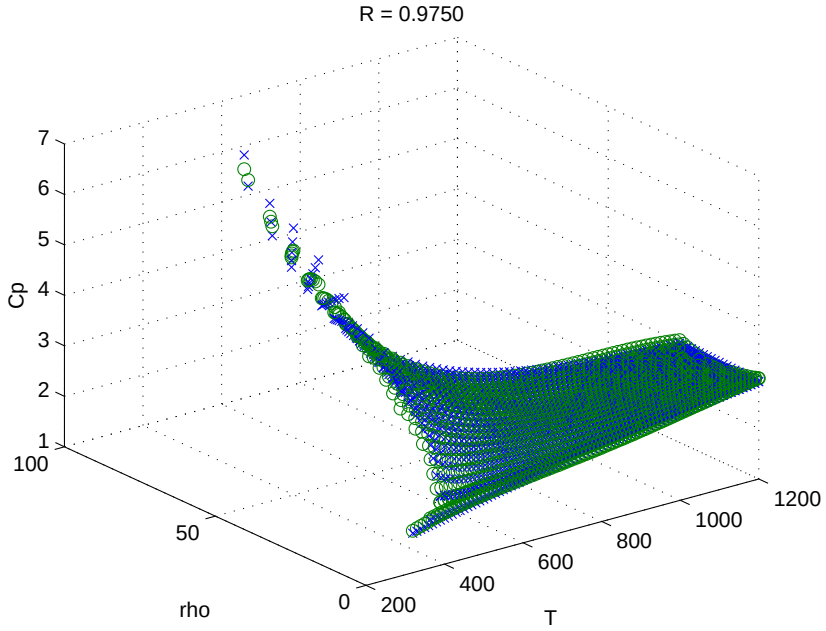

Figure 3.5: ThermoBox Property Fit for Specific Heat Capacity at Constant Pressure, Ethanol-water (Vapor)

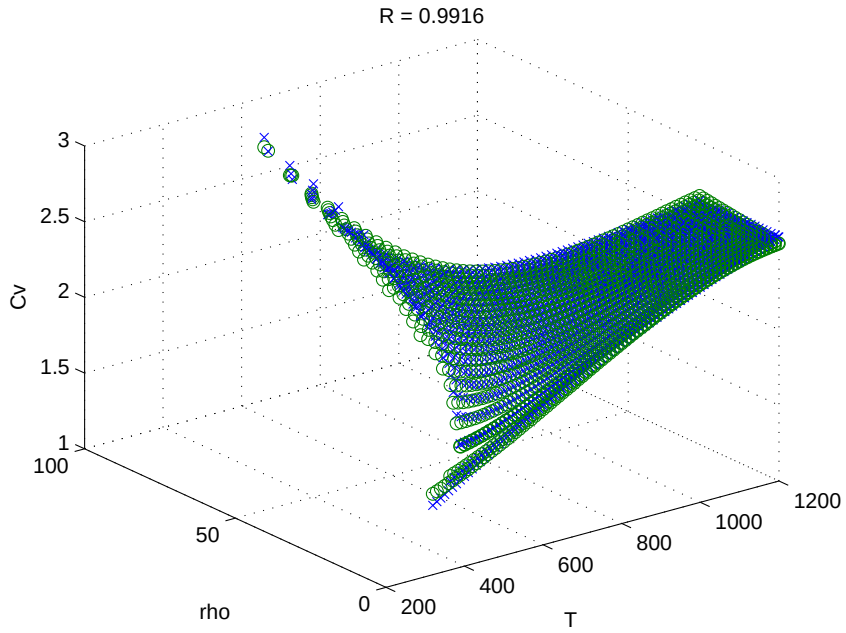

Figure 3.6: ThermoBox Property Fit for Specific Heat Capacity at Constant Volume, Ethanol-water (Vapor)

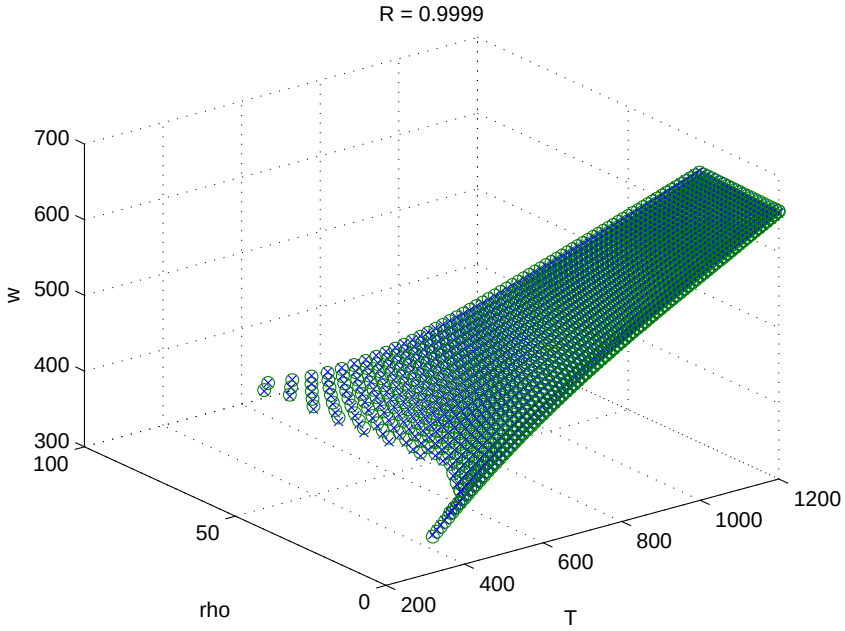

Figure 3.7: ThermoBox Property Fit for Speed of Sound, Ethanol-water (Vapor)

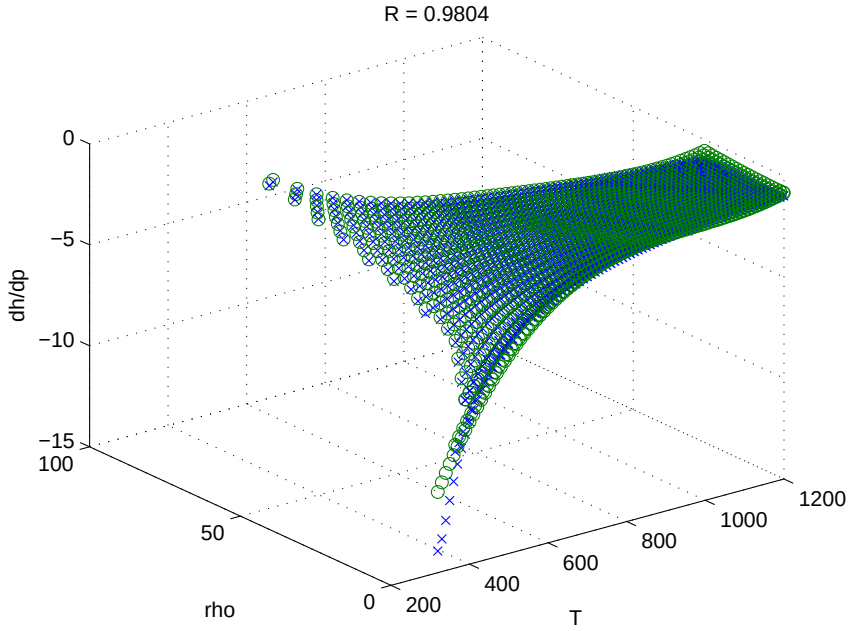

Figure 3.8: ThermoBox Property Fit for Partial Enthalpy Partial Density, Ethanol-water (Vapor)

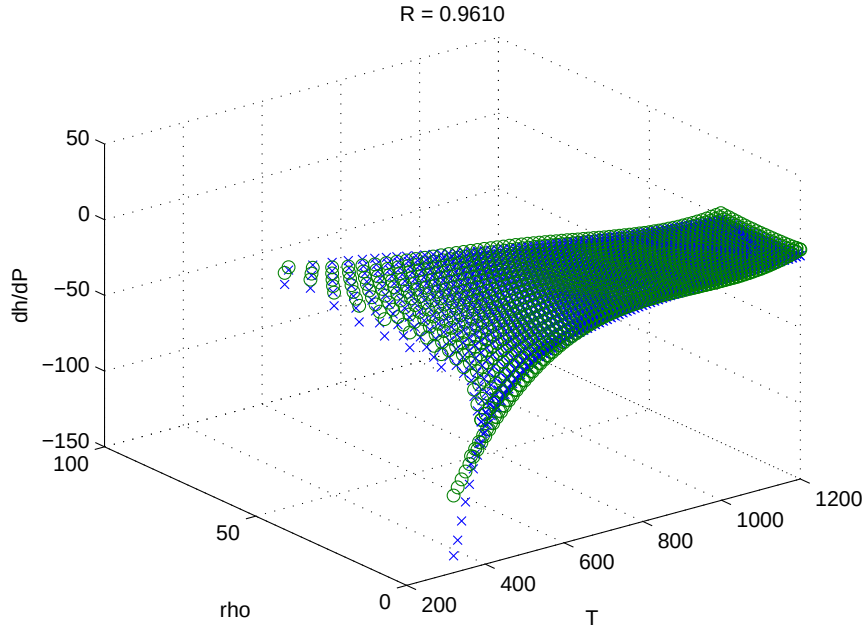

Figure 3.9: ThermoBox Property Fit for Partial Enthalpy Partial Pressure, Ethanol-water (Vapor)

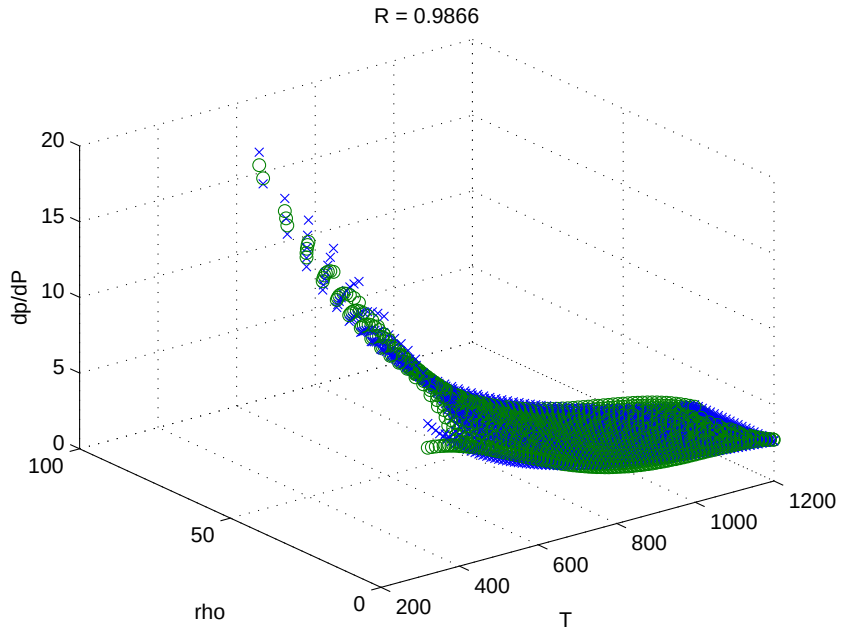

Figure 3.10: ThermoBox Property Fit for Partial Density Partial Pressure, Ethanol-water (Vapor)

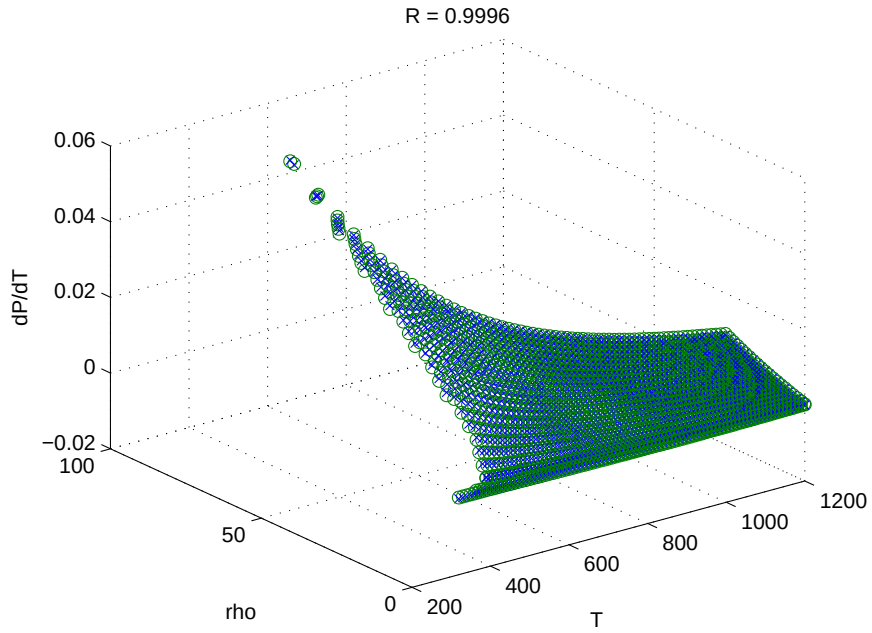

Figure 3.11: ThermoBox Property Fit for Partial Pressure Partial Temperature, Ethanol-water (Vapor)

3.2.3.2 Property Fits for Pressure and Enthalpy as Independent Properties

The following plots show the property values calculated during the Flat Road driving cycle presented in Chapter 2. The retrived properties appear nonlinear around these highlighted regions and deters linearizing the property functions that will sacrifice accuracy for faster computation time.

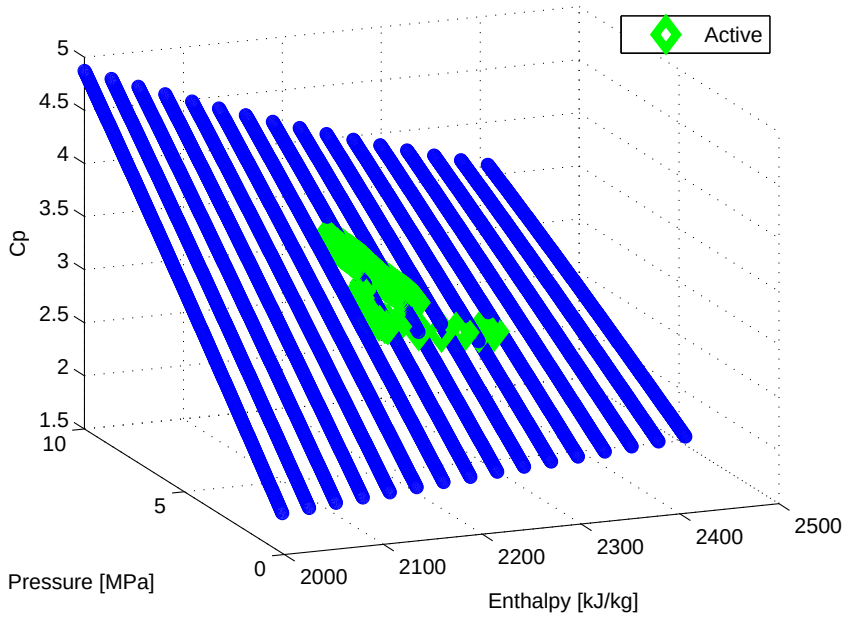

Figure 3.12: ThermoBox Property Fit for Specific Heat Capacity at Constant Pressure, Ethanol-water (Vapor)

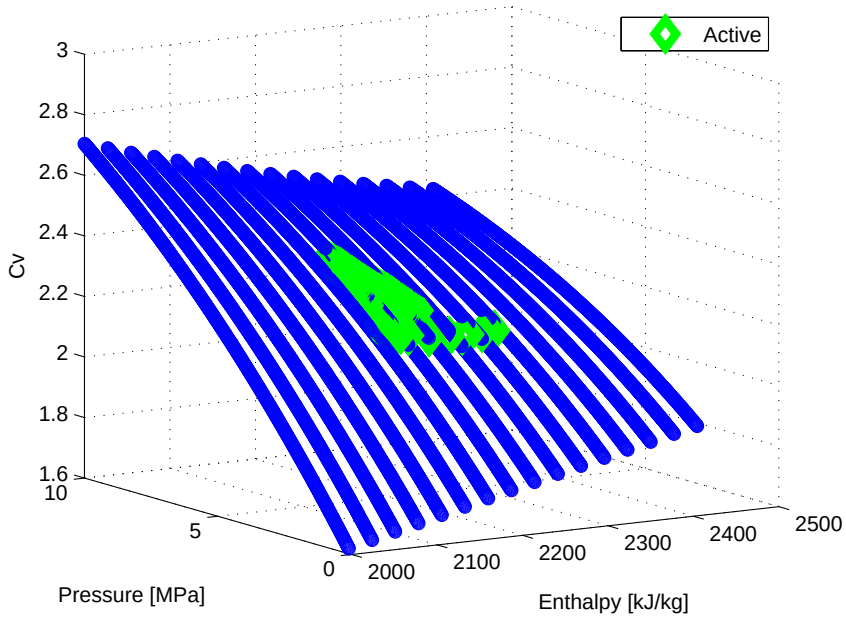

Figure 3.13: ThermoBox Property Fit for Specific Heat Capacity at Constant Volume, Ethanol-water (Vapor)

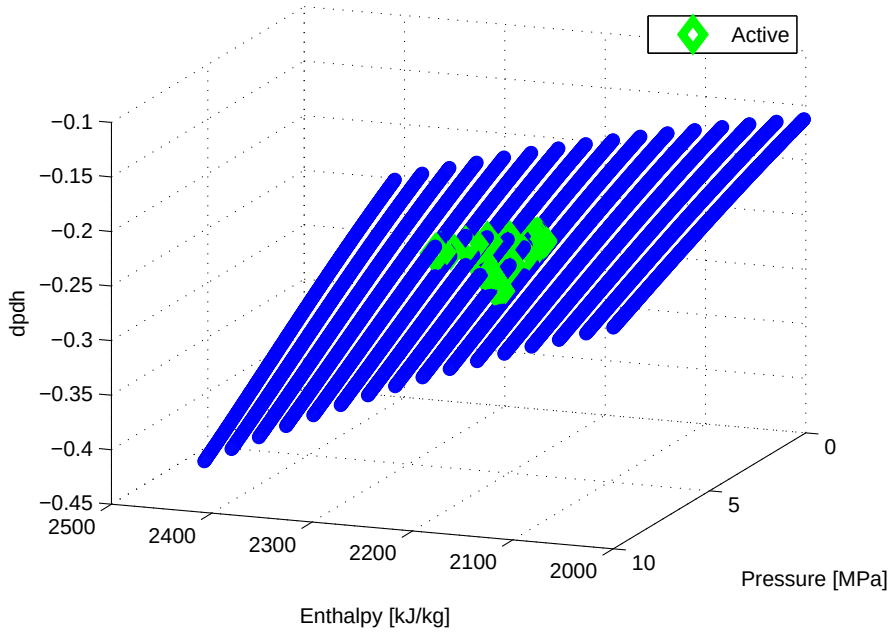

Figure 3.14: ThermoBox Property Fit for Partial Density Partial Enthalpy, Ethanol-water (Vapor)

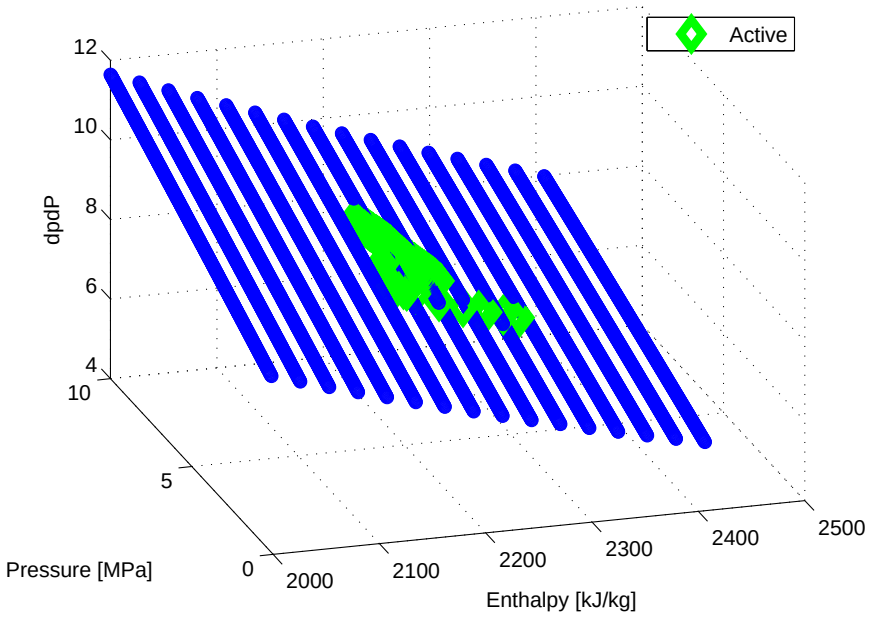

Figure 3.15: ThermoBox Property Fit for Partial Density Partial Pressure, Ethanol-water (Vapor)

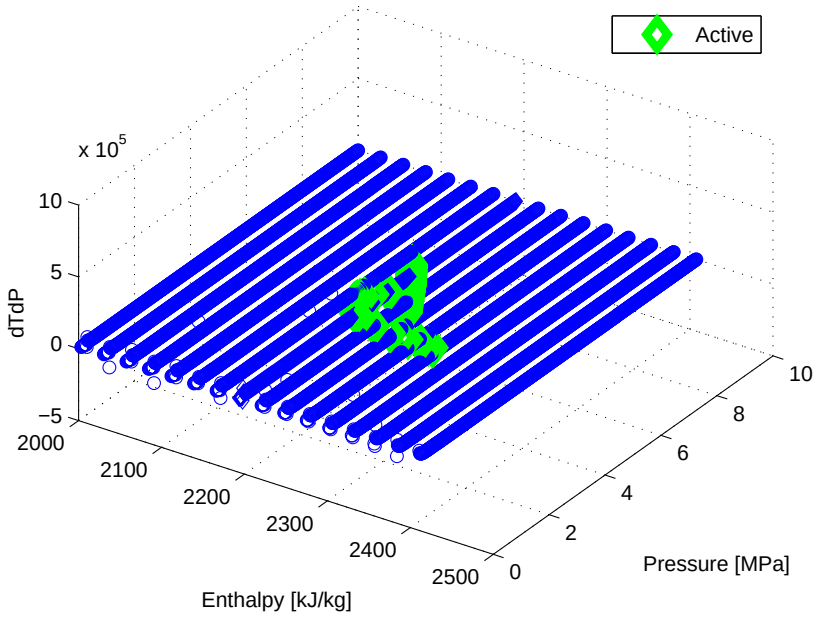

Figure 3.16: ThermoBox Property Fit for Partial Temperature Partial Pressure, Ethanol-water (Vapor)

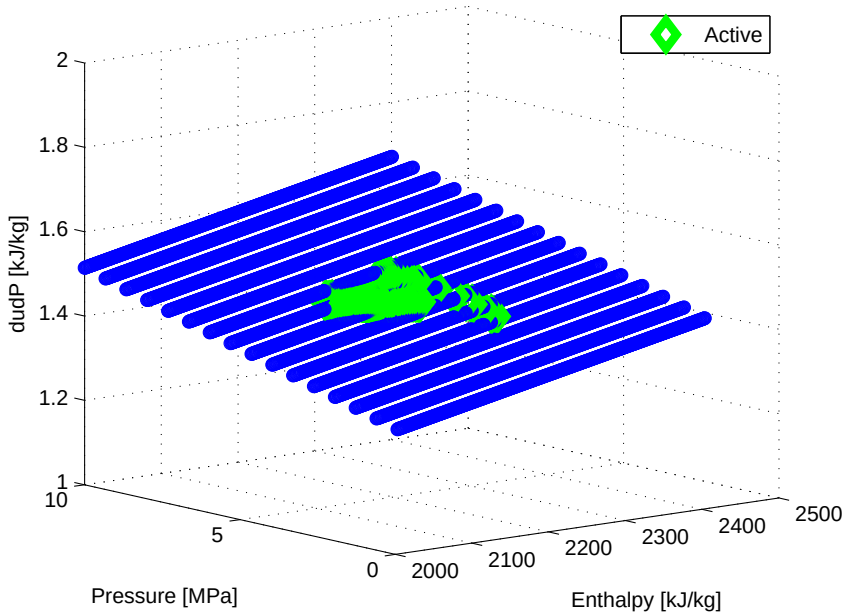

Figure 3.17: ThermoBox Property Fit for Partial Internal Energy Partial Pressure, Ethanol-water (Vapor)

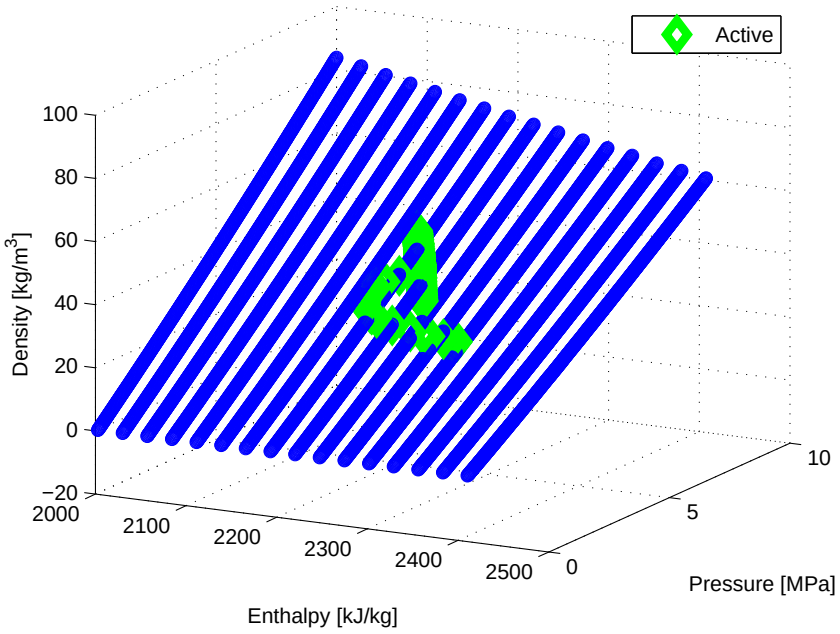

Figure 3.18: ThermoBox Property Fit for Density, Ethanol-water (Vapor)

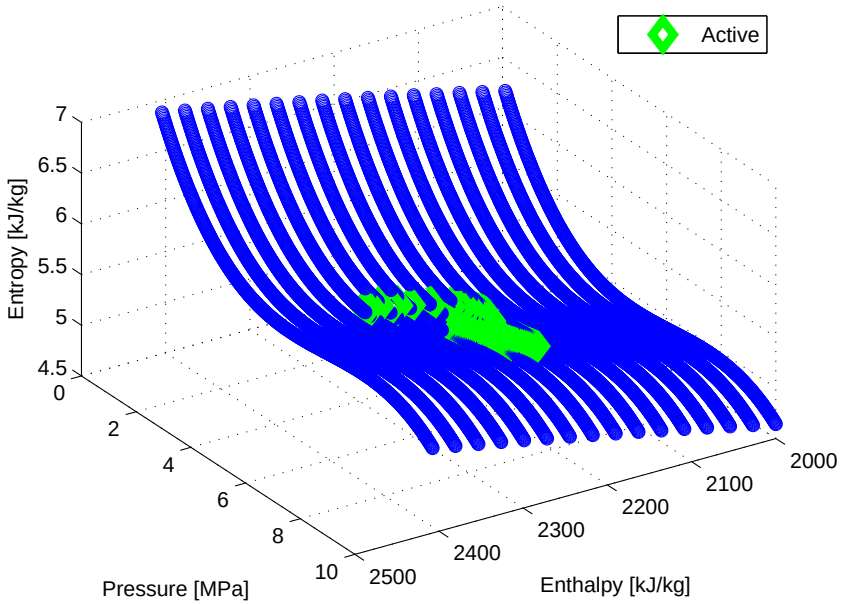

Figure 3.19: ThermoBox Property Fit for Entropy, Ethanol-water (Vapor)

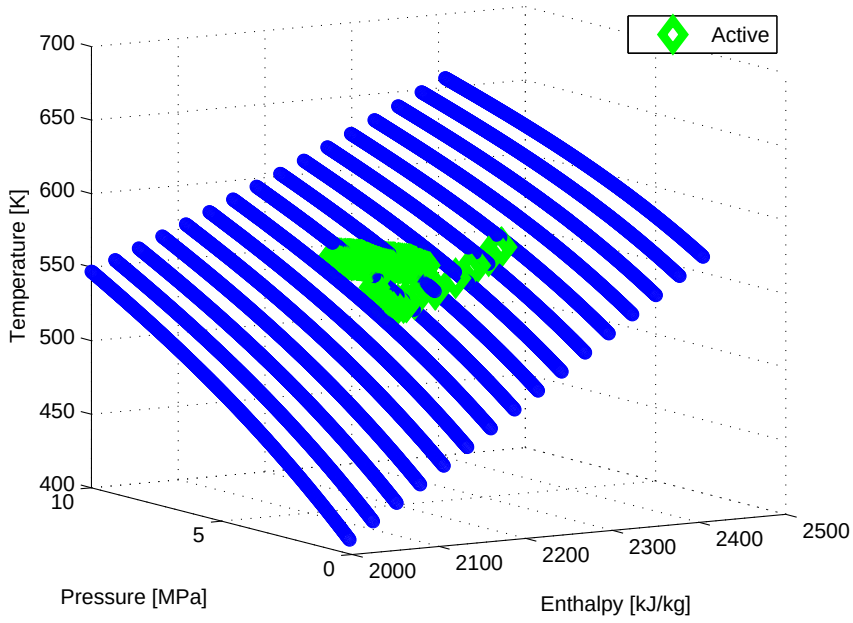

Figure 3.20: ThermoBox Property Fit for Temperature, Ethanol-water (Vapor)

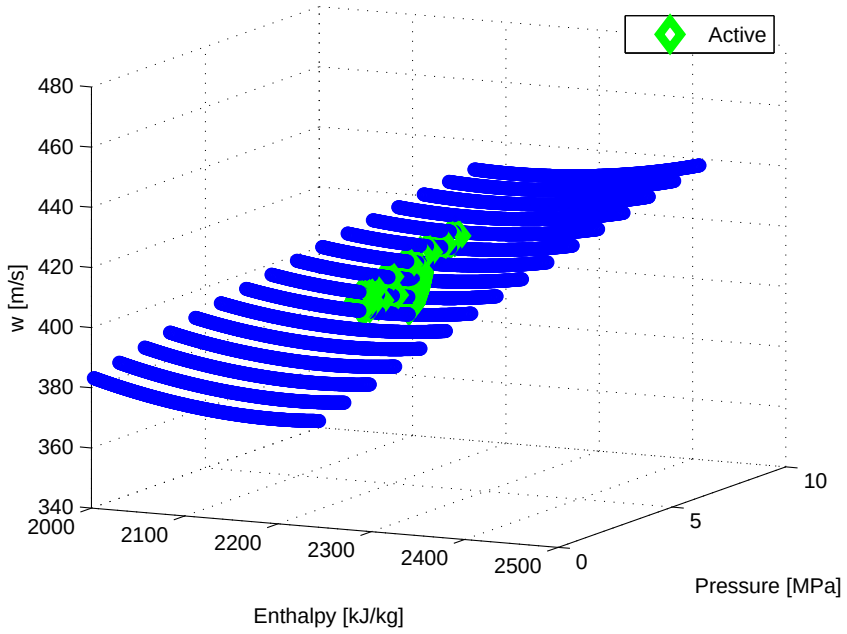

Figure 3.21: ThermoBox Property Fit for Speed of Sound, Ethanol-water (Vapor)

3.2.3.3 Advantages and Disadvantages of Least Squares Fitting

Due to the complexity of the Rankine component models, fast computation speed is important in their simulations. Speed tests show that the 2-D look-up table method in MATLAB is up to ten times slower than the Least Squares Routine. However, the least squares routine is slower than 2-D look-up in Simulink, due to differences in memory and resources are managed in MATLAB and Simulink. For fast computation and retrieval of thermodynamic properties, the 2-D table in Simulink is preferred.

Often times regions of thermodynamic properties are missing, rendering the table lookup method useless. The Least Squares Routine is useful in these situations to retrieve properties within the range of these regions for which properties are missing.

For quicker computation, the recommendation is to use table look up when simulating in Simulink and the Least Squares Routine in MATLAB.

CHAPTER 4

Static Rankine Cycle Modeling

This chapter describes modeling and analysis of Rankine Cycles (RCs) in the steady or static sense by assuming thermodynamics and component dynamics have reached equilibrium. The assumption allows fundamental thermodynamic analysis of static RC models and reveal their operating conditions based on steady heat sources and sinks. Component models for heat exchangers, valves, pumps, and expansion devices do not exhibit dynamic behavior in reaching steady-state operating conditions. The results are useful for establishing nominal RC operating conditions to validate with dynamic modeling in Chapter 5.

The heat transfer coefficients are based on a heat exchanger arrangement with internal working fluid flow through a circular tube and external concentric annular flow around the tube.

4.1 RC Model Design

Traditional thermodynamic analysis of RCs rely on identifying the steady-state operating points by assuming isentropic, isobaric, and adiabatic processes between states. Using the heat exchanger geometries and averaged heat source and sink properties given in Chapter 2, RC model designs are completed at two different evaporating pressures.

Figures 4.1 and 4.2 are the designed RC cycle for averaged heat source and sink

temperature for the Rolling Hills driving cycle at different evaporating pressures. The engine power improvement is based on an averaged engine power of 143 kW. It is given by

$$\text{Engine Power Improvement} = \frac{\text{Expander Power}}{\text{Engine Power}} \tag{4.1}$$

. Note that higher evaporating pressure leads to higher expander power and thus engine power improvement.

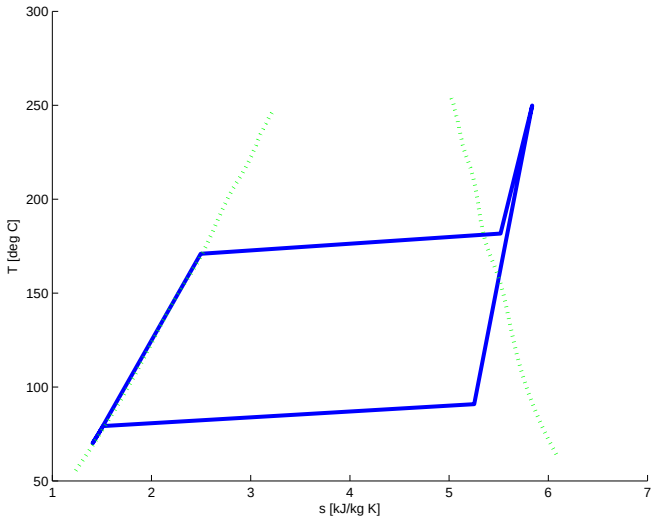

Figure 4.1: Design 1 of Static RC Model for Average Rolling Hills Road Cycle, T-s Diagram

Table 4.1: RC Design 1 ($P_e = 1.5$MPa, $P_c = 0.1$MPa)

$\dot{m}_{wf}$	0.0025 $[\frac{kg}{s}]$
$\dot{m}_h$, $\dot{m}_c$	0.062, 1.5 $[\frac{kg}{s}]$
$T_{h,in}$, $T_{h,out}$	430, 87 $[°C]$
$T_{c,in}$, $T_{c,out}$	60, 69 $[°C]$
N_{exp}, N_{pump}	0.85, 0.023[kW]
η_{exp}, η_{exp}	0.9, 0.9
Engine Improvement	0.6 [%]

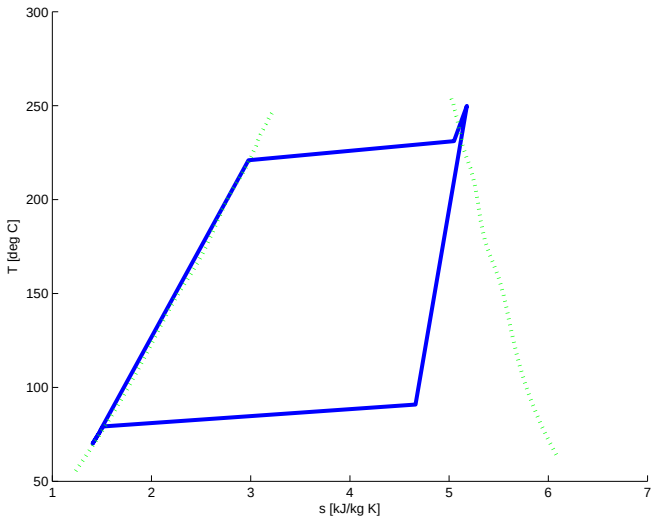

Figure 4.2: Design 2 of Static RC Model for Average Rolling Hills Road Cycle, T-s Diagram

Table 4.2: RC Design 2 ($P_e = 4$MPa, $P_c = 0.1$MPa)

$\dot{m}_{wf}$	0.0025 $[\frac{kg}{s}]$
$\dot{m}_h$, $\dot{m}_c$	0.062, 1.5 $[\frac{kg}{s}]$
$T_{h,in}$, $T_{h,out}$	430, 110 $[°C]$
$T_{c,in}$, $T_{c,out}$	60, 69 $[°C]$
N_{exp}, N_{pump}	1.23, 0.028 [kW]
η_{exp}, η_{exp}	0.9, 0.9
Engine Improvement	0.9 [%]

4.2 RC Model Optimization

This section presents an iterative routine that optimizes the steady-state cycle in the power generation sense by finding the highest working fluid mass flow rate for given pressures and heat addition and heat rejection. Furthermore, the optimized operating points satisfy a desired flow configuration temperature distribution of both working fluid and heat sink/sources. The optimization routine provides a more detailed approach to cycle design over the approach in the previous section. The main steps of the routine are as follows:

1. Define evaporator and condenser cross-sectional geometry and the number of fluid-phase regions. Note the length is intentionally undefined and to be determined by the routine

2. Iteration Parameters: Initialize evaporator pressure P_e and cold fluid flow rate $\dot{m}_c$ to higher than expected values. Set condenser pressure P_c

   (a) Iterate until temperature distribution achieves specified pinch point

gap

i. Initialize $T_{h,in}, \dot{m}$, define desired $T_{h,out}$

ii. Retrieve thermodynamic properties for working fluid in each zone

iii. Calculate boundary temperatures for each zone by energy balance of the (c)old and (h)ot fluid

$$\dot{m}_c C_{pc}(T_{c,out} - T_{c,in}) = \dot{m}_h C_{ph}(T_{h,in} - T_{h,out}) \tag{4.2}$$

iv. Check counter flow temperature distribution of hot and cold fluids make sense e.g. hot and cold fluid temperatures should have opposite slopes across the heat exchanger length

v. Repeat if temperature distribution not achieved, use lower P_e, reset $\dot{m}_c$ to initial high value

vi. Temperature distribution unachievable if $P_e \leq P_c$, end routine

vii. Calculate overall heat transfer coefficients for each zone with internal tubular flow and either concentric annuluar external flow (counter/parallel) or external cross flow

$$U = \frac{1}{\frac{1}{\alpha_i} + \frac{1}{\alpha_o}} \tag{4.3}$$

viii. Perform Log-mean Temperature Distribution analysis to obtain lengths of each zone (ΔT_1 and ΔT_2 defined for counter flow)

$$q = UA\Delta T_{lm} \quad \Delta T_{lm} = \frac{\Delta T_2 - \Delta T_1}{ln(\frac{\Delta T_2}{\Delta T_1})} \tag{4.4}$$

$$\Delta T_1 = T_{h,in} - T_{c,out} \quad \Delta T_2 = T_{h,out} - T_{c,in} \tag{4.5}$$

3. Retrieve thermodynamic properties for working fluid with evaporator outlet temperature and pressure conditions

4. Calculate expander outlet temperature conditions and power assuming isentropic expansion to condenser pressure

   (a) Set inlet temperature and pressure from expander, define desired T_{hout}. Set heat sink temperature and mass flow rate.

   (b) Retrieve thermodynamic properties for working fluid in each zone

   (c) Calculate boundary temperatures for each zone by energy balance

$$\dot{m}_c C_{pc}(T_{cout} - T_{cin}) = \dot{m}_h C_{ph}(T_{hin} - T_{hout}) \tag{4.6}$$

   (d) Calculate heat transfer coefficients for each zone with internal tubular flow and either concentric annuluar external flow (counter/parallel) or external cross flow

$$U = \frac{1}{\frac{1}{\alpha_i} + \frac{1}{\alpha_o}} \tag{4.7}$$

   (e) Perform Log-mean Temperature Distribution analysis to obtain lengths of each zone (ΔT_1 and ΔT_2 defined for counter flow)

$$q = UA\Delta T_{lm} \quad \Delta T_{lm} = \frac{\Delta T_2 - \Delta T_1}{ln(\frac{\Delta T_2}{\Delta T_1})} \tag{4.8}$$

$$\Delta T_1 = T_{h,in} - T_{c,out} \quad \Delta T_2 = T_{h,out} - T_{c,in} \tag{4.9}$$

   (a) Calculate pump power assuming it brings the fluid's enthalpy at condenser outlet to evaporator inlet in an isentropic compression process.

   (a) Retrieve entropy values for temperatures and pressures between each component

   (b) Draw T-s diagram

4.2.0.4 Assumptions and Limitations

In the Log Mean Temperature Difference (LMTD) method for computing lengths of fluid-phase zones, it had been assumed that the rates of change for the fluids' temperatures are proportional to the temperature difference. This assumption is valid for fluids with constant specific heats. Since the working fluid undergoing phase change and large temperature changes, varying specific heats vary significantly and make the LMTD approach inaccurate. Furthermore, the heat transfer coefficients should also be constant as well. To remedy this, averaged temperatures were assumed in each region to maintain constant specific heats and heat transfer coefficients. The engineer should keep this limitation in mind when examining the calculated lengths of the heat exchanger zones.

4.2.1 Simulation Results

4.2.1.1 Optimal RC Design 1

Figure 4.3 shows the design for the optimal static RC a given evaporating and condensing pressure of 1.5 MPa and 0.1 MPa, respectively. The flow configuration is counter flow for the evaporator and condenser. The exhaust gas heat source's temperature and mass flow rate are 443 $^{\circ}C$ and 0.0685 $\frac{kg}{s}$. The water heat sink's temperature and mass flow rate are 60 $^{\circ}C$ and 1.5 $\frac{kg}{s}$. The working fluid is 52% ethanol-48% water mixture.

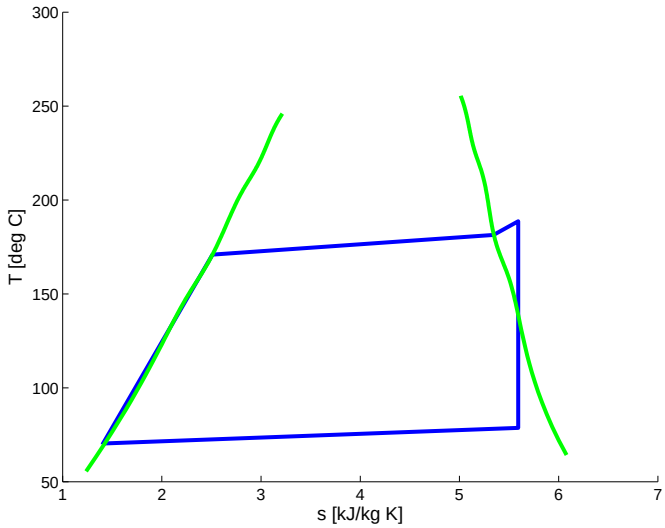

Figure 4.3: Static RC Model Design 1 for Average Rolling Hills Road Cycle, T-s Diagram

The counter flow evaporator assumes three fluid-phase zones while the counter flow condenser assumes two zones (two-phase, subcooled). The expander and pump power are 4.3 kW and 0.0149 kW, respectively. The thermal efficiency of the Rankine Cycle is 45.2 percent.

The temperature distributions of the three-zone evaporator and two-zone condenser are shown in Figures 4.4 and 4.5. The superheat and subcooled regions are small compared to the two-phase regions, which is consistent with the T-s diagram.

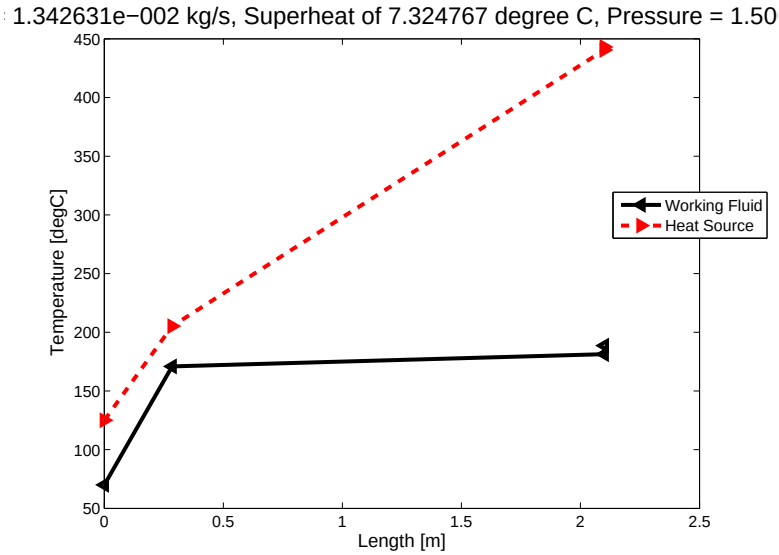

Figure 4.4: Static RC Model Design 1 for Average Rolling Hills Road Cycle, Evaporator Temperature Distribution

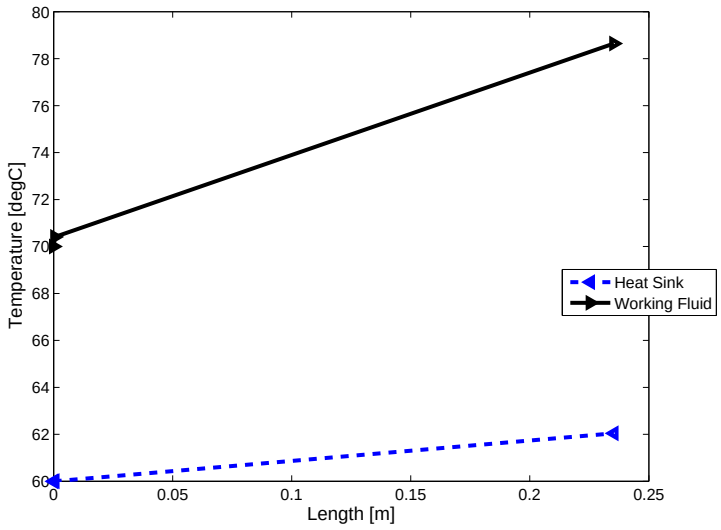

Figure 4.5: Static RC Model Design 1 for Average Rolling Hills Road Cycle, Condenser Temperature Distribution

4.2.1.2 Optimal RC Design 2

Figure 4.6 shows the design for the optimal static RC a given evaporating and condensing pressure of 4 MPa and 0.1 MPa, respectively. The flow configuration is counter flow for the evaporator and condenser. The exhaust gas heat source's temperature and mass flow rate are 443 $°C$ and 0.0685 $\frac{kg}{s}$. The water heat sink's temperature and mass flow rate are 60 $°C$ and 1.5 $\frac{kg}{s}$. The working fluid is 52% ethanol-48% water mixture.

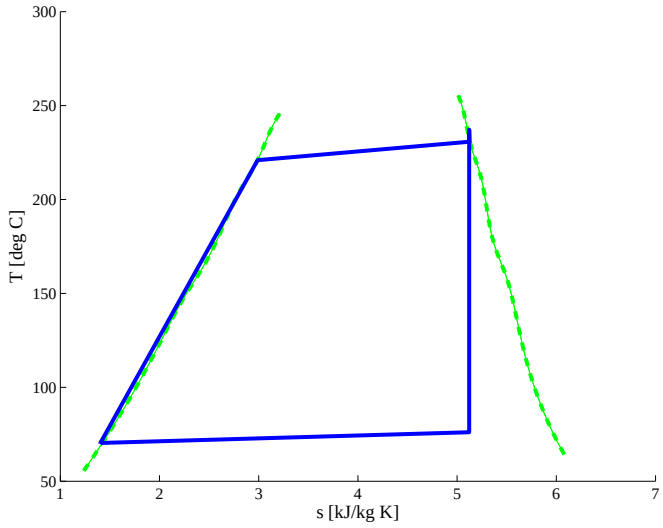

Figure 4.6: Static RC Model Design 2 for Average Rolling Hills Road Cycle, T-s Diagram

The counter flow evaporator assumes three fluid-phase zones while the counter flow condenser assumes two zones (two-phase, subcooled). The expander and pump power are 10.5 kW and 0.0402 kW, respectively. The thermal efficiency of the Rankine Cycle is 45.2 percent.

The temperature distributions of the three-zone evaporator and two-zone condenser are shown in Figures 4.7 and 4.8. The superheat and subcooled regions

are small compared to the two-phase regions, which is consistent with the T-s diagram.

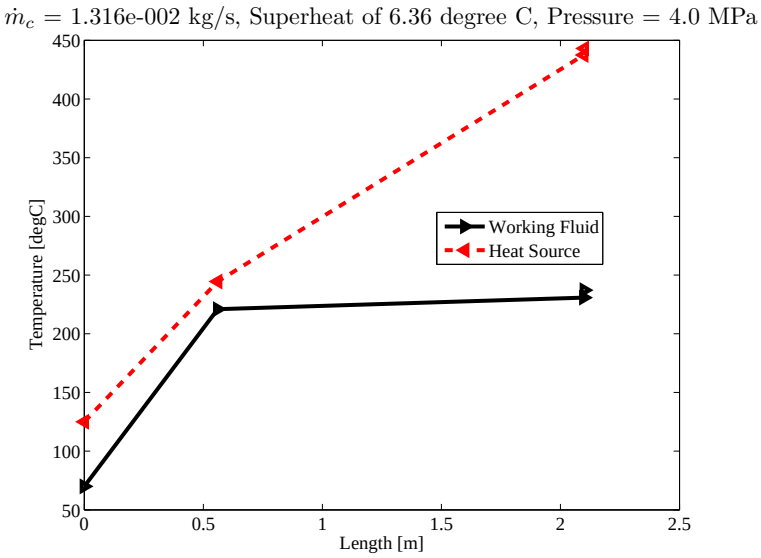

Figure 4.7: Static RC Model Design 2 for Average Rolling Hills Road Cycle, Evaporator Temperature Distribution

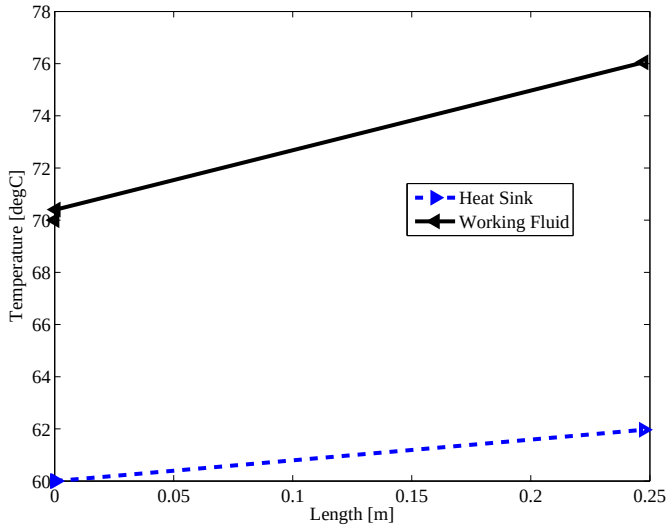

Figure 4.8: Static RC Model Design 2 for Average Rolling Hills Road Cycle, Condenser Temperature Distribution

4.2.2 Remarks

The optimization routine provides a more detailed approach to static RC modeling. Higher working fluid flow rates are achieved while satisfying the temperature distribution for multi-phase evaporating and condensing flows. As a result, the designs in the RC Modeling section report a lower expander power than the optimized model for the same heat source/sink conditions. For the set of heat source and sink conditions, the expander power ranges between 0.8 and 4 kW for Design 1 and between 1 and 10 kW for Design 2. These ranges provide an expected expander power for the dynamic RC model in Chapter 5 to achieve.

4.3 Pump Model

Previous work on Rankine cycle modeling and design suggests treatment of the pump model as a static component; its dynamics are much faster than that of the heat exchangers in the cycle [WLL90]. A general thermodynamic model given by [ZZH12] is presented along with a centrifugal pump model.

4.3.1 General Model

The outlet enthalpy h_{out} of the pump can be described by.

$$h_{out} = h_{in} + \frac{\bar{\nu}\left(P_{out} - P_{in}\right)}{\eta_{pump}} \tag{4.10}$$

where h_{in} is the inlet enthalpy, $\bar{\nu}$ is average specific volume, η_{pump} is the pump's isentropic efficiency, and P_{out} and P_{in} are the outlet and inlet pressures, respectively. The flow rate through the pump is given by

$$\dot{m}_{pump} = \mu K \omega \tag{4.11}$$

where μ is the throttle valve position, K is the pump constant, and ω is the pump speed.

4.3.2 Centrifugal

Centrifugal pumps are comprised of hydraulic and mechanical subsystems, and modeled according to the following fundamental equations [Ise03].

The delivery head $H(t)$ measures the energy difference between the inlet and outlet of pumps. For incompressible fluids such as water, the head is proportional to the pump pressure difference given by

$$H(t) = \frac{\Delta P(t)}{\rho g} \tag{4.12}$$

The pressure difference can be obtained from the following:

$$\Delta P = R_1\omega(t)^2 - 2R_2\omega(t)\frac{\dot{m}}{\rho} - R_3\left(\frac{\dot{m}}{\rho}\right)^2 \tag{4.13}$$

where the R coefficients are obtained from experimental/manufacturer data. The mass flow rate $\dot{m}$ is proportional to the pump angular speed ω.

$$\dot{m} = k\omega \tag{4.14}$$

The mechanical system is described by the torque generated by the motor to accelerate the overall inertia J:

$$T(t) = J\dot{\omega}(t) + T_F(t) + T_P(t) \tag{4.15}$$

The friction losses captured by $T_F(t)$ can be modeled by

$$T_F(t) = T_{Fc}sign(\omega) + T_{Fv}\dot{\omega} \tag{4.16}$$

where T_{Fc} is the Coulomb friction and T_{fv} is the viscous friction torque.

The required pump torque $T_P(t)$ can be expressed by first equating the required pump power

$$\dot{W}_{pump} = \frac{\dot{m}}{\rho}\Delta P \tag{4.17}$$

and

$$\dot{W}_{pump} = T_P\omega \tag{4.18}$$

to get

$$T_P = \frac{\dot{m}}{\omega\rho}\Delta P \tag{4.19}$$

By combining the pump pressure difference expression, we get

$$T_P(t) = R_1\omega\frac{\dot{m}}{\rho} - R_2\left(\frac{\dot{m}}{\rho}\right)^2 - R_3\frac{\dot{m}^3}{\omega\rho^3} \tag{4.20}$$

The last term is frequently omitted.

4.4 Expander Models

The components that generate power from steam expansion can be classified into two categories: turbo-machinery (turbines) and volumetric devices (pistons). Due to the small steam flow rate inherent of small-scale water steam RCs, the use of turbo-machinery is typically associated with low efficiencies, high production costs, and the possibility of rapid erosion of the turbine's blades from moisture content of expanding steam[BM09]. Static models for a turbine and a reciprocating piston expander are presented. A general thermodynamic expansion model coupled to a throttle valve is also presented.

4.4.1 General

The mass flow rate into the expander is given by

$$\dot{m}_v = \frac{\mu \beta P_{in}}{\sqrt{T_{in}}} \tag{4.21}$$

where β is the valve coefficient, μ is the throttle valve position, and T_{in} is the inlet temperature.

The expander outlet enthalpy is given by the rearranged isentropic efficiency definition

$$h_{out} = h_{in} - \eta \left(h_{in} - h_{out,is} \right) \tag{4.22}$$

with an assumed isentropic efficiency η.

The power output of the expander is given by

$$N = \dot{m}_v \left(h_{in} - h_{out} \right) \tag{4.23}$$

4.4.2 Steam Turbine

As with the pump, the turbine is also treated as a static component in its modeling. The following model is based on a steam turbine model developed in [CG08].

High-pressure steams enters the turbine through a stage nozzle to increase its velocity[CG08]. Due to the pressure drop at the nozzle, the mass flow through the turbine is limited. This relationship can be described by

$$\dot{m} = \frac{K_1}{\sqrt{T_{in}}}\sqrt{P_{in}^2 - P_{out}^2} \tag{4.24}$$

with K_1 obtained by data of turbine responses. P_{in} is from the high-side (evaporator) pressure and P_{out} is from the low-side (condenser) pressure.

The steam temperature at the outlet depends on the inlet steam pressure and temperature. Assuming the steam expansion is an adiabatic and isentropic process, the outlet steam temperature is obtained by using the ideal gas pressure-temperature relation:

$$\frac{T_{out}}{T_{in}} = \left(\frac{P_{out}}{P_{in}}\right)^{\frac{k-1}{k}} \tag{4.25}$$

where $k = \frac{C_p}{C_v}$ is the polytropic expansion factor.

The turbine power is given by

$$\dot{W} = \eta\dot{m}(h_{in} - h_{out}) = \eta C_p\dot{m}(T_{in} - T_{out}) \tag{4.26}$$

Combining with the previous equations, we get

$$\dot{W} = \eta C_p\dot{m}T_{in}\left[1 - \left(\frac{P_{out}}{P_{in}}\right)^{\frac{k-1}{k}}\right] \tag{4.27}$$

4.4.3 Piston Expander

The following model is based on an in-line reciprocating piston expander model developed in [BM09]. From its P-V diagram, the expander's operation is seen to

undergo the following phases [BM09]:

1. Compression stroke ($1 \rightarrow 2$): in this phase (from Bottom Dead Center (BDC) to Top Dead Center (TDC)), the residual steam is compressed in the cylinder.

2. Admission ($2 \rightarrow 3$) and ($3 \rightarrow 4$): steam at high pressure is forced into the cylinder through the intake port.

3. Expansion ($4 \rightarrow 5$): the steam at high pressure pushes, the piston towards the BDC; this phase, along with ($3 \rightarrow 4$), is also called the power stroke.

4. Exhaust ($5 \rightarrow 1$): the steam flows out of the engine, and the pressure is thus reduced to the thermodynamic conditions in the condenser.

The area captured by these phases describes the work produced in each cycle. Intuitively, this area depends on the thermodynamic conditions seen at the outlet of the evaporator and the desired condition at the condenser inlet *e.g.* pressures and enthalpies of the working fluid. Moreover, the work depends on the compression ratio ϵ and the steam cut-off timing ϕ which determine the vertices at each phase in the P-V diagram.

$$\epsilon = \frac{V_{max}}{V_{min}} = \frac{V}{V_{min}} + 1 \tag{4.28}$$

$$\phi = \frac{V_4}{V_{max}} = \frac{V_4 - V_{min}}{V} \tag{4.29}$$

An analytic expression for the work-per-cycle is given in terms of ϵ and ϕ by

$$L_c = P_{max} V \left(\phi + \frac{1 + \phi(\epsilon - 1)}{(k-1)(\epsilon - 1)} \left[1 - \left(\frac{1 + \phi(\epsilon - 1)}{\epsilon} \right)^{k-1} \right] \right) - P_{min} V \frac{\epsilon(\epsilon^{k-1} - 1)}{(k-1)(\epsilon - 1)} \tag{4.30}$$

where k is the polytropic expansion factor. The expander's isentropic efficiency is defined as the ratio of the internal and ideal power, given by

$$\eta_{is} = \frac{P_i}{P_{ideal}} = \frac{niL_c}{\dot{m}(h_{in} - h_{out})} \tag{4.31}$$

where n is the engine speed and i is the number of cylinders. It is also given by

$$\eta_{is} = \frac{P_{max}\left(\phi + \frac{1+\phi(\epsilon-1)}{(k-1)(\epsilon-1)}\left[1 - \left(\frac{1+\phi(\epsilon-1)}{\epsilon}\right)^{k-1}\right]\right)}{\frac{h_{in}-h_{out}}{\epsilon-1}\left[\frac{1+\phi(\epsilon-1)}{V_5} - \frac{\epsilon}{V_2}\right]} - \frac{P_{min}\left[\frac{\epsilon(\epsilon^{k-1}-1)}{(k-1)(\epsilon-1)}\right]}{\frac{h_{in}-h_{out}}{\epsilon-1}\left[\frac{1+\phi(\epsilon-1)}{V_5} - \frac{\epsilon}{V_2}\right]} \tag{4.32}$$

Thus, the outlet enthalpy is calculated as

$$h_{out} = h_{in} - \frac{niL_c}{\dot{m}\eta_{is}} \tag{4.33}$$

CHAPTER 5

Dynamic Rankine Cycle Modeling

5.1 Introduction

Dynamic RC modeling focuses on heat exchanger modeling due to their slower dynamics than that of valves, pumps, and expansion devices. Approaches for dynamic heat exchanger modeling span accurate, computational models based on discretizing partial differential conservation equations to computationally less intensive but also less accurate lumped-parameter models. The trade-off is between computational complexity and dynamic accuracy. The Moving Boundary model approach balances these trade-offs and has been an adopted model to describe power generation and refrigeration applications. Research has been conducted on the differences between finite-volume distributed-parameter and Moving Boundary technique applied to the heat exchangers [BB02]. Both methods have been compared for their accuracy to experimental data as well as their simulation complexity. While these two modeling approaches predicted the experimental data with an accuracy of 4%, the Moving Boundary method was more acceptable for control design applications for its smaller order and higher computational speed [WLL90]. The Moving Boundary approach is presented in this section for heat exchangers. This chapter also presents dynamical piston expander model.

The heat transfer coefficients are based on a heat exchanger arrangement internal working fluid flow through a circular tube and external cross flow around the tube.

5.2 Moving Boundary Models for Heat Exchangers

The model captures dynamics for a heat exchanger (HX) undergoing evaporating and condensing phase changes in a tube. The tube is divided into zones for each fluid-phase as shown in Figure 5.3. The process inherently has two-phase as well as single-phase flow. Within each region, the properties are assumed average. As a result, spatial effects are accounted for while lumping the parameters in each zone. Working fluid and refrigerant are used interchangeably to describe the tubular flow.

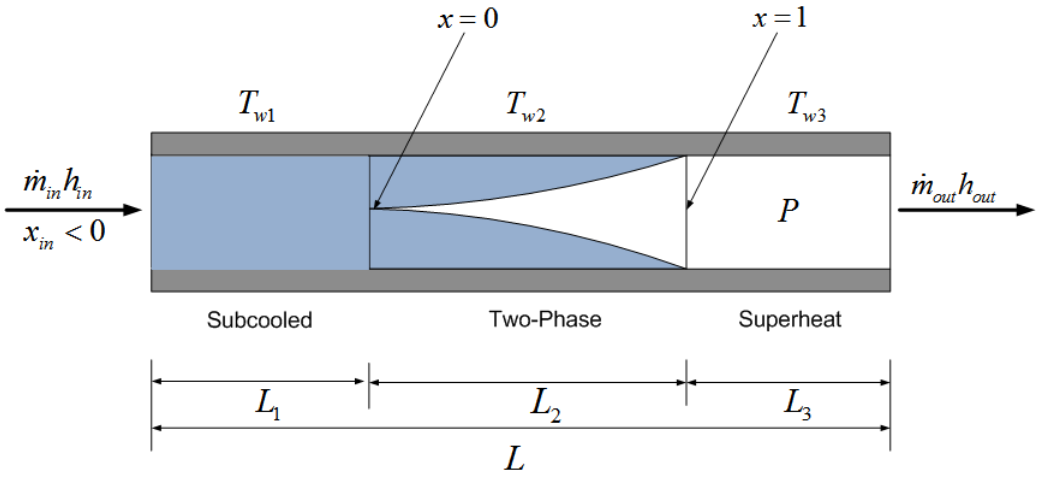

Figure 5.1: Moving Boundary Model for Evaporator

5.2.1 Assumptions

The following are assumed about the fluid flow in the HX's [RA04]:

1. HX is a long and thin horizontal tube.

2. Working fluid flow modeled as a one-dimensional fluid flow.

3. Negligible axial conduction.

4. Pressure drop along HX from momentum change in working fluid and viscous friction is negligible *i.e.* pressure is uniform across HX.

5.2.2 Variable Nomenclature

Variable Parameter	**Description**	**Units**
ρ	Density	$\frac{kg}{m^3}$
P	Pressure	MPa
h	Enthalpy	$\frac{kg}{kJ}$
T	Temperature	K
$\dot{Q}$	Heat Flux	kW
α	Heat Transfer coefficient	$\frac{kW}{m^2K}$
A	Area	m^2
D	Diameter	m
r	Radius	m
$\dot{m}$	Mass flow rate	$\frac{kg}{s}$
$C_p\rho A$	Thermal capacitance per unit length	$\frac{kJ}{m}$
$c = \left(\frac{\rho_g}{\rho_f}\right)^{\frac{2}{3}}$	Constant used to determine Mean Void Fraction	-

Variable Parameter	**Description**	**Units**
x_0	Average refrigerant quality (vapor mass fraction) at inlet	-
x	State Vector	-
u	Input Vector	-
L	Length of Heat Exchanger	m
μ	Dynamic Viscosity	Pa s
k	Thermal Conductivity	$\frac{W}{mK}$
Pr	Prandtl Number	-
Re	Reynolds Number	-
C_p	Specific Heat Capacity at Constant Pressure	$\frac{J}{kgK}$
C_v	Specific Heat Capacity at Constant Volume	$\frac{J}{kgK}$
S	Slip Ratio	-
UA	Overall Heat Transfer Coefficient	$\frac{kW}{m^2K}$
V	Volume	m^3
w	Wall thickness	m^3
SC, TP, SH	Subcooled, Two-phase, Superheat Region	–

Subscript	Description
in	Inlet
out	Outlet
h	Hot (heat source)
e	Evaporator
c	Cold (heat sink), Condenser
rec	Receiver
r	Refrigerant/Working fluid
1	Region 1 of Heat Exchanger
2	Region 2 of Heat Exchanger
3	Region 3 of Heat Exchanger
f	Saturated Liquid
g	Saturated Vapor
i	Inner Tube
o	Outer Tube
a	Air
w	Wall
cs	Cross-sectional
eq	Equilibrium

The cross-sectional area for a flow in a tube is given by $A_{cs} = \pi r_i^2$ where r_i is the tube inner radius.

The wall material is defined by its thermal capacitance, density, and volume.

5.2.3 Derivation for Nonlinear Models

Each zone of the Moving Boundary model is described by mass and energy conservation equations.

The mass conservation equation for working fluid flow is given by

$$\frac{\partial \rho A}{\partial t} + \frac{\partial \dot{m}}{\partial z} = 0 \tag{5.1}$$

The energy conservation equation for working fluid flow is given by

$$\frac{\partial (\rho A h - A P)}{\partial t} + \frac{\partial (\dot{m} h)}{\partial z} = p_i \alpha_i (T_w - T_r) \tag{5.2}$$

The energy conservation for the wall is given by

$$(C_p \rho A)_w \frac{\partial T_w}{\partial t} = p_i \alpha_i (T_r - T_w) + p_o \alpha_o (T_a - T_w) \tag{5.3}$$

The derivation begins by using the Leibniz integral rule to convert the partial differential equations (PDEs) into ordinary differential equations (ODEs). The integral rule is given by

$$\int_{z_1(t)}^{z_2(t)} \frac{\partial f(z,t)}{\partial t} dz = \frac{d}{dt} \int_{z_1(t)}^{z_2(t)} f(z,t) dz - f(z_2(t),t) \frac{d(z_2(t))}{dt} + f(z_1(t),t) \frac{d(z_1(t))}{dt} \tag{5.4}$$

The integration removes spatial dependence and divides the heat exchanger into zones with different phases (SC,TP,SH). Note that the conservation of momentum equation is not needed due to assumption 4. The (P,h) pair is chosen as the independent thermodynamic states in the model derivation though other independent property variables are valid. The models with different choices of independen properties are related through a change of variable as detailed in [Ras02].

The form of the model is

$$Z(x,u)\dot{x} = f(x,u) \tag{5.5}$$

where x is the state vector and u is the input vector. Z is invertible as long as the phase-change boundary state is non-zero or not equal to the heat exchanger length.

The general heat exchanger model has three zones as shown in Figure 5.3, each describing subcooled, two-phase, and superheat flow regions. A two-zone evaporator (condenser) model with two-phase and superheat (subcooled) flows is also of interest should the incoming working fluid enter as two-phase from the pump (expander). In any case, the two- and three-zone models rely on the existence of the zones during simulation. Should any zone disappear in the models, they would no longer be valid and would indicate the flow does not undergo the expected phase changes.

A complete derivation can be found in [RA04] for the two-zone evaporator case with two-phase and superheat regions. A two-zone condenser case with two-phase and subcooled region follows a similar derivation. Models with receivers and accumulators can also be derived. The interested reader is referred to [ERA08] for details. Methods for switching between different Moving Boundary models are presented in the literature should zones disappear and reappear. The interested reader is directed to [MA08].

5.2.4 Derivation for Linear Models

Control design and general analysis of nonlinear systems are often difficult. One common technique is overcome the difficulty is to linearize the nonlinear systems about an equilbrium operating point to so that linear control design tools and analysis methods can be applied.

The nonlinear models described can be linearized about an operating point. The

nonlinear system is given by

$$Z(x,u)\dot{x} = f(x,u) \tag{5.6}$$

The matrix Z is non-singular i.e. invertible as long as none of the modeling assumptions are violated. The phase change boundaries L_1 and L_2 in Figure 5.3 are greater than zero and their sum is less than the total length of the heat exchanger [RA04]. The matrix Z to the right hand side of the equation by finding its inverse to obtain

$$\dot{x} = Z(x,u)^{-1} f(x,u) = g(x,u) \tag{5.7}$$

Linearization is valid for the pair (x_{eq}, u_{eq}) such that $g(x_{eq}, u_{eq}) = f(x_{eq}, u_{eq}) = 0$. (x_{eq}, u_{eq}) is referred to as the equilibrium or operating point. We define

$$x = x_{eq} + \delta x \tag{5.8}$$

and note that $\dot{x} = \delta\dot{x}$ as we take the Jacobians with respect to the state x and input u.

$$\delta\dot{x} = \left[\frac{\partial g}{\partial x}\Big|_{x_e,u_e}\right]\partial x + \left[\frac{\partial g}{\partial u}\Big|_{x_e,u_e}\right]\partial u \tag{5.9}$$

The Jacobians are evaluated at the equilibrium point. We expand the Jacobians as follows:

$$\frac{\partial g}{\partial x}\Big|_{x_e,u_e} = Z(x_e,u_e)^{-1}\frac{\partial f}{\partial x}\Big|_{x_e,u_e} + Z(x_e,u_e)^{-2}\frac{\partial Z^{-1}}{\partial x}\Big|_{x_e,u_e}\underbrace{f(x_e,u_e)}_{0} \tag{5.10}$$

$$\frac{\partial g}{\partial u}\Big|_{x_e,u_e} = Z(x_e,u_e)^{-1}\frac{\partial f}{\partial u}\Big|_{x_e,u_e} + Z(x_e,u_e)^{-2}\frac{\partial Z^{-1}}{\partial u}\Big|_{x_e,u_e}\underbrace{f(x_e,u_e)}_{0} \tag{5.11}$$

The last terms are eliminated from evaluating the function f at the equilibrium point. Thus we have the following linearized system:

$$\delta\dot{x} = \underbrace{\left[Z\Big|_{x_e,u_e}\right]^{-1}\left[\frac{\partial f}{\partial x}\Big|_{x_e,u_e}\right]}_{\text{A}}\partial x + \underbrace{\left[Z\Big|_{x_e,u_e}\right]^{-1}\left[\frac{\partial f}{\partial u}\Big|_{x_e,u_e}\right]}_{\text{B}}\partial u \tag{5.12}$$

5.2.5 Single-Phase Flow

Single-phase flow for the evaporator are characterized by the following relations at the evaporating pressure:

$$h_1 = \frac{h_f + h_{in}}{2}$$
$$T_1 = T(P, h_1)$$
$$h_3 = \frac{h_g + h_{out}}{2}$$
$$T_3 = T(P, h_3)$$

Single-phase flow for the condenser are characterized by the following relations at the condensing pressure:

$$h_1 = \frac{h_g + h_{in}}{2}$$
$$T_1 = T(P, h_1)$$
$$h_3 = \frac{h_g + h_{out}}{2}$$
$$T_3 = T(P, h_3)$$

(1) and (3) denote the entrance and exit regions where their properties are averaged.

5.2.6 Two-Phase Flow

This region is characterized by two-phase flow where thermodynamic properties are at saturation, *i.e.* $T = T_{sat}$ and $P = P_{sat}$. Also important is the temperature-pressure dependence, $T_{sat} = f(P_{sat})$. In other words,

$$T_r = f(P_{sat}) \tag{5.13}$$

5.2.7 Heat Transfer

5.2.7.1 Internal Flow Through a Circular Tube

The internal flow heat transfer coefficient for single-phase flow is calculated from using the Reynold's number (Re) to determine laminar or turbulent flow and the Nusselt number. For laminar single-phase flow through a tube, the Nusselt number is a constant and can be solved for the heat transfer coefficient α_{sp} as

$$\mathrm{Nu} = 4.36 = \frac{\alpha_{sp} D}{k} \tag{5.14}$$

where D is the tube inner diameter and k the thermal conductivity of the working fluid.

For turbulent flow through a tube, the Dittus-Boelter correlation gives

$$\mathrm{Nu} = 0.023 \mathrm{Re}^{0.8} \mathrm{Pr}^{n} = \frac{\alpha_{sp} D}{k} \tag{5.15}$$

where Pr is the Prandtl number and the values for n are empirically determined: $n = 0.4$ for heating and $n = 0.3$ for cooling. The Reynold's number is given by

$$\mathrm{Re} = \frac{4\dot{m}}{\pi \mu D} \tag{5.16}$$

For the two-phase flow heat transfer coefficient α_{tp}, a general correlation is given in [Kan08] for flow through vertical and horizontal tubes. The proposed correlation for the two-phase heat transfer coefficient is given by

$$\alpha_{tp} = \alpha_l \left[C_1 \mathrm{Co}^{C_2} (25 \mathrm{Fr}_{lo})^{C_5} + C_3 \mathrm{Bo}^{C_4} \mathrm{F}_{fl} \right] \tag{5.17}$$

where α_l is the liquid phase heat transfer coefficient, Co is the convection number, Bo is the boiling number, Fr_{lo} is the Froude number with all flow as liquid, and F_{fl} is a fluid-dependent parameter (1.0 for water, also assumed for ethanol-water

Constant	Convective Region	Nucleate Boiling Region
C_1	1.1360	0.6683
C_2	-0.9	-0.2
C_3	667.2	1058.0
C_4	0.7	0.7
C_5^*	0.3	0.3

Table 5.1: Constants in the Kandlikar Correlation $C_5^* = 0$ for vertical tubes, and for horizontal tubes with $\mathrm{Fr}_l > 0.04$

mixtures). The latter is evaluated for particular fluids from their flow boiling or pool boiling data. The correlation accounts for convective (first term) and nucleate boiling (second term). The coefficients $C_1 - C_5$ are provided in Table 5.1.

5.2.7.2 External Flow Through a Concentric Tube Annulus

The heat source/sink is assumed to flow externally through a concentric annulus around a tube where the working fluid flows.

The effective (hydraulic) diameter is given by

$$D_h = \frac{4A_c}{P} \tag{5.18}$$

where P is the wetted perimeter of the tube, given as $P = 2\pi(r_i + r_o)$ for an annulus. r_i and r_o are the inner and outer radii of the concentric tubes.

The Reynold's number is given by

$$\mathrm{Re} = \frac{\dot{m}D_h}{\mu A} = \frac{4\dot{m}}{\mu P} = \frac{2\dot{m}}{\pi\mu(r_o + r_i)} \tag{5.19}$$

where $\dot{m}$ is the mass flow rate of the heat source/sink.

The Nusselt number is given by

$$\mathrm{Nu} = 0.023\mathrm{Re}^{0.8}\mathrm{Pr}^{0.4} \tag{5.20}$$

where Pr is the Prandtl number and the values for n are empirically determined: $n = 0.4$ for heating and $n = 0.3$ for cooling. Finally, the heat transfer coefficient for the external flow is given by

$$\alpha_o = \frac{\mathrm{Nu} \cdot k}{D_h} \tag{5.21}$$

5.2.7.3 External Cross Flow Over a Single Cylindrical Tube

Correlations for convective heat transfer of smooth circular tube heat exchangers with external cross flow were chosen.

The Hilpert correlation is selected for cross flow across a tube.

$$\alpha_o = \frac{\mathrm{Nu} \cdot k}{D_i} \tag{5.22}$$

$$\mathrm{Nu} = C\mathrm{Re}^{m}\mathrm{Pr}^{\frac{1}{3}} \tag{5.23}$$

where the properties are calculated at the film temperature. C and m are constants that depend on the Reynold's number. These values can be found in [IDB06].

For the circular cylinder the characteristic length is the diameter, and the Reynold's number is defined as

$$\mathrm{Re}_D \equiv \frac{\rho V D}{\mu} \tag{5.24}$$

. Because the mass flow rate of the flow is known instead of the free-stream velocity V, the Reynold's number is difficult to calculate.

Assuming the external flow has a cross-sectional area the same as the frontal area of the tube, the mass flow rate can be related to the flow velocity as

$$V = \frac{\dot{m}}{\rho L D} \tag{5.25}$$

The frontal area seen by the external flow is assumed rectangular with area $A = L \cdot D$.

Choosing the characteristic length as the length of the tube L, the Reynold's number is calculated as

$$\mathrm{Re}_L = \frac{\dot{m}}{\mu D} \tag{5.26}$$

where D is the tube diameter.

It should be noted that the calculation of the Reynold's number in this fashion—when only the external mass flow rate is known instead of its free-stream velocity—is not a traditional nor necessarily an accepted approach. The Reynold's number dependence on mass flow rate may be correct, but its resulting magnitude may not be. Improvement is needed to properly calculate the Reynold's number in this situation.

5.2.8 Evaporator Models

5.2.8.1 Two-Zone

The derivation can be found in [RA04]. The resulting model is a set of five nonlinear differential equations, written in descriptor form given by

$$Z(x,u)\dot{x} = f(x,u) \tag{5.27}$$

$$x = \begin{bmatrix} L_1 & P & h_{out} & T_{w1} & T_{w2} \end{bmatrix}^T \tag{5.28}$$

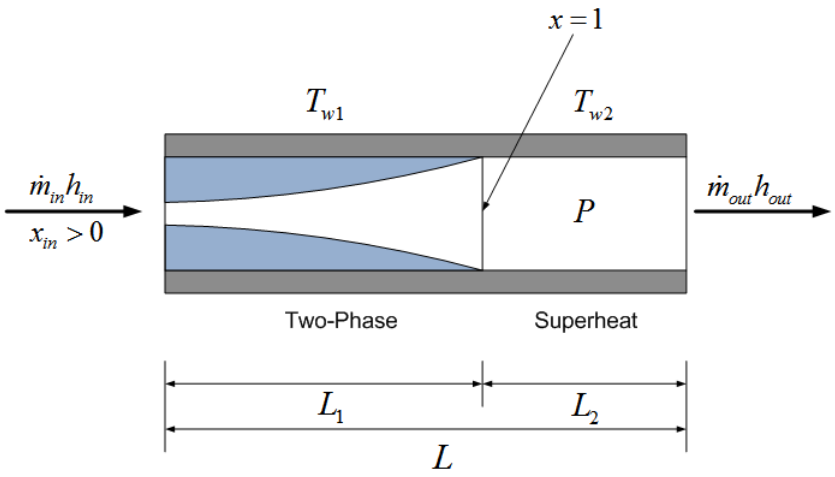

Figure 5.2: Two-Zone Moving Boundary Model for Evaporator

$$u = \begin{bmatrix} \dot{m}_{in} & \dot{m}_{out} & h_{in} & T_{h,in} & \dot{m}_h \end{bmatrix}^T \tag{5.29}$$

$$Z(x,u) = \begin{bmatrix} z_{11} & z_{12} & 0 & 0 & 0 \\ z_{21} & z_{22} & z_{23} & 0 & 0 \\ z_{31} & z_{32} & z_{33} & 0 & 0 \\ 0 & 0 & 0 & z_{44} & 0 \\ z_{51} & 0 & 0 & 0 & z_{55} \end{bmatrix} \tag{5.30}$$

$$f(x,u) = \begin{bmatrix} \dot{m}_{in}(h_{in} - h_g) + \alpha_{i1} A_i (\frac{L_1}{L})(T_{w1} - T_{r1}) \\ \dot{m}_{out}(h_g - h_{out}) + \alpha_{i2} A_i (\frac{L - L_1}{L})(T_{w2} - T_{r2}) \\ \dot{m}_{in} - \dot{m}_{out} \\ \alpha_o A_o (T_h - T_{w1}) - \alpha_{i1} A_i (T_{w1} - T_{r1}) \\ \alpha_o A_o (T_h - T_{w2}) - \alpha_{i2} A_i (T_{w2} - T_{r2}) \end{bmatrix} \tag{5.31}$$

For circular tubes, the inner and outer tube surface areas are given by $A_i = 2\pi r_i L$ and $A_o = 2\pi r_o L$, respectively.

Entries of $Z(x,u)$ for the Two-Zone Evaporator Model

z_{11}	$\left[\rho_f(h_f - h_g)\right](1-\bar{\gamma})A_{cs}$
z_{12}	$\left[\left(\frac{d(\rho_f h_f)}{dP} - \frac{d\rho_f}{dP}h_g\right)(1-\bar{\gamma}) + \left(\frac{d(\rho_g h_g)}{dP} - \frac{d\rho_g}{dP}h_g\right)\bar{\gamma} - 1\right] A_{cs}L_1$
z_{21}	$\rho_2(h_g - h_2)A_{cs}$
z_{22}	$\left[\left(\left.\frac{\partial\rho_2}{dP}\right\|_{h_2} + \frac{1}{2}\left.\frac{\partial\rho_2}{\partial h_2}\right\|_P \frac{dh_g}{dP}\right)(h_2 - h_g) + \frac{\rho_2}{2}\frac{dh_g}{dP} - 1\right] A_{cs}(L - L_1)$
z_{23}	$\left[\frac{1}{2}\left.\frac{\partial\rho_2}{\partial h_2}\right\|_P (h_2 - h_g) + \frac{\rho_2}{2}\right] A_{cs}(L - L_1)$
z_{31}	$\left[(\rho_g - \rho_2) + (\rho_f - \rho_g)(1-\bar{\gamma})\right] A_{cs}$
z_{32}	$\left\{\left[\left.\frac{\partial\rho_2}{\rho P}\right\|_{h_2} + \frac{1}{2}\left.\frac{\partial\rho_2}{\partial h_2}\right\|_h P\frac{dh_g}{dP}\right](L - L_1) + \left[\frac{d\rho_f}{dP}(1-\bar{\gamma}) + \frac{d\rho_g}{dP}\bar{\gamma}\right] L_1\right\} A_{cs}$
z_{33}	$\frac{1}{2}\left.\frac{\partial\rho_2}{\partial h_2}\right\|_P A_{cs}(L - L_1)$
z_{44}	$(C_p\rho V)_w$
z_{51}	$(C_p\rho V)_w\left(\frac{T_{w1} - T_{w2}}{L - L_1}\right)$
z_{55}	$(C_p\rho V)_w$
A_{cs}	$\pi\left((r_i + w)^2 - r_i^2\right)$

A constant, mean void fraction is assumed to simplify the derivation. This is empircally calculated as prescribed in [BW81].

$$\bar{\gamma} = \frac{1}{1-c} + \frac{c}{(1-x_0)(1-c)^2}\ln[c + (1-c)x_0] \tag{5.32}$$

The Jacobians for the two-zone evaporator model are

$$\frac{\partial f}{\partial x} = \begin{bmatrix} a_{11} & a_{12} & 0 & a_{14} & 0 \\ a_{21} & a_{22} & a_{23} & 0 & a_{25} \\ 0 & 0 & 0 & 0 & 0 \\ a_{41} & a_{42} & 0 & a_{44} & a_{45} \\ a_{51} & a_{52} & a_{53} & a_{54} & a_{55} \end{bmatrix} \quad \frac{\partial f}{\partial u} = \begin{bmatrix} b_{11} & 0 & b_{13} & 0 & 0 \\ 0 & b_{22} & 0 & 0 & 0 \\ b_{31} & b_{32} & 0 & 0 & 0 \\ 0 & 0 & 0 & b_{44} & b_{45} \\ 0 & 0 & 0 & b_{54} & b_{55} \end{bmatrix}$$

Entries of Jacobian Matrices for the Two-Zone Evaporator Model

$\frac{\partial f}{\partial x}$

a_{11}	$\frac{\alpha_{i1}A_i}{L}(T_{w1} - T_{r1})$
a_{12}	$-\dot{m}_{in}\frac{dh_g}{dP} - \alpha_{i1}A_i\frac{L_1}{L}\frac{dT_{r1}}{dP}$
a_{14}	$\alpha_i A_i \frac{L_1}{L}$
a_{21}	$-\frac{\alpha_{i2}A_i}{L}(T_{w2} - T_{r2})$
a_{22}	$\dot{m}_{out}\frac{dh_g}{dP} - \alpha_{i2}A_i(\frac{L_2}{L})\frac{\partial T_{r2}}{\partial P}\Big\vert_{h_2}$
a_{23}	$-\dot{m}_{out} - \alpha_{i2}A_i(\frac{L_2}{L})\frac{\partial T_{r2}}{\partial h_{out}}\Big\vert_{P}$
a_{25}	$\alpha_{i2}A_i(\frac{L_2}{L})$
a_{41}	$\alpha_o A_o \frac{\partial T_h}{\partial L_1}$
a_{42}	$\alpha_{i1}A_i\frac{\partial T_{r1}}{\partial P}$
a_{44}	$-\alpha_o A_o - \alpha_{i1}A_i + \alpha_o A_o \frac{\partial T_h}{\partial T_{w1}}$
a_{45}	$\alpha_o A_o \frac{\partial T_h}{\partial T_{w2}}$
a_{51}	$\alpha_o A_o \frac{\partial T_h}{\partial L_1}$
a_{52}	$\alpha_{i2}A_i\frac{\partial T_{r2}}{\partial P}$
a_{53}	$\alpha_{i2}A_i\frac{\partial T_{r2}}{\partial h_{out}}$
a_{54}	$\alpha_o A_o \frac{\partial T_h}{\partial T_{w1}}$
a_{55}	$-\alpha_o A_o - \alpha_{i2}A_i + \alpha_o A_o \frac{\partial T_h}{\partial T_{w2}}$

$\frac{\partial f}{\partial u}$

b_{11}	$h_{in} - h_g$
b_{13}	$\dot{m_{in}}$
b_{22}	$h_g - h_{out}$
b_{31}	1
b_{32}	-1
b_{44}	$\alpha_o A_o \frac{\partial T_h}{\partial T_{h,in}}$
b_{45}	$A_o(T_h - T_{w1})\frac{\partial \alpha_o}{\partial \dot{m}_h} + \alpha_o A_o \frac{\partial T_h}{\partial \dot{m}_h}$
b_{54}	$\alpha_o A_o \frac{\partial T_h}{\partial T_{h,in}}$
b_{55}	$A_o(T_h - T_{w2})\frac{\partial \alpha_o}{\partial \dot{m}_h} + \alpha_o A_o \frac{\partial T_h}{\partial \dot{m}_h}$

5.2.8.2 Three-Zone

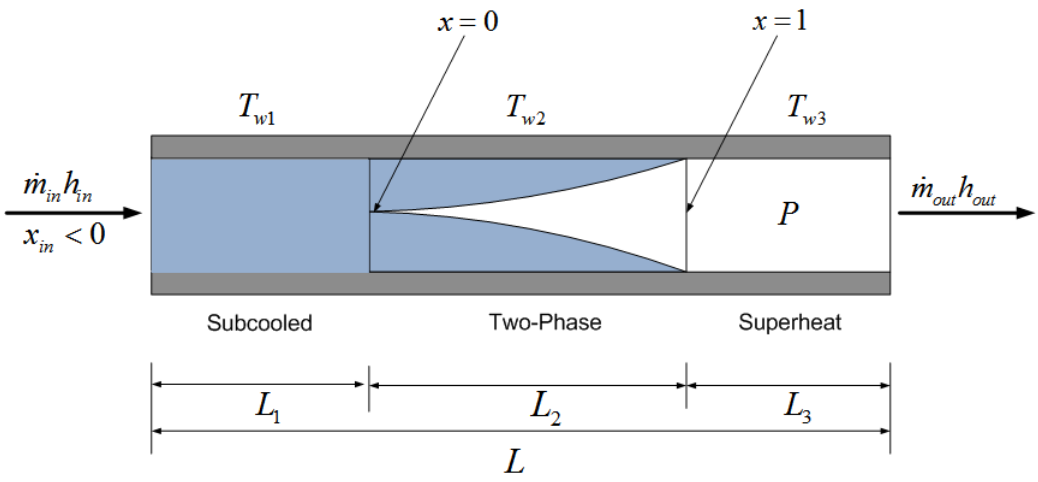

Figure 5.3: Three-Zone Moving Boundary Model for Evaporator

Formulation of this model is found in [JT02]. The model is a set of seven non-linear differential equations based on working fluid mass/energy and wall energy conservation equations, written in descriptor form.

$$Z(x,u)\dot{x} = f(x,u) \tag{5.33}$$

$$x = \begin{bmatrix} L_1 & L_2 & P & h_{out} & T_{w1} & T_{w2} & T_{w3} \end{bmatrix}^T \tag{5.34}$$

$$u = \begin{bmatrix} \dot{m}_{in} & \dot{m}_{out} & h_{in} & \dot{h}_{in} & T_{h,in} & \dot{m}_h \end{bmatrix}^T \tag{5.35}$$

$$Z(x,u) = \begin{bmatrix} z_{11} & 0 & z_{13} & 0 & 0 & 0 & 0 \\ z_{21} & z_{22} & z_{23} & 0 & 0 & 0 & 0 \\ z_{31} & z_{32} & z_{33} & z_{34} & 0 & 0 & 0 \\ z_{41} & z_{42} & z_{43} & z_{44} & 0 & 0 & 0 \\ z_{51} & 0 & 0 & 0 & z_{55} & 0 & 0 \\ z_{61} & z_{62} & 0 & 0 & 0 & z_{66} & 0 \\ 0 & z_{72} & 0 & 0 & 0 & 0 & z_{77} \end{bmatrix} \tag{5.36}$$

$$f(x,u) = \begin{bmatrix} f_1 & f_2 & f_3 & f_4 & f_5 & f_6 & f_7 \end{bmatrix}^T \tag{5.37}$$

Entries of $Z(x,u)$ for the Three-Zone Evaporator Model

z_{11}	$\frac{1}{2}A_{cs}\rho_1(h_{in}-h_f)$
z_{13}	$\frac{1}{2}A_{cs}L_1\left[\rho_1\frac{dh_f}{dP}+(h_{in}+h_f)(a-2)-2ah_f\right]$
z_{21}	$A_{cs}\left[\rho_f h_f-\rho_g h_g-h_g(\rho_1-\rho_g)+h_f(\rho_1-\rho_f)\right]$
z_{22}	$A_{cs}\left[\rho_f(1-\bar{\gamma})(h_f-h_g)\right]$
z_{23}	$A_{cs}\left[L_2\bar{\gamma}\left(\frac{d(\rho_g h_g)}{dP}-h_g\frac{d\rho_g}{dP}\right)\right]+$ $A_{cs}L_2\left[(1-\bar{\gamma})\left(\frac{d(\rho_f h_f)}{dP}-h_g\frac{d\rho_f}{dP}\right)-1\right]+A_{cs}L_1 a\left(h_f-h_g\right)$
z_{31}	$A_{cs}\left[\rho_3 h_g-\frac{1}{2}\rho_3(h_g+h_{out})\right]$
z_{32}	$A_{cs}\left[\rho_3 h_g-\frac{1}{2}\rho_3(h_g+h_{out})\right]$
z_{33}	$A_{cs}L_3\left[\frac{1}{2}(h_g+h_{out})(\frac{1}{2}\frac{\partial\rho_3}{\partial h_3}\Big\|_P\frac{dh_g}{dP}+\frac{\partial\rho_3}{\partial P}\Big\|_h)\right]$ $+A_{cs}L_3\left[\frac{1}{2}\rho_3\frac{dh_g}{dP}-1-\frac{1}{2}h_g\frac{\partial\rho_3}{\partial h_3}\Big\|_P\frac{dh_g}{dP}-\frac{\partial\rho_3}{\partial P}\Big\|_h h_g\right]$
z_{34}	$\frac{A_{cs}}{2}\left[\rho_3 L_3+\frac{1}{2}\frac{\partial\rho_3}{\partial h_3}\Big\|_P(h_g+h_{out})L_3-h_g L_3\frac{\partial\rho_3}{\partial h_3}\Big\|_P\right]$
z_{41}	$A_{cs}(\rho_1-\rho_3)$
z_{42}	$A_{cs}\left[(\rho_g-\rho_3)+(1-\bar{\gamma})(\rho_f-\rho_g)\right]$
z_{43}	$A_{cs}\left[L_2(\bar{\gamma}\frac{d\rho_g}{dP}+(1-\bar{\gamma})\frac{d\rho_f}{dP})+aL_1+L_3(\frac{1}{2}\frac{\partial\rho_3}{\partial h_3}\Big\|_P\frac{dh_g}{dP}+\frac{\partial\rho_3}{\partial P}\Big\|_h)\right]$
z_{44}	$\frac{A_{cs}}{2}L_3\frac{\partial\rho_3}{\partial h_3}\Big\|_P$
z_{51}	$(C_p\rho A)_w\left[T_{w1}-T_w\Big\|_{L_1}\right]$
z_{55}	$(C_p\rho A)_w L_1$
z_{61}	$(C_p\rho A)_w\left[T_w\Big\|_{L_1}-T_w\Big\|_{L_1+L_2}\right]$
z_{62}	$(C_p\rho A)_w\left[T_{w2}-T_w\Big\|_{L_1+L_2}\right]$
z_{66}	$(C_p\rho A)_w L_2$
z_{72}	$(C_p\rho A)_w\left[T_w\Big\|_{L_1+L_2}-T_{w3}\right]$
z_{77}	$(C_p\rho A)_w L_3$
A_{cs}	$\pi\left((r_i+w)^2-r_i^2\right)$

Entries of $Z(x,u)$ for the Three-Zone Evaporator Model (continued)

a	$\left.\frac{\partial \rho_1}{\partial P}\right\|_h + \frac{1}{2}\left.\frac{\partial \rho_1}{\partial h_1}\right\|_P \frac{dh_f}{dP}$
$\left.T_w\right\|_{L_1}$	T_{w2} if $\dot{L}_1 > 0$ $\quad$ T_{w1} if $\dot{L}_1 \leq 0$
$\left.T_w\right\|_{L_1+L_2}$	T_{w3} if $\dot{L}_2 > 0$ $\quad$ T_{w2} if $\dot{L}_2 \leq 0$

Entries of $f(x,u)$ for the Three-Zone Evaporator Model

f_1	$\dot{m}_{in}(h_{in} - h_f) + \alpha_{i1}\pi D_i L_1 (T_{w1} - T_{r1}) -$
	$\frac{A_{cs}}{2}\left[\rho_1 L_1 + \frac{1}{2}(h_{in} + h_f)\left.\frac{\partial \rho_1}{\partial h_1}\right\|_P - h_f L_1 \left.\frac{\partial \rho_1}{\partial h_1}\right\|_P\right]\dot{h}_{in}$
f_2	$\dot{m}_{in}(h_f - h_g) + \alpha_{i2}\pi D_i L_2 (T_{w2} - T_{r2}) + \frac{1}{2}A_{cs}L_1 \left.\frac{\partial \rho_1}{\partial h}\right\|_P (h_g - h_f)\dot{h}_{in}$
f_3	$\dot{m}_{out}(h_g - h_{out}) + \alpha_{i3}\pi D_i L_3 (T_{w3} - T_{r3})$
f_4	$\dot{m}_{in} - \dot{m}_{out} - \frac{A_{cs}L_1}{2}\left.\frac{\partial \rho_1}{\partial h_1}\right\|_P \dot{h}_{in}$
f_5	$\alpha_o \pi D_o L_1 (T_{h,in} - T_{w1}) + \alpha_{i1}\pi D_i L_1 (T_{r1} - T_{w1}))$
f_6	$\alpha_o \pi D_o L_2 (T_{h,in} - T_{w2}) + \alpha_{i2}\pi D_i L_2 (T_{r2} - T_{w2}))$
f_7	$\alpha_o \pi D_o L_3 (T_{h,in} - T_{w3}) + \alpha_{i3}\pi D_i L_3 (T_{r3} - T_{w3}))$
A_{cs}	$\pi\left((r_i + w)^2 - r_i^2\right)$

A constant, mean void fraction is assumed to simplify the derivation. A simple and commonly used correlation is the one from Zivi (1964) cited in [JT02] which minimizes the total kinetic energy flow locally at each position along the pipe. The slip ratio S is used in its calculation.

$$S = \frac{u_g}{u_f} = \left(\frac{\rho_f}{\rho_g}\right)^{\frac{1}{3}} = \mu^{\frac{1}{3}} \tag{5.38}$$

The average vapor fraction in the pipe is the complement of the average liquid fraction $\bar{\eta}$:

$$\bar{\gamma} = 1 - \bar{\eta} = 1 - \frac{1 + (1/\mu)^{\frac{2}{3}}(\frac{2}{3}ln(1/\mu) - 1)}{((1/\mu)^{\frac{2}{3}} - 1)^2} \tag{5.39}$$

The Jacobians and their matrix structures for the three-zone evaporator model are

$$\frac{\partial f}{\partial x} = \begin{bmatrix} a_{11} & 0 & a_{13} & 0 & a_{15} & 0 & 0 \\ 0 & a_{22} & a_{23} & 0 & 0 & 0 & a_{26} \\ a_{31} & a_{32} & a_{33} & a_{34} & 0 & 0 & a_{37} \\ 0 & 0 & 0 & 0 & 0 & 0 & 0 \\ a_{51} & a_{52} & a_{53} & 0 & a_{55} & a_{56} & a_{57} \\ a_{61} & a_{62} & a_{63} & 0 & a_{65} & a_{66} & a_{67} \\ a_{71} & a_{72} & a_{73} & a_{74} & a_{75} & a_{76} & a_{77} \end{bmatrix} \quad \frac{\partial f}{\partial u} = \begin{bmatrix} b_{11} & 0 & b_{13} & 0 & 0 & 0 \\ b_{21} & 0 & 0 & 0 & 0 & 0 \\ 0 & b_{32} & 0 & 0 & 0 & 0 \\ b_{41} & b_{42} & 0 & 0 & 0 & 0 \\ 0 & 0 & 0 & 0 & b_{55} & b_{56} \\ 0 & 0 & 0 & 0 & b_{65} & b_{66} \\ 0 & 0 & 0 & 0 & b_{75} & b_{76} \end{bmatrix}$$

Entries of Jacobian Matrices for the Three-Zone Evaporator Model $\frac{\partial f}{\partial x}$

a_{11}	$\alpha_{i1}\pi D_i(T_{w1}-T_{r1})$
a_{13}	$-\dot{m}_{in}\frac{dh_f}{dP}-\alpha_{i1}\pi D_i L_1\frac{\partial T_{r1}}{\partial P}\Big\vert_{h_1}$
a_{15}	$\alpha_{i1}\pi D_i L_1$
a_{22}	$\alpha_{i2}\pi D_i L_2$
a_{23}	$\dot{m}_{in}(\frac{dh_f}{dP}-\frac{dh_g}{dP})-\alpha_{i2}\pi D_i L_2\frac{dT_{r2}}{dP}$
a_{26}	$\alpha_{i2}\pi D_i L_2$
a_{31}	$-\alpha_{i3}\pi D_i(T_{w3}-T_{r3})$
a_{32}	$-\alpha_{i3}\pi D_i(T_{w3}-T_{r3})$
a_{33}	$\dot{m}_{out}\frac{dh_g}{dP}-\alpha_{i3}\pi D_i L_3\frac{\partial T_{r3}}{\partial P}\Big\vert_{h_3}$
a_{34}	$-\dot{m}_{out}-\alpha_{i3}\pi D_i L_3\frac{\partial T_{r3}}{\partial h_{out}}\Big\vert_{P}$
a_{37}	$\alpha_{i3}\pi D_i L_3$
a_{51}	$\alpha_o\pi D_o(T_h-T_{w1})+\alpha_o\pi D_o L_1\frac{\partial T_h}{\partial L_1}$
a_{52}	$\alpha_o\pi D_o L_1\frac{\partial T_h}{\partial L_2}$
a_{53}	$\alpha_{i1}\pi D_i L_1\frac{\partial T_{r1}}{\partial P}\Big\vert_{h_1}$
a_{55}	$-\alpha_o\pi D_o L_1-\alpha_{i1}\pi D_i L_1+\alpha_o\pi D_o L_1\frac{\partial T_h}{\partial T_{w1}}$
a_{56}	$\alpha_o\pi D_o L_1\frac{\partial T_h}{\partial T_{w2}}$
a_{57}	$\alpha_o\pi D_o L_1\frac{\partial T_h}{\partial T_{w3}}$
a_{61}	$\alpha_o\pi D_o L_2\frac{\partial T_h}{\partial L_1}$
a_{62}	$\alpha_o\pi D_o(T_h-T_{w2})+\alpha_{i2}\pi D_i(T_{r2}-T_{w2})+\alpha_o\pi D_o L_2\frac{\partial T_h}{\partial L_2}$
a_{63}	$\alpha_{i2}\pi D_i L_2\frac{dT_{r2}}{dP}$
a_{65}	$\alpha_o\pi D_i L_2\frac{\partial T_h}{\partial T_{w1}}$
a_{66}	$-\alpha_o\pi D_o L_2-\alpha_{i2}\pi D_i L_2+\alpha_o\pi D_o L_2\frac{\partial T_h}{\partial T_{w2}}$
a_{67}	$\alpha_o\pi D_o L_2\frac{\partial T_h}{\partial T_{w3}}$

Entries of Jacobian Matrices for the Three-Zone Evaporator Model $\frac{\partial f}{\partial x}$ (continued)

a_{71}	$-\alpha_o \pi D_o (T_h - T_{w3}) - \alpha_{i3} \pi D_i (T_{r3} - T_{w3}) - \alpha_o \pi D_o L_3 \frac{\partial T_h}{\partial L_1}$
a_{72}	$-\alpha_o \pi D_o (T_h - T_{w3}) - \alpha_{i3} \pi D_i (T_{r3} - T_{w3}) - \alpha_o \pi D_o L_3 \frac{\partial T_h}{\partial L_2}$
a_{73}	$\alpha_{i3} \pi D_i L_3 \frac{\partial T_{r3}}{\partial P}\Big\vert_{h_3}$
a_{74}	$\alpha_{i3} \pi D_i L_3 \frac{\partial T_{r3}}{\partial h_{out}}\Big\vert_{P}$
a_{75}	$\alpha_o \pi D_o L_3 \frac{\partial T_h}{\partial T_{w1}}$
a_{76}	$\alpha_o \pi D_o L_3 \frac{\partial T_h}{\partial T_{w2}}$
a_{77}	$-\alpha_o \pi D_o L_3 - \alpha_{i3} \pi D_i L_3 + \alpha_o \pi D_o L_3 \frac{\partial T_h}{\partial T_{w3}}$

Entries of Jacobian Matrices for the Three-Zone Evaporator Model $\frac{\partial f}{\partial u}$ (continued)

b_{11}	$h_{in} - h_f$
b_{13}	$\dot{m}_{in}$
b_{21}	$h_f - h_g$
b_{32}	$h_g - h_{out}$
b_{41}	1
b_{42}	-1
b_{55}	$\alpha_o \pi D_o L_1 \frac{\partial T_h}{\partial T_{hi}}$
b_{56}	$\pi D_o L_1 (T_h - T_{w1}) \frac{\partial \alpha_o}{\partial \dot{m}_{h,in}} + \alpha_o \pi D_o L_1 \frac{\partial T_h}{\partial \dot{m}_h}$
b_{65}	$\alpha_o \pi D_o L_2 \frac{\partial T_h}{\partial T_{hi}}$
b_{66}	$\pi D_o L_2 (T_h - T_{w2}) \frac{\partial \alpha_o}{\partial \dot{m}_{h,in}} + \alpha_o \pi D_o L_2 \frac{\partial T_h}{\partial \dot{m}_h}$
b_{75}	$\alpha_o \pi D_o L_3 \frac{\partial T_h}{\partial T_{hi}}$
b_{76}	$\pi D_o L_3 (T_h - T_{w3}) \frac{\partial \alpha_o}{\partial \dot{m}_{h,in}} + \alpha_o \pi D_o L_3 \frac{\partial T_h}{\partial \dot{m}_h}$

5.2.9 Condenser Model

5.2.9.1 Two-Zone

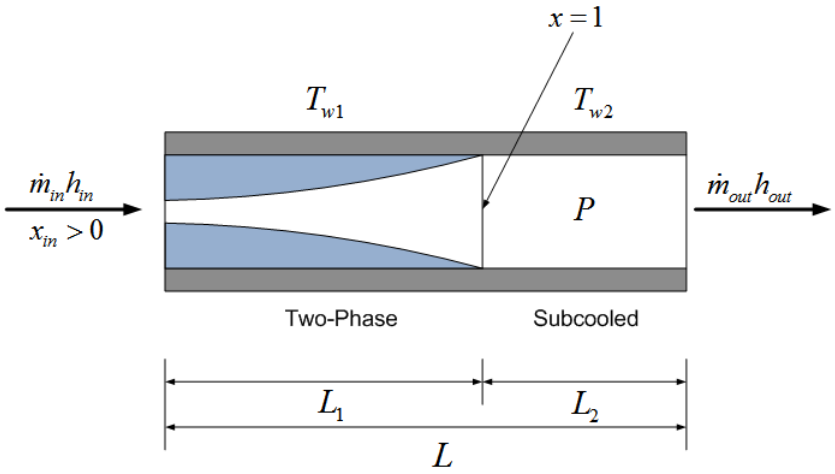

Figure 5.4: Two-Zone Moving Boundary Model for Condenser

The derivation is similar to that of the two-zone evaporator found in [RA04]. The resulting model is a set of five nonlinear differential equations, written in descriptor form given by

$$Z(x,u)\dot{x} = f(x,u) \tag{5.40}$$

$$x = \begin{bmatrix} L_1 & P & h_{out} & T_{w1} & T_{w2} \end{bmatrix}^T \qquad u = \begin{bmatrix} \dot{m}_{in} & \dot{m}_{out} & h_{in} & T_{c,in} & \dot{m}_c \end{bmatrix}^T \tag{5.41}$$

$$Z(x,u) = \begin{bmatrix} z_{11} & z_{12} & 0 & 0 & 0 \\ z_{21} & z_{22} & z_{23} & 0 & 0 \\ z_{31} & z_{32} & z_{33} & 0 & 0 \\ 0 & 0 & 0 & z_{44} & 0 \\ z_{51} & 0 & 0 & 0 & z_{55} \end{bmatrix} \tag{5.42}$$

$$f(x,u) = \begin{bmatrix} \dot{m}_{in}(h_{in} - h_f) + \alpha_{i1}A_i(\frac{L_1}{L})(T_{w1} - T_{r1}) \\ \dot{m}_{out}(h_f - h_{out}) + \alpha_{i2}A_i(\frac{L-L_1}{L})(T_{w2} - T_{r2}) \\ \dot{m}_{in} - \dot{m}_{out} \\ \alpha_o A_o(T_c - T_{w1}) - \alpha_{i1}A_i(T_{w1} - T_{r1}) \\ \alpha_o A_o(T_c - T_{w2}) - \alpha_{i2}A_i(T_{w2} - T_{r2}) \end{bmatrix} \tag{5.43}$$

For circular tubes, the inner and outer tube surface areas are given by $A_i = 2\pi r_i L$ and $A_o = 2\pi r_o L$, respectively.

Entries of $Z(x,u)$ for the Two-Zone Condenser Model

z_{11}	$\left[\rho_g(h_g - h_f)\right](1-\bar{\gamma})A_{cs}$
z_{12}	$\left[\left(\frac{d(\rho_g h_g)}{dP} - \frac{d\rho_g}{dP}h_f\right)(1-\bar{\gamma}) + \left(\frac{d(\rho_f h_f)}{dP} - \frac{d\rho_f}{dP}h_f\right)\bar{\gamma} - 1\right]A_{cs}L_1$
z_{21}	$\rho_2(h_f - h_2)A_{cs}$
z_{22}	$\left[\left(\left.\frac{\partial\rho_2}{dP}\right\|_{h_2} + \frac{1}{2}\left.\frac{\partial\rho_2}{\partial h_2}\right\|_P \frac{dh_f}{dP}\right)(h_2 - h_f) + \frac{\rho_2}{2}\frac{dh_f}{dP} - 1\right]A_{cs}(L - L_1)$
z_{23}	$\left[\frac{1}{2}\left.\frac{\partial\rho_2}{\partial h_2}\right\|_P (h_2 - h_f) + \frac{\rho_2}{2}\right]A_{cs}(L - L_1)$
z_{31}	$\left[(\rho_f - \rho_2) + (\rho_g - \rho_f)(1-\bar{\gamma})\right]A_{cs}$
z_{32}	$\left\{\left[\left.\frac{\partial\rho_2}{\rho P}\right\|_{h_2} + \frac{1}{2}\left.\frac{\partial\rho_2}{\partial h_2}\right\|_h P\frac{dh_f}{dP}\right](L - L_1) + \left[\frac{d\rho_g}{dP}(1-\bar{\gamma}) + \frac{d\rho_f}{dP}\bar{\gamma}\right]L_1\right\}A_{cs}$
z_{33}	$\frac{1}{2}\left.\frac{\partial\rho_2}{\partial h_2}\right\|_P A_{cs}(L - L_1)$
z_{44}	$(C_p\rho V)_w$
z_{51}	$(C_p\rho V)_w\left(\frac{T_{w1} - T_{w2}}{L - L_1}\right)$
z_{55}	$(C_p\rho V)_w$
A_{cs}	$\pi\left((r_i + w)^2 - r_i^2\right)$

A constant, mean void fraction is assumed to simplify the derivation. This is empircally calculated as prescribed in [BW81].

$$\bar{\gamma} = \frac{1}{1-c} + \frac{c}{(1-x_0)(1-c)^2}\ln[c + (1-c)x_0] \tag{5.44}$$

The Jacobians for the two-zone condenser model are

$$\frac{\partial f}{\partial x} = \begin{bmatrix} a_{11} & a_{12} & 0 & a_{14} & 0 \\ a_{21} & a_{22} & a_{23} & 0 & a_{25} \\ 0 & 0 & 0 & 0 & 0 \\ a_{41} & a_{42} & 0 & a_{44} & a_{45} \\ a_{51} & a_{52} & a_{53} & a_{54} & a_{55} \end{bmatrix} \quad \frac{\partial f}{\partial u} = \begin{bmatrix} b_{11} & 0 & b_{13} & 0 & 0 \\ 0 & b_{22} & 0 & 0 & 0 \\ b_{31} & b_{32} & 0 & 0 & 0 \\ 0 & 0 & 0 & b_{44} & b_{45} \\ 0 & 0 & 0 & b_{54} & b_{55} \end{bmatrix}$$

Entries of Jacobian Matrices for the Two-Zone Condenser Model

$\frac{\partial f}{\partial x}$

a_{11}	$\frac{\alpha_{i1}A_i}{L}(T_{w1}-T_{r1})$
a_{12}	$-\dot{m}_{in}\frac{dh_f}{dP}-\alpha_{i1}A_i\frac{L_1}{L}\frac{dT_{r1}}{dP}$
a_{14}	$\alpha_i A_i\frac{L_1}{L}$
a_{21}	$-\frac{\alpha_{i2}A_i}{L}(T_{w2}-T_{r2})$
a_{22}	$\dot{m}_{out}\frac{dh_f}{dP}-\alpha_{i2}A_i(\frac{L_2}{L})\frac{\partial T_{r2}}{\partial P}\Big\vert_{h_2}$
a_{23}	$-\dot{m}_{out}-\alpha_{i2}A_i(\frac{L_2}{L})\frac{\partial T_{r2}}{\partial h_{out}}\Big\vert_{P}$
a_{25}	$\alpha_{i2}A_i(\frac{L_2}{L})$
a_{41}	$\alpha_o A_o\frac{\partial T_c}{\partial L_1}$
a_{42}	$\alpha_{i1}A_i\frac{\partial T_{r1}}{\partial P}$
a_{44}	$-\alpha_o A_o-\alpha_{i1}A_i+\alpha_o A_o\frac{\partial T_c}{\partial T_{w1}}$
a_{45}	$\alpha_o A_o\frac{\partial T_c}{\partial T_{w2}}$
a_{51}	$\alpha_o A_o\frac{\partial T_c}{\partial L_1}$
a_{52}	$\alpha_{i2}A_i\frac{\partial T_{r2}}{\partial P}$
a_{53}	$\alpha_{i2}A_i\frac{\partial T_{r2}}{\partial h_{out}}$
a_{54}	$\alpha_o A_o\frac{\partial T_c}{\partial T_{w1}}$
a_{55}	$-\alpha_o A_o-\alpha_{i2}A_i+\alpha_o A_o\frac{\partial T_c}{\partial T_{w2}}$

$\frac{\partial f}{\partial u}$

b_{11}	$h_{in}-h_f$
b_{13}	$\dot{m}_{in}$
b_{22}	h_f-h_{out}
b_{31}	1
b_{32}	-1
b_{44}	$\alpha_o A_o\frac{\partial T_c}{\partial T_{c,in}}$
b_{45}	$A_o(T_h-T_{w1})\frac{\partial \alpha_o}{\partial \dot{m}_c}+\alpha_o A_o\frac{\partial T_c}{\partial \dot{m}_c}$
b_{54}	$\alpha_o A_o\frac{\partial T_c}{\partial T_{c,in}}$
b_{55}	$A_o(T_c-T_{w2})\frac{\partial \alpha_o}{\partial \dot{m}_c}+\alpha_o A_o\frac{\partial T_c}{\partial \dot{m}_c}$

5.2.9.2 Three-Zone

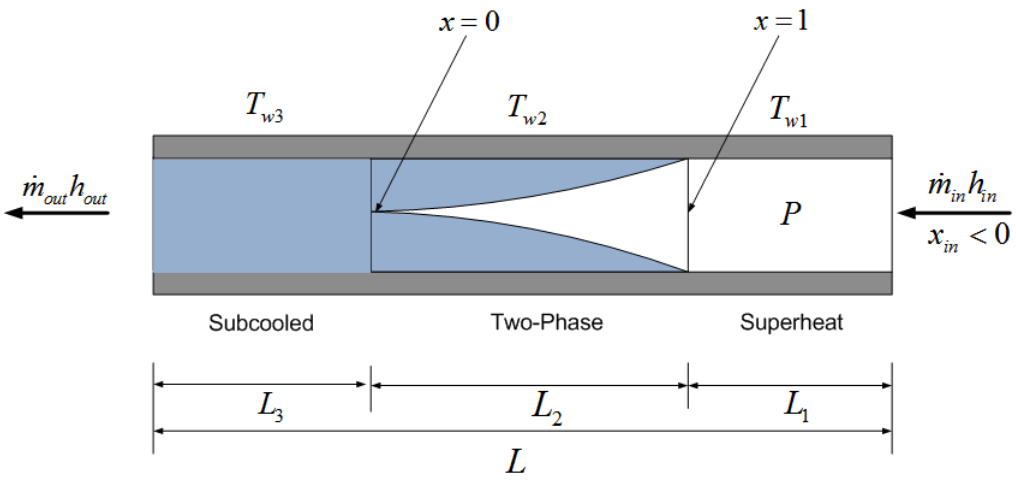

Figure 5.5: Three-Zone Moving Boundary Model for Condenser

Similar to the 3-zone evaporator model, the condenser model is a set of seven nonlinear differential equations, written in descriptor form.

$$Z(x,u)\dot{x} = f(x,u) \tag{5.45}$$

$$x = \begin{bmatrix} L_1 & L_2 & P & h_{out} & T_{w1} & T_{w2} & T_{w3} \end{bmatrix}^T \tag{5.46}$$

$$u = \begin{bmatrix} \dot{m}_{in} & \dot{m}_{out} & h_{in} & \dot{h}_{in} & T_{c,in} & \dot{m}_c \end{bmatrix}^T \tag{5.47}$$

$$Z(x,u) = \begin{bmatrix} z_{11} & 0 & z_{13} & 0 & 0 & 0 & 0 \\ z_{21} & z_{22} & z_{23} & 0 & 0 & 0 & 0 \\ z_{31} & z_{32} & z_{33} & z_{34} & 0 & 0 & 0 \\ z_{41} & z_{42} & z_{43} & z_{44} & 0 & 0 & 0 \\ z_{51} & 0 & 0 & 0 & z_{55} & 0 & 0 \\ z_{61} & z_{62} & 0 & 0 & 0 & z_{66} & 0 \\ 0 & z_{72} & 0 & 0 & 0 & 0 & z_{77} \end{bmatrix} \tag{5.48}$$

$$f(x,u) = \begin{bmatrix} f_1 & f_2 & f_3 & f_4 & f_5 & f_6 & f_7 \end{bmatrix}^T \tag{5.49}$$

Entries of $Z(x,u)$ for the Three-Zone Condenser Model

z_{11}	$A_{cs}\rho_1(h_{in}-h_f)$
z_{13}	$\left[\frac{d\rho}{dP}+\frac{1}{2}\frac{d\rho_f}{dh}\frac{\partial h_g}{dP})(h_{in}-h_g)+\frac{1}{2}\frac{dh_g}{dP}\rho_f-1\right]A_{cs}L_1$
z_{21}	$A_{cs}\left[\rho_f h_g-\rho_3 h_f\right]$
z_{22}	$A_{cs}\left[(\rho_g h_g-\rho_f h_f)\bar{\gamma}+(\rho_f-\rho_3)h_f\right]$
z_{23}	$A_{cs}\left[(\frac{d\rho_f}{dP}+\frac{1}{2}\frac{d\rho_f}{dh}\frac{dh_g}{dP})h_g L_1+(\frac{\partial\rho_3}{\partial P}+\frac{1}{2}\frac{\partial\rho_3}{\partial h}\frac{dh_f}{dP})h_f L_3\right]$ $+A_{cs}\left[(\frac{d\rho_f h_f}{dP}(1-\bar{\gamma})+\frac{d\rho_g h_g}{dP}\bar{\gamma}-1)L_2\right]$
z_{24}	$\frac{1}{2}\frac{\partial\rho_3}{\partial h}h_f A_{cs}L_3$
z_{31}	$\rho_3(h_f-h_3)A_{cs}$
z_{32}	$\rho_3(h_f-h_3)A_{cs}$
z_{33}	$\left[(\frac{\partial\rho_3}{\partial P}+\frac{1}{2}\frac{\partial\rho}{\partial h}\frac{dh_f}{dP}(h_3-h_f)+(\frac{1}{2}\frac{dh_f}{dP})\rho_3-1\right]A_{cs}L_3$
z_{34}	$\left[\frac{1}{2}\frac{\partial\rho_3}{\partial h}(h_3-h_f)+\frac{1}{2}\rho_3\right]A_{cs}L_3$
z_{41}	$A_{cs}(\rho_1-\rho_3)$
z_{42}	$A_{cs}\left[(\rho_g-\rho_f)\bar{\bar{\gamma}}+(\rho_f-\rho_3)\right]$
z_{43}	$A_{cs}\left[(\frac{d\rho_f}{dP}+\frac{1}{2}\frac{d\rho_f}{dh}\frac{dh_g}{dP})L_1+(\frac{\partial\rho_3}{\partial P}+\frac{1}{2}\frac{\partial\rho_3}{dh}\frac{dh_f}{dP})L_3+(\frac{d\rho_f}{dP}(1-\gamma)+\frac{d\rho_g}{dP}\bar{\gamma})L_2\right]$
z_{44}	$\frac{A_{cs}}{2}L_3\frac{\partial\rho_3}{\partial h}$
z_{51}	$(C_p\rho V)_w\frac{T_{w1}-T_{w2}}{L_1}$
z_{55}	$(C_p\rho V)_w$
z_{66}	$(C_p\rho V)_w$
z_{71}	$(C_p\rho V)_w\frac{T_{w2}-T_{w3}}{L_3}$
z_{72}	$(C_p\rho V)_w\frac{T_{w2}-T_{w3}}{L_3}$
z_{77}	$(C_p\rho V)_w$
A_{cs}	$\pi\left((r_i+w)^2-r_i^2\right)$

Entries of $f(x,u)$ for the Three-Zone Condenser Model

f_1	$\dot{m}_{in}(h_{in}-h_g)+\alpha_{i1}\pi D_i L_1(T_{w1}-T_{r1})$
	$-\frac{A}{2}\left[\rho_1 L_1+\frac{1}{2}(h_{in}+h_f)\left.\frac{\partial\rho_1}{\partial h_1}\right\|_P-h_f L_1\left.\frac{\partial\rho_1}{\partial h_1}\right\|_P\right]\dot{h}_{in}$
f_2	$\dot{m}_{in}(h_g-h_f)+\alpha_{i2}\pi D_i L_2(T_{w2}-T_{r2})$
	$+\frac{1}{2}A_{cs}L_1\left.\frac{\partial\rho_1}{\partial h}\right\|_P(h_g-h_f)\dot{h}_{in}$
f_3	$\dot{m}_{out}(h_f-h_{out})+\alpha_{i3}\pi D_i L_3(T_{w3}-T_{r3})$
f_4	$\dot{m}_{in}-\dot{m}_{out}-\frac{A_{cs}L_1}{2}\left.\frac{\partial\rho_1}{\partial h_1}\right\|_P\dot{h}_{in}$
f_5	$\alpha_o\pi D_o L_1(T_c-T_{w1})+\alpha_{i1}\pi D_i L_1(T_{r1}-T_{w1})$
f_6	$\alpha_o\pi D_o L_2(T_c-T_{w2})+\alpha_{i2}\pi D_i L_2(T_{r2}-T_{w2})$
f_7	$\alpha_o\pi D_o L_3(T_c-T_{w3})+\alpha_{i3}\pi D_i L_3(T_{r3}-T_{w3})$

5.3 Dynamic Piston Expander Model

ThermoBox, a MATLAB toolbox for thermodynamic modeling, provides the general thermodynamic blocks to create a dynamic piston expander model based on mass and energy conservation principles applied to a control volume with arbitrary number of inlet and outlet ports. The input, output, and state features of each block are presented. The interested reader is directed to [Lim11] for derivation details of each of these blocks.

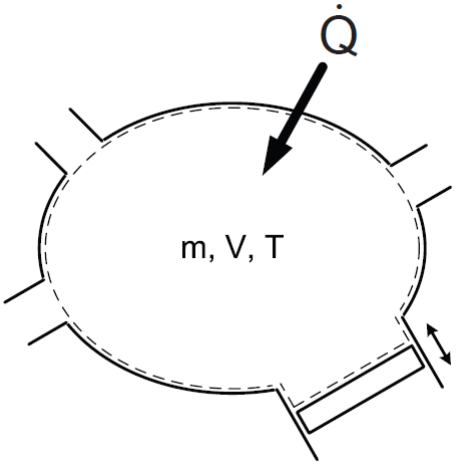

Figure 5.6: Control Volume of a General Open System with Variable Volume

The cylinder is modeled using mass and energy balances for a control volume of an open system with arbitrary number of inlet and outlet ports. Heat transfer across the volume boundaries is accounted for through a user-defined model. The model also accounts for a variable volume to represent the piston volume displacement in the cylinder.

The model assumes the following

1. Zero-dimensional, that is properties are uniform throughout the volume
2. Only displacement work is done by the system
3. Kinetic and potential energies of the fluid are neglected

The governing equations describing mass and energy are given by

$$\frac{dm}{dt} = \sum_i \dot{m}_i \tag{5.50}$$

$$\frac{dE}{dt} = \dot{Q} - \dot{W} + \sum_i \dot{m}_i h_i \tag{5.51}$$

where E is the total energy state of the system, $\dot{Q}$ is the rate of heat transfer into the system, $\dot{W}$ is the rate of work done by the system, and h_i is the enthalpy at port i. The dynamic equation for the temperature state is given by

$$\frac{dT}{dt} = \frac{\left[\frac{\partial T}{\rho}(\frac{\partial \rho}{\partial T})_\rho - h\right]\frac{dm}{dt} - \left[T(\frac{\partial P}{\partial T})_\rho\right]\frac{dV}{dt} + \dot{Q} + \sum_i \dot{m}_i h_i}{\left[mC_p = \frac{VT}{\rho}(\frac{\partial P}{\partial T})_\rho^2(\frac{\partial P}{\partial \rho})_T^{-1}\right]} \tag{5.52}$$

5.3.1 Orifice Model

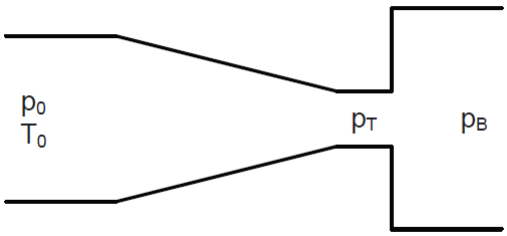

Figure 5.7: Compressible Flow due to Pressure Differential

This model is for open systems with inlet and outlet ports to depict pressure-driven flow through a constriction. The assumptions of the model are:

1. One-dimensional, steady flow
2. Isentropic process
3. n is constant along the flow path
4. Negligible potential energy

Without a pressure difference, the mass flow rate is zero. Non-zero mass flow rate is induced by a difference in the fluid pressure P_0 (also known as the stagnation presure) and the back pressure P_b. The flow direction is from the higher pressure to the lower one. As the back pressure decreases, flow is towards the back pressure and at some point the throat pressure P_T will reach a critical pressure when the flow becomes sonic at the throat. The flow reaches the speed of sound for the throat state. A further decrease in P_B does not affect the throat condition. The mass flow rate does not increase for choked flow, and the fluid continues to expand from the throat pressure to the back pressure outside the throat.

Accounting for choked flow, the mass flow rate of a compressible fluid is described by

$$\dot{m} = \begin{cases} A_T \left(\frac{P_B}{P_0}\right)^{\frac{1}{n}} \sqrt{P_0 \rho_0 \frac{2n}{n-1} \left[1 - \left(\frac{P_B}{P_0}\right)^{\frac{n-1}{n}}\right]} & \text{if } P_B > P_0 \left(\frac{2}{n+1}\right)^{\frac{n}{n-1}} \\ A_T \left(\frac{2}{n+1}\right)^{\frac{n+1}{2(n-1)}} & \text{if } P_B \leq P_0 \left(\frac{2}{n+1}\right)^{\frac{n}{n-1}} \end{cases}$$

where n is given by

$$n = \frac{C_P \rho}{C_v P} \left(\frac{\partial P}{\partial \rho}\right)_T \tag{5.53}$$

.

5.3.2 Piston-Crankshaft Assembly

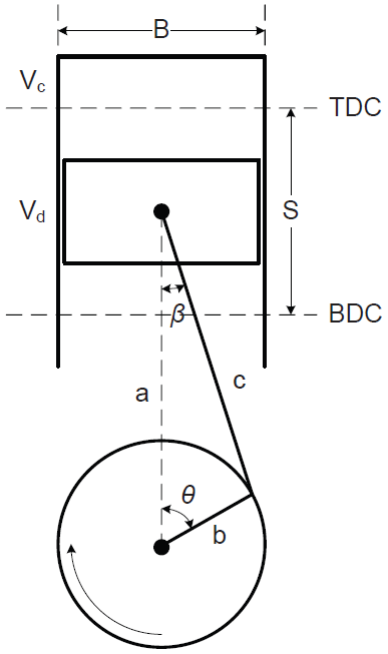

Figure 5.8: Piston-Cylinder Assembly Connected to Crankshaft

The piston-cylinder is connected to a crankshaft as shown in Figure 5.8. For a crank position angle θ, the cylinder volume is described by

$$V(\theta) = V_d \left[\frac{1}{r_c - 1} + \frac{1}{2} \left(R + 1 - \cos(\theta) - \sqrt{R^2 - \sin^2(\theta)} \right) \right] \tag{5.54}$$

where V_d is the swept volume, r_c is the compression ratio, R is the ratio of the connecting rod to the crank radius. Taking the time derivative yields the following:

$$\frac{dV(\theta, \dot{\theta})}{dt} = \frac{1}{2} V_d \left[\sin(\theta) \left(1 + \frac{\cos(\theta)}{\sqrt{R^2 - \sin^2(\theta)}} \right) \right] \dot{\theta} \tag{5.55}$$

To calculate the heat transfer rate, the expression for the surface area of the cylinder is needed and described below.

$$A(\theta) = \frac{\pi B^2}{2} + \frac{4}{B} V(\theta) \tag{5.56}$$

where B is the bore diameter. The input to the block is the crank speed in RPM and the outputs are the rate of volume change $\dot{V}$ in m^3 and the crank position θ in degrees. The initial parameters are the following:

1. Crank position in degrees
2. Displaced volume of the cylinder in liters
3. Ratio of the connecting rod length to the crank radius

5.3.3 Simulations

The two-cylinder piston expander in this research application is connected to the engine crankshaft in a 1:1.33 ratio (1.3 expander rotations for every crankshaft rotation). Working fluid expansion provides additional torque to the crankshaft. The intake port valve is driven by the position of the piston. The exhaust port is a sleeve valve, but considered a pin valve like the intake port. The lift of the valve determines the port opening area. The lift profiles for the intake and exhaust ports of both cylinders are identical and are shown in Figure 5.9 with zero degrees as top-dead-center (TDC).

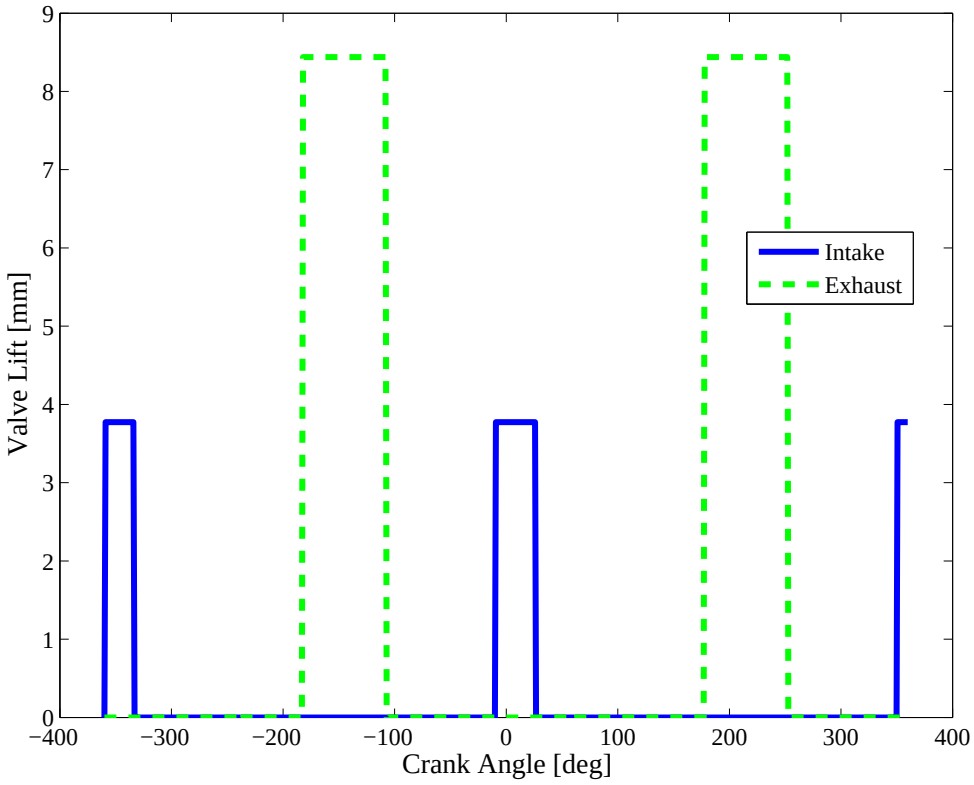

Figure 5.9: Intake and Exhaust Port Lift Profile

The piston expander is simulated for a water-ethanol mixture and the results are shown in Figures 5.10 and 5.11. The evaporating and condensing pressures are 4 MPa and 0.115 MPa, respectively. The inlet and outlet working fluid enthalpies are 2300 $\frac{kJ}{kg}$ and 1950 $\frac{kJ}{kg}$, respectively. The engine crankshaft speed is 1200 revolutions per minute. The expander power generated is within the expected range established by the static RC model design in Chapter 4.

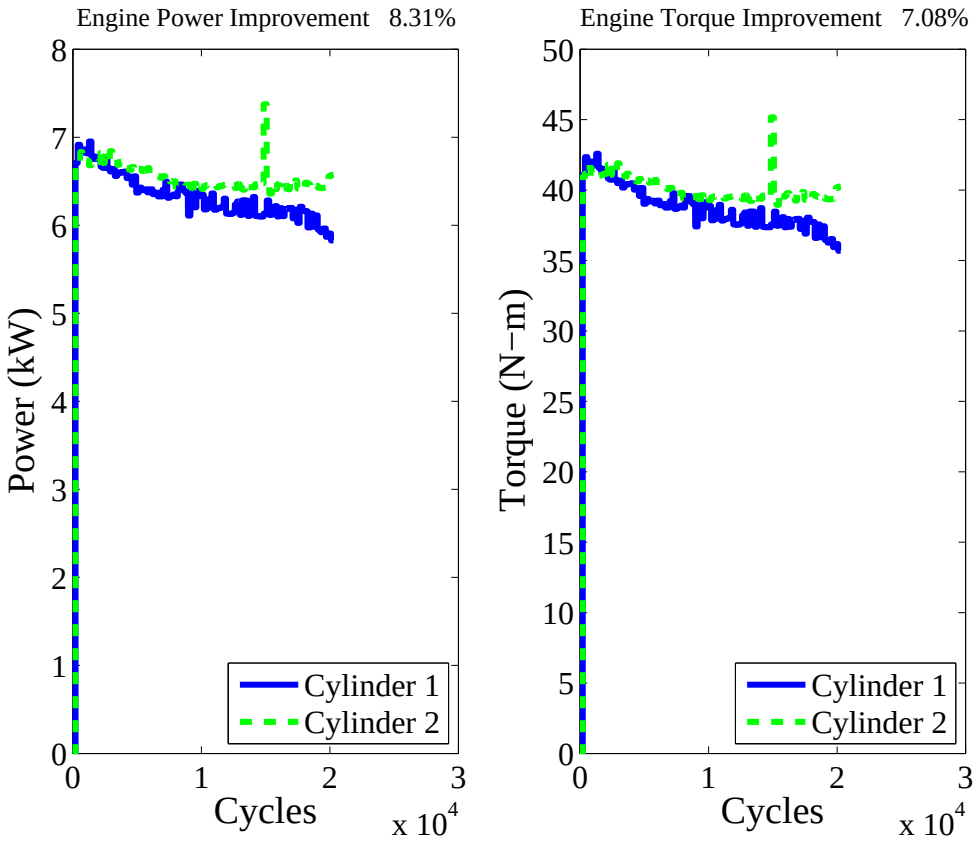

Figure 5.10: Expander Power and Torque

The power and torque from each cylinder is expected to be identical due to a common geometry and valve timing. The differences are attributed to the numerical solver handling the initial condition of each piston 180 degree out of phase of each other. The engine power improvement from the RC is given by

$$\text{Engine Power Improvement} = \frac{\text{Expander Power}}{\text{Average Engine Power}} \tag{5.57}$$

The average engine power and torque are 143 kW and 987 N-m, respectively, and are representative of the driving cycles examined in this dissertation.

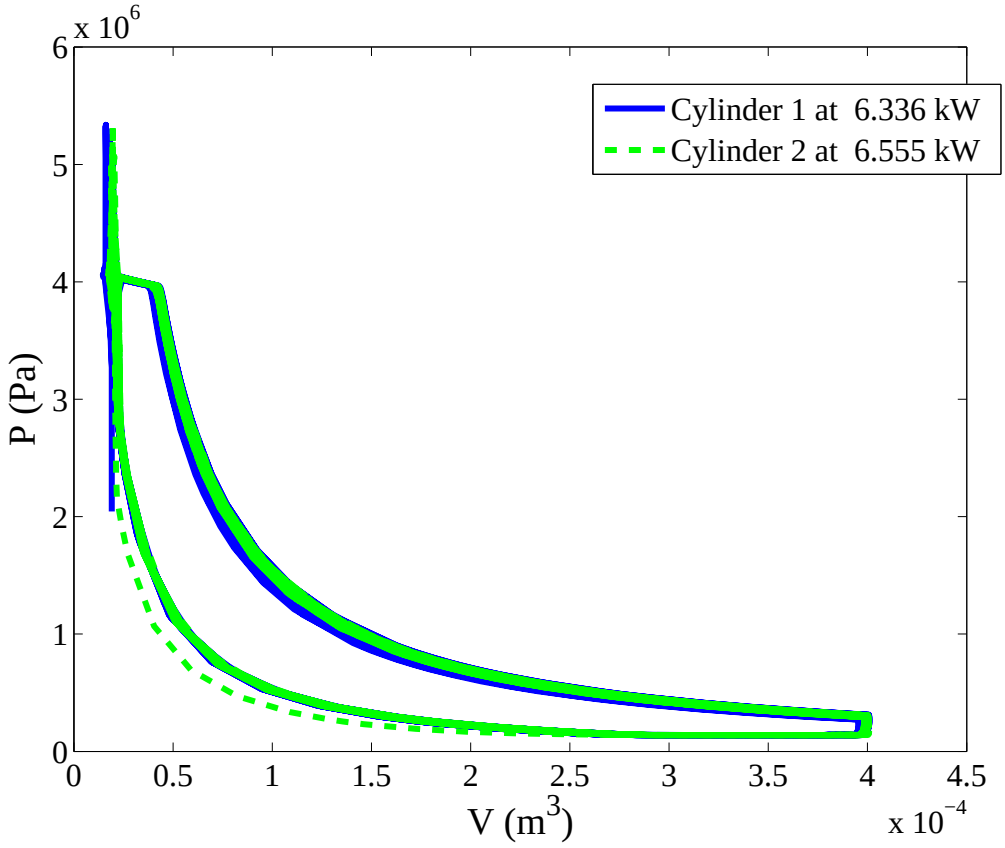

Figure 5.11: Expander Pressure-Volume Diagram

CHAPTER 6

State Estimation for Rankine Cycles

There has been a growing need for modeling, controlling, and monitoring waste heat recovery (WHR) systems during transient operations. Depending on the driving terrain, the engine's exhaust can experience large exhaust temperature and flow rate swings. Heat source transients are presented in Chapter 2 for a 13 liter heavy-duty diesel engine. The transients create a challenge in operating the WHR as a steady-state cycle and introduce concerns of drying out and flooding components as well undesirably high and low working fluid temperatures. These critical conditions must be known before so corrective action can be taken.

Furthermore, some process variables are difficult to measure. Even if possible, the extra measurement sensors may add to system complexity and cost. The limited space under the engine hood necessitates minimal, automotive grade sensors that adequately measure system state. Pressure, temperature, and mass flow rate sensors are typically available. Other process variables are difficult to measure such as wall temperatures and phase boundaries in two-phase flow. While phase-change boundary detectors exist, they are typically expensive research grade sensors. Practically, this boundary cannot be measured directly in automotive applications for this reason.

State estimation is discussed in the literature and often required in feedback control and monitoring for fouling. Nonlinear observers were applied on a low-order evaporator model based on sensor measurements of evaporating temperature and

used to synthesize feedback control [CHA04]. The fixed observer gains were obtained for specified operating points and guaranteed state estimation convergence. An Extended Kalman Filter (EKF) has been applied on a dynamic heat exchanger model to detect fouling [JLP07]. However, the considered working fluid does not undergo a phase change. To the knowledge of the authors, estimation has not been explored for the mathematically richer Moving Boundary heat exchanger models describing multi-phase evaporating and condensing flows. Furthermore, evaluating state estimation performance using different and minimal measurement sensors has received little attention. The availability and cost of these sensors can impact whether feedback control can be achieved, if at all depending on state observability.

This chapter examines model-based state estimation techniques useful for monitoring heat exchanger state of health and control design for critical condition avoidance. Depending on the operating conditions, controls may be needed to steer the system away from the mentioned critical conditions. Details for a model-based nonlinear estimation method of a nonlinear open organic Rankine cycle (ORC) model are presented. A linear state estimator is also developed for estimating the linear and nonlinear open ORC. The measurements considered are typically available pressure and temperature and their ability to individually and collectively infer the unmeasurable states or process variables is examined.

This chapter begins with state observer design on a linear moving boundary model for an evaporator before focusing on nonlinear state estimation. A nonlinear Extended Kalman Filter (EKF) and a Fixed-Gain estimator are presented, both using typically available pressure and/or temperature sensor measurements to estimate evaporator states. Estimation performance based on a numerical (Full) and analytical (Approximated) process Jacobian is shown.

Simulations of the state estimators are given under transient step inputs. The chapter examines state estimation performance based on measurement choice and investigates the relative observability for selected measurements. State estimation performance is also presented for the selected Jacobian method in the estimator design.

The chapter concludes with simulations of a exhaust gas recirculation (EGR) evaporator coupled to an expander for waste heat recovery in a heavy-duty truck. Transient heat source data are provided from driving cycles of a 13 liter diesel powertrain described in Chapter 2. The results are useful for predicting power recovery in heat recovery applications. The estimation results are useful for controller design and performance monitoring including fouling detection and scheduling maintenance.

6.1 Linear State Estimation

State estimators are useful for state feedback control design when one or more states cannot be measured. A linear estimator is designed from a small-signal linear model of the nonlinear Moving Boundary models. The linear heat exchanger model for the nonlinear model $\dot{x} = Z^{-1}f$ is given by

$$\begin{aligned} \delta\dot{x} &= A\delta x + B\delta u \\ \delta y &= C\delta x + D\delta u \end{aligned} \tag{6.1}$$

where the system matrices A and B are given in Chapter 5. For pressure and temperature output measurements, the C matrix is given by and its linear estimator is given by

$$C = \begin{bmatrix} \delta P \\ \\ \delta T_{out} \end{bmatrix} \tag{6.2}$$

where δT_{out} is a thermodynamic function of working fluid states δP and δh_{out}.

Its linear state estimator is given by

$$\delta\hat{x}_k = A\delta\hat{x}_{k-1} + B\delta u_{k-1} + L\delta\tilde{y}_{k-1} \tag{6.3}$$

$$\delta\hat{y}_k = C\delta\hat{x}_k + D\delta u_k \tag{6.4}$$

$$\delta\tilde{y}_k = \delta z_k - \delta\hat{y}_k \tag{6.5}$$

$$\delta u_k = u_k - u_{eq} \tag{6.6}$$

$$\delta z_k = z_k - z_{eq} \tag{6.7}$$

$$\hat{x}_k = x_{eq} + \delta\hat{x}_k \tag{6.8}$$

The gain L can be obtained from pole-placement.

The three-zone evaporator model is linearized about the operating or linearization point. Depending on the linearization point, the model may contain a zero eigenvalue for continuous-time systems or an eigenvalue on the unit circle for discrete-time systems, rendering the system unobservable. This arises from the mass conservation equation, with h_{out} being the uncontrollable and unobservable state. For the purpose of designing a closed-loop state estimator, the h_{out} state is temporarily removed. This is justified since this state has minimal influence on the other states, despite being highly influenced by them. It is added back to the system after designing the closed-loop state estimator via pole placement. The observer poles are made five times larger than the model's eigenvalues.

Figures 6.1-6.3 show that the three-zone linear evaporator states are fully observable, allowing the use of full state feedback control. A pressure measurement is able to reconstruct the other states.

The abbreviations SC, TP, and SH are **S**ub**C**ooled, **T**wo-**P**hase, and **S**uper**H**eat, respectively.

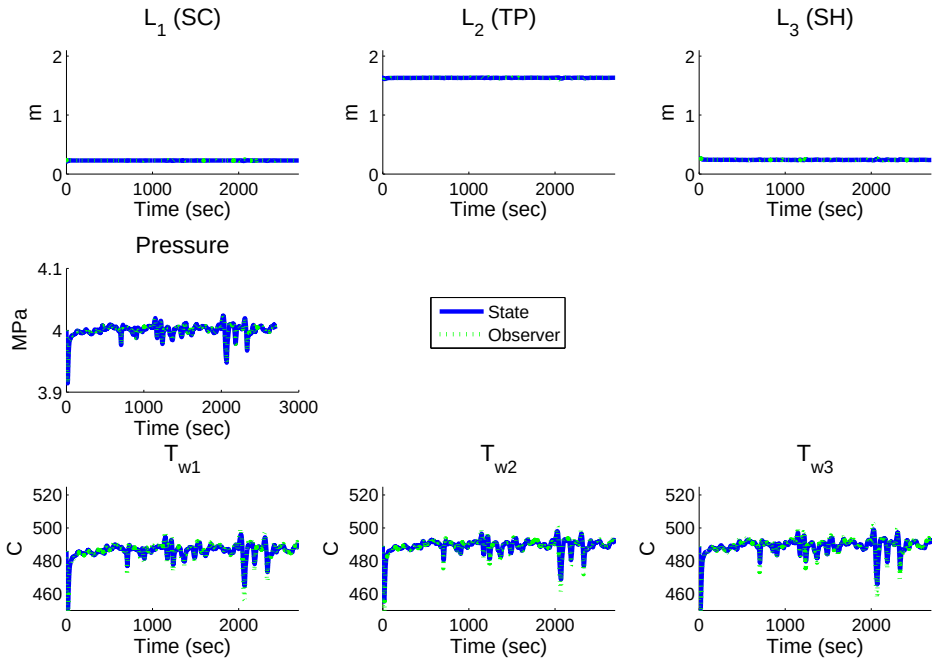

Figure 6.1: State Estimator for Linear Three-Zone Moving Boundary Evaporator Model for Flat Road Cycle

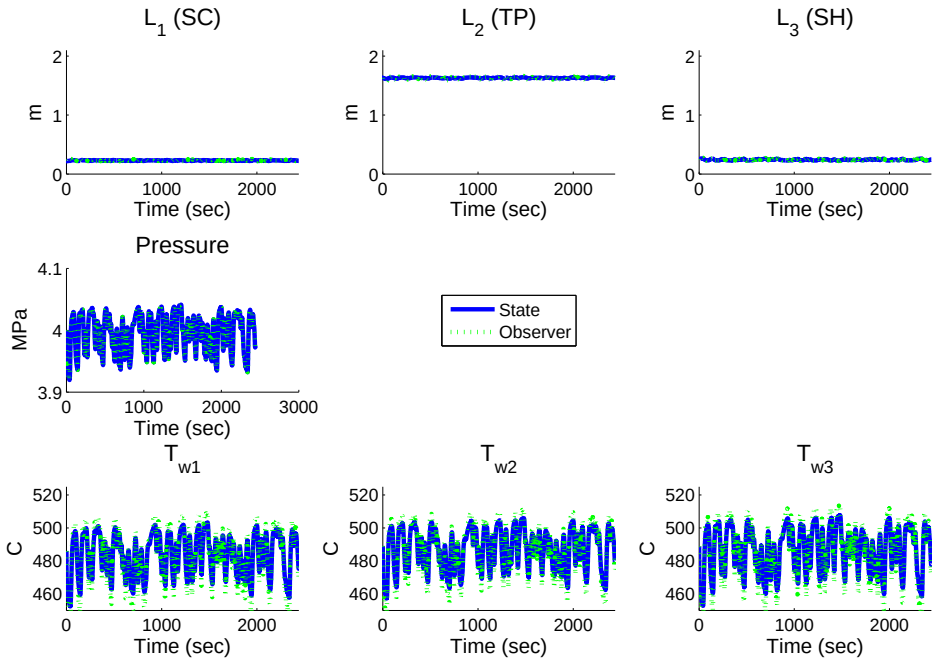

Figure 6.2: State Estimator for Linear Three-Zone Moving Boundary Evaporator Model for Hilly Road Cycle

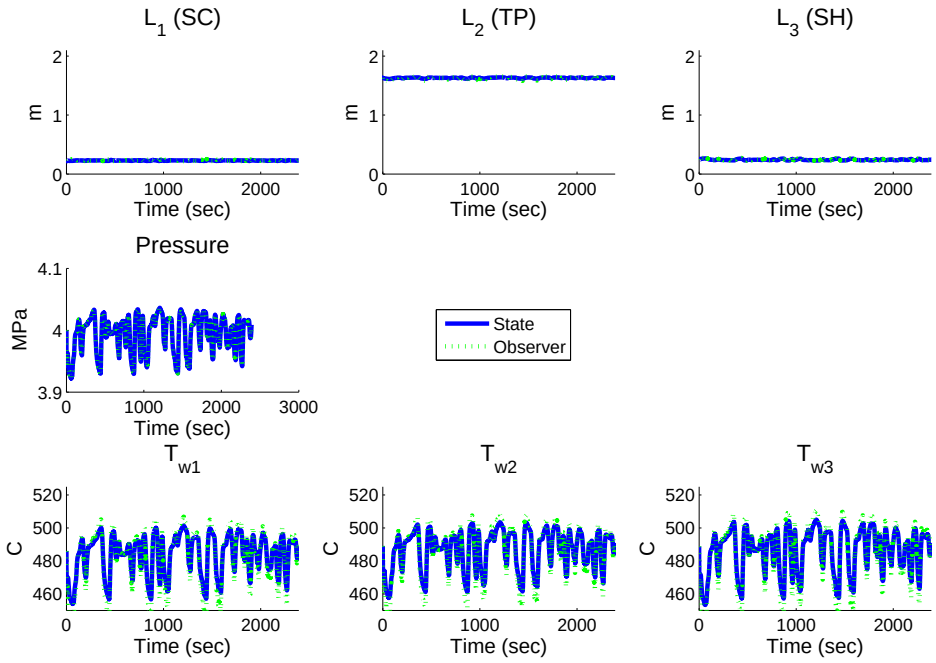

Figure 6.3: State Estimator for Linear Three-Zone Moving Boundary Evaporator Model for Rolling Hills Road Cycle

The simulations show that the linear estimator works well for the linear model. Because real systems do not necessarily remain around the operating point, the linear model and thus the estimator may no longer apply. A new linear model and estimator may be computed at the new operating point, which may work well. Too many operating points may make the approach cumbersome. A nonlinear estimator is investigated in the next section for the nonlinear model to avoid the limited validity of linear models and their linear estimators.

6.2 Nonlinear State Estimation

Nonlinear estimators are useful when linear models are not available or difficult to obtain. Nonlinear control design can be directly executed without needing to linearize. The standard Extended Kalman Filter and its Fixed-Gain version are presented and compare.

6.2.1 Extended Kalman Filter (EKF)

The continuous-time plant is given by

$$\dot{x} = g(x, u) + w(t) \qquad w(t) \sim N(0, Q) \tag{6.9}$$

where $g(x, u) = Z^{-1}f$ and w is process noise with zero mean and covariance Q.

The discrete-time plant is obtained using Forward Euler with a sampling time of t_s.

$$x_k = x_{k-1} + t_s g(x_{k-1}, u_{k-1}) \tag{6.10}$$

The measurement equation is given by

$$z_k = h(x_k) + v_k \qquad v_k \sim N(0, R) \tag{6.11}$$

where v is the measurement noise with zero mean and covariance R. In general, the measurement function h is a nonlinear function of the states and inputs.

The discrete-time extended Kalman Filter (EKF) estimator model is given by

$$\hat{x}_{k|k} = \hat{x}_{k|k-1} + t_s g(\hat{x}_{k|k-1}, u_k) + K_k \tilde{y}_k \tag{6.12}$$

where $\tilde{y}_k = z_k - h(\hat{x}_{k|k-1})$ is the innovation or measurement residual. K_k is the

Kalman Gain computed by the following update equations

$$K_k = P_{k|k-1} H_k^T S_k^{-1} \tag{6.13}$$

$$S_k = H_k P_{k|k-1} H_k^T + R_k \tag{6.14}$$

$$P_{k|k-1} = F_{k-1} P_{k-1|k-1} F_{k-1}^T + Q_{k-1} \tag{6.15}$$

$$P_{k|k} = (I - K_k H_k) P_{k|k-1} \tag{6.16}$$

6.2.2 Fixed-Gain State Estimator

A Fixed-Gain EKF estimator has the same structure as Equation 6.12 but with K fixed. Its value is obtained from the steady-state gain of the EKF found at equilibrium.

6.2.3 For Moving Boundary Condenser Model

Nonlinear state estimation for a stand-alone Moving Boundary heat exchanger model is presented in this section. The states of a two-zone condenser model are estimated by an EKF for constant and step inputs. Both pressure and temperature measurements are used. The Approximated Jacobian is assumed.

6.2.4 Simulations

Figure 6.4 show the estimation performance for constant inputs to the condenser model. The net mass flow is zero. The estimation error all converge to the model states with exception of the phase-change boundary having an estimation bias within 10% of the plant model value.

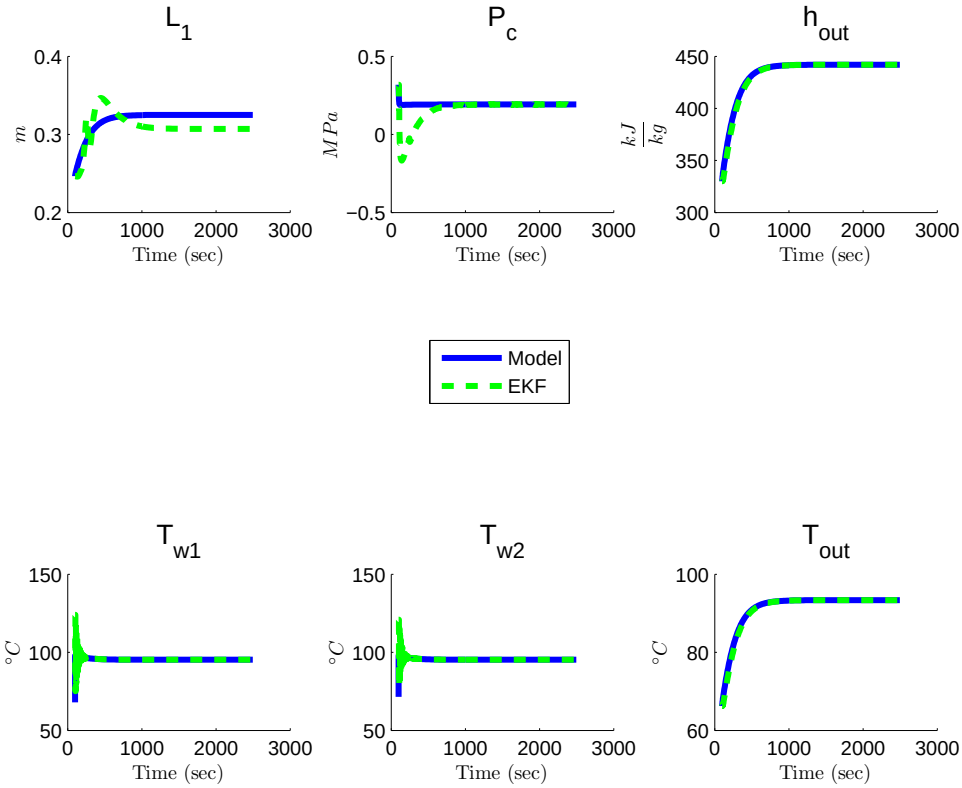

Figure 6.4: EKF Estimator States using Pressure and Temperature Measurements, Constant Inputs

Figure 6.5 shows step changes in the heat sink temperature and mass flow rate. At time 200 and 1000 seconds, the temperature and mass flow rate increased by 25% and decreased by 33%, respectively. The phase-change boundary state also experiences the worst estimation performance.

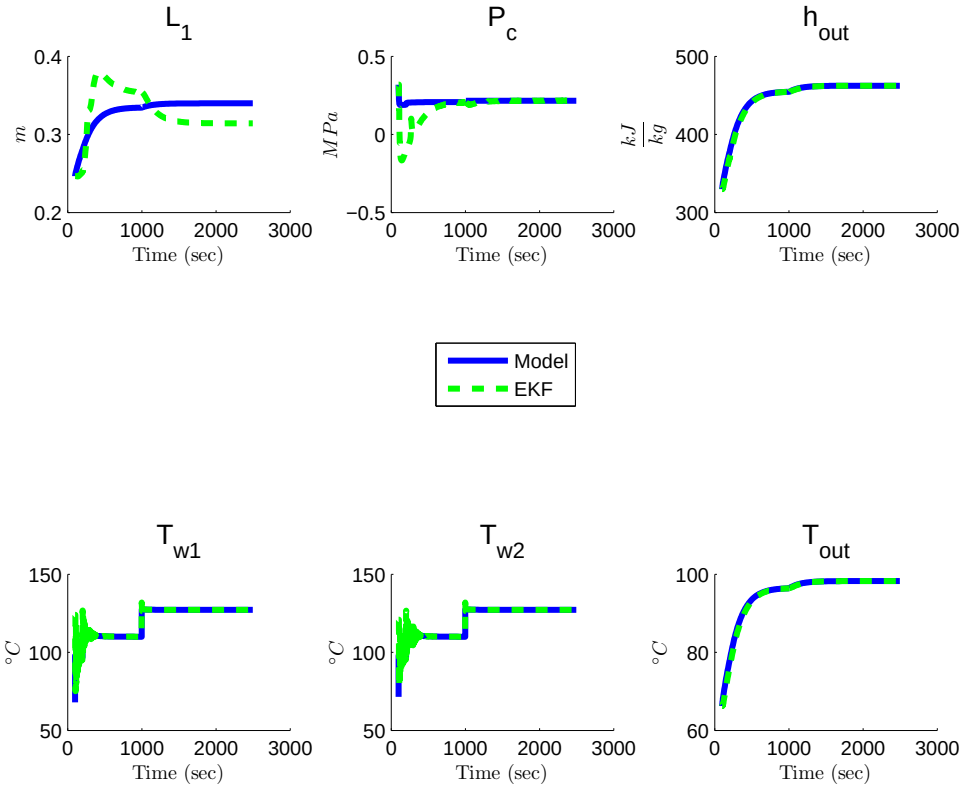

Figure 6.5: EKF Estimator States using Pressure and Temperature Measurements, Step Inputs

6.3 Nonlinear State Estimation for Open Organic Rankine Cycle (ORC)

To meet emission standards, exhaust gas recirculation (EGR) coolers are found in modern day heavy-duty engines for nitrogen oxide reduction. The cooler rejects heat from the engine manifold exhaust before recirculating it to the piston combustion chamber to displace combustible components. This leads to lower temperature combustion and lower production of nitrogen oxides. The heat rejec-

tion provides an opportunity to recover energy through a ORC.

The EGR cooler from a 13 liter diesel powertrain serves as the ORC evaporator and is coupled to an expander for waste heat recovery. Simulations were conducted for the Rolling Hills driving cycle. Its transient heat conditions in temperature and mass flow rate are shown in Chapter 2. The other inputs to the ORC model were kept constant as described in the Setup section.

The states of a control-oriented two-zone evaporator Moving Boundary model are estimated. An expander model is connected to the evaporator through a throttle valve as seen in Figure 6.6. Because the heat exchanger dynamics are much slower than that of the expander and throttle, the latter components are treated as static models.

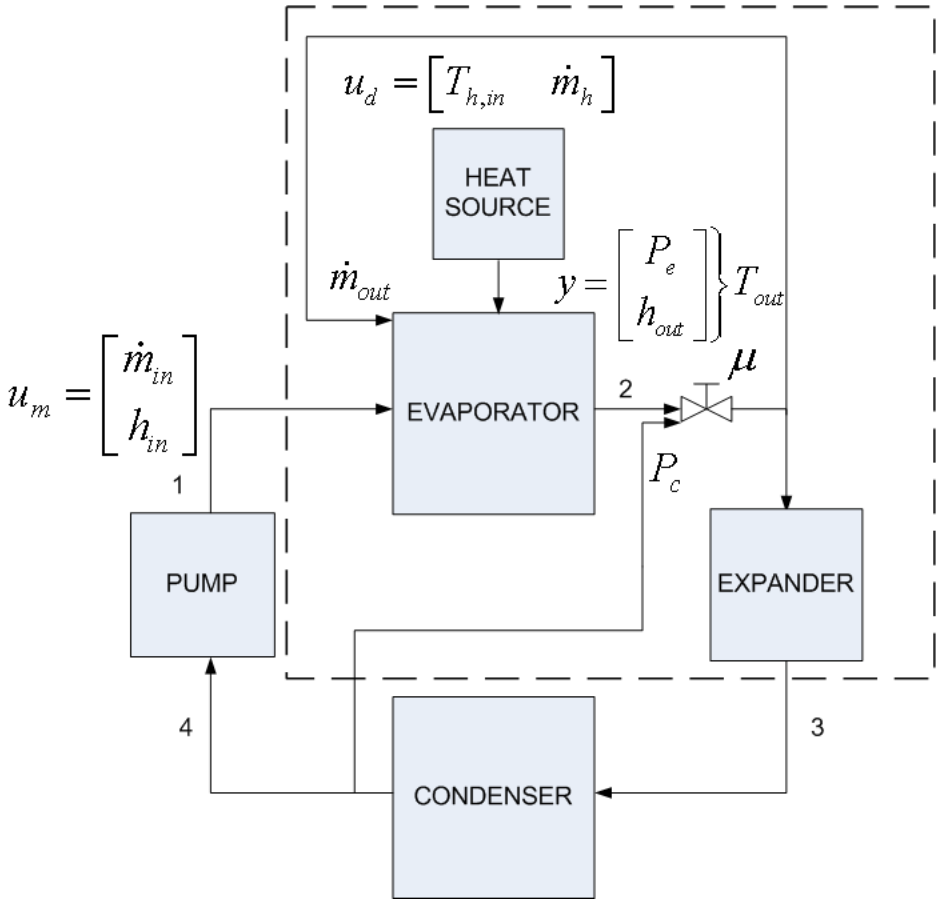

Figure 6.6: Open Rankine Cycle Model

6.3.1 Evaporator Model

The two-zone evaporator model is given by

$$Z(x_e, u_e)\dot{x}_e = f(x_e, u_e) \tag{6.17}$$

where the state x_e and input u_e vectors are

$$x_e = [L_1 \quad P \quad h_{out} \quad T_{w1} \quad T_{w2}]^T \tag{6.18}$$

$$u_e = [\dot{m}_{in} \quad \dot{m}_{out} \quad h_{in} \quad T_{h,in} \quad \dot{m}_h]^T \tag{6.19}$$

Z and f are a five-dimensional matrix and vector, respectively.

6.3.2 Expander and Throttle Valve Models

The following models are static due to the slower heat exchanger dynamics. The mass flow rate into the expander is given by

$$\dot{m}_v = \frac{\beta \mu P_{in}}{\sqrt{T_{in}}} \tag{6.20}$$

where β is the valve coefficient, μ is throttle valve position, and T_{in} is the inlet temperature, also the evaporator outlet temperature calculated as P and h_{out} in Figure 6.6.

The expander outlet enthalpy is given by the rearrranged isentropic efficiency definition

$$h_{out} = h_{in} - \eta \left(h_{in} - h_{out,s} \right) \tag{6.21}$$

with an assumed isentropic efficiency η.

The power output of the expander is given by

$$N = \dot{m}_v \left(h_{in} - h_{out} \right) \tag{6.22}$$

Equation 6.20 for the throttle valve mass flow rate is connected to the evaporator's $\dot{m}_{out}$ input as shown in Figure 6.6. The evaporator pressure P and enthalpy h_{out} determine the T_{in} for the turbine model.

6.3.3 Open ORC System Model

The system model with the evaporator, valve, and expander connected still has the nonlinear form in Equation 6.17:

$$Z(x,u)\dot{x} = f(x,u) \tag{6.23}$$

where the state x and input u vectors are now

$$x = [L_1 \quad P \quad h_{out} \quad T_{w1} \quad T_{w2}]^T \tag{6.24}$$

$$u = [\dot{m}_{in} \quad h_{in} \quad T_{h,in} \quad \dot{m}_h \quad \mu]^T \tag{6.25}$$

The output measurements are pressure and outlet temperature of the working fluid, defined as

$$y = [P \quad T_{out}]^T \tag{6.26}$$

Linearizing Equation 6.17 at equilibrium x_{eq} and u_{eq} yields

$$\begin{aligned} \delta\dot{x} &= A\delta x + B\delta u \\ \delta y &= C\delta x + D\delta u \end{aligned} \tag{6.27}$$

where

$$A = Z^{-1}\frac{\partial f}{\partial x}\Big|_{x_{eq},u_{eq}} \tag{6.28}$$

$$B = Z^{-1}\frac{\partial f}{\partial u}\Big|_{x_{eq},u_{eq}} \tag{6.29}$$

While this is a valid step for sufficiently small signals around that operation point, the linearization may not describe the nonlinear dynamics for large enough transients. This chapter focuses on simulation and analysis with the nonlinear model to capture a larger operating range.

The filter will assume combinations of pressure and temperature measurements available for state estimation. That is,

$$h(x) = \begin{bmatrix} P \\ T_{out} \end{bmatrix} \tag{6.30}$$

where T_{out} is a thermodynamic function of working fluid states P and h_{out}.

6.3.4 State and Relative Observability

Pressure and temperature sensors are typically available for heat exchanger measurements. Because these sensors are not always desired due to physical and cost requirements, this section examines state estimation effectiveness for each sensor and their combinations. State and relative observability are examined through the empirical observability gramian for nonlinear systems. The same relative observability measures for linear systems are applied.

For the purpose of defining the gramians, a nonlinear system control system is assumed:

$$\dot{x} = f(x,u) \tag{6.31}$$

$$y = h(x,u) \tag{6.32}$$

The initial state perturbation sets are given in [Him] as

$$E_x = \{f_i \in \mathbb{R}^n; \|f_i\| = 1; f_i f_{j\neq i} = 0; i = 1,\ldots,n\} \tag{6.33}$$

$$R_x = \{T_i \in \mathbb{R}^{n\times n}; T_i^* T_i = \mathbb{1}; i = 1,\ldots,t\} \tag{6.34}$$

$$R_u = \{S_i \in \mathbb{R}^{j\times j}; S_i^* S_i = \mathbb{1}; i = 1,\ldots,s\} \tag{6.35}$$

$$Q_x = \{d_i \in \mathbb{R}; d_i > 0; i = 1,\ldots,r\} \tag{6.36}$$

These sets should correspond to the ranges in initial states the system is operating in. For the sets defined above and the steady-state $\bar{x}$ and corresponding output $\bar{y}$, the empirical observability gramian is given by

$$W_o = \frac{1}{|Q_x||R_x|}\sum_{k=1}^{|Q_x|}\sum_{l=1}^{|R_x|}\frac{1}{d_k^2}T_l\int_0^\infty \Psi^{kl}(t)dtT_l^* \tag{6.37}$$

$$\Psi_{ab}^{kl} = \left(y^{kla}(t) - \bar{y}\right)^* \left(y^{klb}(t) - \bar{y}\right) \in \mathbb{R}$$

where y^{kla} is the system output for the initial state $x_0^{kla} = d_k S_l f_a + \bar{x}$.

To measure the relative observability of nonlinear systems, the empirical observability gramian in Equation 6.38 is computed using the Unified Software Framework for Empirical Gramians described in [Him]. The gramian is calculated at every time-step, from the current time to the next sampling step. The calculations use the current states and inputs, which are then perturbed by rotations and scaling. The sets of rotations are $\{\mathbf{1}\}$ (unit matrix) and $\{-\mathbf{1}, \mathbf{1}\}$ (negative unit matrix and unit matrix). The restricted rotations simplifies Equation 6.38 to

$$W_o = \frac{1}{|Q_x||R_x|} \sum_{k=1}^{|Q_x|} \sum_{l=1}^{|R_x|} \frac{1}{d_k^2} \int_0^\infty \Psi^{kl}(t) dt \tag{6.38}$$

and the initial state perturbation to $x_o^{kla} = -\mathbf{1}^l d_k f_a + \bar{x}$.

Candidates for measuring the degree of observability of a linear system are typically based upon the linear observability gramian. The same measures are applied on the empirical observability gramian for the nonlinear system. These measures typically examine the gramian's smallest and the largest eigenvalues. Both are used for analysis.

The following observability measures are used in [SH04] and are based on the eigenvalues λ_i of the observability gramian W_o. Larger values of the following measures indicate a higher degree of observability.

$$\mu_1 = \frac{n}{\text{trace}(W_o^{-1})} \tag{6.39}$$

$$\mu_3 = \lambda_{\min}(W_o) \tag{6.40}$$

$$\mu_4 = \frac{n}{\text{trace}(W_o^{-1})} \tag{6.41}$$

$$\mu_5 = \det(W_o)^{1/n} \tag{6.42}$$

The condition number relates the relative observability between the most and least observable states. Smaller condition numbers generally imply increased system

observability.

$$\mu_7 = \text{CN} = \frac{\sigma_{\max}}{\sigma_{\min}} \tag{6.43}$$

The smallest singular value is a measure of how far the system is away from being unobservable.

$$\mu_2 = \text{NS} = \sigma_{\min}(W_o) \tag{6.44}$$

The largest singular value measures the maximal response in the direction of the most observable state in the state space. The spectral radius is given by

$$\mu_6 = \rho(W_o) = \sigma_{max}(W_o) \tag{6.45}$$

Finally, the overall observability from sensor measurements can be measured by summing all singular values through the matrix trace function.

$$\mu_7 = \text{trace}(W_o) = \sum \sigma_i(W_o) \tag{6.46}$$

Table 6.1 evaluates the observability measures mainly based on the smallest eigenvalue. The measures are the largest across every observability measure using both pressure and temperature measurements. As expected, observability is less using only one measurement. The results indicate that a temperature measurement provides more observability than a pressure measurement. Furthermore, adding pressure to temperature measurements did not substantially increase observability.

Table 6.2 reports the measures which are predominantly influenced by the observability gramian's largest eigenvalue. The results indicate that a temperature measurement provides more observability than a pressure measurement. Furthermore, adding pressure to temperature measurements did not substantially increase observability.

Table 6.1: Smallest Eigenvalue Observability Measures for Nonlinear Model at Equilibrium

	μ_1	μ_2	μ_3	μ_4	μ_5
P	$4.3 \cdot 10^{-12}$	$8.8 \cdot 10^{-13}$	0	$2.2 \cdot 10^{-4}$	$1.2 \cdot 10^{14}$
T	$5.4 \cdot 10^{-6}$	$1.1 \cdot 10^{-6}$	$1.2 \cdot 10^{-12}$	103	$2.01 \cdot 10^{14}$
$P\&T$	$6.6 \cdot 10^{-6}$	$1.3 \cdot 10^{-6}$	$1.7 \cdot 10^{-12}$	108	$2.4 \cdot 10^{18}$

Table 6.2: Largest Eigenvalue Observability Measures for Nonlinear Model at Equilibrium

	μ_6	μ_7
P	110	130
T	$2.6 \cdot 10^{12}$	$2.6 \cdot 10^{12}$
$P\&T$	$2.6 \cdot 10^{12}$	$2.6 \cdot 10^{12}$

State observability is in general a function of the input signal. Since the aim is to determine state observability during driving cycles, the heat source inputs are used in computing the observability measures. The observability measures are shown as a function of time in Figure 6.7 for μ_1 and μ_2. Because these measures are calculated from a non-singular empirical observability gramian, observability exists at all time for these inputs and suggests stability of the nonlinear state estimation error dynamics for the driving cycle.

Furthermore, note that relative observability does not change for the different measurements in the presence of transient inputs. As with the measures evaluated

at equilibrium, using both measurements provide more observability than just one. Temperature measurements make the system relatively more observable than pressure measurements.

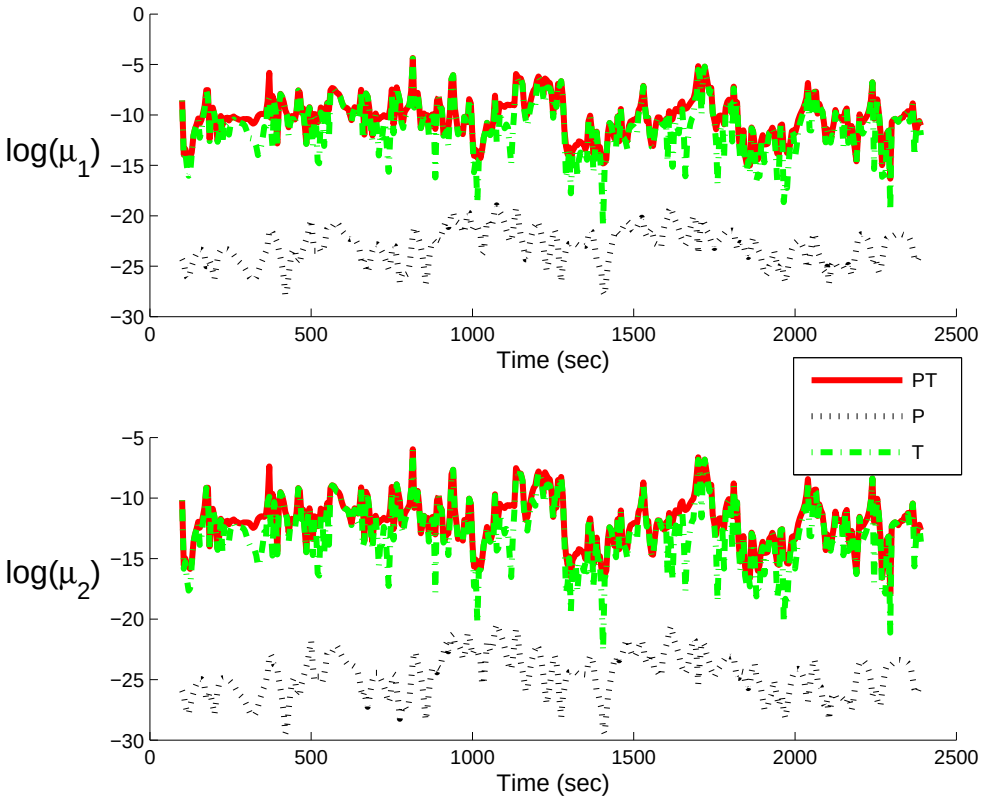

Figure 6.7: Relative Observability using Empirical Observability Gramian for Rolling Hills Driving Cycle

Each of the linear model's observability matrices corresponding to pressure, temperature, and both measurements is rank deficient. This indicates the linear model is unobservable for any combination of measurements and suggests the Fixed-Gain linear estimator is ineffective when the plant operates away from the linearization point.

6.3.5 EKF Design

6.3.5.1 Measurement Jacobian

The filter assumes combinations of pressure and temperature measurements available for state estimation. That is,

$$h(x) = [P \quad T_{out}]^T \tag{6.47}$$

where T_{out} is a thermodynamic function of working fluid states P and h_{out}.

The linearized pressure and temperature measurement function H_k is given by

$$H_k = \left.\frac{\partial h}{\partial x}\right|_{\hat{x}_{k|k-1}} = \begin{bmatrix} 0 & 1 & 0 & 0 & 0 \\ 0 & \frac{\partial T}{\partial P} & \frac{\partial T}{\partial h_{out}} & 0 & 0 \end{bmatrix} \tag{6.48}$$

6.3.5.2 Numerical (Full) and Analytical (Approximated) Jacobian

The state estimates are computed at every time step by linearizing the discretized plant dynamics:

$$\begin{aligned} F_{k-1} &= I + t_s \left.\frac{\partial g}{\partial x}\right|_{\hat{x}_{k-1|k-1}, u_{k-1}} \\ &= I + t_s \left[Z_k^{-1} \left.\frac{\partial f}{\partial x}\right|_{\hat{x}_{k-1|k-1}, u_k} + \left.\frac{\partial Z_k^{-1}}{\partial x}\right|_{\hat{x}_{k-1|k-1}, u_k} f \right] \end{aligned} \tag{6.49}$$

The term $\frac{\partial f}{\partial x}$ has a closed-form solution. The other term $\frac{\partial Z^{-1}}{\partial x}$, however, does not have an analytical form. Two methods are proposed to handle its computation.

The first method is numerically computing the full Jacobian term $\frac{\partial g}{\partial x}$. The (i, j) entry of the $n \times n$ Jacobian is given by

$$\frac{\partial g_i}{\partial x_j} = \frac{g_i(x + e_j \Delta x, u) - g_i(x_i, u)}{e_j \Delta x} \quad i = 1, 2 \ldots n \quad j = 1, 2 \ldots n \tag{6.50}$$

where g_i is the i^{th} column of g, x_i is the i^{th} state variable of the state vector x, and e are basis vectors. The state perturbation vector Δx is selected sufficiently small ensuring it captures the nonlinearity of g.

Δx is selected sufficiently small by examining the nonlinearity of g and capturing the slope of the $g - x$ curve of each state. This must be true over the entire operating state space. Since evaporators typically operate in steady-state with transients, a first step in determining the correctly sized Δx is to examine the nonlinearity at an equilibrium state. Figure 6.8 plots g around an equilibrium as a function of deviations for each state Δx_i with $\Delta x_{j \neq i} = 0$ for $i = 1, 2, \ldots, 5$ and $j = 1, 2, \ldots, 5$. The EKF using this Δx determined at the (x_{eq}, u_{eq}) point in Figure 6.8 computes an F that properly estimates states in this chapter's simulations, even though F is evaluated at other non-equilibrium points.

Based on Figure 6.8, the Δx chosen is

$$\Delta x = \begin{bmatrix} 0.02m & 0.1MPa & 5\frac{kJ}{kg} & 1°C & 1°C \end{bmatrix}^T \tag{6.51}$$

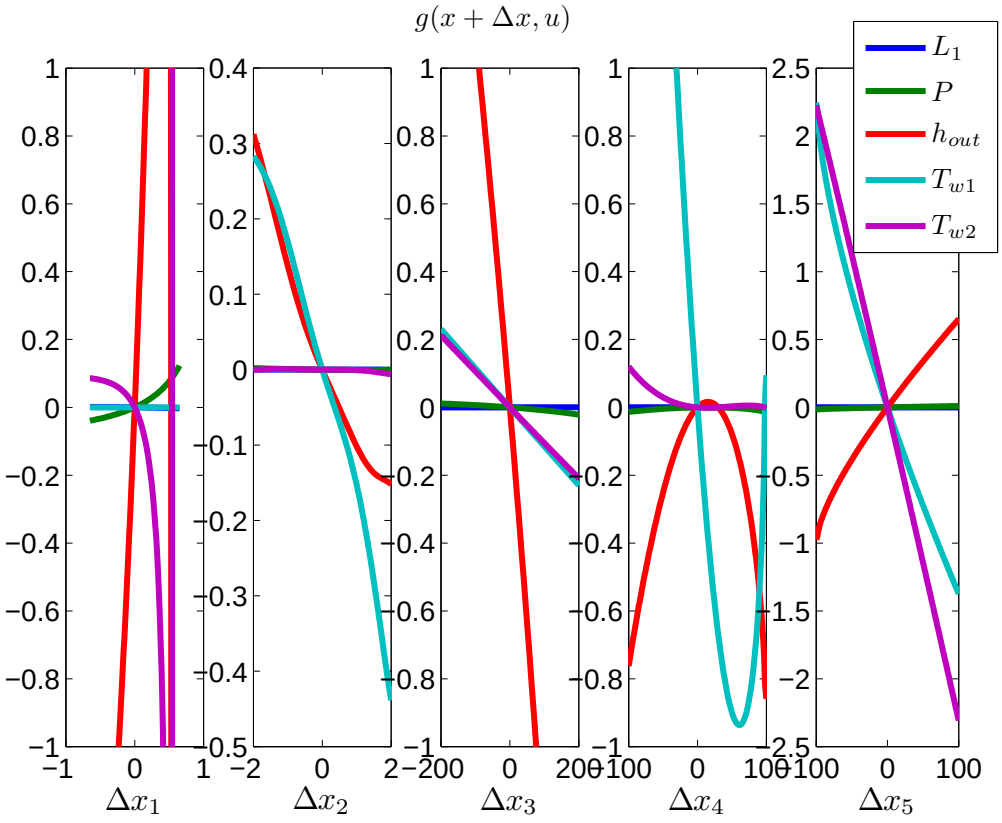

Figure 6.8: Nonlinearity of $g(x_{eq}, u_{eq})$

The second method is an analytical approximation of the Jacobian by assuming the evaporator operates at or near an equilibrium. The term f is or near zero, making the entire $\frac{\partial Z^{-1}}{\partial x} f$ term negligible. F can then be approximated by eliminating that term so that

$$F_{k-1} \cong I + t_s Z_k^{-1} \left. \frac{\partial f}{\partial x} \right|_{\hat{x}_{k-1|k-1}, u_k} \tag{6.52}$$

This approximation is valid for Jacobian evaluations near the equilibrium and reduces computation complexity and possible inaccuracies using the numerical Jacobian calculation. The trade-off is the filter using the Approximated Jacobian may be less accurate the farther away from the equilibrium point.

6.3.6 Simulation

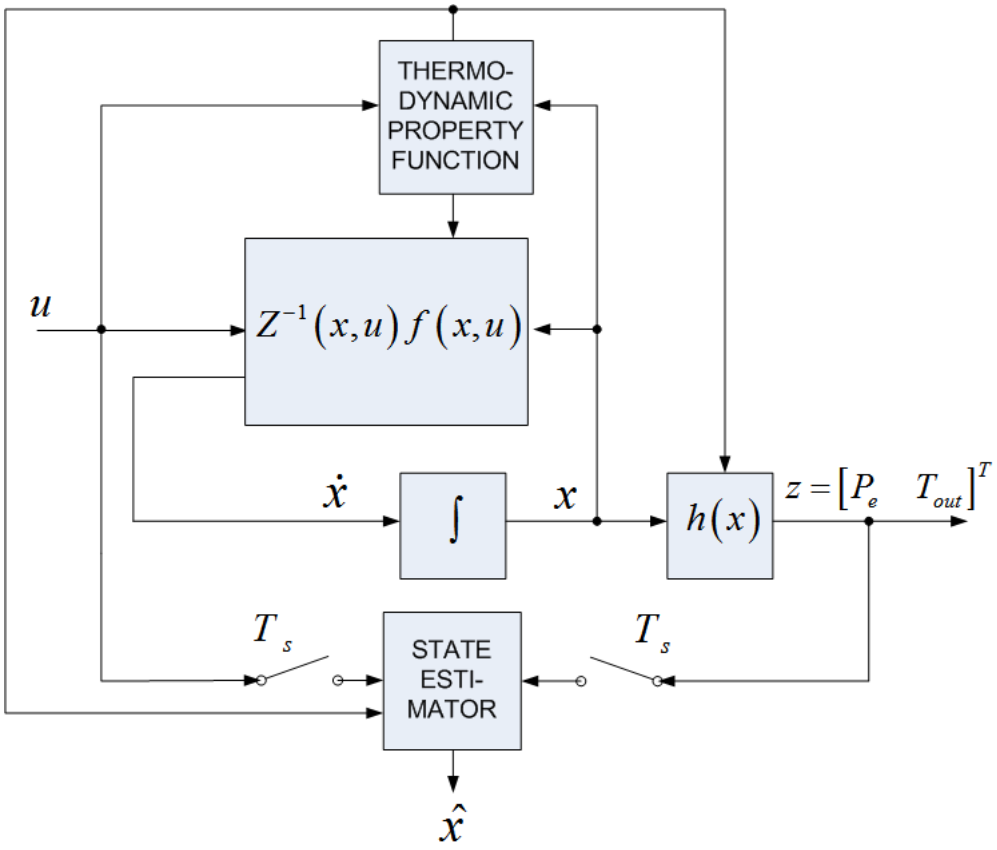

Figure 6.9: Open Rankine Cycle Model with State Estimator

Simulations were conducted in MATLAB/Simulink to estimate evaporator states from available measurements of pressure and/or temperature. The EKF used either a Full or Approximated Jacobian and their estimation performances are compared. The block diagram for the simulation is shown in Figure 6.9.

A Fixed-Gain estimator is obtained from the steady-state EKF using pressure and temperature measurements. The simulations included constant and step changes in evaporator inputs to compare their estimation performance under these transients. The values and timing of the step changes in the inputs are presented in

Table 6.3 for comparing different measurement and Jacobian choices.

Finally, simulations of an open power cycle using an actual driving cycle heat source data are presented.

6.3.6.1 Setup

The evaporator is initialized to an equilibrium $x(t_0) = x_{eq}$ associated with constant inputs $u = u_{eq}$, different from the estimator's initialization. The EKF estimator in both Full and Approximated Jacobian cases assumes process and measurement noise in its update equations while the plant model does not. Noise is added to the plant model to evaluate its effect on estimation. Fouling is also introduced by reducing the heat transfer coefficients of the plant model while the estimator's values remain the same (unfouled).

The design parameters are representative of a heat exchanger from a heavy-duty diesel powertrain:

1. Working Fluid: 52% Ethanol, 48% Water Mixture
2. Tube material: Copper
3. Evaporator tube length: 0.7 m
4. Inner tube diameter: 14 mm
5. Outer tube diameter: 16 mm

The expander and throttle operating and design variables are given by:

1. Outlet Pressure: 2 MPa
2. Isentropic Efficiency η: 90 %

Table 6.3: Step Changes in Evaporator Inputs for Comparing Measurement and Jacobian Choice

Step Input	t (seconds)	Initial Value	Final Value
$T_{h,in}$	1100	450 $°C$	350 $°C$
$\dot{m}_h$	2000	0.062 $\frac{kg}{s}$	0.108 $\frac{kg}{s}$
h_{in}	2500	350 $\frac{kJ}{kg}$	570 $\frac{kJ}{kg}$
$\dot{m}_{in}$	3000	0.0066 $\frac{kg}{s}$	0.0067 $\frac{kg}{s}$

3. Valve Coefficient β: 0.03
4. Throttle Position μ: 81.25 %

The estimator parameters are defined by:

1. $Q = 10^{-3}I$
2. $R = 10^{-3}I$
3. $L = K$ at equilibrium
4. $\hat{x}(t_0) = E[x(t_0)] \neq x_0$ estimator initialized away from model initial conditions
5. $P(t_0) = \text{Var}[x(t_0)] = 10^{-3}I$
6. $t_s = 5$ seconds

Figure 6.10 compares the different measurement choices for the Full Jacobian case. Although relative observability differs between the choices, all provide successful state estimation.

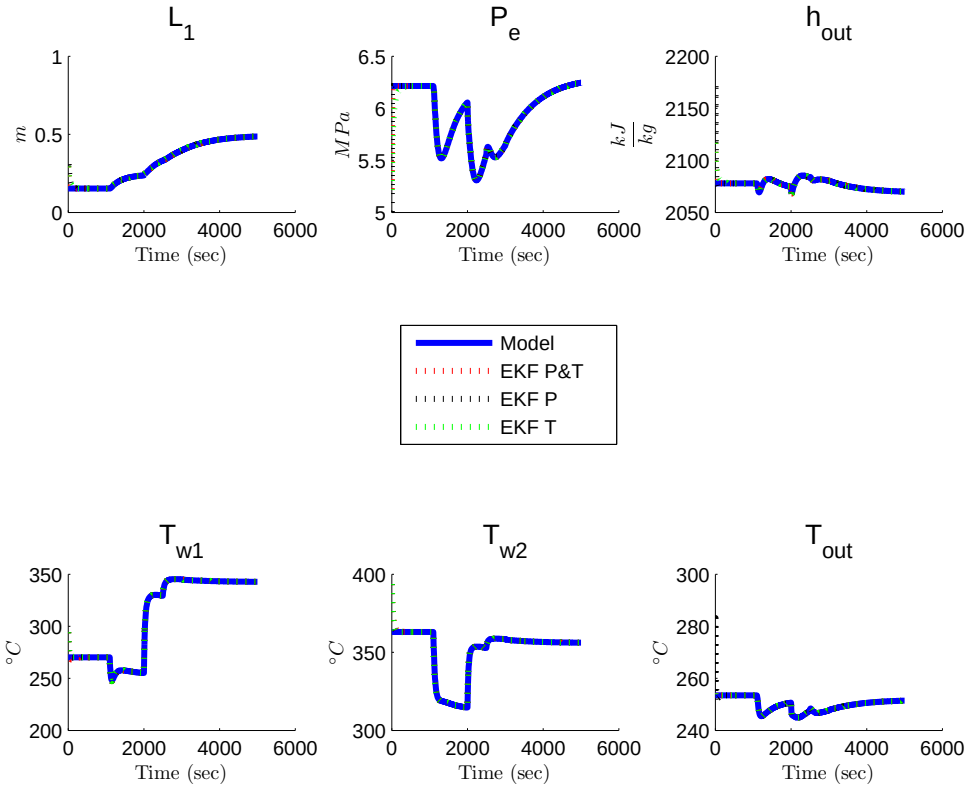

Figure 6.10: Evaporator and EKF Estimator States, Full F

Figure 6.11 compares the different measurement choices for the Approximated Jacobian case. The estimation errors spike at the onset of step changes, but converge shortly after.

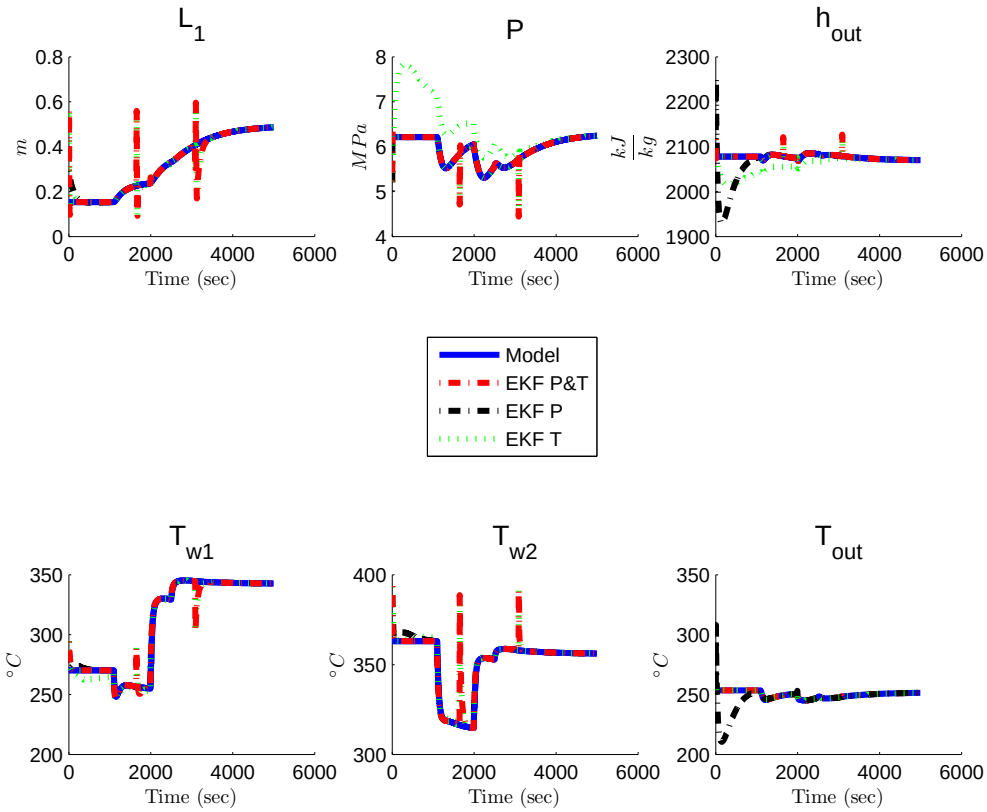

Figure 6.11: Evaporator and EKF Estimator States, Approximate F

Figure 6.12 shows a Fixed-Gain Estimator is inadequate for state estimation. The error grows out of bound quickly after initialization and never recovers.

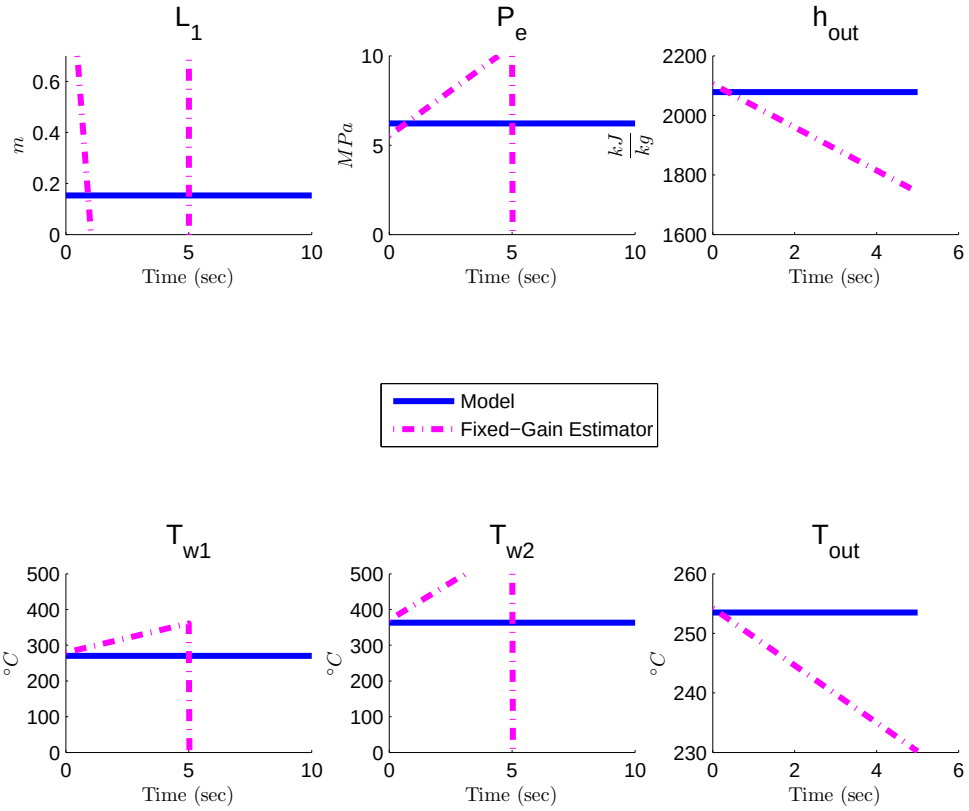

Figure 6.12: Evaporator and Fixed-Gain Estimator States using Pressure and Temperature Measurements

Figures 6.13 and 6.14 show the EKF state estimator subjected to noise and fouling. Zero-mean measurement and process noises exist throughout the simulation with variances defined in the Setup section. At $t = 1000$ seconds, fouling is simulated with the evaporator heat transfer coefficients reduced by 25% of their unfouled values. The EKF continues to use the unfouled heat transfer coefficients. The EKF estimation error in L_1 increased as the fouling was not known by the estimator. However, the estimation error for the other states did not increase as significantly. The growing error in the L_1 state is an indicator that fouling has occurred.

Comparing the noise and noise-free Approximated Jacobian cases in Figures 6.11 and 6.13, the estimation spikes seem to disappear with noise. A possible reason is that the filter is kept open by noise, allowing the estimator to track the model states better at the onset of step inputs.

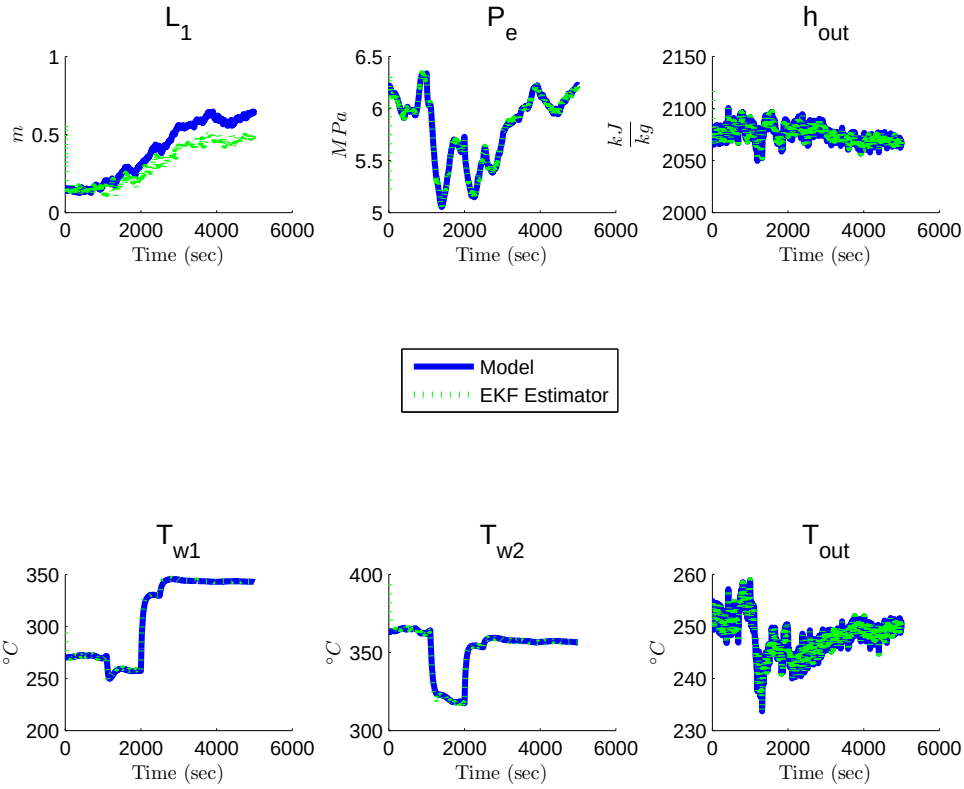

Figure 6.13: Evaporator with Process Noise and EKF Estimator States using Noisy Pressure and Temperature Measurements, Approximated F

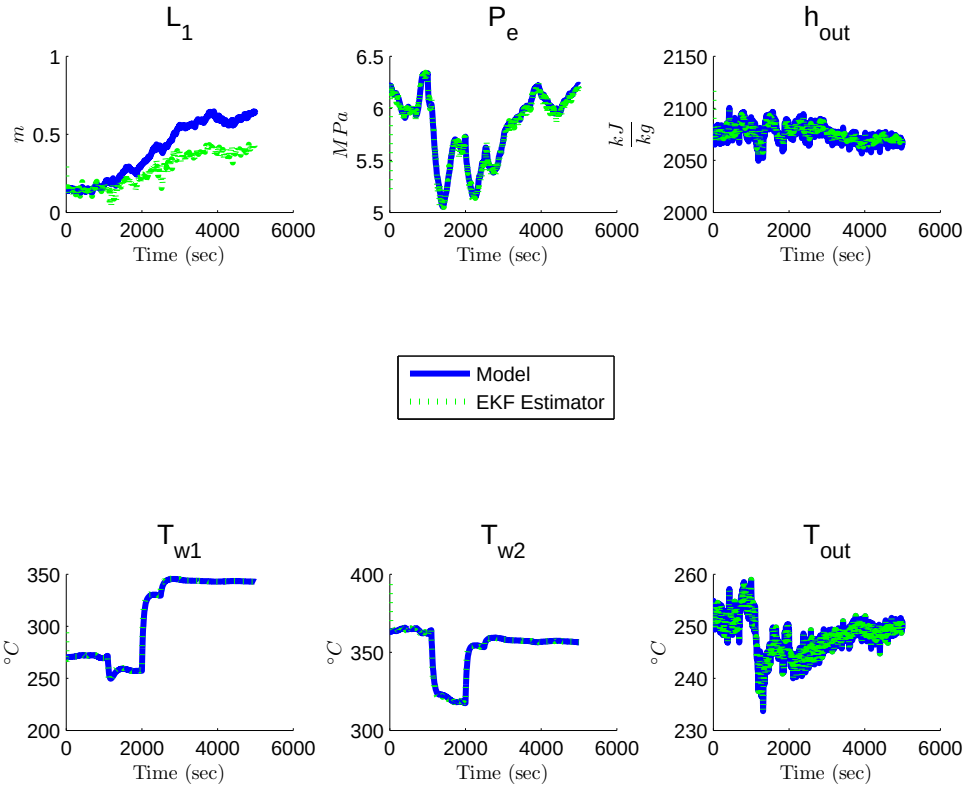

Figure 6.14: Evaporator with Process Noise and EKF Estimator States using Noisy Pressure and Temperature Measurements, Full F

Figures 6.15-6.17 all show reasonable estimation for either Jacobian method. The estimation error is smaller for the Full Jacobian case and only slightly larger for the Approximated Jacobian. Figure 6.17 compares the estimation error between the two Jacobian cases and shows modest inaccuracies in the state estimate for the Approximated case.

WHR systems typically must satisfy operating constraints. In this application, the evaporator pressure has a soft and hard limit of 4 and 6 MPa, respectively. Short excursions in that range is acceptable. The pressure is clearly violated throughout the entire driving cycle. However, the working fluid outlet temperature

T_{out} remains below the 300 $°C$ limit and the phase change boundary L_1 is within acceptable range. Exhaust outlet temperature (not shown) must be within a specified temperature range for proper EGR operation. These constraints must be met through a controller that determines the appropriate evaporator and expander actuator inputs. The state estimator presented in this chapter is a requirement for controllers depending on full state estimator feedback. This will be the focus of Chapter 7.

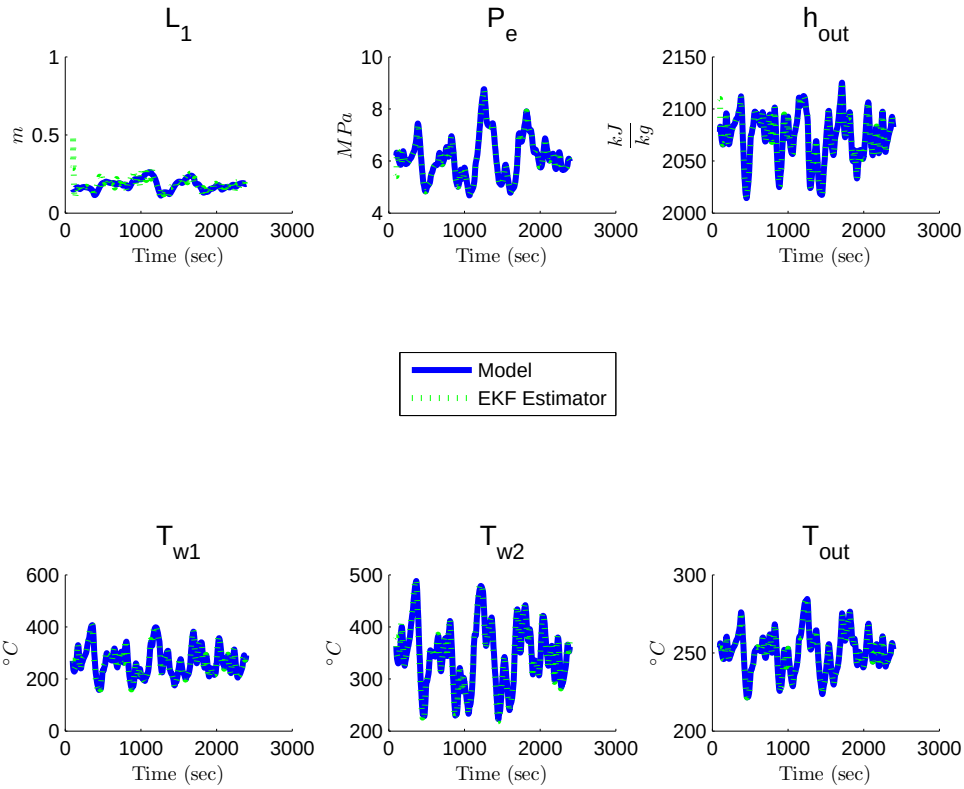

Figure 6.15: EKF Estimator States using Pressure and Temperature Measurements, Rolling Hills Cycle, Approximated F

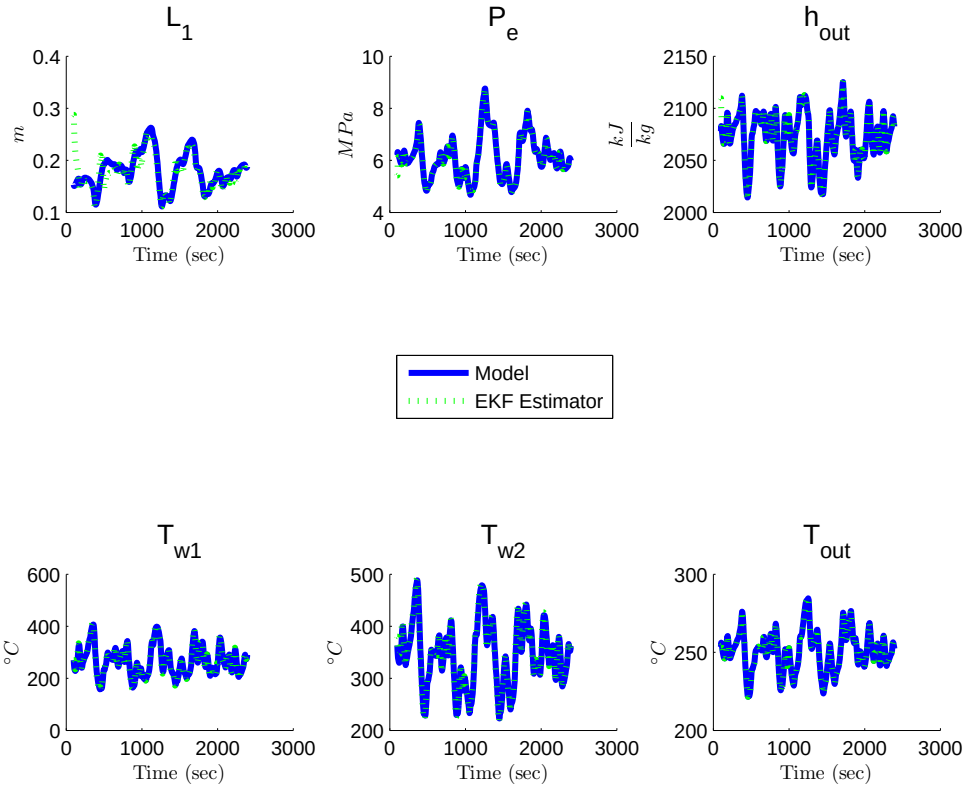

Figure 6.16: EKF Estimator States using Pressure and Temperature Measurements, Rolling Hills Cycle, Full F

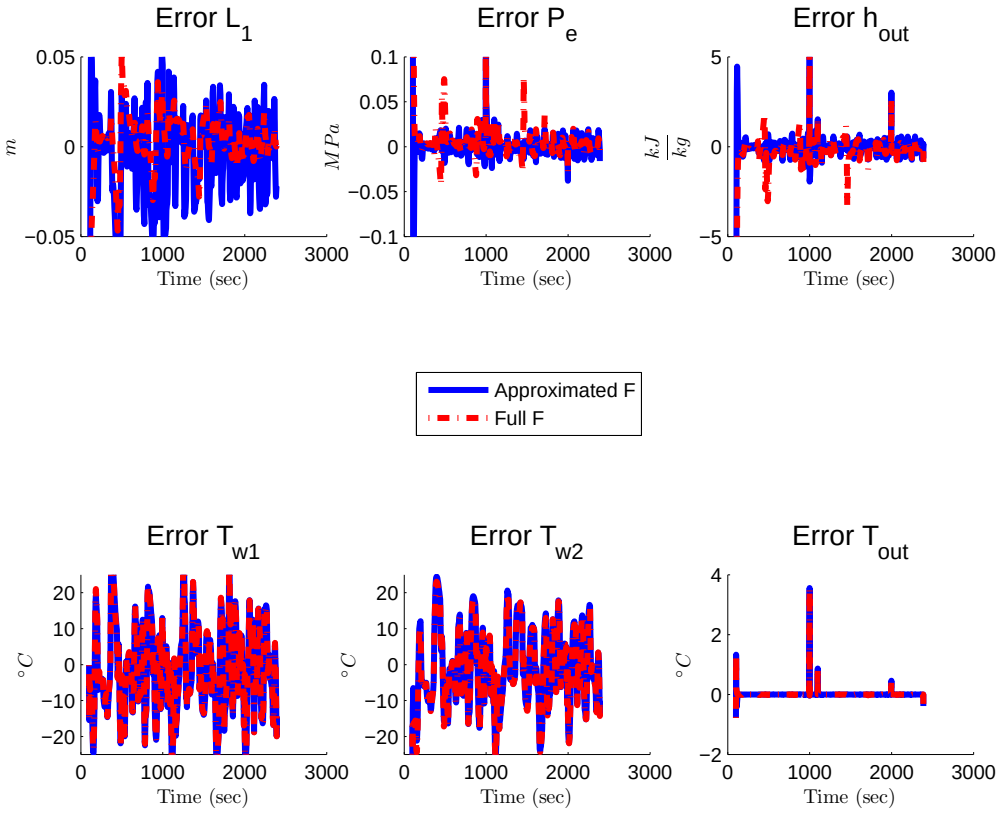

Figure 6.17: EKF Estimation Error using Pressure and Temperature Measurements, Rolling Hills Cycle

6.3.7 Remarks

A two-zone Moving Boundary nonlinear evaporator model was implemented in the MATLAB/Simulink environment as part of an open ORC. An expander model is connected to the evaporator via a throttle valve. The expander and throttle models are assumed static due to their relatively faster dynamics.

Linear and nonlinear state estimation for the ORC model using typically available pressure and temperature measurements are addressed. Simulations showed that both the nonliner and linear fixed-gain estimators are inadequate for state estima-

tion, even with both pressure and temperature measurements. This is attributed to the model nonlinearity. The empirical observability gramian determined that either pressure or temperature measurements resulted in an observable system. Having both pressure and temperature measurements provided the most relative observability followed by temperature and then pressure measurements. For robust state estimation of the nonlinear model, the EKF with either a pressure or temperature measurement sufficed. Estimation performance improves with both measurements and agrees with observability measures using the empirical obsrvability gramian. The EKF handles the nonlinearity for either Jacobian choice with similar performance, independent of measurement choice. However, the Approximaed Jacobian case results in higher estimation error at the onset of transients.

Finally, this section simulated a power cycle to recover waste heat from diesel engine exhaust and showed that the EKF performed well in estimating all model states. The simulations included driving cycle transients and both process and measurement noise. The EKF also performs well in estimating most plant states in the presence of plant fouling. The overall results provide an essential step for future feedback control development in heat exchangers and its performance monitoring for fouling and maintenance. Specifically for WHR in the heavy-duty powertrain application, controls is needed to satisfy system constraints that were not met with constant input operation. This provides motivation for Chapter 7.

CHAPTER 7

Control Methods for Rankine Cycles

7.1 Introduction

This chapter investigates control schemes to operate the Rankine cycles (RCs) under heat source and heat sink transients, which may deviate the working fluid from the desired operating conditions and lead to other critical conditions. Operating conditions are often specified in ranges that process variables should remain in. When reaching outside these ranges, critical conditions such as dry-out, flooding, and temperature shocks in components. The control problem is formulated for a RC intended to convert waste heat to useful power in a heavy-duty diesel powertrain system while satisfying operating constraints and avoid critical conditions. Attention is given towards tracking operating pressures as a way to produce the maximum expansion power while satisfying other constraints. Two RC architectures are considered, each differing in available control actuators. Both single-input single-output (SISO) and multi-input multi-output (MIMO) controllers in the form of Proportional Integral, Linear Quadratic, and Model Predictive controllers are designed and implemented on both linear and nonlinear dynamic RC models in simulation. The controllers' performances are compared in their tracking performance and ability to satisfy other operating constraints.

This chapter concludes with RC simulations in operating pressure tracking on base and peak loading power plants as well as load following plants where the RC

must deliver a demanded power curve.

7.2 Control-Oriented RC Dynamic Modeling

The RC models in this chapter use the Moving Boundary approach to describe and capture heat exchanger dynamics while assuming static models for the pump, valves, and expansion device. The heat exchangers considered are two-zone models where the evaporator has two-phase and superheat regions and the condenser with two-phase and subcooled regions. This choice of two-zone heat exchanger models is intended to simplify the modeling by reducing system order. Secondly, the RC may not be necessarily described by isentropic compression and expansion processes resulting in two-phase fluid-phases in the heat exchangers. The dynamics of the valves, pump, and expander are assumed much faster than that of heat exchangers. In simplifying the RC model, they are treated as static thermodynamic models described in Chapter 4.

The static RC design provided in Chapter 4 define setpoints and actuator limits for the dynamical RC model and its control design. The Single Valve RC Architecture relies on the setpoints of design 1 of the static RC model while the Dual Valve RC Architecture uses the setpoints of design 2 of the static RC model. The static RC models' operating conditions in mass flow rates also establish a range for the control actuator limits.

The heat transfer coefficients (HTCs) for the heat exchangers are calculated based on the external heat source/sink cross flow across a single tube where the 52% ethanol-48% water mixture flows internally. The geometry assumes effective cross-sectional area and lengths described in Chapter 2. Correlations for the HTCs are provided in Chapter 5.

7.3 Control Problem Formulation

In the presence of operating disturbances stemming from varying heat source or sink, RCs can reach a variety of critical conditions such as dry-out, flooding, and temperature shocks in components. For heavy-duty diesel powertrains, such disturbances include

1. **Heat Source/Sink** conditions vary significantly depending on the driving cycle and determine how much heat can be added and rejected in the RC.
2. **Engine Crankshaft** driving the pump and coupled to the expander affect their rotational speeds.

The disturbance input variables are given by

$$u_d = [T_{h,in} \quad \dot{m}_h \quad \omega \quad T_{c,in}]^T \tag{7.1}$$

where $T_{h,in}$ and $\dot{m}_h$ are the heat source's temperature and flow rate, respectively, ω is the engine crankshaft speed, and $T_{c,in}$ is the heat sink temperature.

These disturbances are found in vehicular RC applications, but may also be common to other applications including geothermal, industrial, and solar. Disturbances can lead to critical conditions defined as the following variables being out of range:

1. **Pressure** cannot be too high in the evaporator or too low in the condenser. This range is governed by the limitation of the components' material and their designed operating range.
2. **Temperature** of the evaporatoring working fluid must be high enough to be superheated to avoid liquid droplets in the expander, but not too high to

cause temperature shocks in the components' materials. In the condenser, the working fluid must be cool enough to enter the pump as a liquid, but high enough so that the available heat achieves evaporation in the evaporator.

3. **Phase-change Boundaries** in the heat exchangers must remain in range to ensure evaporation and condensation occur.

The goal of controls is to avoid these critical conditions through manipulating actuators during operation. Possible ways to control RCs are:

1. **Mass flow rate** through the pump and expander valves: determines the evaporator outlet (expander inlet) conditions. If more/less heat is available, pass more/less working fluid through the evaporator to achieve (superheated) vapor.

2. **Heat Source/Sink** temperature and flow rate: determines the evaporator/condenser outlet (expander/pump inlet) conditions. Subject to a varying working fluid mass flow and inlet enthalpy, modulate the temperature and mass flow of the heat source/sink to achieve (superheated) vapor or (subcooled) liquid.

The RC MIMO system has cross-coupling between the inputs and outputs mentioned above. Depending on how strong those couplings are, the SISO couplings above may be adequate in achieving the desired effect.

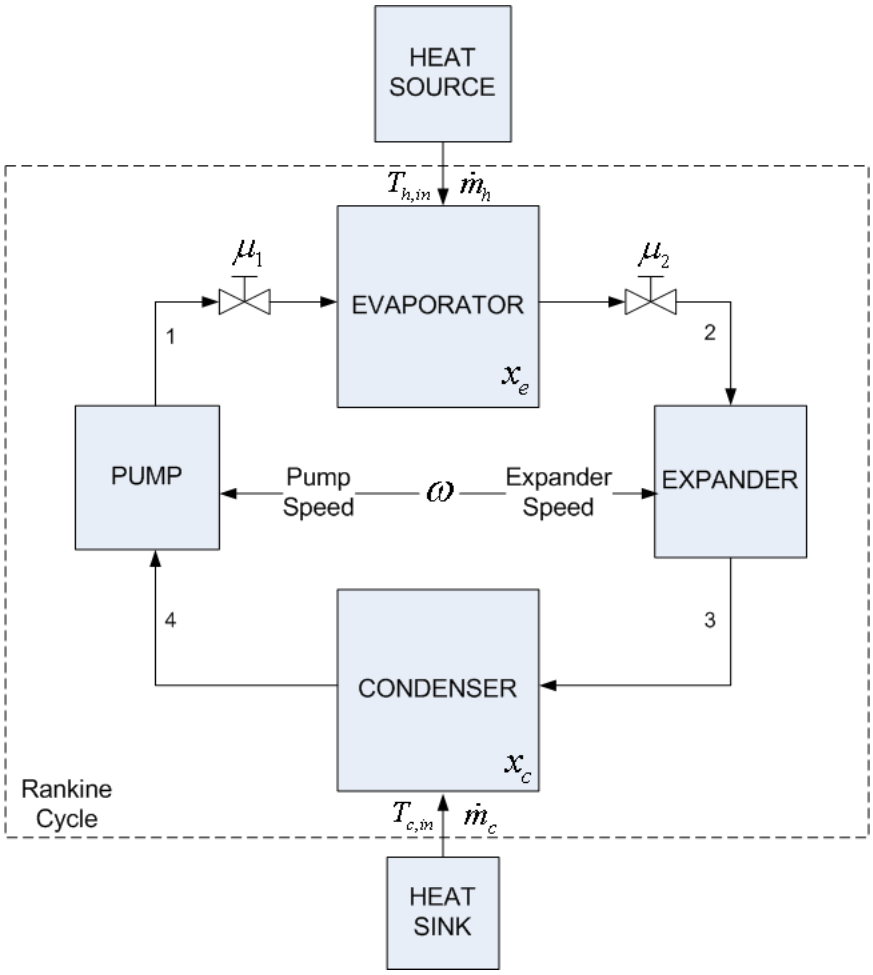

Figure 7.1: RC Architecture

The examined RC architecture is shown in Figure 7.1. The state variables are

$$u_m = [x_e \quad x_c]^T \tag{7.2}$$

where x_e and x_c are the evaporator and condenser's states, respectively.

The manipulated input variables and their combinations are given by

$$u_m = [\dot{m}_c \quad \mu_1 \quad \mu_2]^T \tag{7.3}$$

where $\dot{m}_c$ is the heat sink flow rate and μ_1 and μ_2 are throttle positions of the pump and expander valves, respectively.

The disturbance input variables are given by

$$u_d = [T_{h,in} \quad \dot{m}_h \quad T_{c,in} \quad \omega]^T \tag{7.4}$$

where $T_{h,in}$ and $\dot{m}_h$ are the heat source's temperature and flow rate, respectively and ω is the angular speed of the load connected to the pump and/or expansion device(s).

The measured output variables are

$$y = [P_c \quad P_e]^T \tag{7.5}$$

State estimators can be used for feedback control when access to unmeasured states are required.

Feedback control for setpoint or reference tracking is considered to keep key state variables within constraints. The controller should minimize the output error of the tracking loop while satisfying the other constraints. The control structure is shown in Figure 7.2.

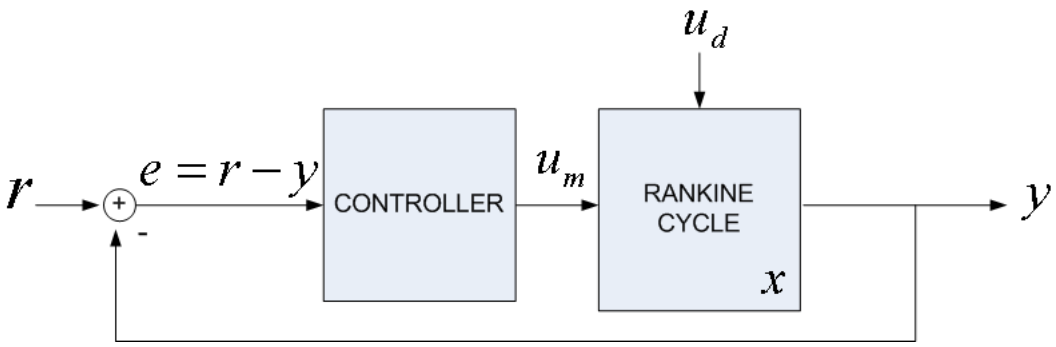

Figure 7.2: RC Control Diagram

7.4 Control of Single Valve RC Architecture

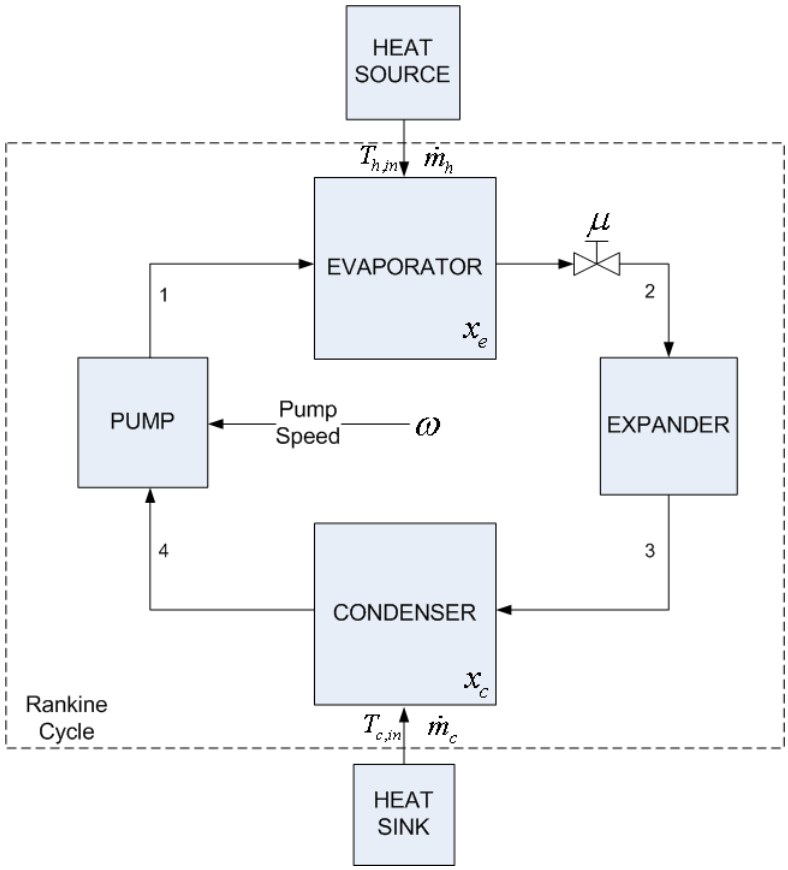

Figure 7.3: RC with Expander Throttle Valve

7.4.1 Objective

Flooding avoidance and pressure regulation are desired in the operation of this architecture. Static RC model design 2 in Chapter 4 provides the nominal operating points.

The throttle valve, pump speed, and heat sink flow rate are designated as manipulated control variables. The expander's speed is not controlled.

7.4.2 Controller Formulation

Three independent PI single-input single-output (SISO) controllers are designed and applied to a RC model with two-zone heat exchangers connected to static pump and expander models as shown in Figure 7.3. The control diagram is shown in Figure 7.4.

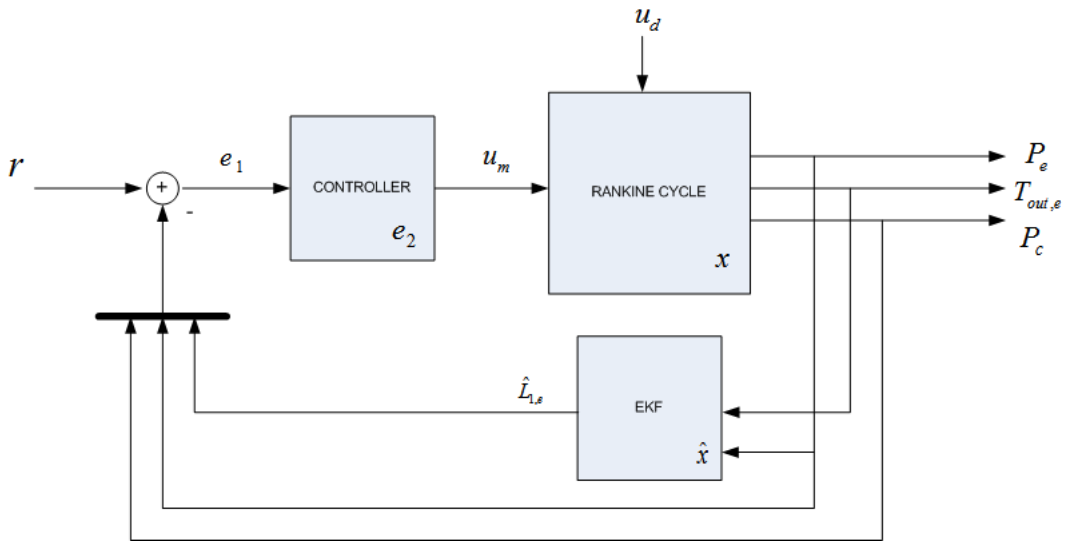

Figure 7.4: RC PI Control Diagram

The control and actuator relationship is given by the following:

1. The evaporator's working fluid pressure is regulated to P_e^* by manipulating pump speed ω

2. The evaporator's phase change boundary $L_{1,e}$ is regulated to $L_{1,e}^*$ by varying the throttle valve position μ

3. The condenser's working fluid pressure is regulated to P_c^* by manipulating the coolant mass flow rate $\dot{m}_c$

The controllers regulate the RC to the setpoint r by minimizing the regulation error

$$e_1 = r - y$$

where $y = [P_c \quad L_{1,e} \quad P_e]^T$ and r is the corresponding vector of setpoints for each output signal.

The anti-windup feature minimizes the saturation error e_2 due to exceeding actuator limits. The saturation error is given by

$$e_2 = \left\{ \begin{array}{ll} 0 & \text{if } u_{sat,low} \leq u \leq u_{sat,high} \\ u - u_{sat_high} & \text{if } u > u_{sat,high} \\ u - u_{sat_low} & \text{if } u < u_{sat,low} \end{array} \right\} \tag{7.6}$$

The back-calculating anti-windup PI controller is mathematically expressed as

$$u_m = [\omega \quad \mu \quad \dot{m}_c]^T = b + k_p e_1 + \int (k_i e_1 + k_b e_2) dt \tag{7.7}$$

The disturbance input u_d due to heat source and sink conditions is given by

$$u_d = [T_{h,in} \quad \dot{m}_h \quad T_{c,in}]^T \tag{7.8}$$

7.4.3 $L_{1,e}$, P_e, and P_c Regulation for Flooding Avoidance

The phase change boundary and pressures are regulated under constant step inputs using the control structure shown in Figure 7.4 where the flooding occurs due to insufficient heat. Manual and controlled corrective action is taken to steer the system away from the critical condition. The PI controllers' parameters are manually tuned to the design parameters shown in Table 7.1.

The phase change boundary state is first assumed accessible for feedback control. An nonlinear EKF estimator developed in Chapter 6 is then used to obtain the state estimate and compared to the perfect state access case.

Controller	Parameters	Actuator	Feedback Signal	Saturation Limits
C_1	$b = 500, k_p = 333$ $k_i = 1, k_b = 1$	Pump Speed RPM	P_e	$[100, 2000]$
C_2	$b = 1.5, k_p = 0.1$ $k_i = 0.1, k_b = 1$	Coolant Flow Rate $\frac{kg}{s}$	P_c	$[0.5, 4.5]$
C_3	$b = 0.5, k_p = 1000$ $k_i = 10, k_b = 1$	Throttle Position %	$L_{1,e}$	$[0.3, 0.9]$

Table 7.1: PI Controller Design Parameters

Input	Variable	Time	Initial Value	Final Value
Step	$T_{h,in}$	2000 seconds	450 $°C$	290 $°C$

Table 7.2: Simulation Inputs

7.4.3.1 Perfect State Access of $L_{1,e}$

The evaporator's phase change boundary is regulated to the setpoint r by varying the throttle valve position as shown in Figure 7.5. In Figure 7.4, this is the innermost control loop; the outer two are not considered here. Access to the $L_{1,e}$ state is first assumed and then compared to its estimated value using an Extended Kalman Filter.

The setpoint r is given by

$$r = \begin{bmatrix} P_e^* & L_{1,e}^* & P_c^* \end{bmatrix}^T = [4\text{MPa} \quad 0.5\text{m} \quad 0.1\text{MPa}]^T \tag{7.9}$$

A step reduction in the heat source's temperature occurs according to Table 7.2 to place the heat exchanger into a critical condition. The phase change boundary increases until out of range without any throttle response to correct it.

Manual and feedback controlled throttle responses are simulated and compared.

The manual throttle response is a step and the controller's parameters are manually tuned to the design parameters shown in Table 7.1 for C_3.

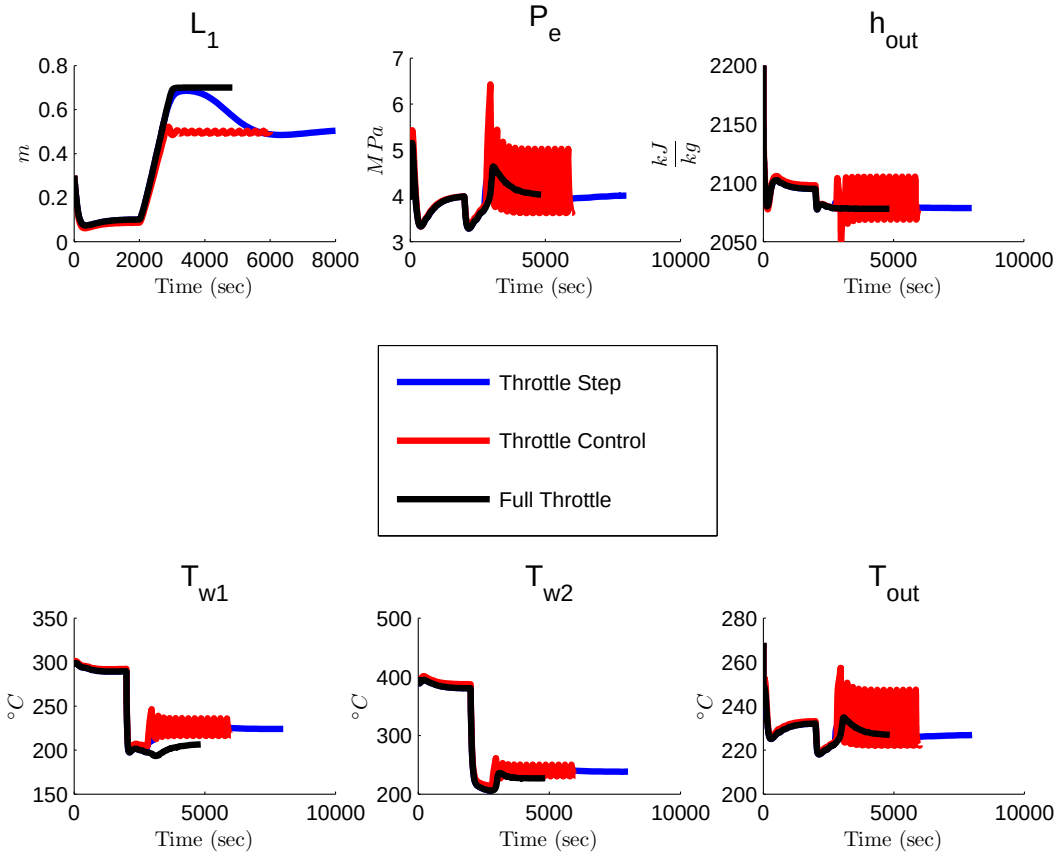

Figure 7.5: RC with PI Control for Phase-Change Boundary Regulation: Evaporator States

The full throttle case resulted in flooding where the phase change boundary approached the length of the evaporator in Figure 7.5. Recall this scenario is both physically and mathematically undesirable. The working fluid never became superheated and a caused the model to become singular.

A step change in the throttle limits the mass flow rate entering the evaporator, allowing the working fluid flow to become superheat for the available heat . The

phase change boundary steered away from flooding as a result.

The throttle control also avoids flooding by tracking the desired setpoint. The oscillations were due to the lack of dynamics in the throttle valve. Note that the controller did not achieve setpoint before the temperature reduction, indicating the setpoint was not feasible with the prior operating conditions.

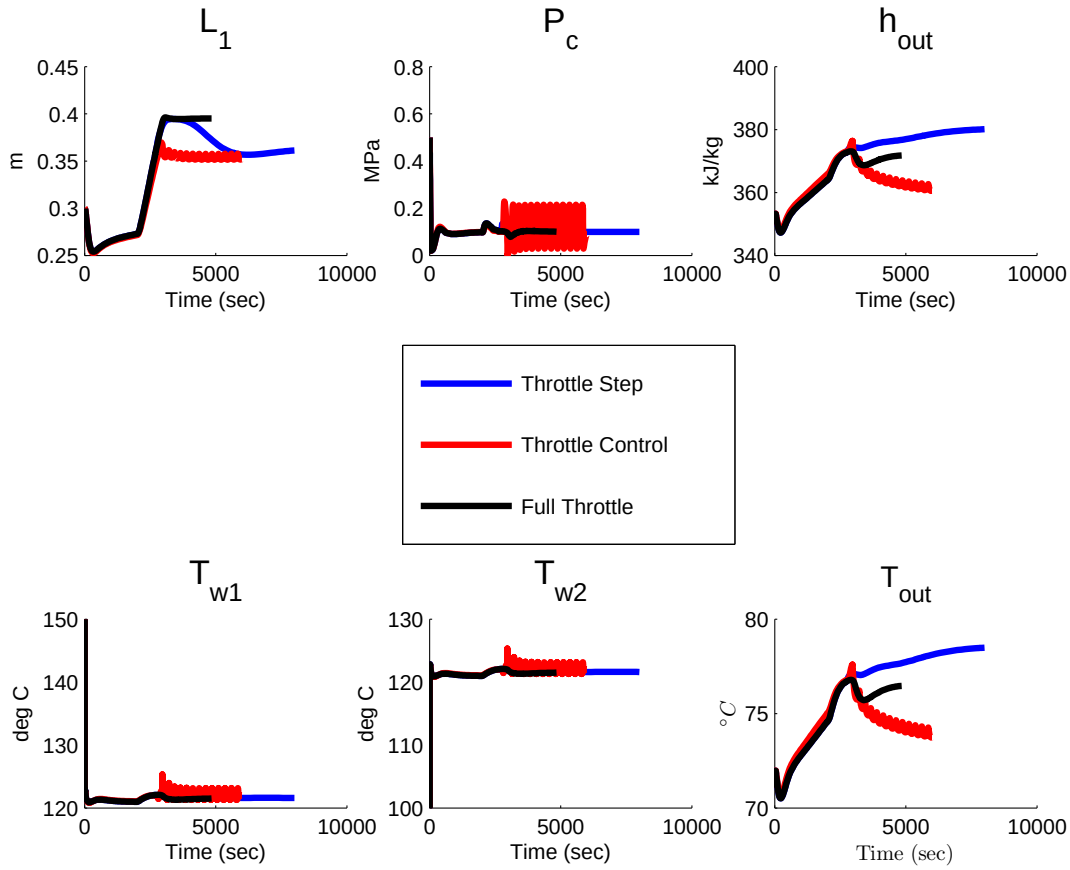

Figure 7.6: RC with PI Control for $L_{1,e}$ Regulation [$r = L^*_{1,e} = 0.5$m]: Condenser States

The condenser states are shown in Figure 7.6. Note that the condenser phase change boundary saturates due to the evaporator's phase change saturating. How-

ever, the condenser phase change boundary did not reach the critical flooding condition.

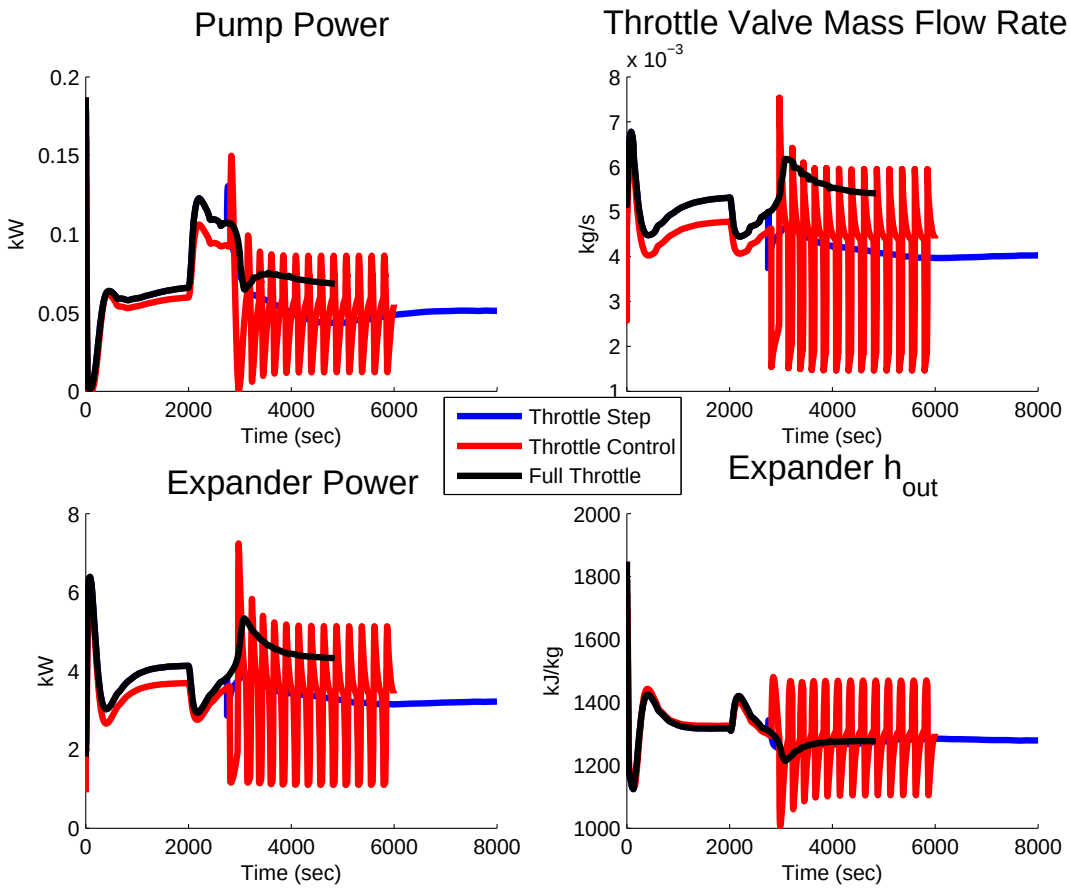

Figure 7.7: RC with PI Control for L_1 Regulation: Pump and Expander States

The expander and pump power, throttle valve flow rate, and expander outlet enthalpy are shown in Figure 7.7. The net power is significant and is in the expected range obtained from the static RC model at similar operating conditions. The expander's outlet enthalpy is useful to determine working fluid quality if desired.

7.4.3.2 State Estimation of $L_{1,e}$

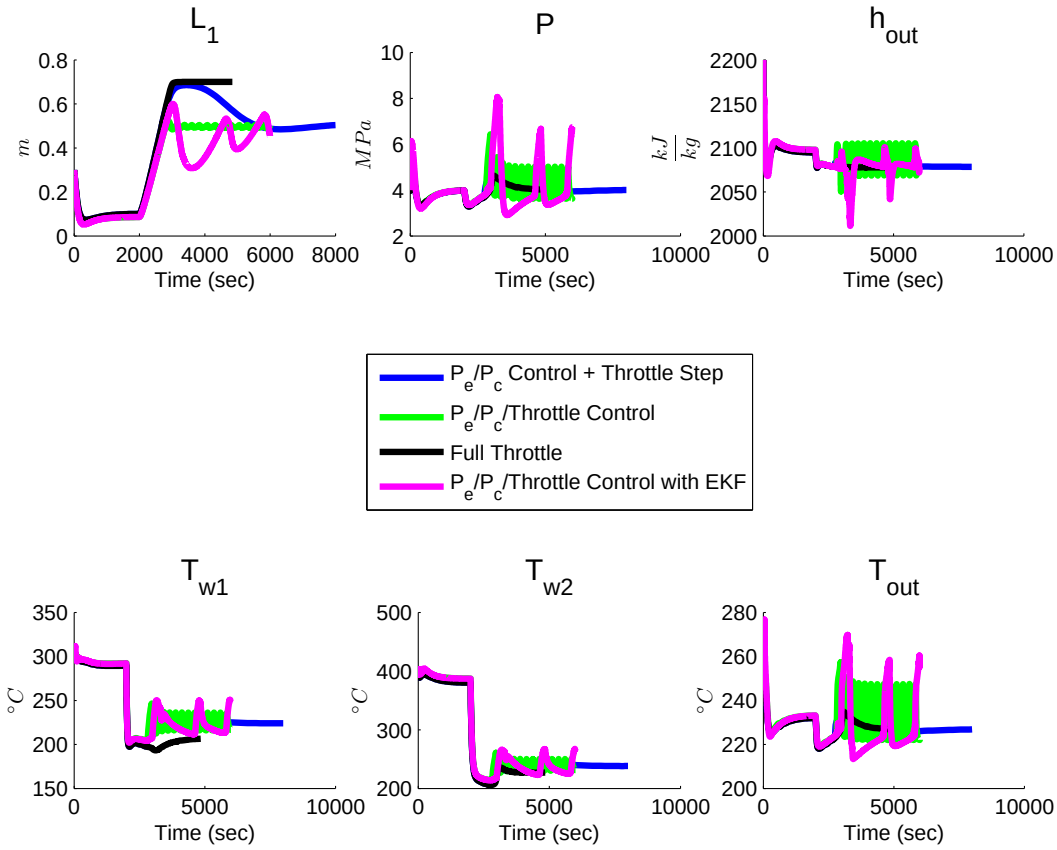

Figure 7.8: RC with PI Control: Evaporator States

Because L_1 is typically unmeasurable, the Extended Kalman Filter (EKF) is used to provide its estimate. Figures 7.8, 7.9, and 7.10 compare the pressure regulation control with perfect state feedback and state estimator feedback with the EKF. The estimator uses the Approximated Jacobian with both pressure and temperature measurements.

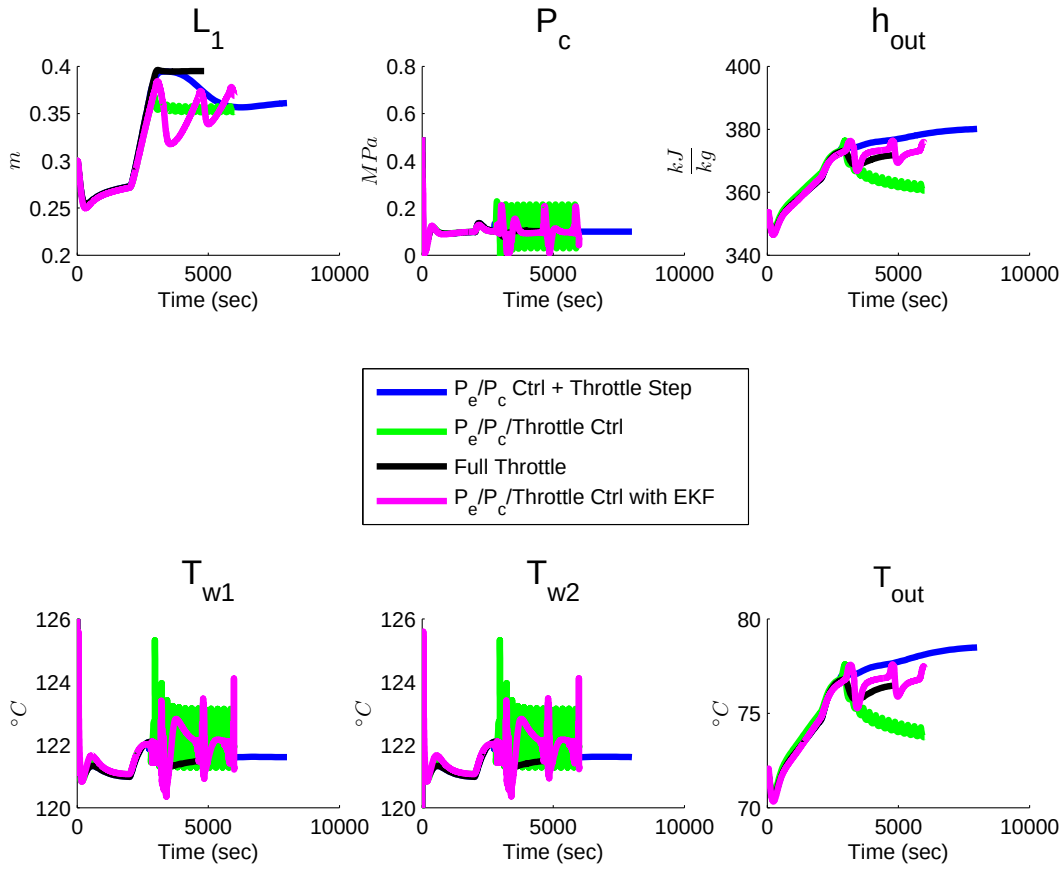

Figure 7.9: RC with PI Control: Condenser States

Note the longer oscillatory response time for the evaporator's phase change boundary to converge. This is attributed to the EKF's Approximated Jacobian. Because this state is not as tightly controlled around the setpoint, the state estimator feedback creates ringing oscillations in the other states.

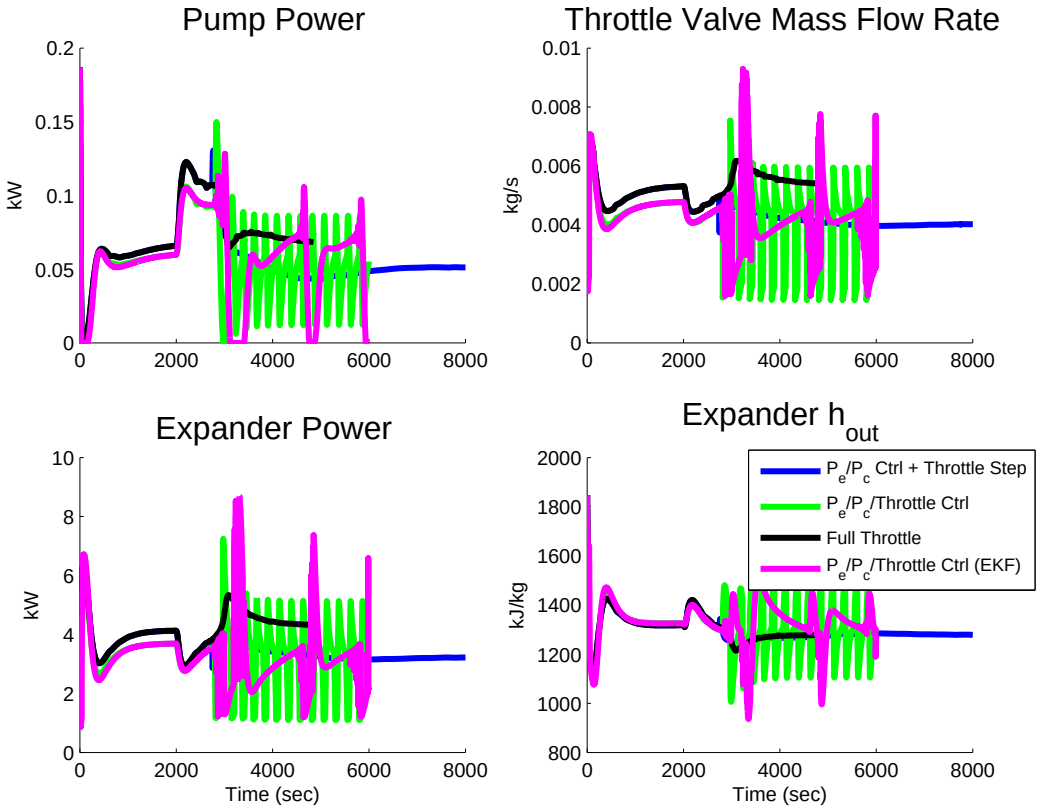

Figure 7.10: RC with PI Control: Pump and Expander States

7.4.4 $L_{1,e}$, P_e, and P_c Regulation under Driving Cycle Transients

The following simulations feature an evaporator not close to flooding so that pressure regulation performance can be examined. The evaporator's phase-change boundary is set to a low setpoint to ensure a large superheat region.

The setpoint r is given by

$$r = \begin{bmatrix} P_e^* & L_{1,e}^* & P_c^* \end{bmatrix}^T = [4\text{MPa} \quad 0.1\text{m} \quad 0.1\text{MPa}]^T \tag{7.10}$$

Two sets of simulations are presented. The first set uses constant, average heat source from a driving cycle described in Table 7.3. The second set is the actual

	Value	Units
$T_{h,in}$	450	$^{\circ}C$
$\dot{m}_h$	0.062	$\frac{kg}{s}$
$T_{c,in}$	80	$^{\circ}C$
ω	1500	RPM

Table 7.3: Constant RC Heat Source and Sink Conditions

transient heat source values. Additionally, an EKF is used in the second set for state estimator feedback of the evaporator's phase-change boundary.

7.4.4.1 Constant (Averaged) Heat Source

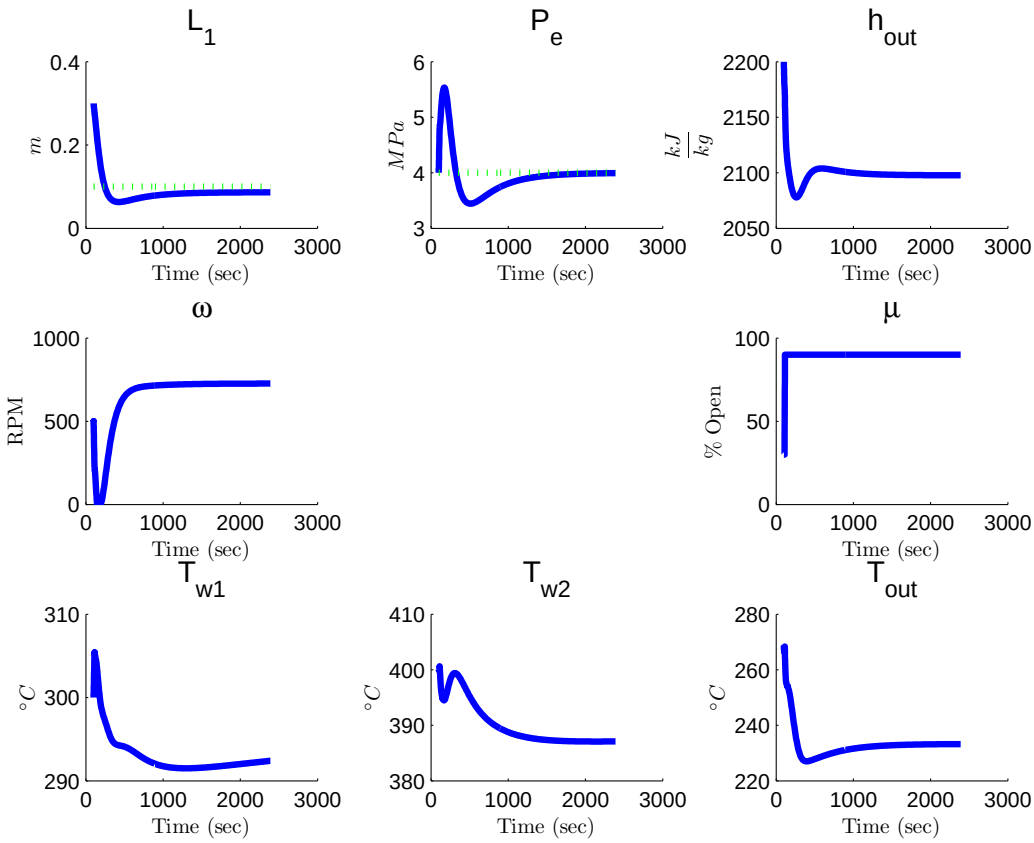

Figure 7.11: RC with PI Control under Averaged Rolling Hills Driving Cycle: Evaporator States (State: Solid Line, Setpoint: Dashed Line)

Note how the actuator signals in Figures 7.11 and 7.12 reach steady-state in achieving setpoint tracking. The pressure setpoints are reached with zero-error, but the phase-change boundary setpoint is not. The steady-state error is approximately 13% from setpoint and is attributed to the throttle valve position saturating.

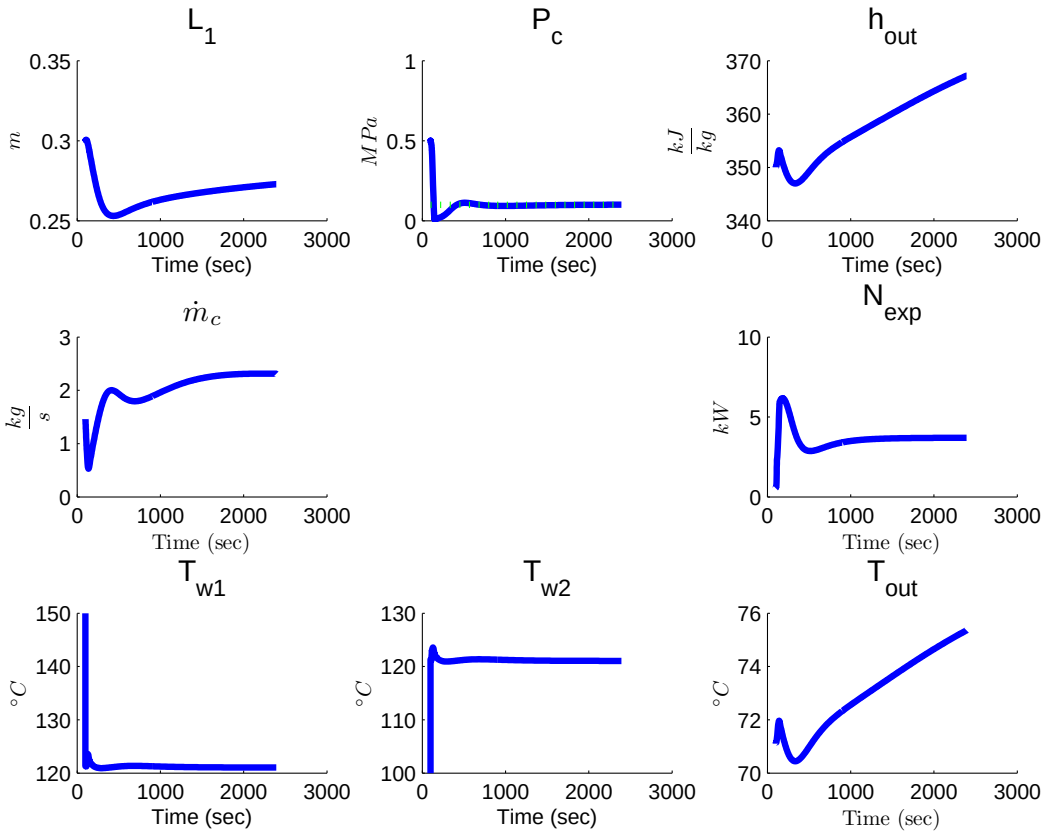

Figure 7.12: RC with PI Control under Averaged Rolling Hills Driving Cycle: Condenser States (State: Solid Line, Setpoint: Dashed Line)

7.4.4.2 Perfect State Access to Phase-Change Boundary

As seen in Figures 7.13 and 7.14, the pressures were better regulated to setpoint than the phase-change boundary under transient heat input. The transient is a cause for non-zero steady-state setpoint error with the designed controller.

Saturation is a cause for the apparent bias in the phase-change boundary that is absent in the pressures. The throttle valve control signal used for the latter's regulation is saturated and results in the non-zero steady-state error.

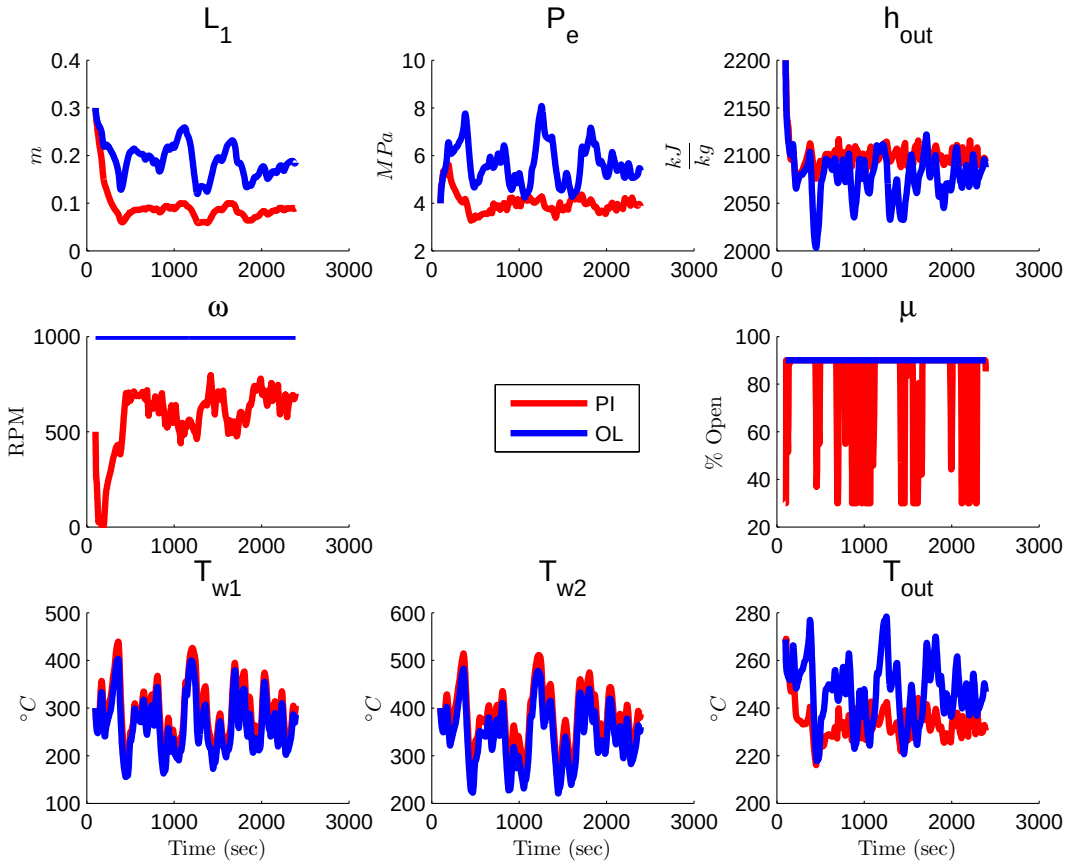

Figure 7.13: RC with PI Control under Rolling Hills Driving Cycle: Evaporator States (PI: Lighter Line, Open-Loop: Darker Line)

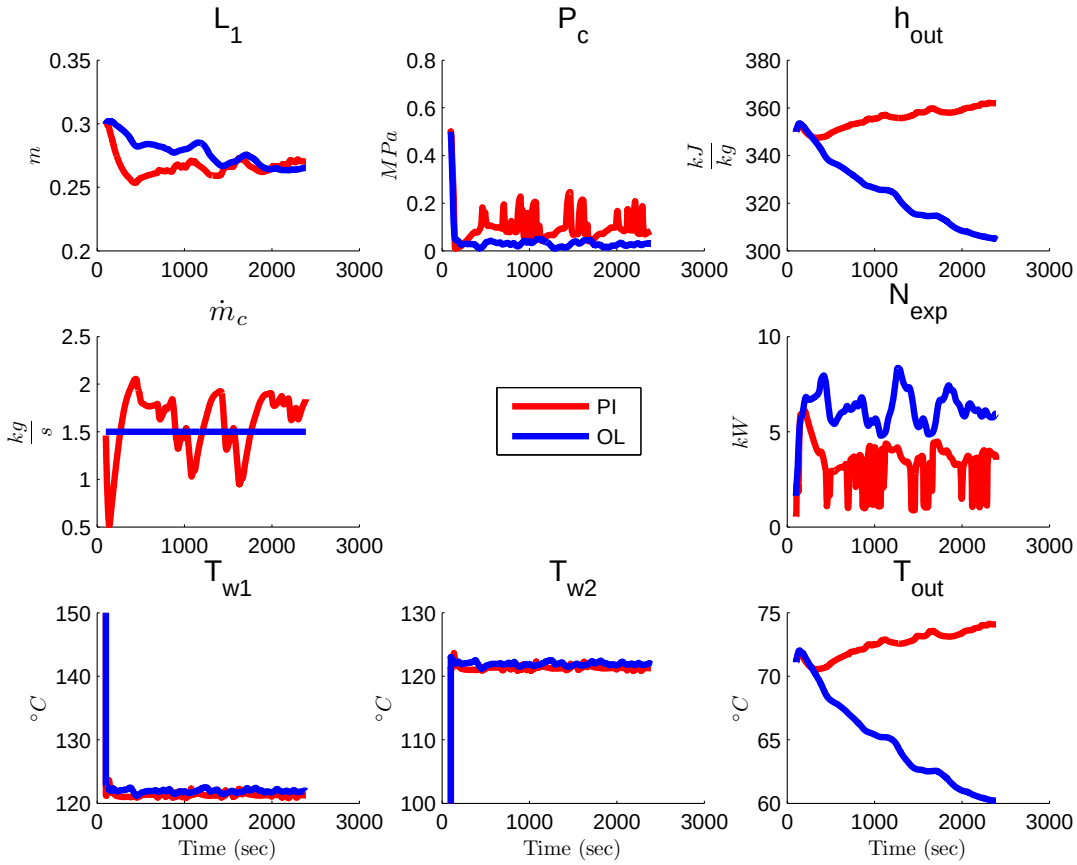

Figure 7.14: RC with PI Control under Rolling Hills Driving Cycle: Condenser States (PI: Lighter Line, Open-Loop: Darker Line)

7.4.4.3 State Estimate of $L_{1,e}$

An estimate of the phase-change boundary is used instead of assuming perfect access to the state. Figure 7.15 shows the performance of the EKF estimator for the evaporator. The estimator uses pressure and outlet temperature measurements in constructing the state estimates. Although initial estimation error is present, the estimates converge quickly to the state values and exhibit the same dynamical trends.

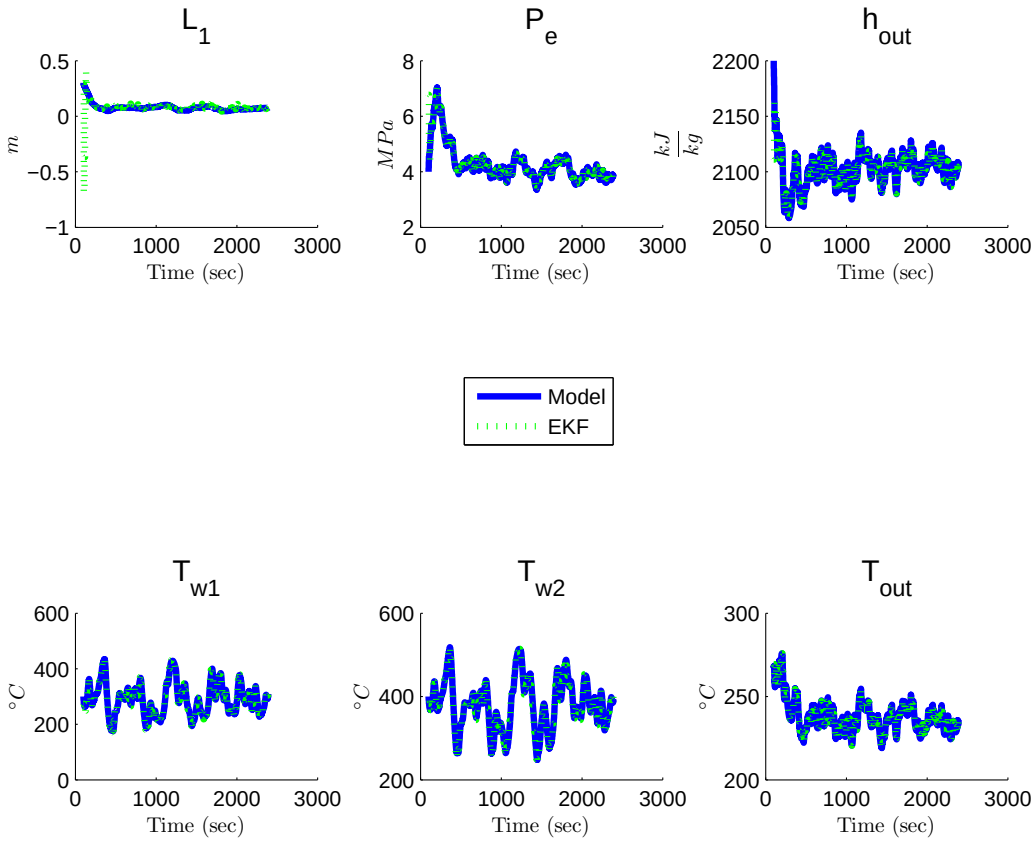

Figure 7.15: RC with PI Control under Rolling Hills Driving Cycle: Evaporator States and EKF State Estimates

Figures 7.16 and 7.17 show that setpoint tracking of the pressures and phase-change boundary appears similar to the case of perfect access to the phase-change boundary. The significant difference appears in the throttle valve control signal, which is more responsive with state estimation.

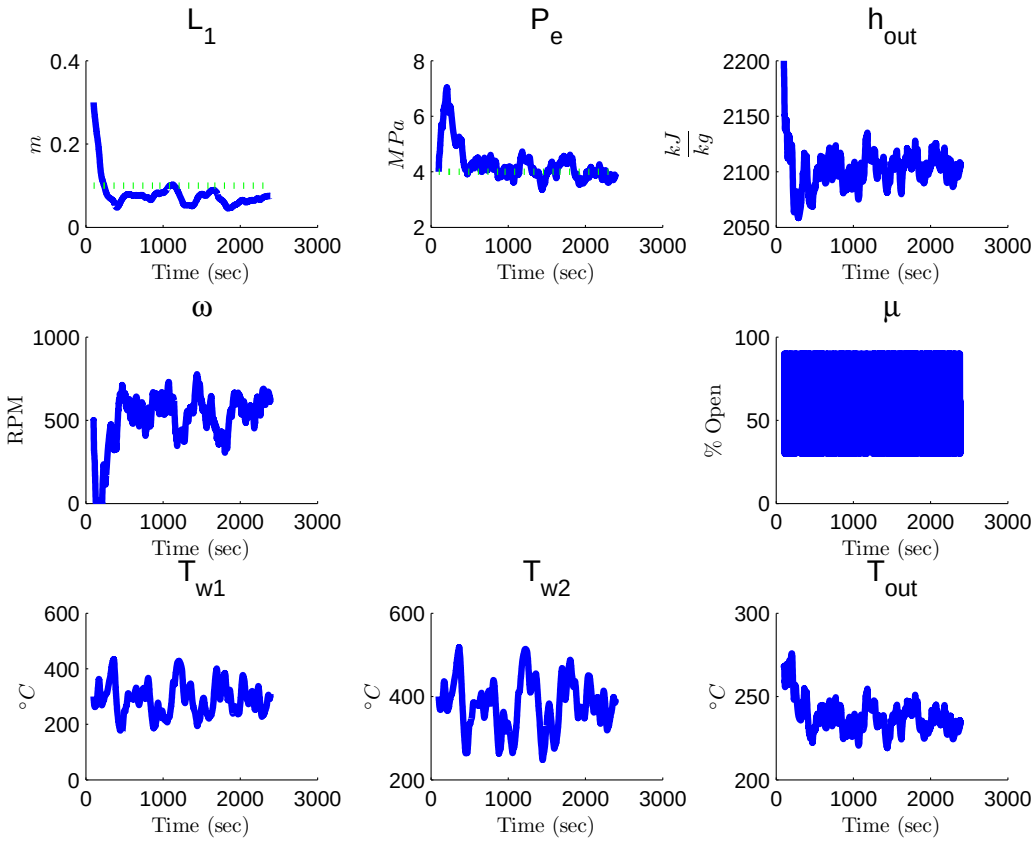

Figure 7.16: RC with PI Control with EKF State Estimator Feedback under Rolling Hills Driving Cycle: Evaporator States (State: Solid Line, Setpoint: Dashed Line)

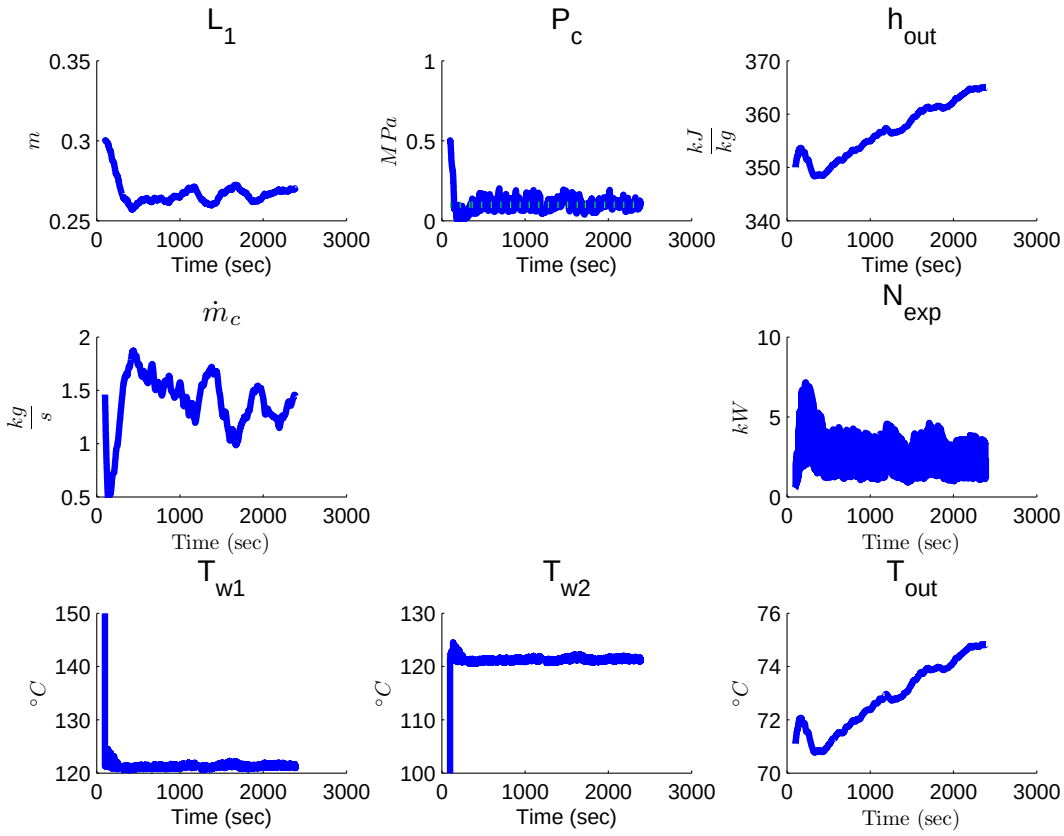

Figure 7.17: RC with PI Control with EKF State Estimator Feedback under Rolling Hills Driving Cycle: Condenser States (State: Solid Line, Setpoint: Dashed Line)

7.4.4.4 Controller Comparisons

Figures 7.18 and 7.19 compare controllers of pressure regulation, phase-change boundary regulation, and their combinations. Independently, the controllers' regulation performance is similar to that of the combined controllers. The results indicate pressure and phase-boundary regulation control loops do not impact each other.

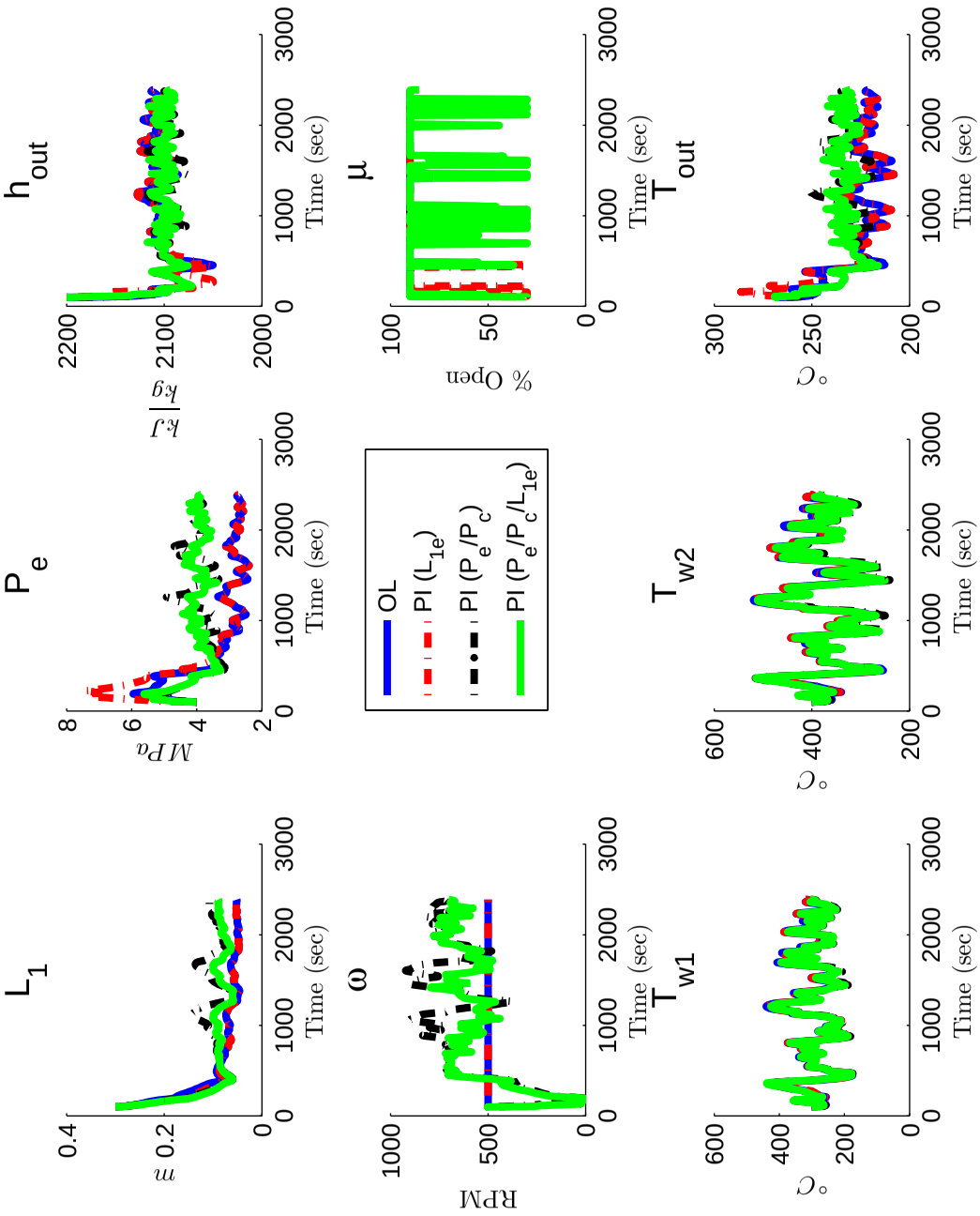

Figure 7.18: RC with PI Control under Rolling Hills Driving Cycle: Evaporator States

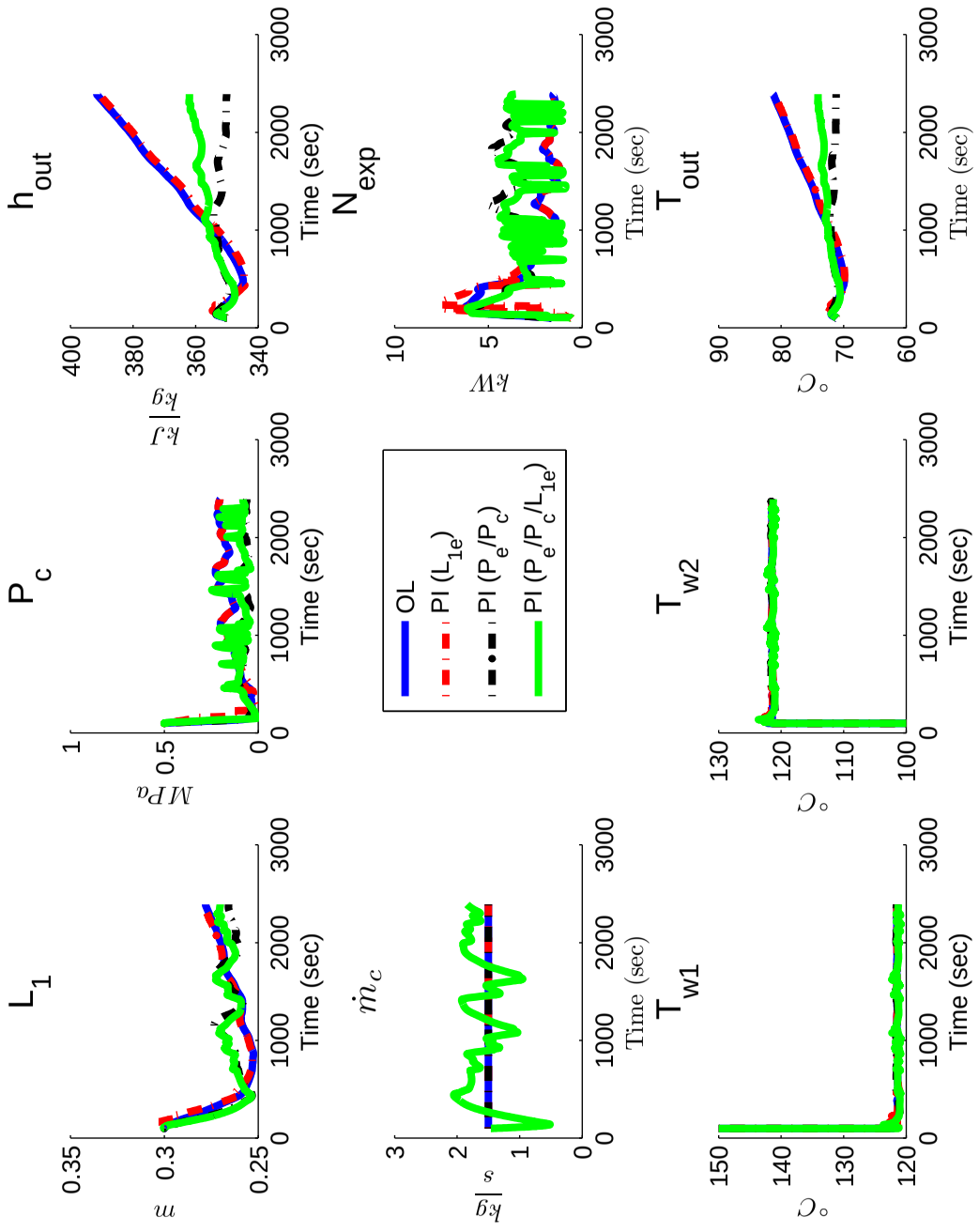

Figure 7.19: RC with PI Control under Rolling Hills Driving Cycle: Condenser States

7.4.5 Remarks

Three independent Proportional Integral SISO controllers using the actuator and feedback variable pairings successfully provided high performance setpoint tracking for pressures and phase-change boundary. The controller performed favorably in flooding avoidance, although oscillatory effects were observed in the other states even with perfect access of the phase-change state. Larger oscillations occurred using the EKF's estimate for the phase-change state.

Regulation was simulated under heat source transients from a driving cycle. Open-loop simulations show undesirable high evaporating pressure and low condensing pressure. This resulted in the highest expander power, but the operating pressures were out of the desirable operating range. Actuation of pump speed, throttle valve position, and heat sink flow rate resulted in desirable pressures close to setpoint, but the transients did not allow for zero tracking error, which was expected. Compared to the open-loop case, the controllers regulated the pressures much closer to the setpoints.

Furthermore, the evaporator's phase-change boundary was controlled to around setpoint with oscillatory tracking error even under constant inputs. This was due to throttle valve saturation. The EKF estimate of this state for feedback control appeared acceptable when comparing the estimates to the states. However, when the estimate is used for feedback, the throttle valve control signal differed significantly to the same signal in the case of perfect state access. This was probably due to the linearization accuracy using the EKF's Approximated Jacobian.

The independent regulation of the pressures and phase-change boundary under driving cycles indicated that the three setpoints can be achieved in a SISO manner.

The expander power generated in the simulations are comparable to the power

range established from static RC model design 1 found in Chapter 4.

7.5 Control of Dual Valve RC Architecture

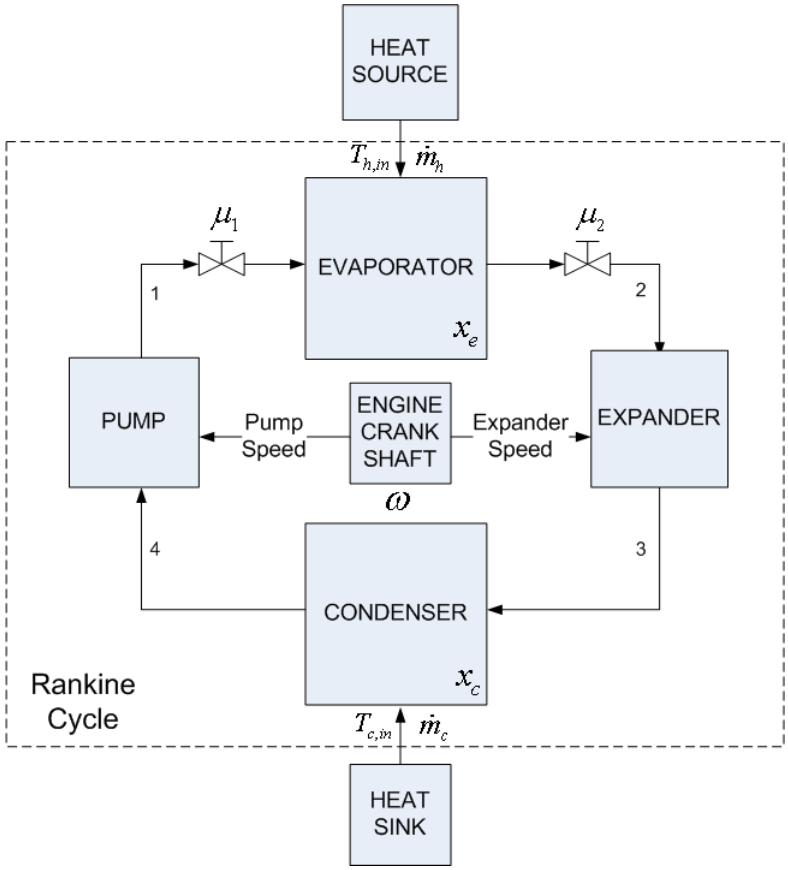

Figure 7.20: RC with Pump and Expander Throttle Valves

7.5.1 Objective

The aim of the architecture is to maximize expander power under automotive WHR constraints specified in Chapter 2. and transient driving conditions. Pressure regulation to high evaporating pressure and low condensing pressure indirectly leads to the highest expander power. The other constraints should be

maintained to acceptable ranges while performing pressure regulation. Static RC model design 2 in Chapter 4 provides the nominal operating points.

The architecture is shown in Figure 7.20 is directed towards automotive WHR systems where the engine crankshaft is coupled to the pump and expander. In addition to the exhaust heat source, this setup provides angular speed disturbance input to the RC system. To replace the loss of pump speed as a control actuator, the architecture features an additional control valve between the evaporator and pump, referred to as the pump throttle valve. The valve between the evaporator and expander will be referred to as the expander throttle valve. These two control valves are available for the controllers to manipulate their open and close positions. The heat sink flow rate is also a manipulated control variable, controlled by a valve not shown.

Advanced controllers are presented to satisfy system operating constraints as described in this section. These advanced controllers will attempt pressure regulation in addition to ensuring other key states such as phase-change boundaries and heat exchanger outlet temperatures remain in range. Step and driving cycle transients are considered in the simulations.

This section concludes with an application to power load following demanded from the expander. The RC system is controlled to meet square-wave and sinusoidal power demands from the load in the presence of driving cycle transients. While this application may not have direct relevance to automotive WHR where maximum power is typically called for at all times, the effort here is more meaningful and extends to applications with precise power production. Example applications include demand-based solar energy recovery for building heat and cooling or applications without energy storage capabilities and need to produce and deliver instantanteous power.

The RC system can be operated as a base loading power plant appropriate for automotive WHR. Instead of demanding low capacity power from the expander, maximum power can be achieved by setting an unachievable high constant power load demand.

7.5.2 Controller Overview

The performance of the following controllers are designed with emphasis placed on pressure regulation while satisfying temperature and phase-boundary constraints.

1. Proportional Integral (PI)
2. Linear Quadratic Integral (LQI)
3. Model Predictive Control (MPC)

The methodology for controller design is as follows. A linear model is first constructed at a steady-state operating point of the nonlinear model. Actuator and feedback variable configurations are chosen to determine the control loop(s) appropriate to meeting the system operating constraints. Control design is performed on the linear model before applying it on the nonlinear model. Controller performance and robustness are then analyzed and compared across controllers.

7.5.3 WHR Constraints

Table 7.4 describes operating constraints for a RC-based WHR system in a 13-liter heavy-duty diesel truck engine. The evaporating pressure P_e must also be higher than the condensing pressure P_c. The proposed controllers in this section will attempt to satisfy these constraints. These constraints are determined from Chapter 2.

Variable	Low Limit	High Limit	Units
P_e	1 (s)	1.5 (h)	MPa
P_c	0.1 (h)	0.2(s)	MPa
$L_{1,e}$, L_{1c}	0 (h)	0.7 (h)	m
$T_{out,e}$	$T_{sat,g}$(h)	300 (s)	$^\circ C$
$T_{out,c}$	-	$T_{sat,f}$, 70 (for oil separation) (h)	$^\circ C$

Table 7.4: RC Constraints for Dual Valve RC Architecture: (s)oft, (h)ard

7.5.4 Linear RC Model

Figures 7.21 and 7.22 compare the Linear and Nonlinear RC models for the Rolling Hills driving cycle.

The small-signal model in state-space form is given by

$$\delta\dot{x} = A\delta x + B\delta u \tag{7.11}$$

$$\delta y = C\delta x + D\delta u \tag{7.12}$$

The deviations δx and δu are added to the equilibrium state x_{eq} and input u_{eq} to obtain the linear model (different from the small-signal model) for comparison to the nonlinear model.

Note the comparison is poor in the beginning because the nonlinear model has not reached the equilibrium point that the linear models are linearized about. Once the nonlinear model settles to its equilibrium, its states match that of the linear model and the trends are comparable. After about 2000 seconds, both the linear and nonlinear models match fairly well.

Feedback controllers are designed on the linear model and applied to the nonlinear one.

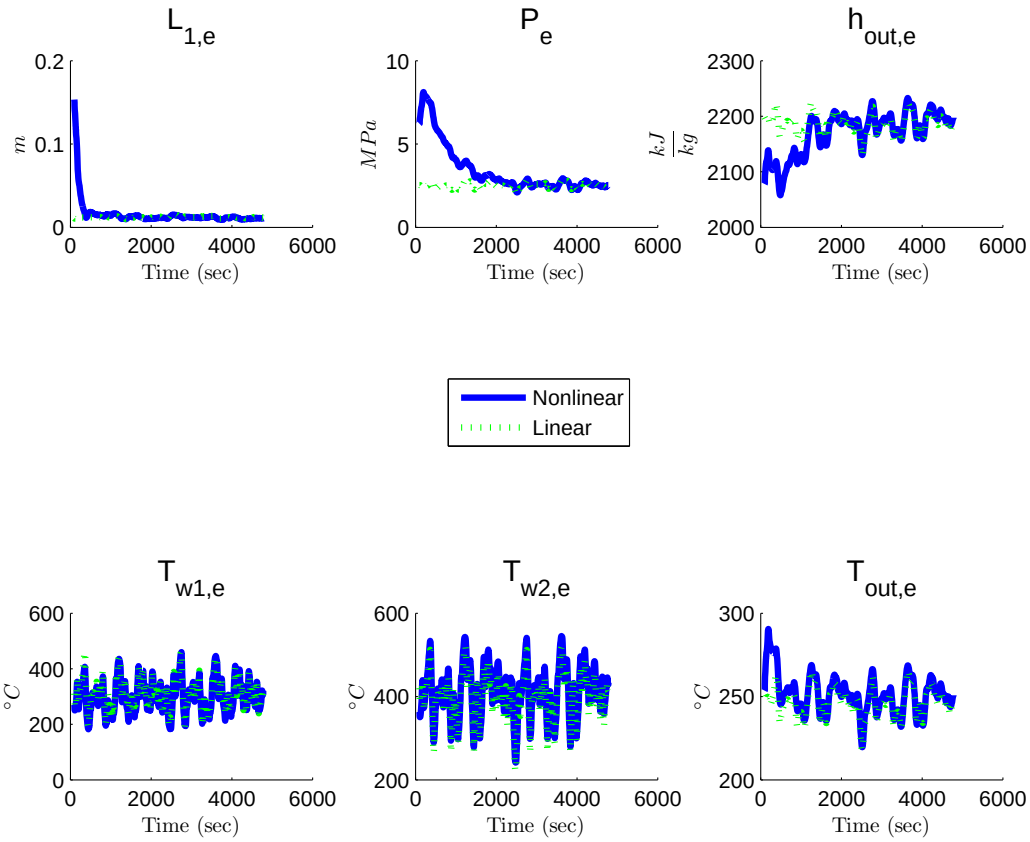

Figure 7.21: Comparison of Linear and Nonlinear Model: Evaporator

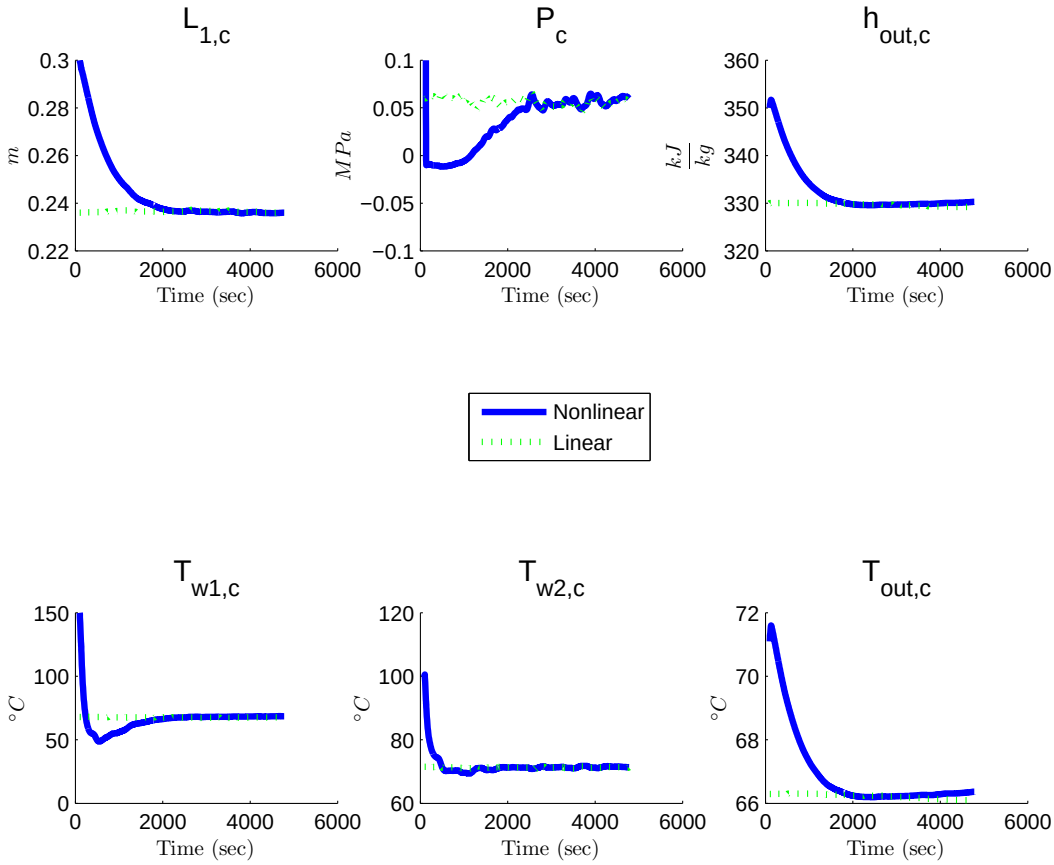

Figure 7.22: Comparison of Linear and Nonlinear Model: Condenser

7.5.5 Actuator and Feedback Variable Configurations

The configurations for the controllers depend on the actuator combinations. The ones considered have the following manipulated inputs shown in Table 7.5.

The feedback configurations are shown in Table 7.6. Pressures are measured for their regulation to setpoints.

Actuator Configuration	u_m
2	$[\dot{m}_c \quad \mu_1]^T$
3	$[\dot{m}_c \quad \mu_1 \quad \mu_2]^T$

Table 7.5: Actuator Configuration for Dual Valve Architecture

Feedback Configuration	y
Pressures	$[P_c \quad P_e]^T$

Table 7.6: Feedback Configuration for Dual Valve Architecture

7.5.6 Proportional Integral Control

The PI controllers are designed as described in Table 7.7 with Actuator Configuration 2. The valve positions vary continuously between 10% and 100% with a non-zero low limit to avoid stagnant working fluid and pressure build-up. This can lead to pressure being out of range and cause numerical problems in simulation. The saturation limits for the heat sink flow rate is obtained from the range found in static RC model design 2 in Chapter 4.

The controllers regulate the RC to the setpoint r by minimizing the regulation error

$$e_1 = r - y \tag{7.13}$$

where $y = [P_c \quad P_e]^T$ and r is the corresponding vector of setpoints for each output signal.

The anti-windup feature minimizes the saturation error e_2 due to exceeding actuator limits. The saturation error is given by

$$e_2 = \left\{ \begin{array}{ll} 0 & \text{if } u_{sat,low} \leq u \leq u_{sat,high} \\ u - u_{sat_high} & \text{if } u > u_{sat,high} \\ u - u_{sat_low} & \text{if } u < u_{sat,low} \end{array} \right\} \tag{7.14}$$

Controller	Parameters	Actuator	Signal	Sat. Limits
C_1	$b = 0.5, k_p = 333$	μ_1	P_e	$[0.1, 1]$
	$k_i = 10, k_b = 1$			
C_2	$b = 0.05, k_p = -3.3$	$\dot{m}_c$	P_c	$[0.05, 0.1]$
	$k_i = -0.064, k_b = 1$			

Table 7.7: Proportional Integral Controller Design Parameters for Dual Valve Architecture

The back-calculating anti-windup PI controller is mathematically expressed as

$$u_m = [\dot{m}_c \quad \mu_1]^T = b + k_p e_1 + \int (k_i e_1 + k_b e_2) dt \tag{7.15}$$

The disturbance input u_d due to heat source and sink conditions is given by

$$u_d = [T_{h,in} \quad \dot{m}_h \quad T_{c,in}]^T \tag{7.16}$$

The gains are tuned using the PID Tuner in MATLAB's Simulink environment [Inc].

Control action is only given to the pump throttle valve μ_1 while the heat sink flow rate $\dot{m}_c$ saturates. As a result, the condensing pressure in Figure 7.24 is unregulated and its setpoint tracking error grows. The evaporating pressure in Figure 7.23 hovers near the setpoint with large deviations.

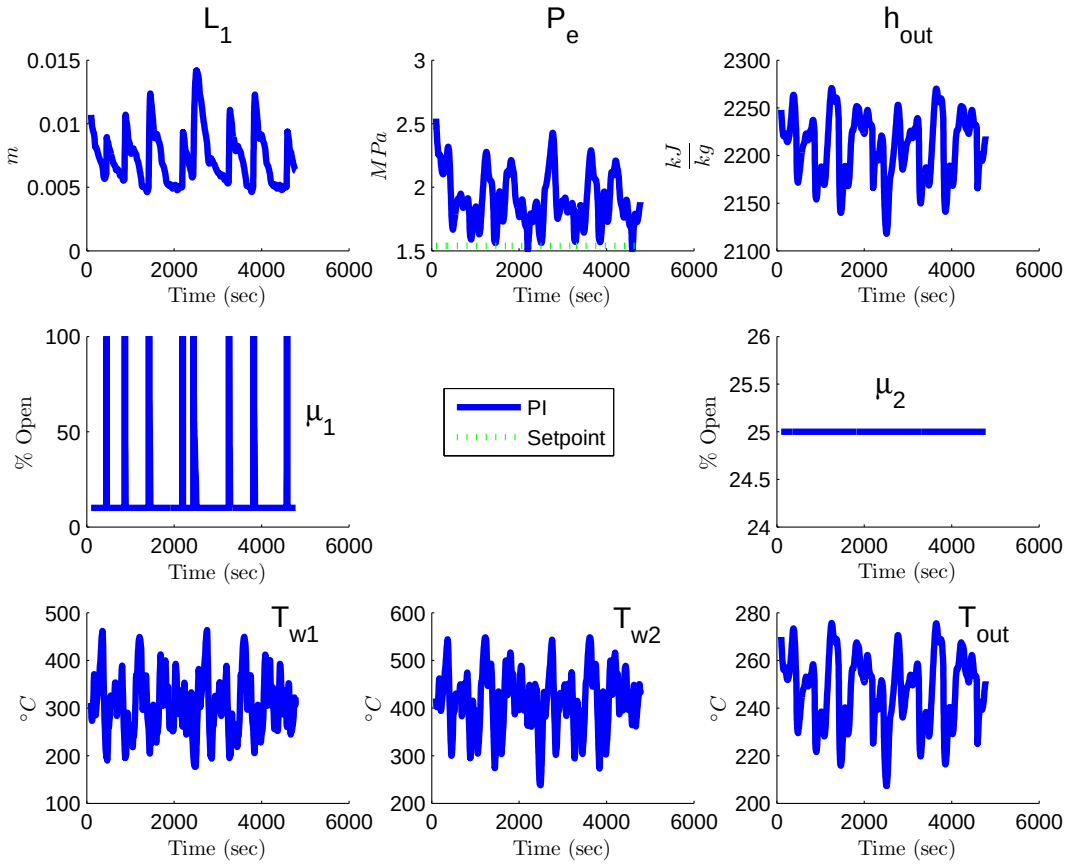

Figure 7.23: RC with PI Control (Actuator 2) under Rolling Hills Driving Cycle: Evaporator States

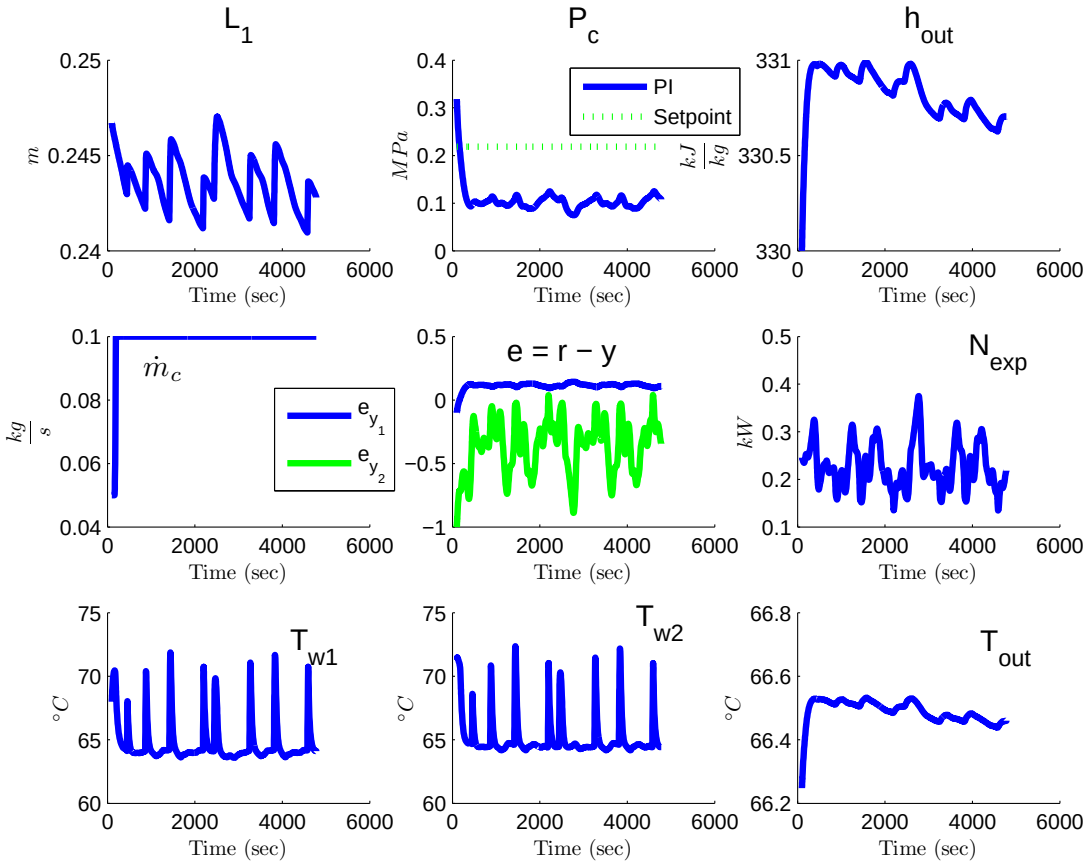

Figure 7.24: RC with PI Control (Actuator 2) under Rolling Hills Driving Cycle: Condenser States

7.5.7 Linear Quadratic Integral Control

Linear Quadratic Regulation (LQR) affords the advantage of multi-input multi-output (MIMO) control that Proportional Integral (PI) does not feature. Furthermore, state and input objectives may be achievable with a specified performance index and proper choice of weights.

A linear model of the RC system is obtained about an equilibrium point x_{eq} and u_{eq}. The controllable and observable linear model has the form given in Equation

7.12.

The infinite-horizon LQR problem is posed as minimizing the pressure fluctations in both the evaporator and condenser. The performance index is described as

$$J(u) = \int_0^\infty \left(\delta x^T Q \delta x + \delta u^T R \delta u\right) dt \tag{7.17}$$

where Q and R are assigned desired weightings for states or state estimates. More weighting can be given to the pressure fluctuations to emphasize their minimization. The key advantage that LQR has over PI is the ability to minimize other states in an optimal form without extra control loops. Furthermore, weighting can be assigned to the manipulated inputs to dictate preference of the control action.

Solving the Riccati equation yields an optimal control law

$$\delta u = -K \delta x \tag{7.18}$$

where a linear state observer is used for state feedback. The optimal control is applied to the Nonlinear RC system by adding the equilibrium point to the control law.

$$u = u_{eq} + \delta u \tag{7.19}$$

The optimal control gain is fixed though it can be updated (time-varying) with subsequent linearizations and LQR solutions applied along the RC system's state trajectories. Because the linear model matches the nonlinear model fairly well during driving cycle transients as seen in Figures 7.21 and 7.22, updated linearizations are not performed.

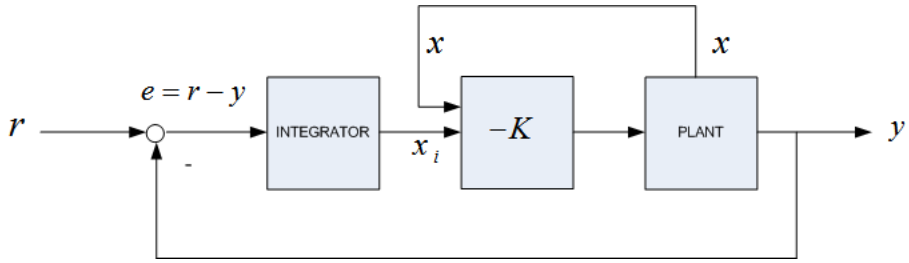

Figure 7.25: Linear Quadratic Integral Control Structure

LQI is a variation on LQR by computing an optimal state-feedback control law for the tracking loop shown in Figure 7.25. The control law comes from the Riccati equation solution as in the LQR framework with the added integral tracking of measured output variables. For a plant with state-space equations

$$\frac{dx}{dt} = Ax + Bu \tag{7.20}$$

$$y = Cx + Du \tag{7.21}$$

the state-feedback control is of the form

$$u = -Kz = -K\begin{bmatrix} x & x_i \end{bmatrix}^T \tag{7.22}$$

where x_i is the integrator output. This control law ensures that the output y tracks the reference command r. For MIMO systems, the number of integrators is equal to the dimension of the output y.

The control law minimizes the cost function

$$J(u) = \int_0^\infty \left(z^T Q z + u^T R u + 2z^T N u\right) dt \tag{7.23}$$

in continuous time or

$$J(u) = \sum_{k=0}^{\infty} \left(z_k^T Q z_k + u_k^T R u_k + 2z_k^T N u_k\right) \tag{7.24}$$

in discrete time. In discrete time, the integrator output x_i is computed using the forward Euler formula:

$$(x_i)_{k+1} = (x_i)_k + T_s(r_k - y_k) \tag{7.25}$$

where T_s is the sampling time of the plant [Inc].

Note that for small-signal linear models, deviation variables are implied in these equations. In other words, $x := \delta x$, $u := \delta u$, $r := \delta r$, and $y := \delta y$. To recover the original variables x, u, r, and y, their equilibrium values x_{eq}, u_{eq}, r_{eq}, and y_{eq} must be added to the small signal values.

7.5.7.1 Design

The matrices Q, R, and N are tuned to reflect interested state deviations to be minimized by applying normalized weights to those states. In other words, a scaling transformation is performed such that

$$z_{scaled} = S_z z \tag{7.26}$$

$$u_{scaled} = S_u u \tag{7.27}$$

where the state and input scaling matrices are given as

$$S_z = \begin{bmatrix} \frac{1}{z_{1,max} - z_{1,min}} & 0 & \cdots & 0 \\ 0 & \frac{1}{z_{2,max} - z_{2,min}} & \cdots & 0 \\ 0 & 0 & \ddots & 0 \\ 0 & \cdots & 0 & \frac{1}{z_{n,max} - z_{n,min}} \end{bmatrix} \tag{7.28}$$

$$S_u = \begin{bmatrix} \frac{1}{u_{1,max} - u_{1,min}} & 0 & \cdots & 0 \\ 0 & \frac{1}{u_{2,max} - u_{2,min}} & \cdots & 0 \\ 0 & 0 & \ddots & 0 \\ 0 & \cdots & 0 & \frac{1}{u_{n,max} - u_{n,min}} \end{bmatrix} \tag{7.29}$$

The weighting matrices then become $Q = qS_x^T S_x$ and $R = rS_u^T S_u$, which are now normalized to the square of the range of each state variable. Additionally, the diagonal matrices q and r are embedded and act as tuning parameters.

For this particular design, q is such that the corresponding entries weight the pressures states by a factor of 10 more than the other states. The tuning parameter r is such that the corresponding entries for the control actuators are several magnitudes smaller (10^{-5}) than the other inputs. The state-input cross matrix N is taken as zero.

These matrices are designed for the actuator and feedback configurations presented in Tables 7.5 and 7.6.

7.5.7.2 Simulations with Perfect State Feedback

Figures 7.26-7.29 show the LQI controller with Actuator Configuration 2. The controllers are applied to the linear models and the nonlinear models. The open-loop (OL) linear and nonlinear models are also shown for comparison.

In the linear simulations, although the pressures are closer to setpoint with control than in the OL case, the control signals saturate for most of the driving cycle, preventing the pressures from being regulated.

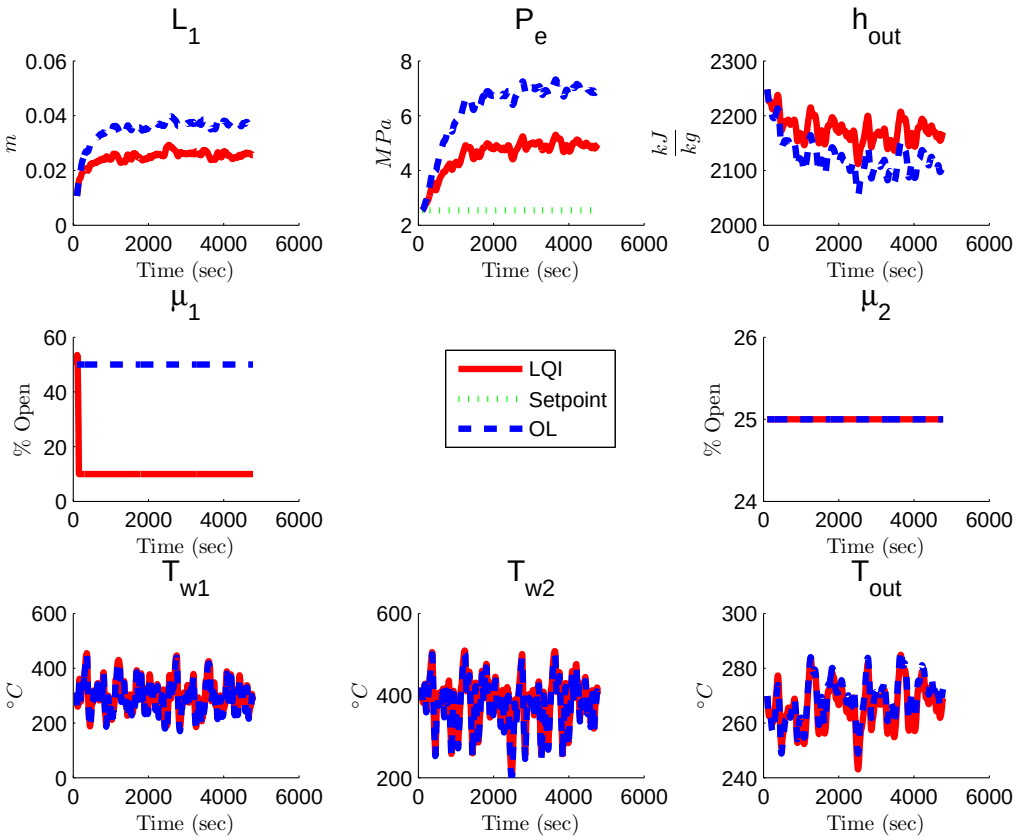

Figure 7.26: Linear RC with LQI Control (Actuator 2) under Rolling Hills Driving Cycle: Evaporator States

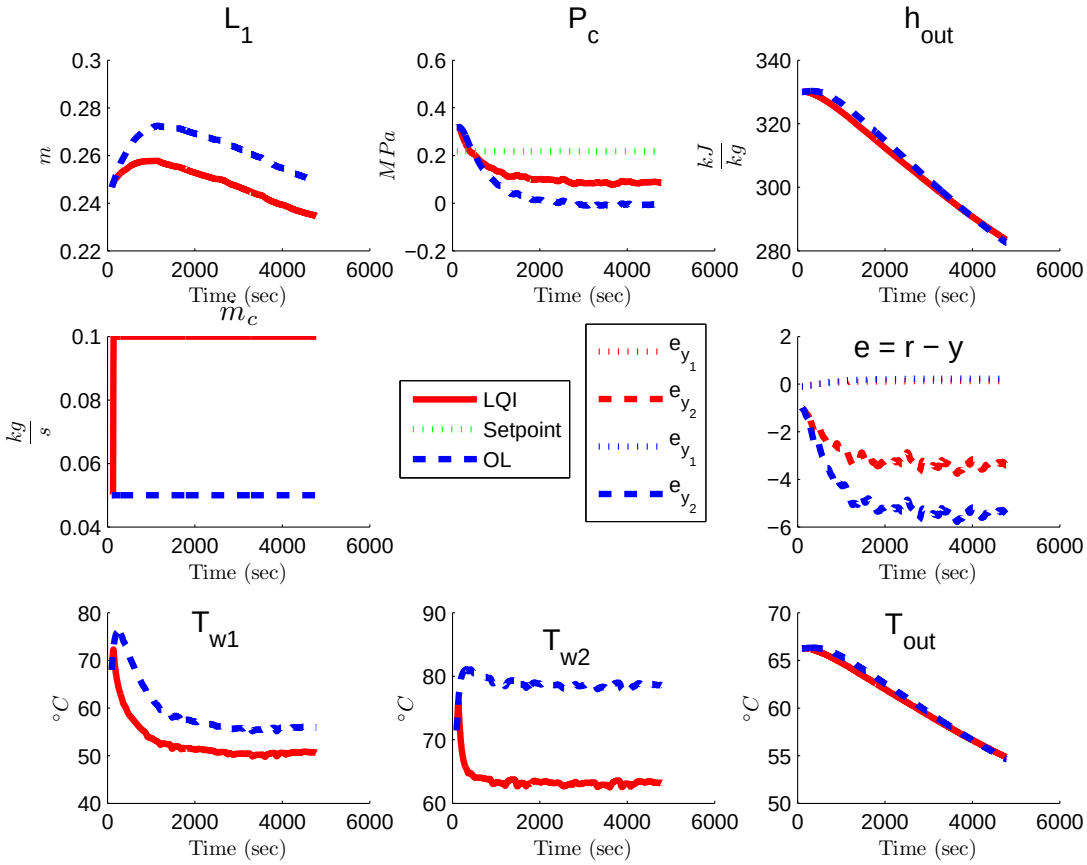

Figure 7.27: Linear RC with LQI Control (Actuator 2) under Rolling Hills Driving Cycle: Condenser States

Both the linear and nonlinear simulations exhibit control signal saturation for most of the driving cycle. During the short period before saturation, the control signals are able to reduce the pressures closer to setpoint than in the OL case.

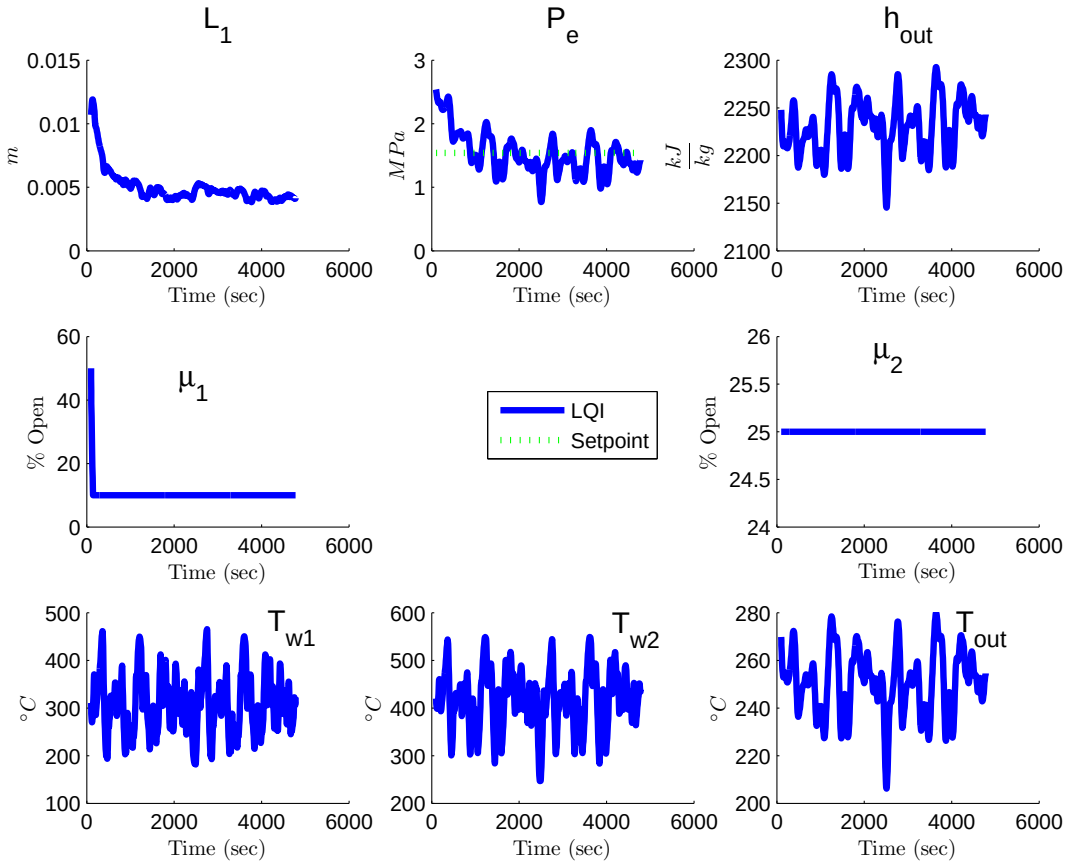

Figure 7.28: Nonlinear RC with LQI Control (Actuator 2) under Rolling Hills Driving Cycle: Evaporator States

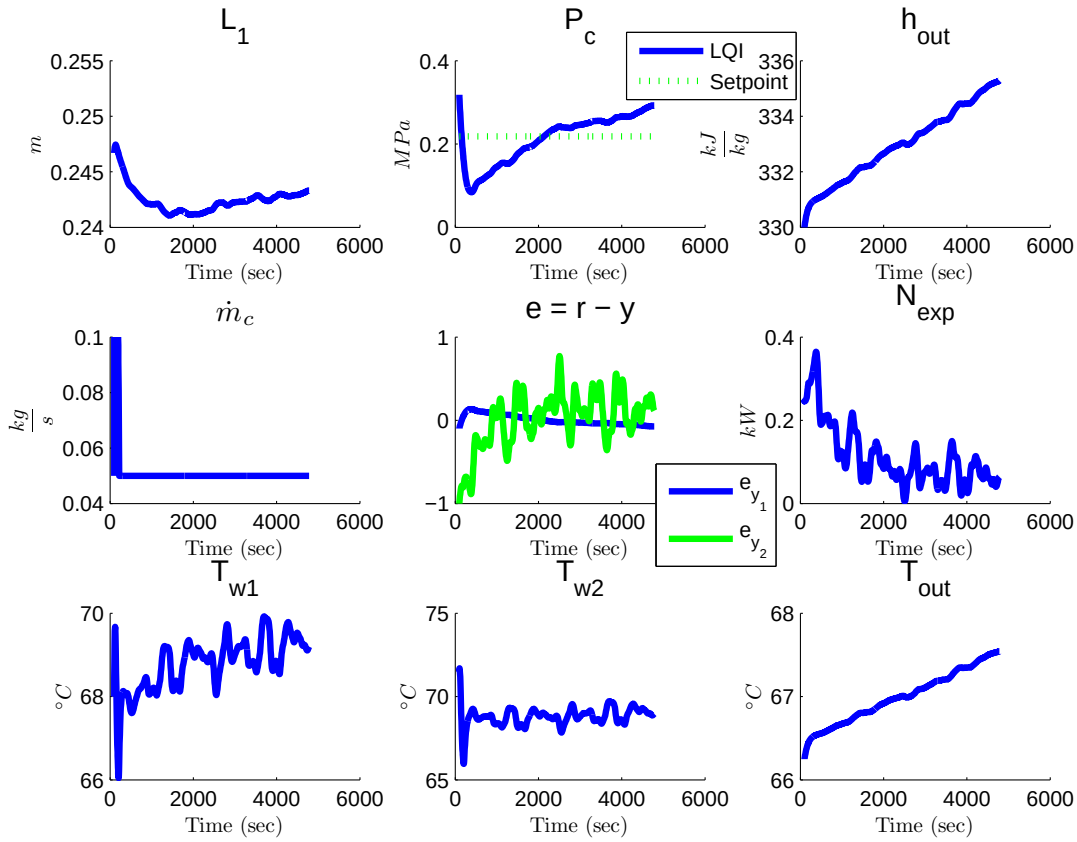

Figure 7.29: Nonlinear RC with LQI Control (Actuator 2) under Rolling Hills Driving Cycle: Condenser States

The formulation of the LQI controller allows for additional actuators in the regulation problem. Actuator Configuration 3 is simulated in Figures 7.30-7.33.

Using Actuator Configuration 3, the control action brings the pressures to setpoint in a superior fashion over Actuator Configuration 2.

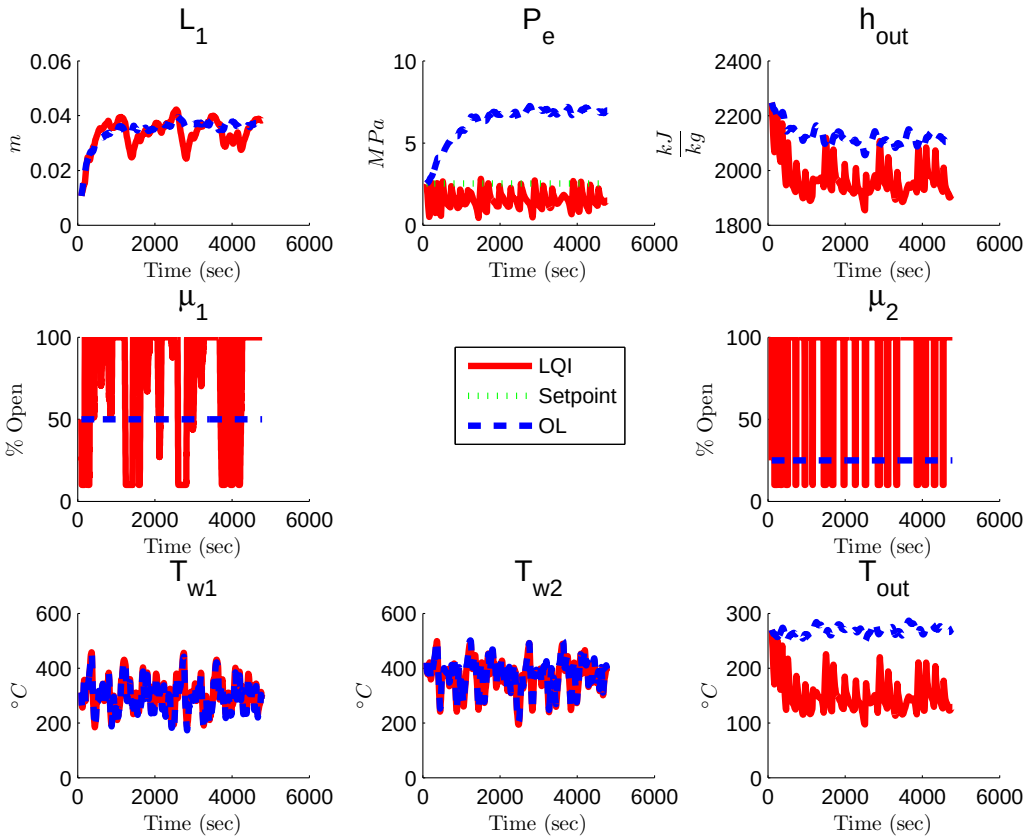

Figure 7.30: Linear RC with LQI Control (Actuator 3) under Rolling Hills Driving Cycle: Evaporator States

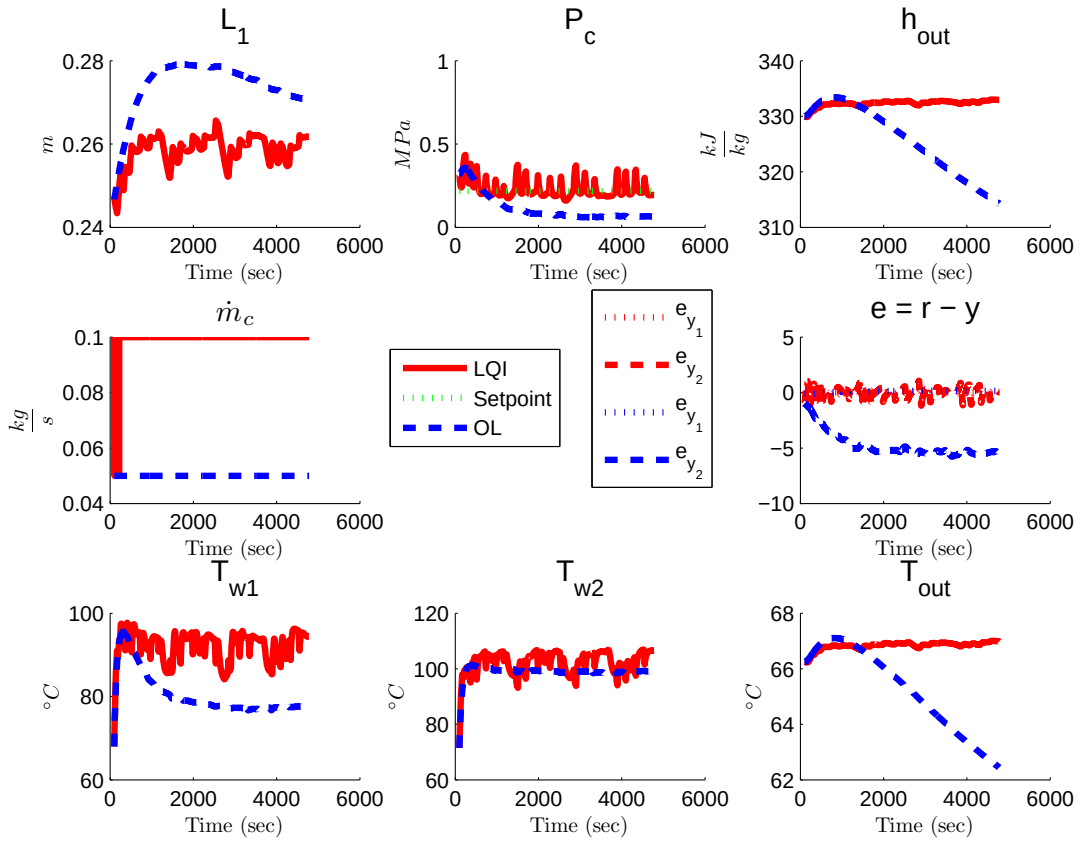

Figure 7.31: Linear RC with LQI Control (Actuator 3) under Rolling Hills Driving Cycle: Condenser States

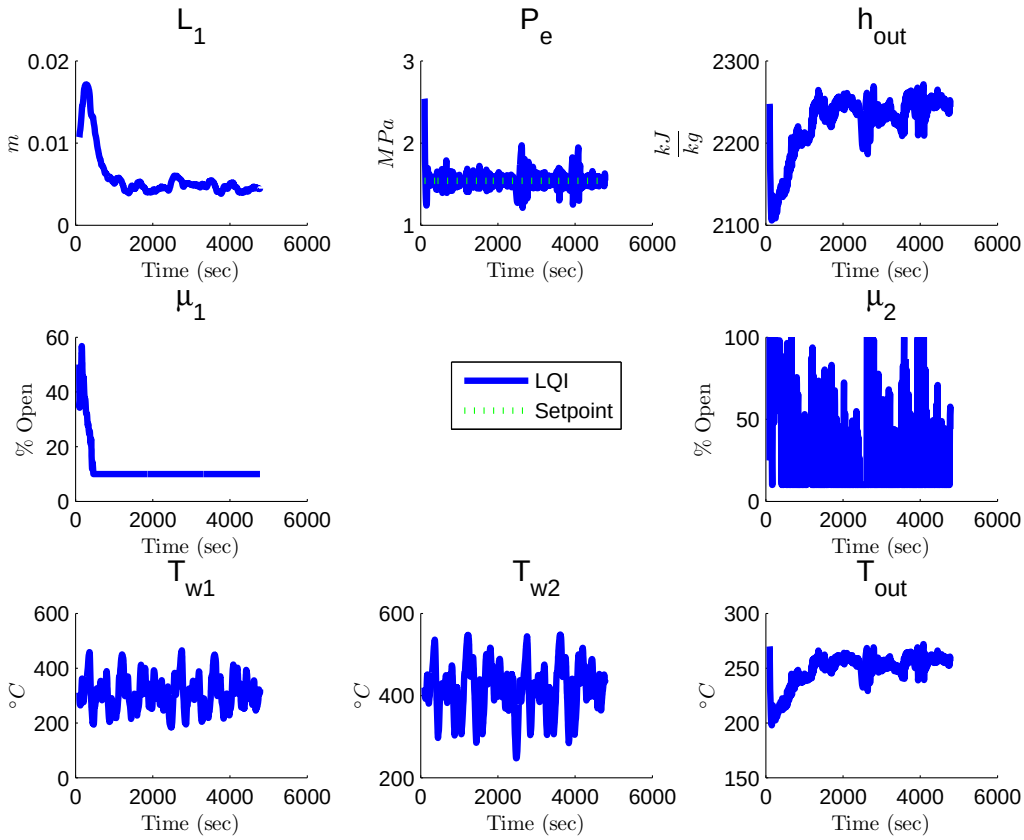

Figure 7.32: Nonlinear RC with LQI Control (Actuator 3) under Rolling Hills Driving Cycle: Evaporator States

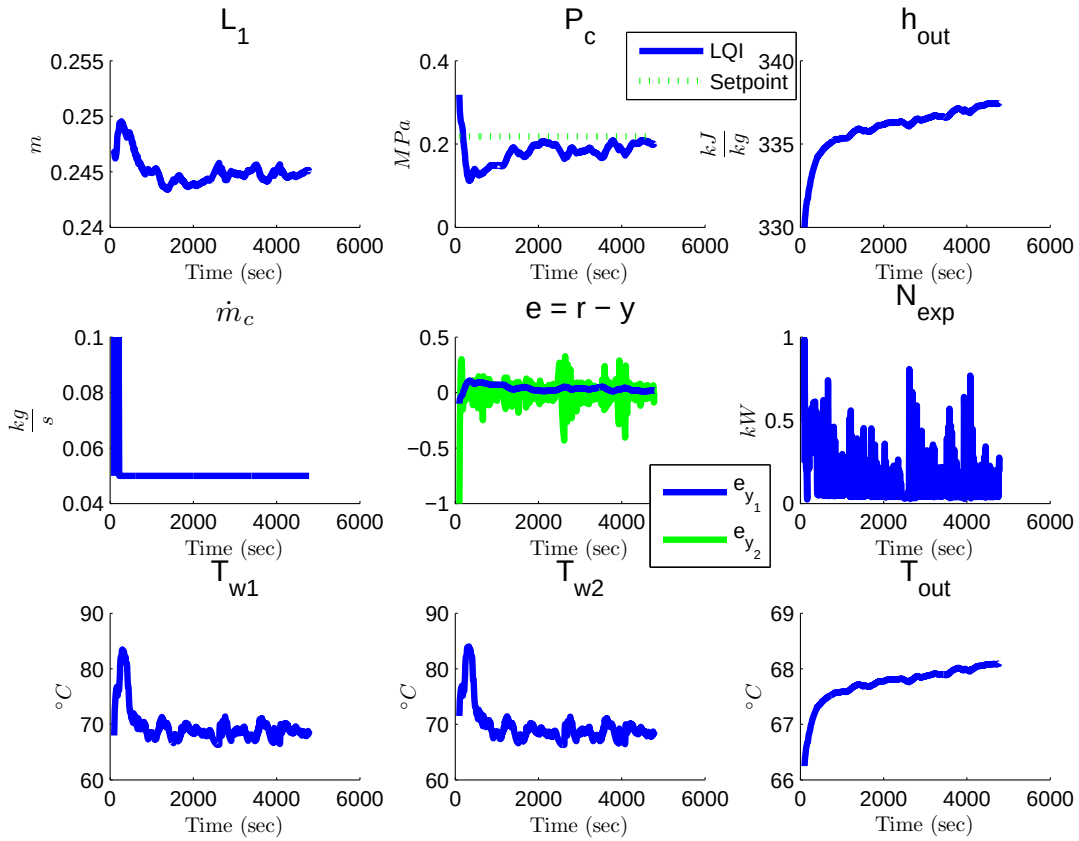

Figure 7.33: Nonlinear RC with LQI Control (Actuator 3) under Rolling Hills Driving Cycle: Condenser States

The open-loop response due to step changes in inputs for the Actuator 3 configuration is shown in Figures 7.34 and 7.35. The step changes in the inputs are given in Table 7.8. Note the pressures are both away from their setpoints.

Table 7.8: Step Changes in RC Inputs to Compare LQI (Actuator 3) and Open-Loop Cases

Step Input	t (seconds)	Initial Value	Final Value
ω	500	500 RPM	750 RPM
$T_{h,in}$	1000	450 $^{\circ}C$	400 $^{\circ}C$
$\dot{m}_h$	1500	0.062 $\frac{kg}{s}$	0.108 $\frac{kg}{s}$
T_c	2000	60 $^{\circ}C$	75 $^{\circ}C$
$\dot{m}_c$	3000	0.05 $\frac{kg}{s}$	0.1 $\frac{kg}{s}$

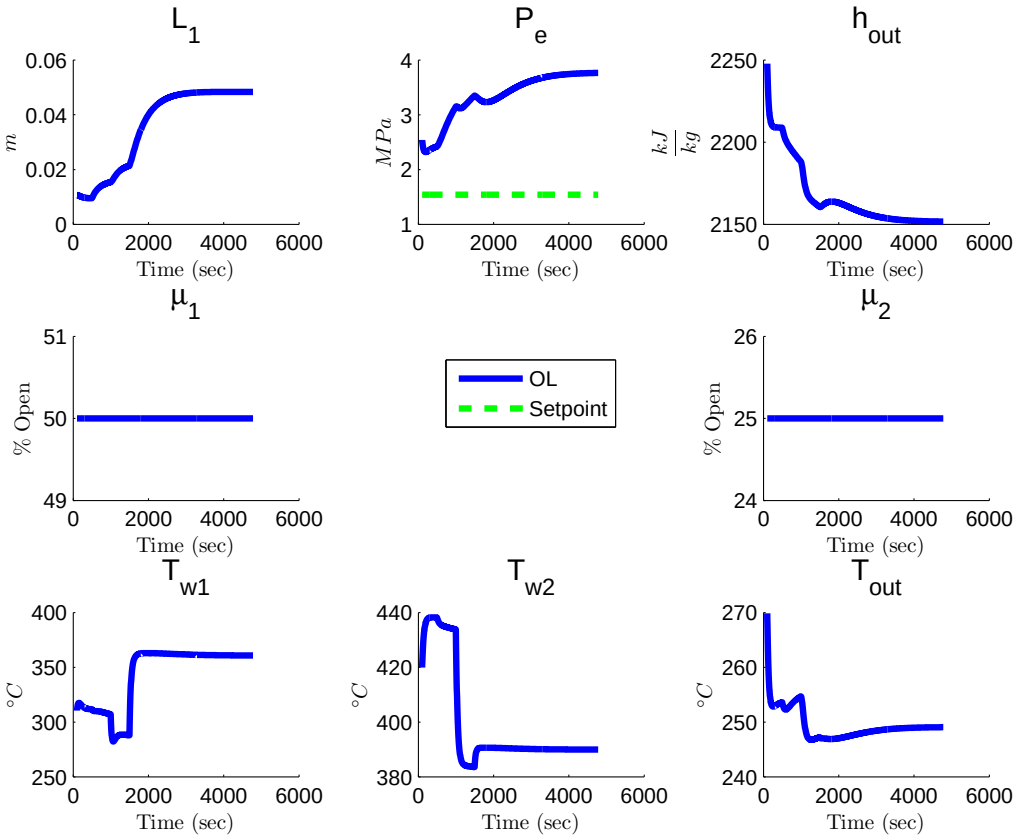

Figure 7.34: Open-loop Nonlinear RC under Step Inputs: Evaporator States

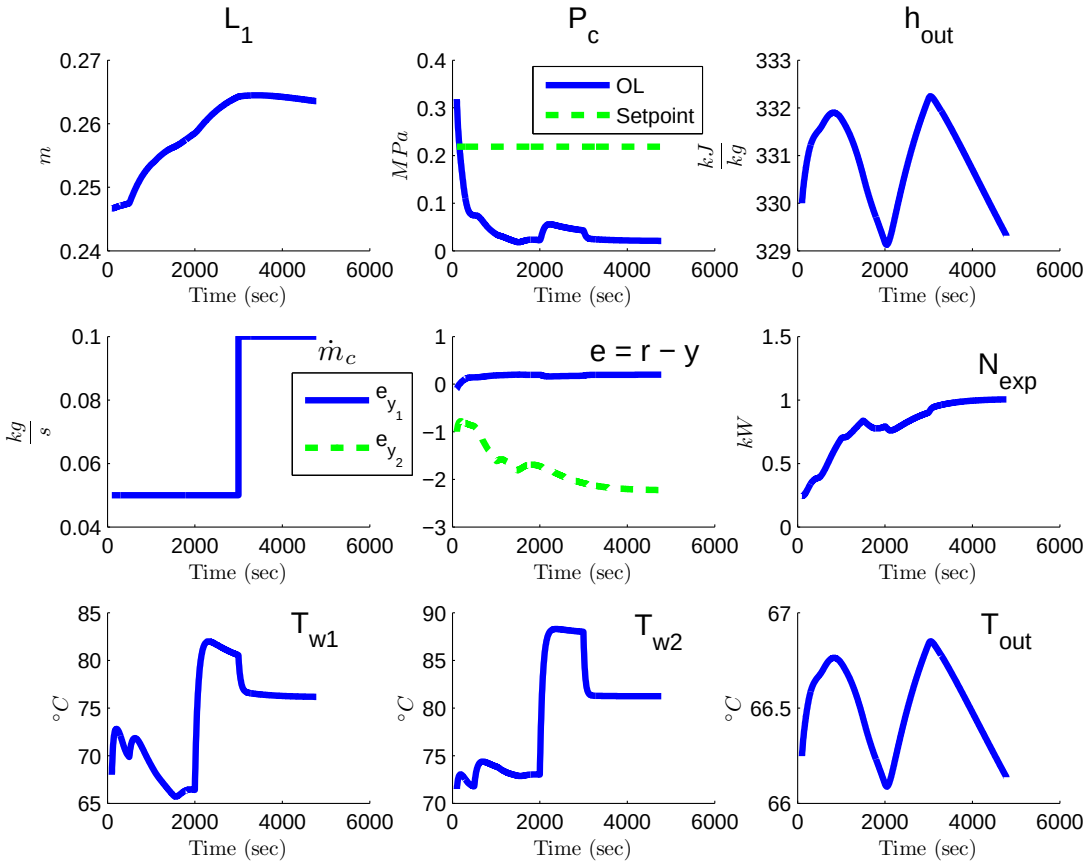

Figure 7.35: Open-loop Nonlinear RC under Step Inputs: Condenser States

Figures 7.36 and 7.37 show the LQI controlled case for Actuator Configuration 3 and demonstrates improved pressure regulation to setpoint.

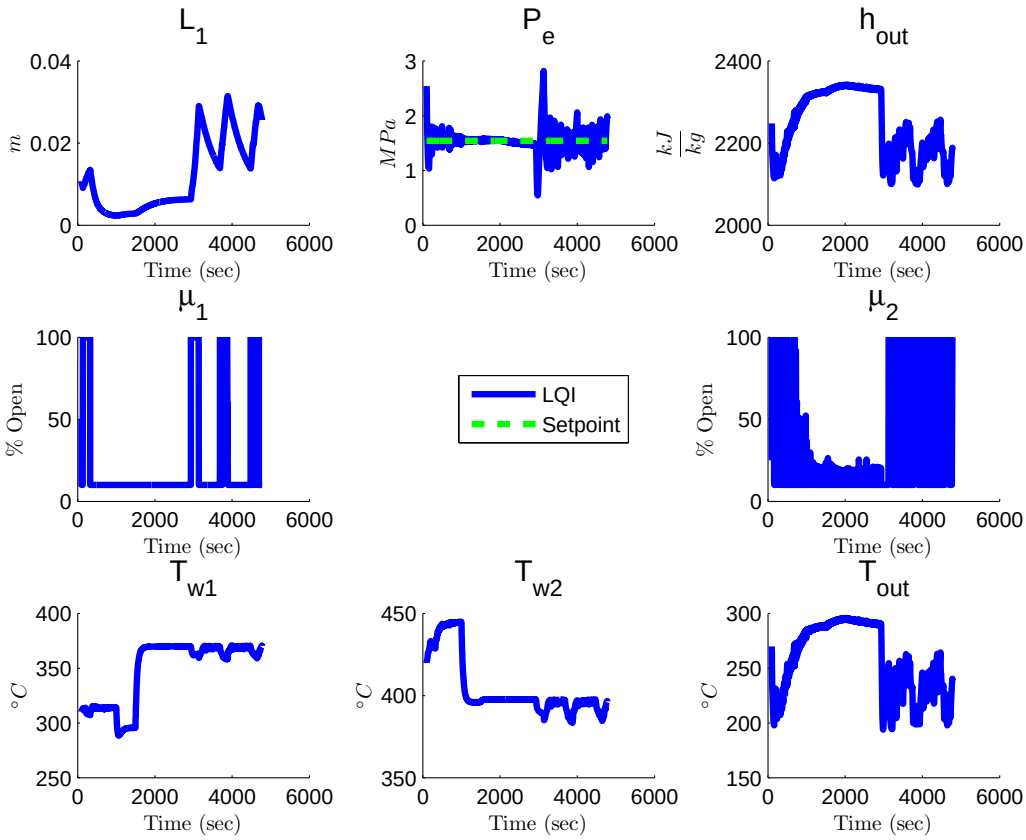

Figure 7.36: Nonlinear RC with LQI Control (Actuator 3) under Step Inputs: Evaporator States

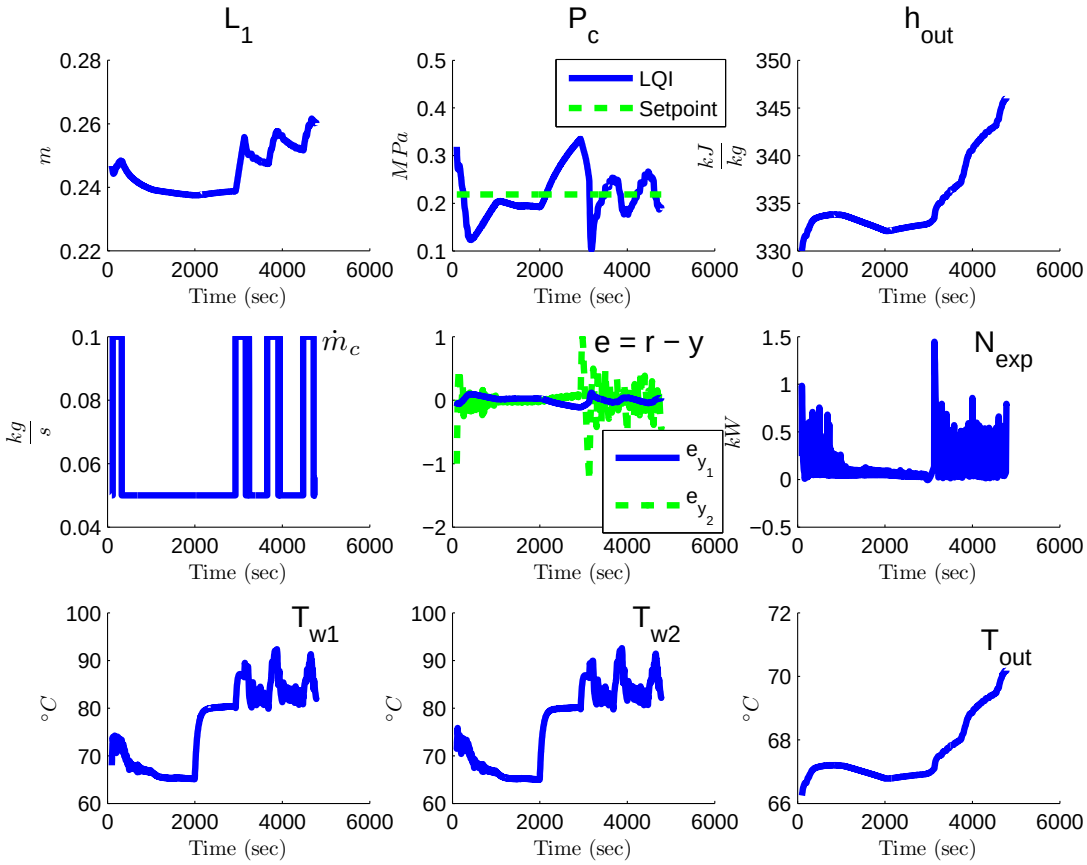

Figure 7.37: Nonlinear RC with LQI Control (Actuator 3) under Step Inputs: Condenser States

7.5.7.3 Simulations with State Estimation Feedback

This last set of simulations shows superior performance of Actuator Configuration 3 over 2. Because perfect state access for feedback is not possible, the next set of simulations shows control with state estimate feedback using available pressure and temperature measurements. The Approximated Jacobian is used to reduce computational load.

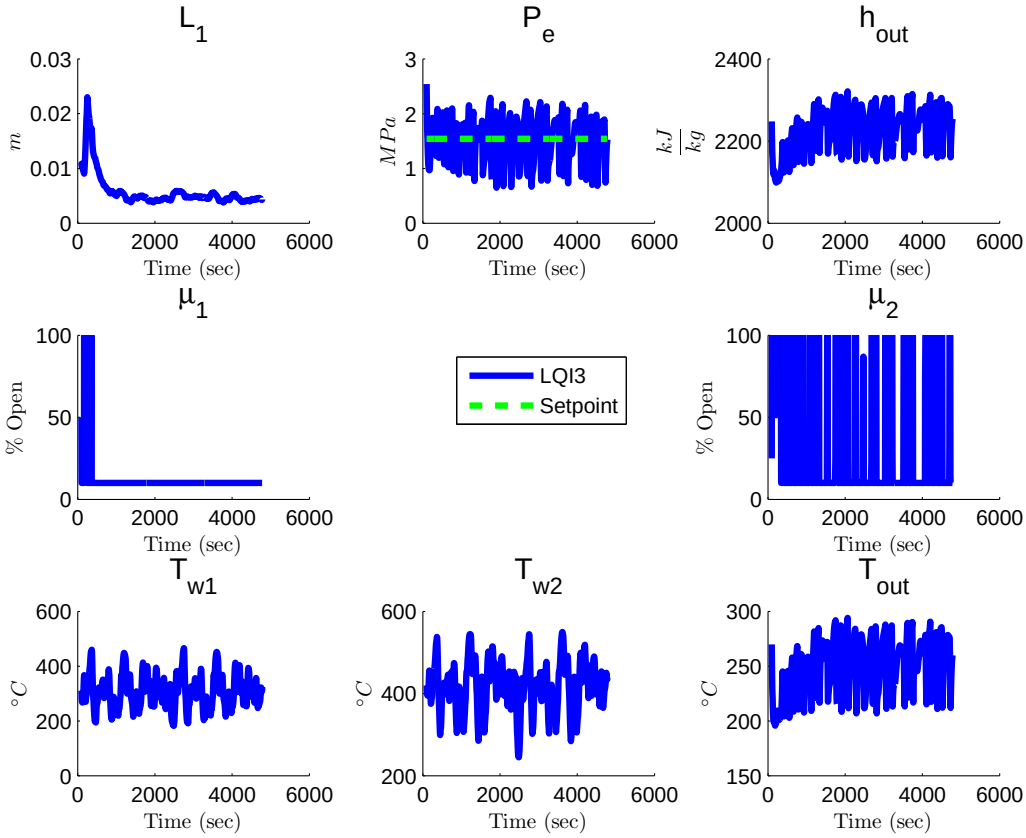

Figure 7.38: Nonlinear RC with LQI/EKF State Estimation Feedback Control (Actuator 3) under Rolling Hills Driving Cycle: Evaporator States

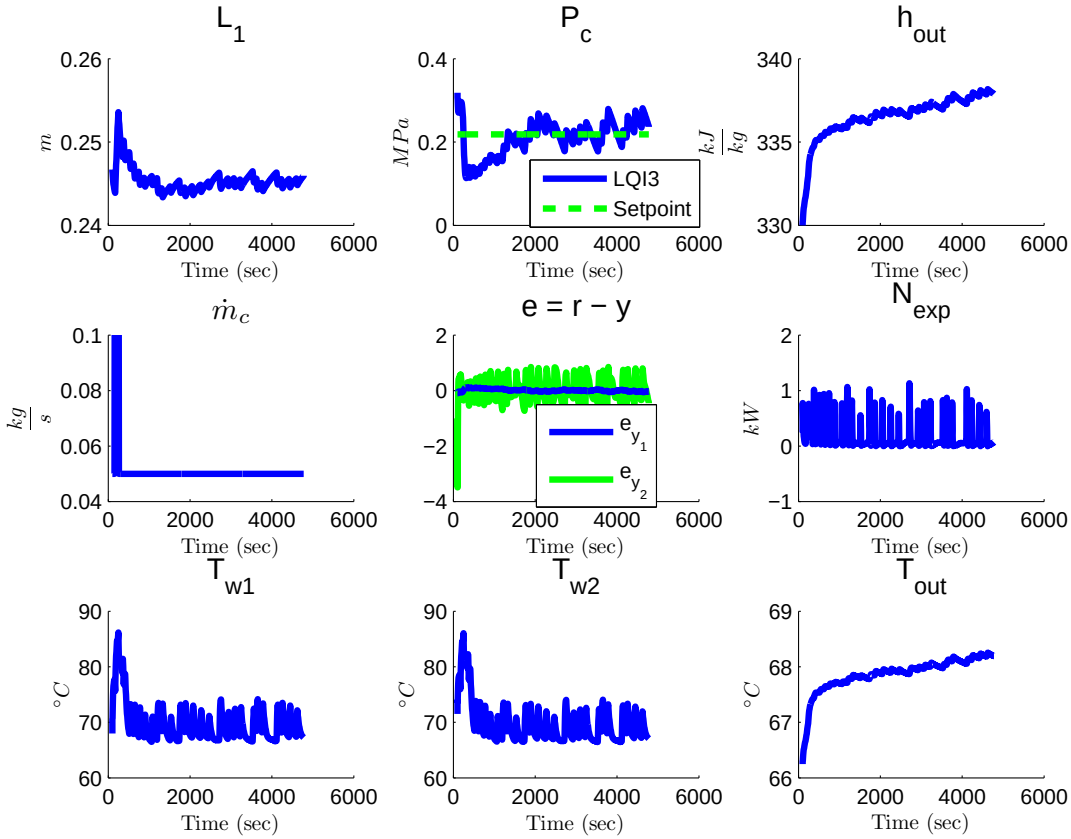

Figure 7.39: Nonlinear RC with LQI/EKF State Estimation Feedback Control (Actuator 3) under Rolling Hills Driving Cycle: Condenser States

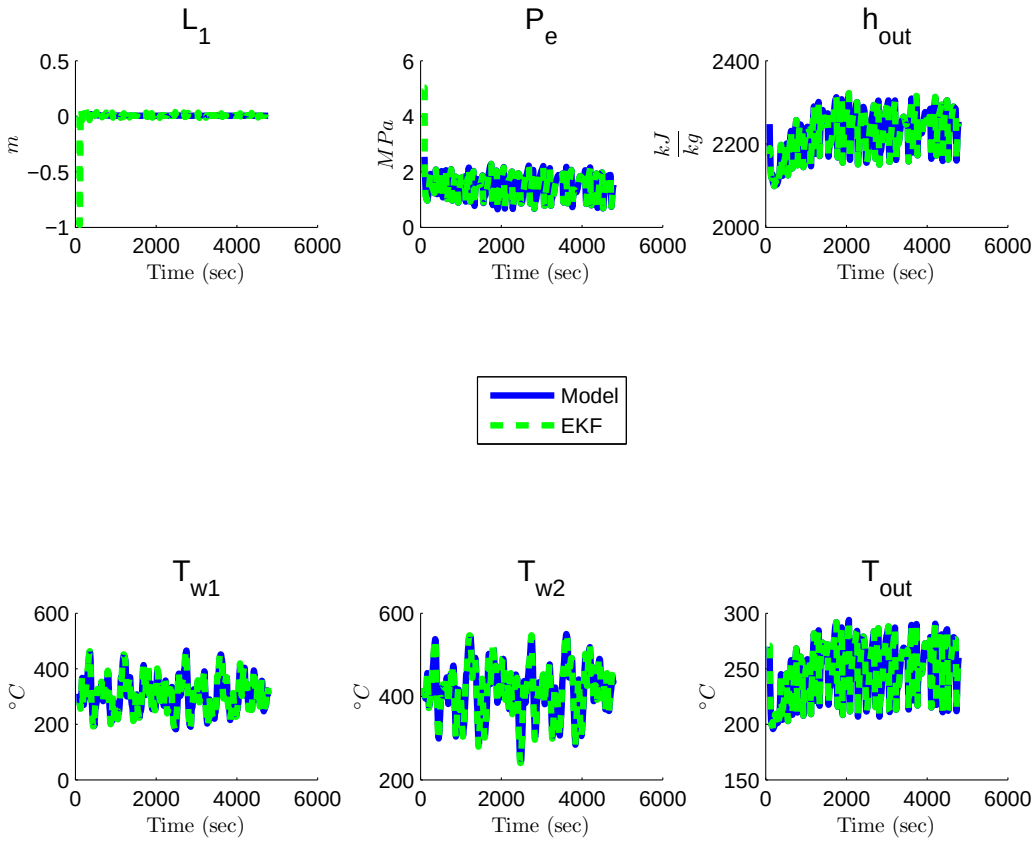

Figure 7.40: EKF State Estimation of Nonlinear RC under Rolling Hills Driving Cycle: Evaporator States

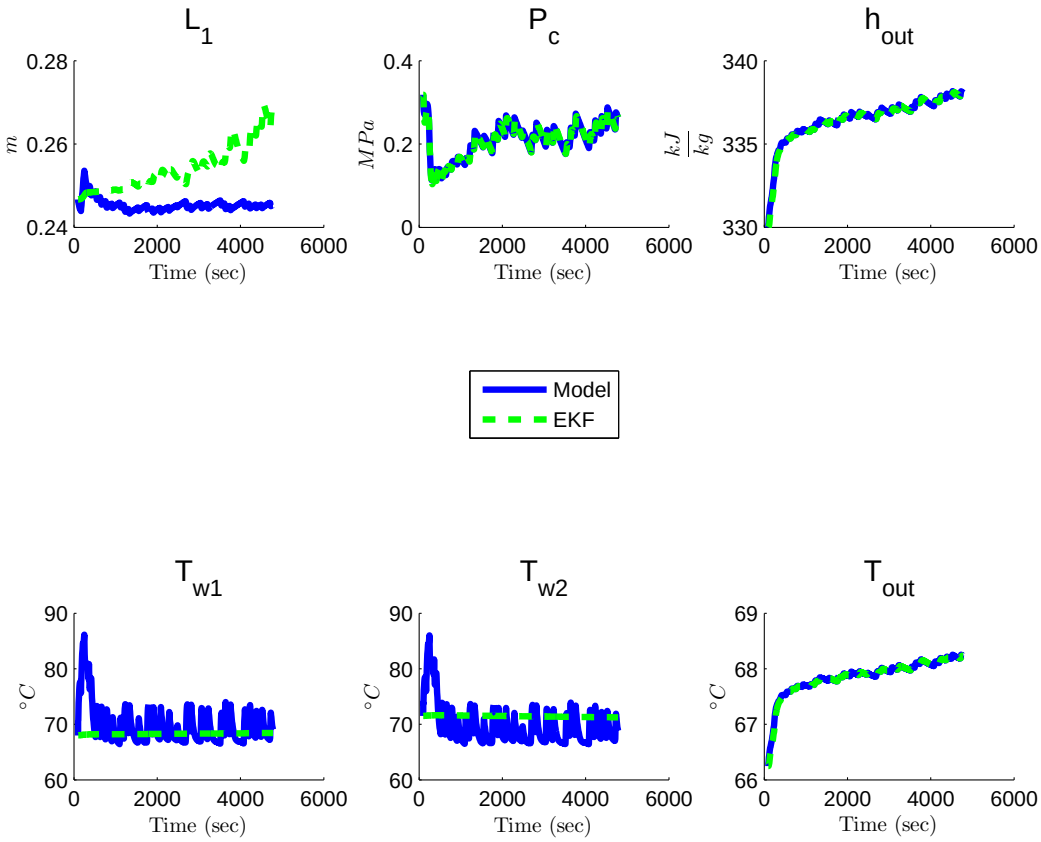

Figure 7.41: EKF State Estimation of Nonlinear RC under Rolling Hills Driving Cycle: Condenser States

7.5.8 Model Predictive Control

Model Predictive Control (MPC) is a special case of Linear Quadratic Regulation (LQR) control. Both compute an optimal MIMO control law based on a horizon and solve a quadratic performance index. Unlike LQR, MPC has the advantage of specifying constraints that the control law must meet in a receding finite-horizon manner. This lends naturally to the operating physical constraints, for example, bounded temperature and pressure ranges, that are specified for RC systems.

The constraints in MPC can be specified as bounds on input and output. These bounds can be both hard (equality) or soft (inequality) constraints. Rate constraints can also be specified for the inputs.

MPC solves an optimization problem that typically does not have an analytical solution. This is due to the existence of constraints, for example, that must be incorporated into the solution of a quadratic programming problem. Without constraints, the performance index reduces to the performance index in the LQR problem whose analytical solution is found by solving the Riccati equation.

The receding finite-horizon feature of MPC allows for prediction and corrective action through an updated control law. The performance index is solved for a specified prediction interval into the future. The plant dynamics are projected in this interval, which allows for a predictive look-ahead in computing a control law. Given sufficiently long horizons, the predictive control not only satisfies constraints (if feasible), but also takes corrective action immediately when the plant is predicted to reach a constraint bound. The first solution of the control law is applied with the rest discarded. This procedure repeats at the next sampling instant with the next horizon.

The Model Predictive Control Toolbox MATLAB/Simulink is used to design and simulate controllers on the Linear RCs to meet operating constraints under driving cycle transients. The controllers are then implemented on the Nonlinear RCs. The MPC controller computes control laws based on the Linear RC model, and uses a linear state observer for feedback control for both Linear and Nonlinear RCs. Thus, a nonlinear state estimator is not needed. Specific details of the toolbox functions can be found in [BMR13].

7.5.8.1 Design

As with the other controllers in this chapter, the objective is pressure regulation with the same saturation limits on the control acutators. Table 7.9 show these as manipulated constraints. The values are the minimum and maximum deviations from the equilibrium point of the linear model.

Manipulated Variables	Units	Min	Max
$\dot{m}_c$	$\frac{kg}{s}$	0	0.05
μ_1	%	-40	50
μ_2	%	-15	75

Table 7.9: MPC Constraints for Dual Valve Architecture

The expander throttle valve μ_2 is available only for Actuator Configuration 3. The maximum up and down rates are set to $\pm\infty$. There are no imposed constraints on output variables so the MPC controller can be compared to the other controllers discussed in this section.

The horizons for the MPC designs are given in Table 7.10.

	Units	Values
Control Interval	Seconds	5
Prediction Horizon	Intervals	10
Control Horizon	Intervals	2

Table 7.10: MPC Horizons for Dual Valve Architecture

The input weights are given in Table 7.11. μ_2 is available only for Actuator Configuration 3.

Input Weights	Weight	Rate Weight
$\dot{m}_c$	0	0.1
μ_1	0	0.1
μ_2	0	0.1

Table 7.11: MPC Weights for Dual Valve Architecture

Output weights are set to 1 for both pressures.

7.5.8.2 Simulations

Figures 7.42 and 7.43 show results for Actuator Configuration 2. As in the LQI case for the same configuration, the pressure tracking performance is poor due to the expander throttle valve position μ_2 being saturated.

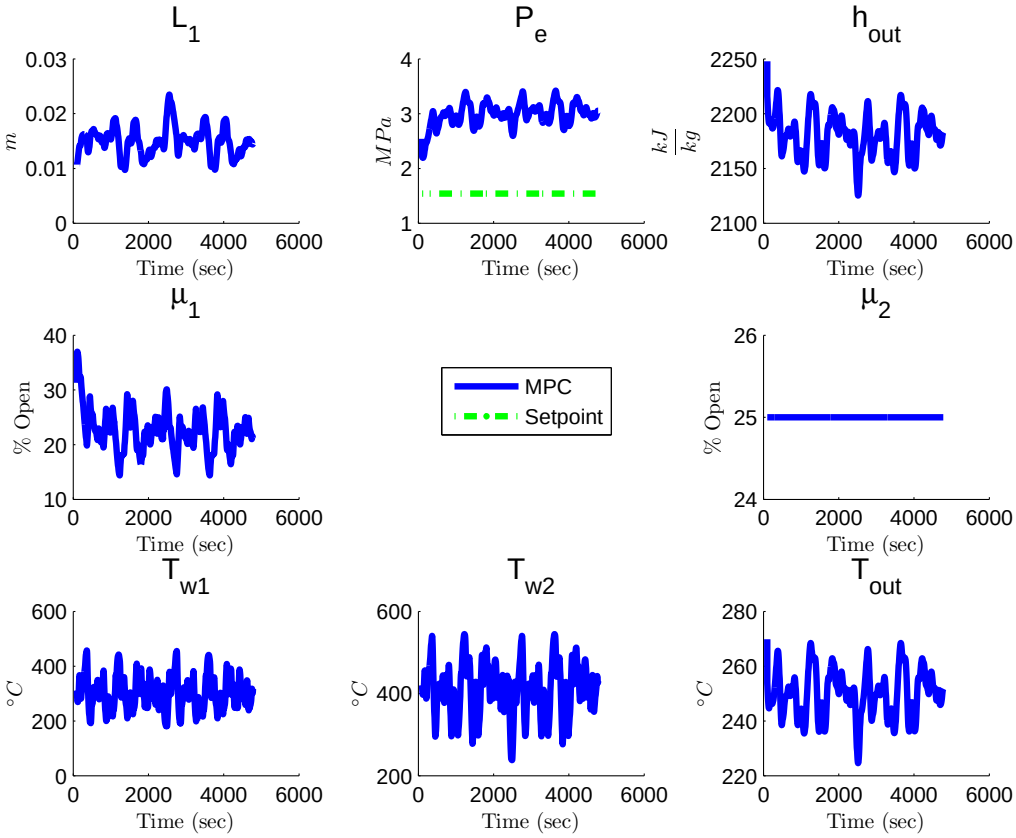

Figure 7.42: Nonlinear RC with MPC Control (Actuator 2) under Rolling Hills Driving Cycle: Evaporator States

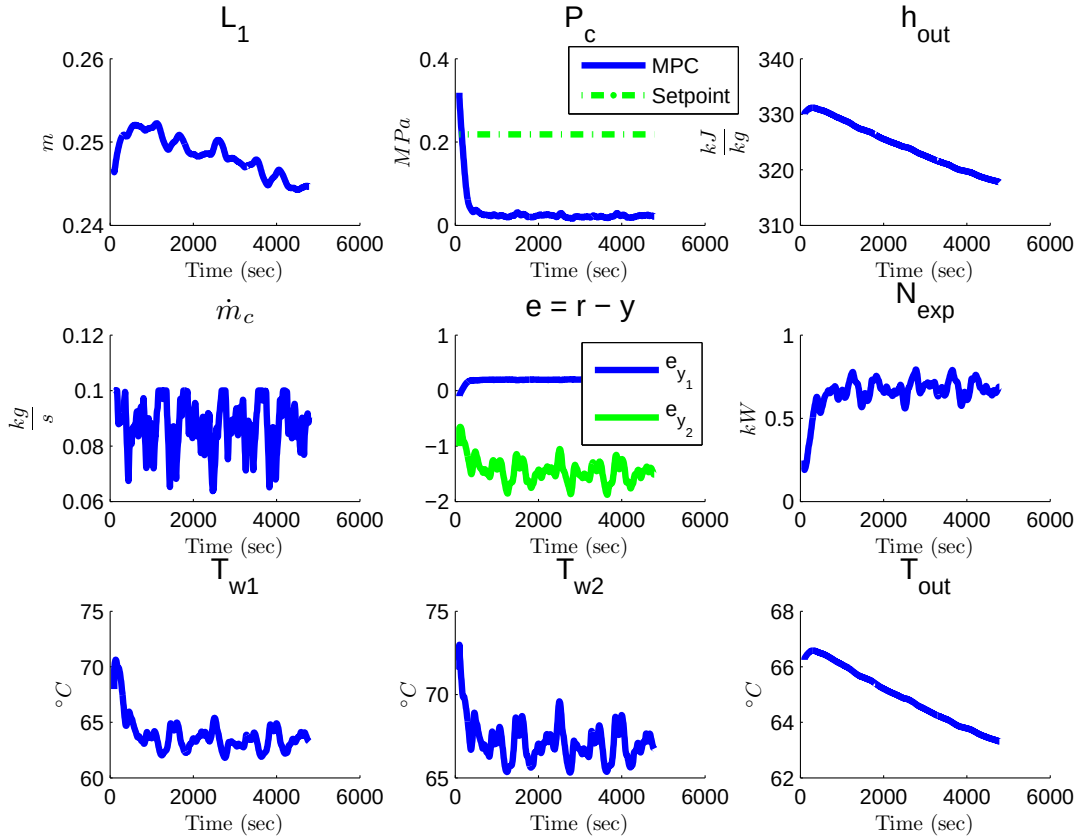

Figure 7.43: Nonlinear RC with MPC Control (Actuator 2) under Rolling Hills Driving Cycle: Condenser States

Figures 7.44 and 7.45 show results for Actuator Configuration 3 where the tracking performance is satisfactory with proper control action of the expander throttle valve.

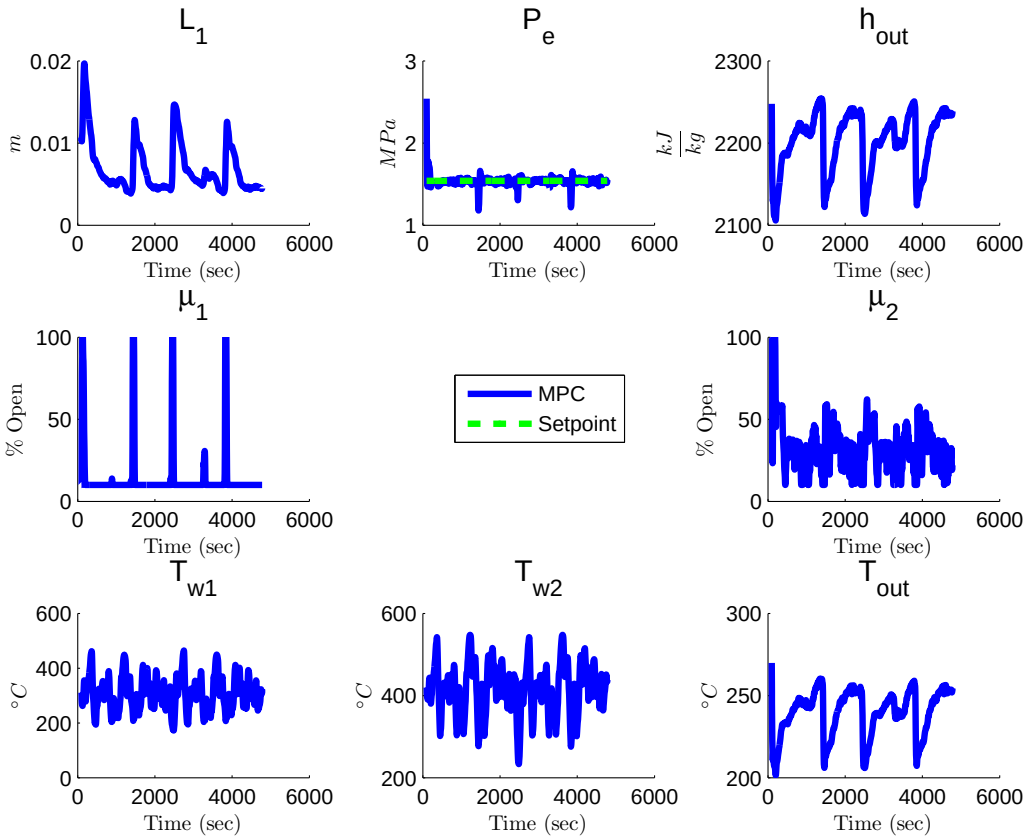

Figure 7.44: Nonlinear RC with MPC Control (Actuator 3) under Rolling Hills Driving Cycle: Evaporator States

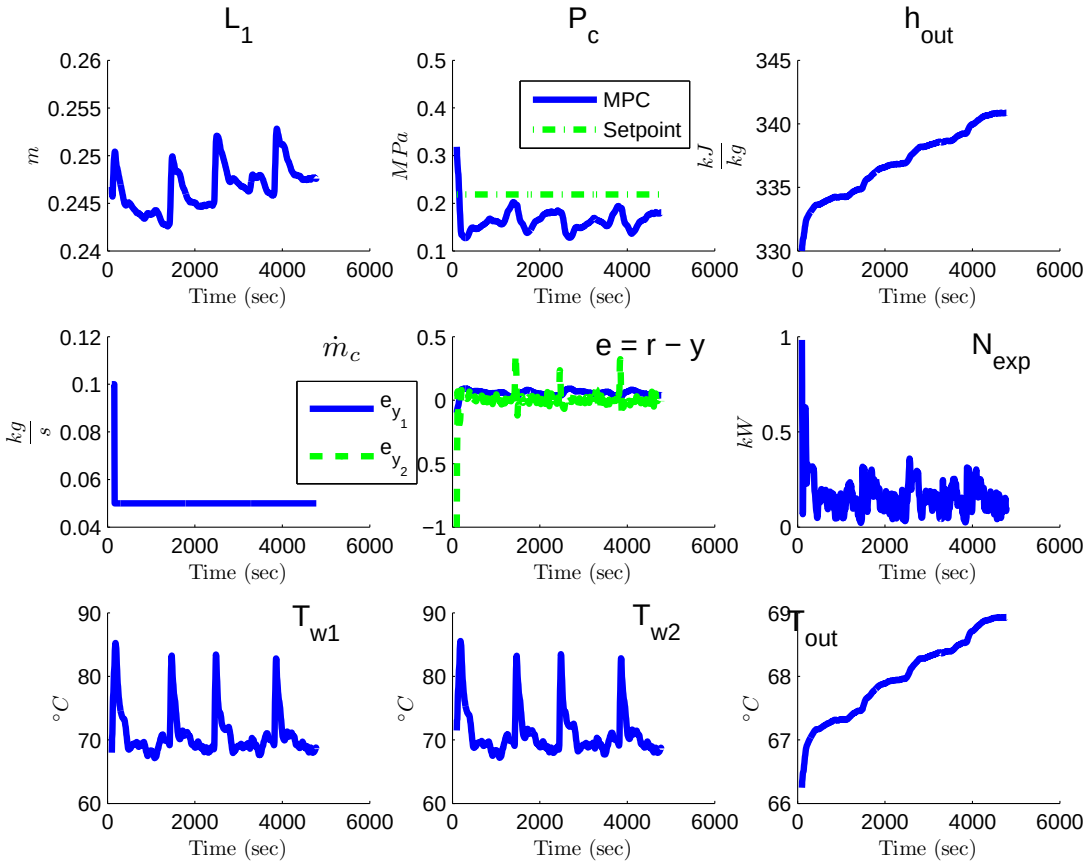

Figure 7.45: Nonlinear RC with MPC Control (Actuator 3) under Rolling Hills Driving Cycle: Condenser States

Better tracking performance is achieved by leveraging the anticipative feature in MPC as shown in Figures 7.46 and 7.47. The look-ahead feature takes corrective action at each time step when variables are predicted to break their constraints within the prediction horizon interval.

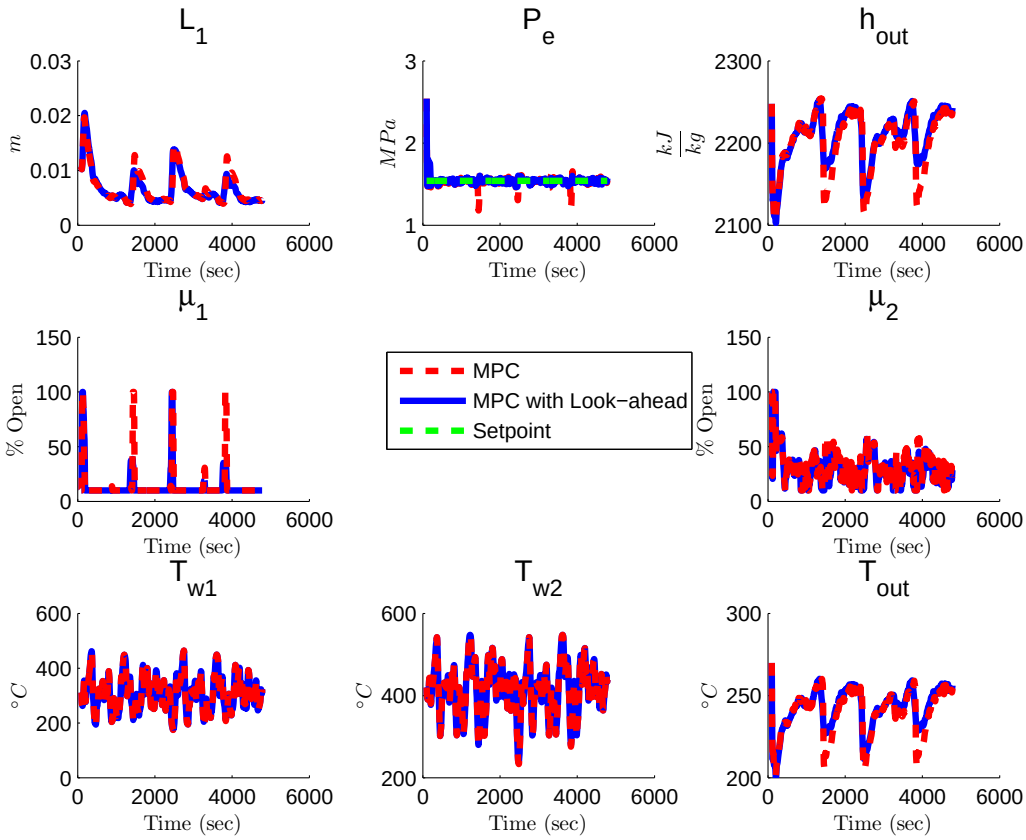

Figure 7.46: Nonlinear RC with Anticipative MPC Control (Actuator 3) under Rolling Hills Driving Cycle: Evaporator States

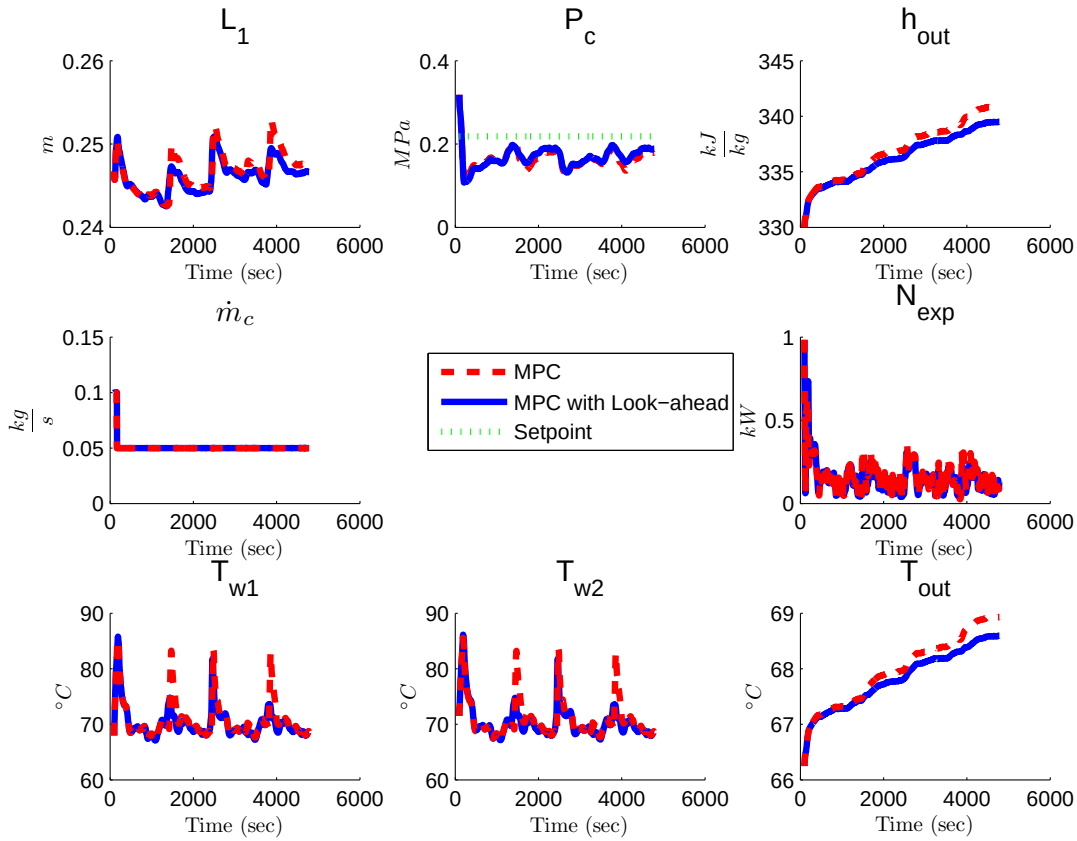

Figure 7.47: Nonlinear RC with Anticipative MPC Control (Actuator 3) under Rolling Hills Driving Cycle: Condenser States

7.5.9 Controller Comparison

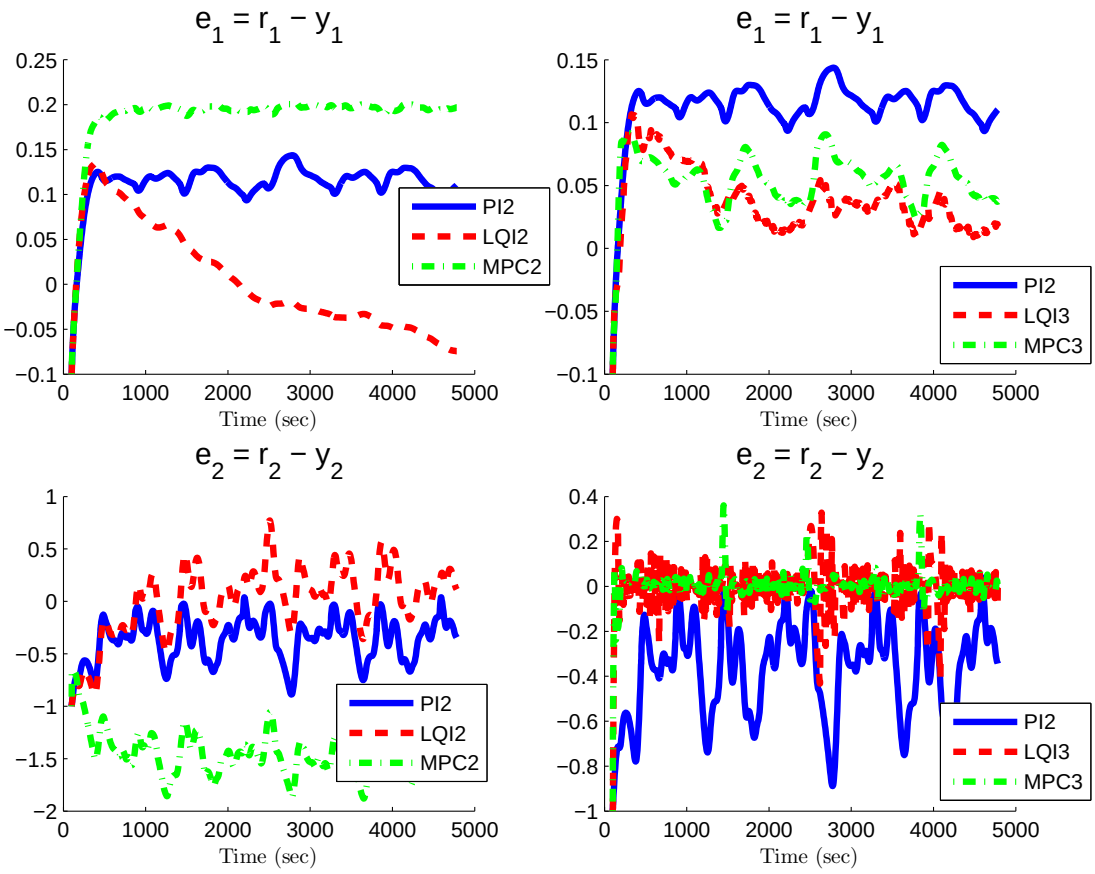

Figure 7.48: Control Tracking Error of Nonlinear RC under Rolling Hills Driving Cycle

Figure 7.48 compares the tracking errors of the two advanced controllers (LQI and MPC) to a PI controller. The PI controller assumes Actuator Configuration 2 while the advanced controllers assume either Configuration 2 or 3. The PI, LQI2, and MPC2 controllers are unable to remove the steady-state tracking error due to the heat source transients. However, the MPC3 controllers reduce the tracking error significantly better than the other controllers, especially for the

$y_2(P_e)$ variable.

Even with the look-ahead feature inactive, the MPC controllers have the best performance of the presented controllers.

Figure 7.49 compares the LQI controller with EKF state estimation feedback. The same conclusions can be made as in the perfect state access case for the LQI, though the tracking errors are more oscillatory due to the use of the EKF's Approximated Jacobian.

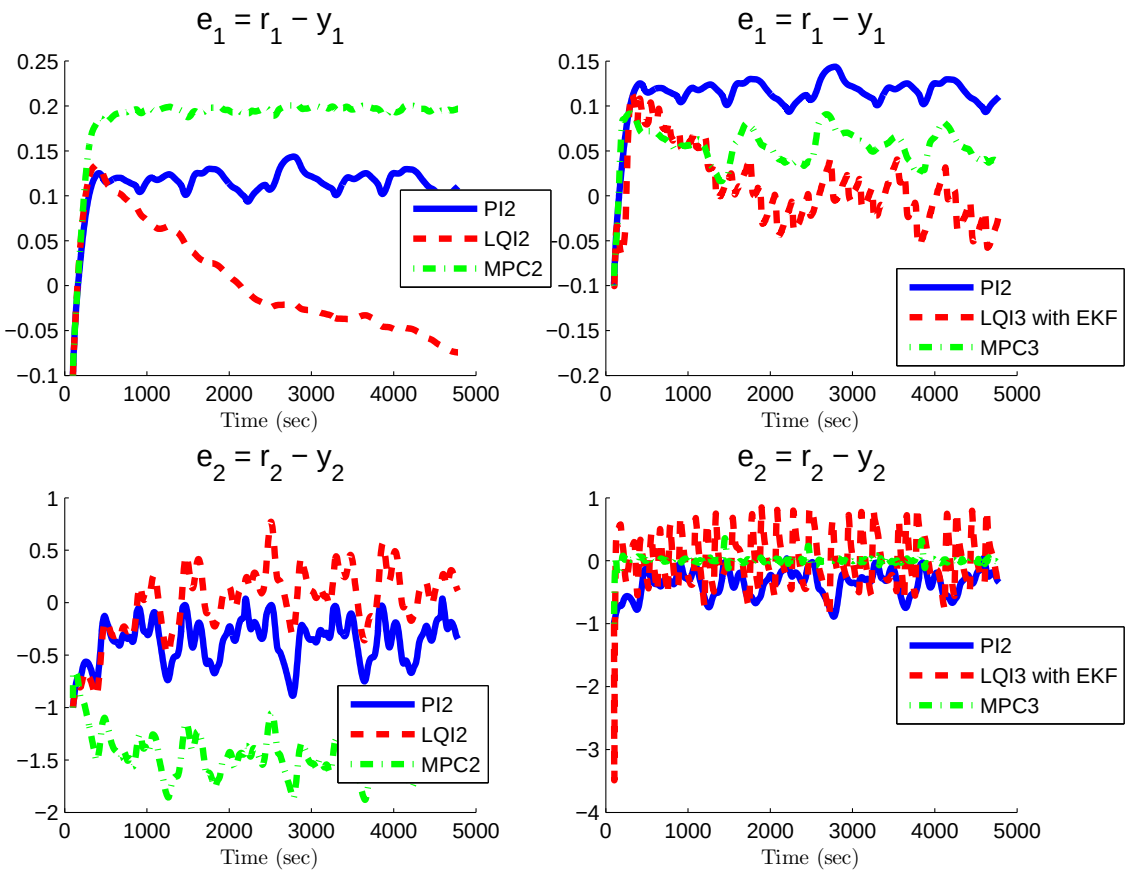

Figure 7.49: Control Tracking Error of Nonlinear RC under Rolling Hills Driving Cycle

7.5.10 Remarks

This architecture has been used in automotive WHR and provides opportunities for control design to meet operating constraints and objectives under driving disturbances. Maximum power is the WHR goal while satisfying temperature, pressure, and phase-change boundary ranges. Transients came from heat source temperature and flow rate disturbing the evaporator and engine crankshaft speed coupled to the pump and expander. The goal of controls is to maintain these operating constraints through regulation.

In an effort to understand the minimum number of and ideal actuators to meet the constraints and objectives, different control feedback and actuator configurations were examined. The control feedback configuration comprised of pressures while actuator configurations involved throttle valve positions and heat sink flow rate.

Pressure regulation achieved mixed success in driving the pressures to their respective setpoints. In PI control, pairing each pressure with an actuator to form control feedback loops resulted in steady-state tracking error. Depending on the configuration, advanced controls in the form of LQI did not necessarily improve the tracking error. The LQI controller with the same actuator configuration as PI did not conclusively lead to better tracking error. However, adding an extra actuator to the LQI controller significantly reduced the tracking error. This suggests controllability of the system improved with the extra actuator.

It should be noted that although PI control was not successful for regulation in the Dual Valve RC Architecture, the controller performed well in the Single Valve RC Architecture. The reason(s) for this is not discussed in this dissertation but could include differences in actuators configuration and operating conditions.

Model Predictive Control attempts to improve tracking performance by solving

constrained optimization problems at each time interval. The updated control law from the receding horizon approach is expected to perform better than the infinite-horizon LQI that also lacks the predictive capability. The results in fact supported these benefits of MPC by better regulating the pressures with and without the look-ahead feature.

With state estimation, other feedback configurations are possible that are not explored in this dissertation. Controllability and feasibility, and their existence, are topics of future research activities.

The expander power generated in the simulations are comparable to the power range established from static RC model design 2 found in Chapter 4.

7.6 Base Loading and Power Load Following

Conventional power plants for electric generation can either operate at base load, peaking, or load following depending on the application and objective. Base load power plants operate most efficiently and cost-effectively at maximum output and only reduce their power for maintenance or repair. Peaking power plants, on the other hand, only operate during periods of peak demand. In regions with widespread air conditioning use, demand peaks mid-afternoon, so peaking power plants may start-up and shutdown a few hours before and after, respectively, to meet the demand. In between base and peaking power plants are load following plants that track a known or predictable time-varying load demand.

Like conventional power plants, RC applications may either call for base load, peaking or power load following operation. Automotive WHR typically desires maximum power recovery to contribute mechanical torque to the engine drivetrain as often as possible. Time-varying, demand-based operation here would make little

sense. However, if the power recovery is used to run vehicle accessories like air conditioning or lights at anticipated periods of times e.g. hot humid days or night time driving, then peaking or load following mode might be useful. Also, without an energy storage device such as batteries, the recovered power must be used immediately or else wasted. Base loading here makes little sense while peaking or load following appear more appropriate.

Consequently, some RC applications must be operated as a peaking or load following power plant. For solar or geothermal RCs used to power home air conditioning compressors, the demand peaks in the afternoon and can vary based on the amount of cooling requested. Due to the varying demand, the RCs are operated in power load following mode.

This section examines base load as well as load following power plants. Constant and time-varying demand loads are given to the RC's expander to follow, the former representing base loading and the latter power load following. The power plant operation is to maintain pressure setpoints, so a pair of PI controllers are used for pressure regulation. The results demonstrate proper pressure regulation to setpoint while performing base load and load following operations.

7.6.1 Controller Design

Three independent Proportional Integral loops are designed for regulation control of pressures and expander power.

The controllers regulate the RC to the setpoint r by minimizing the regulation error

$$e_1 = r - y$$

where $y = [P_c \quad P_e \quad N_{exp}]^T$ and r is the corresponding vector of setpoints for each

output signal.

The anti-windup feature minimizes the saturation error e_2 due to exceeding actuator limits. The saturation error is given by

$$e_2 = \left\{ \begin{array}{ll} 0 & \text{if } u_{sat,low} \leq u \leq u_{sat,high} \\ u - u_{sat_high} & \text{if } u > u_{sat,high} \\ u - u_{sat_low} & \text{if } u < u_{sat,low} \end{array} \right\} \tag{7.30}$$

The back-calculating anti-windup PI controller is mathematically expressed as

$$u_m = [\dot{m}_c \quad \mu_1 \quad \mu_2]^T = b + k_p e_1 + \int (k_i e_1 + k_b e_2) dt \tag{7.31}$$

The disturbance input u_d due to heat source and sink conditions is given by

$$u_d = [T_{h,in} \quad \dot{m}_h \quad T_{c,in}]^T \tag{7.32}$$

The gains are tuned using the PID Tuner in MATLAB's Simulink environment [Inc].

Controller	Parameters	Actuator	Feedback Signal	Sat. Limits
C_1	$b = 0.5, k_p = 333$	μ_1	P_e	$[0, 1]$
	$k_i = 10, k_b = 1$			
C_2	$b = 1.5, k_p = 0.1$	$\dot{m}_c$	P_c	$[0, 4.5]$
	$k_i = 0.1, k_b = 1$			
C_3	$b = 05., k_p = 0.2602$	μ_2	N_{exp}	$[0, 1]$
	$k_i = 8.8241, k_b = 1$			

Table 7.12: Proportional Integral Controller Design Parameters for Dual Valve Architecture Power Load Following

7.6.2 Simulations

The following simulations show the following power demand cases:

1. Base Loading
    (a) Constant
    (b) Maximum
2. Power Load Following
    (a) Square Wave
    (b) Sinusoidal Wave

The heat source used in the simulations are from a driving cycle given in Table 7.13 though other transient may be used.

	Value	Units
T_h	450	$°C$
$\dot{m}_h$	0.062	$\frac{kg}{s}$
T_c	100	$°C$
ω	1500	RPM

Table 7.13: Constant RC Heat Source and Sink Conditions

In each of the above base and peak loading cases, the constraints in Table 7.14 are imposed.

Variable	Low Limit	High Limit	Units
P_e	4 (s)	6 (h)	MPa
P_c	0.1 (h)	-	MPa
$L_{1,e}$, L_{1c}	0 (h)	0.7 (h)	m
$T_{out,e}$	$T_{sat,g}$(h)	300 (s)	$^{\circ}C$
$T_{out,c}$	-	$T_{sat,f}$, 70 (for oil separation) (h)	$^{\circ}C$

Table 7.14: RC Constraints for Base Loading and Power Load Following: (s)oft, (h)ard

7.6.2.1 Pressure Regulation without Power Load Following

Figures 7.50-7.53 seek to regulate evaporating and condensing pressures without any tracking in power for Constant and Rolling Hills driving cycles. The expander throttle valve is set to 25% open for both cases. The controllers meet both pressure setpoints and show expander pressure is slightly below 1 kW.

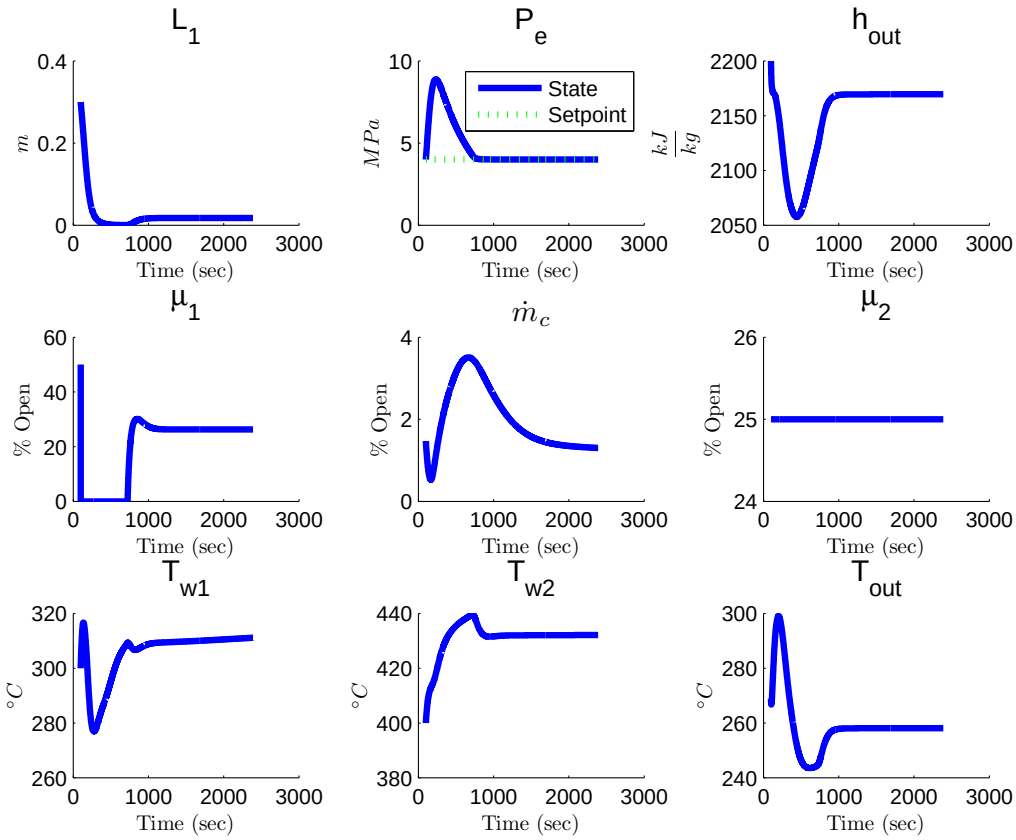

Figure 7.50: Nonlinear RC without Power Load Following under Constant Driving Cycle: Evaporator

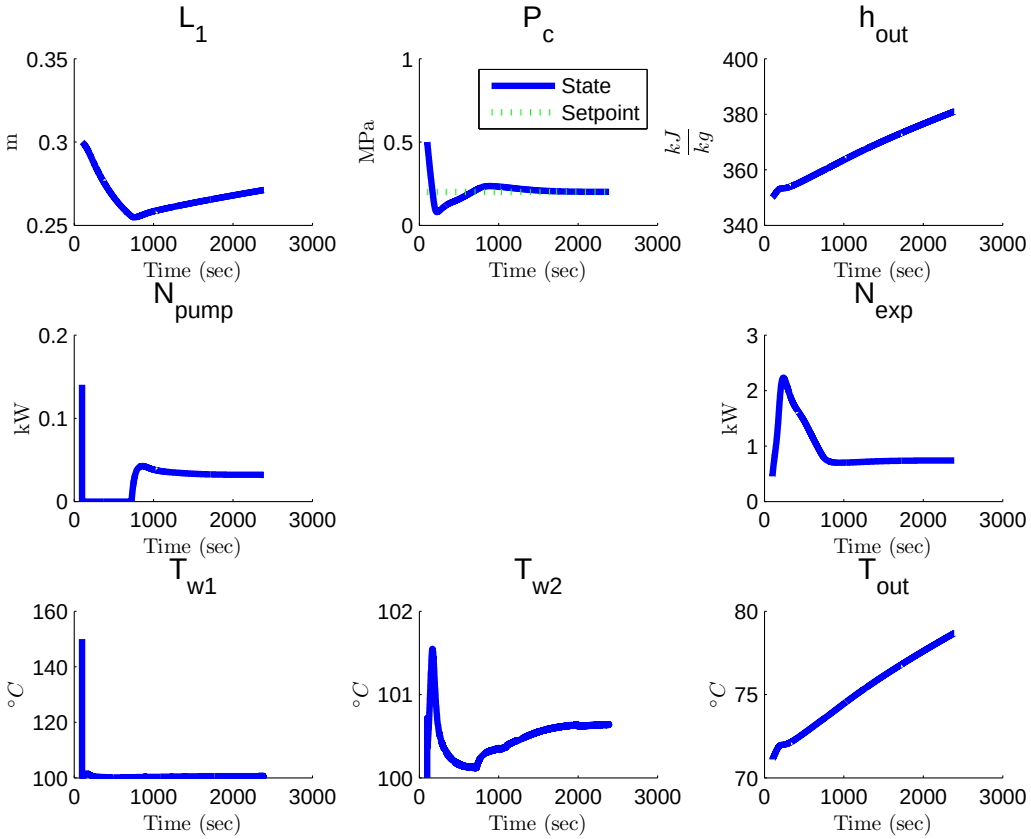

Figure 7.51: Nonlinear RC without Power Load Following under Constant Driving Cycle: Condenser

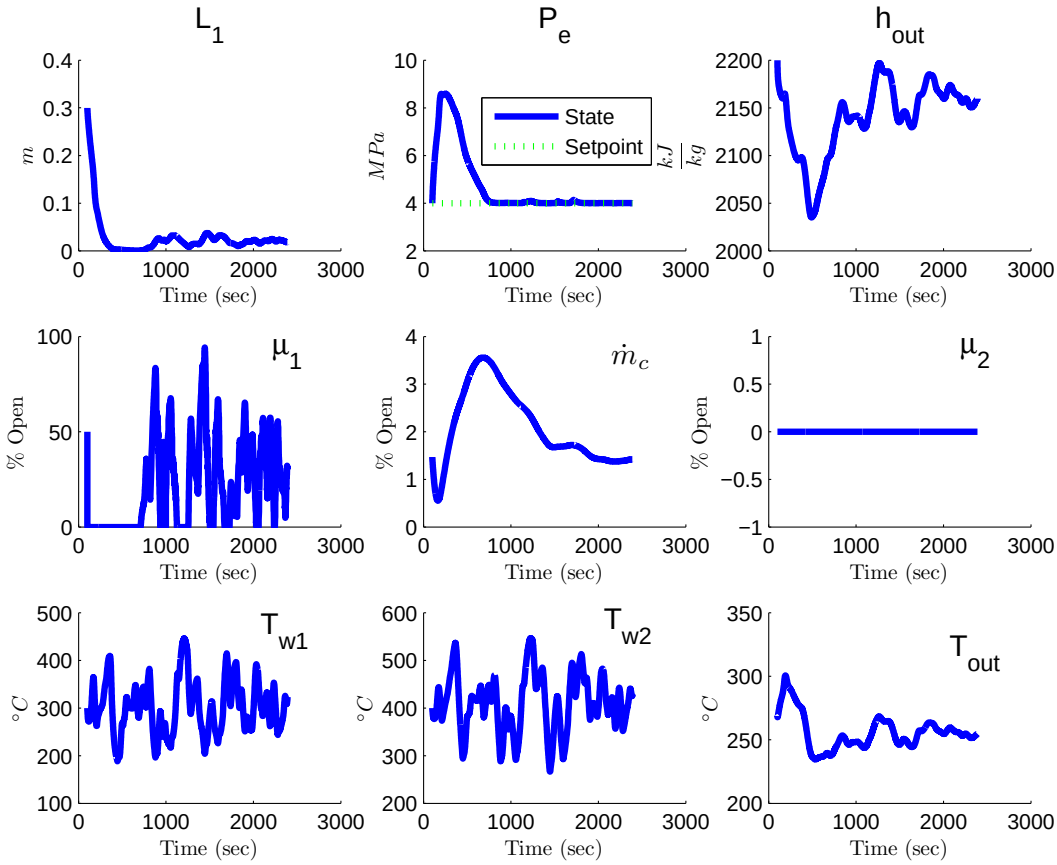

Figure 7.52: Nonlinear RC without Power Load Following under Rolling Hills Driving Cycle: Evaporator

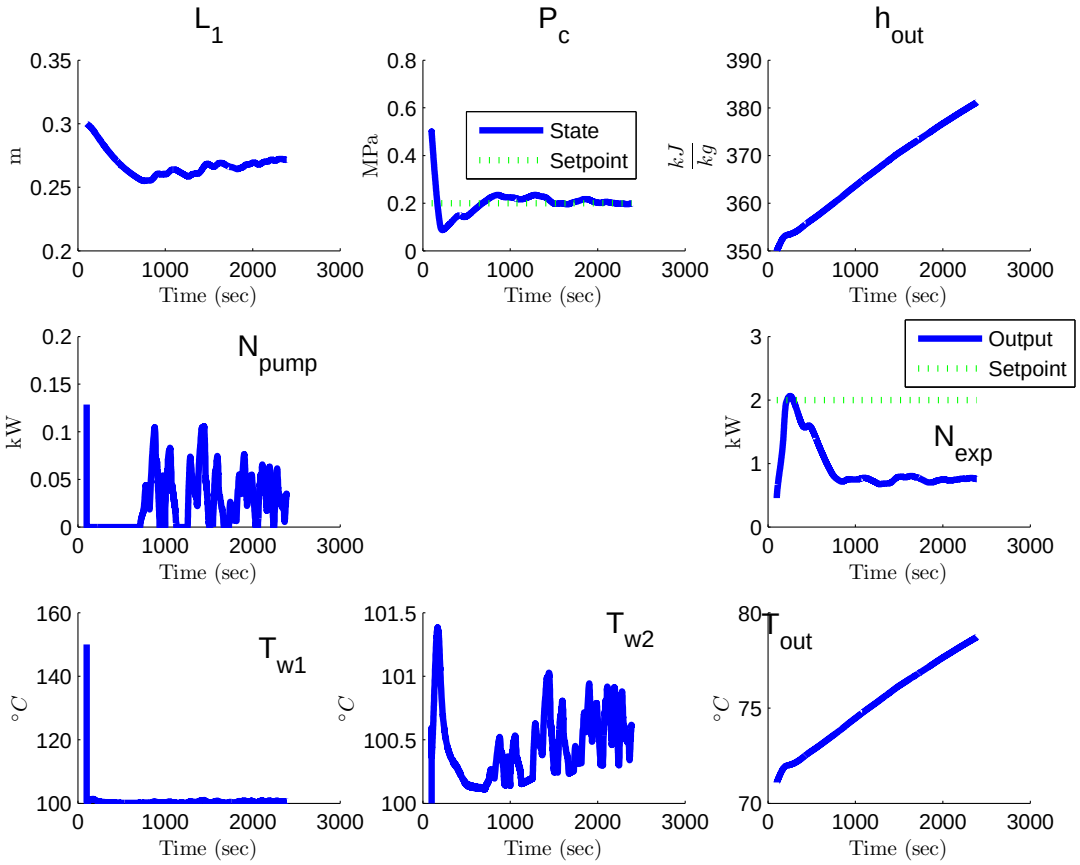

Figure 7.53: Nonlinear RC without Power Load Following under Rolling Hills Driving Cycle: Condenser

7.6.2.2 Base Load Following

Figures 7.54 and 7.55 attempt to provide 1 kW of base load while maintaining pressure setpoints.

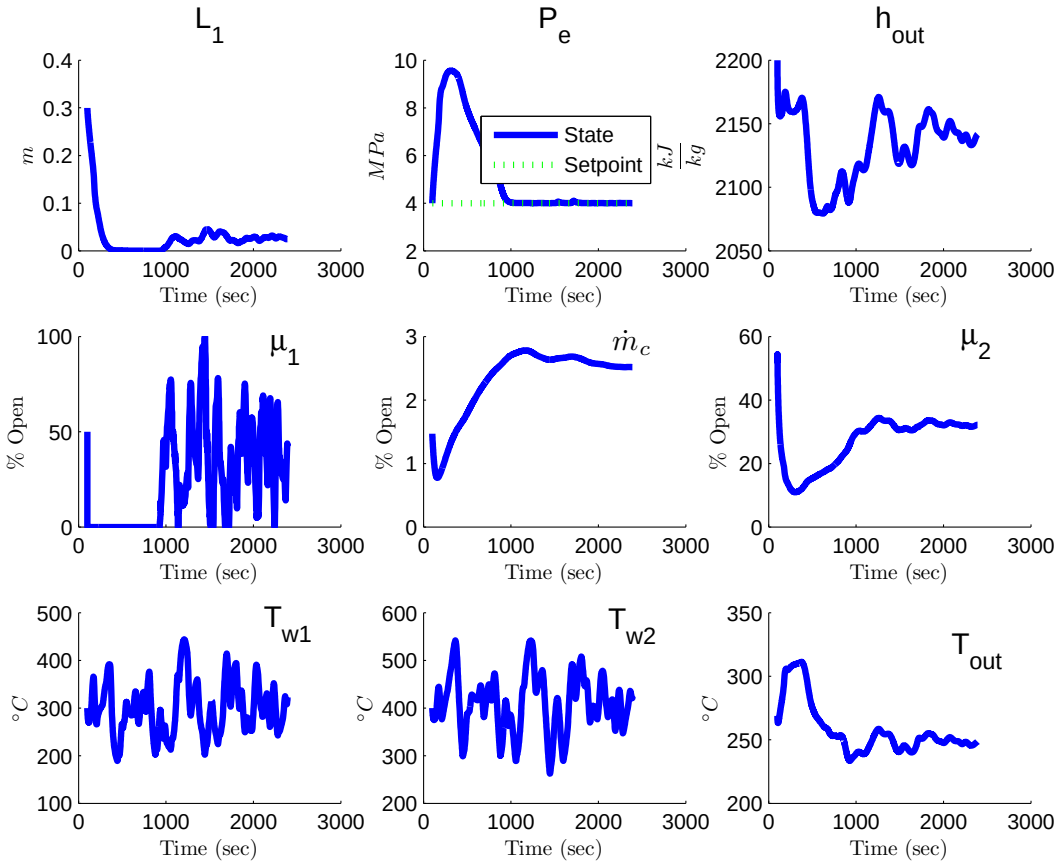

Figure 7.54: Base Load Following [$N_{exp} = 1$] for Nonlinear RC under Rolling Hills Driving Cycle: Evaporator

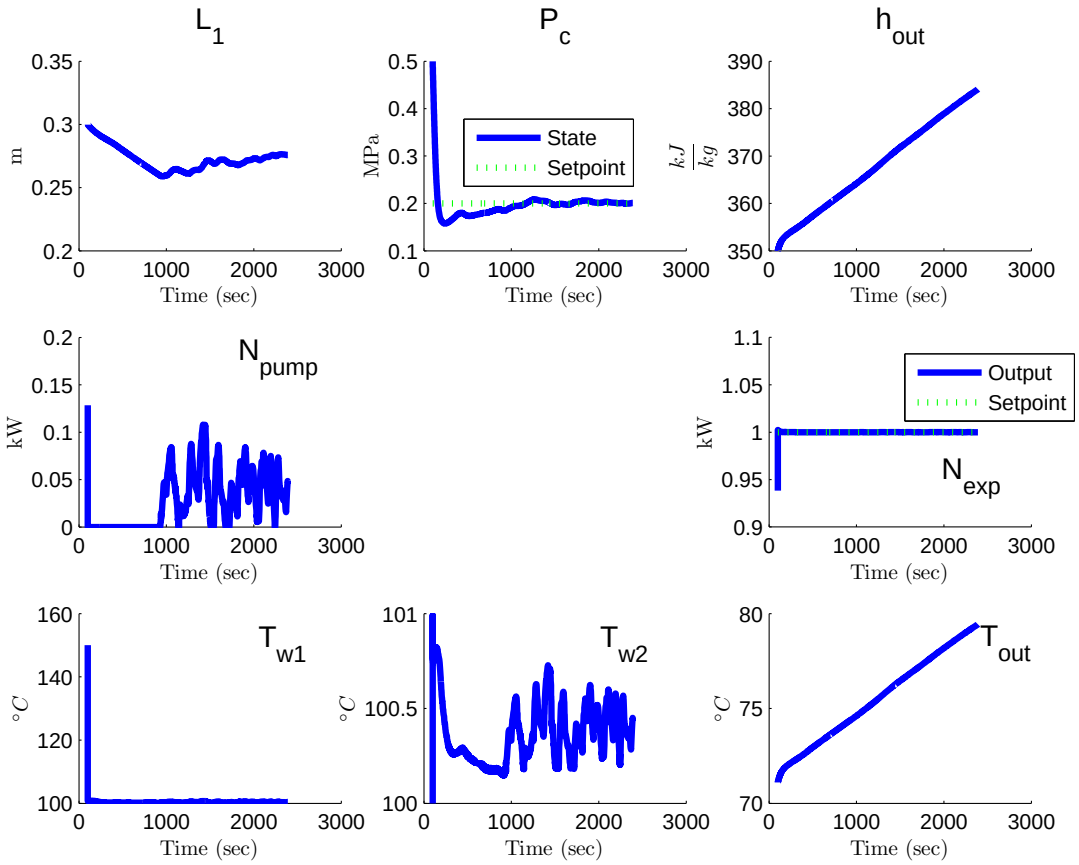

Figure 7.55: Base Load Following [$N_{exp} = 1$] for Nonlinear RC under Rolling Hills Driving Cycle: Condenser

Figures 7.56 and 7.57 show power demand of 10 kW that the RC is unable to supply. The simulations show both pressures also do not reach their setpoints while providing the most power possible.

By setting an unachievable demand, the RC is operating at full load. Note the expander throttle position is fully open to achieve maximum power while the pump throttle position varies to meet the evaporating pressure setpoint.

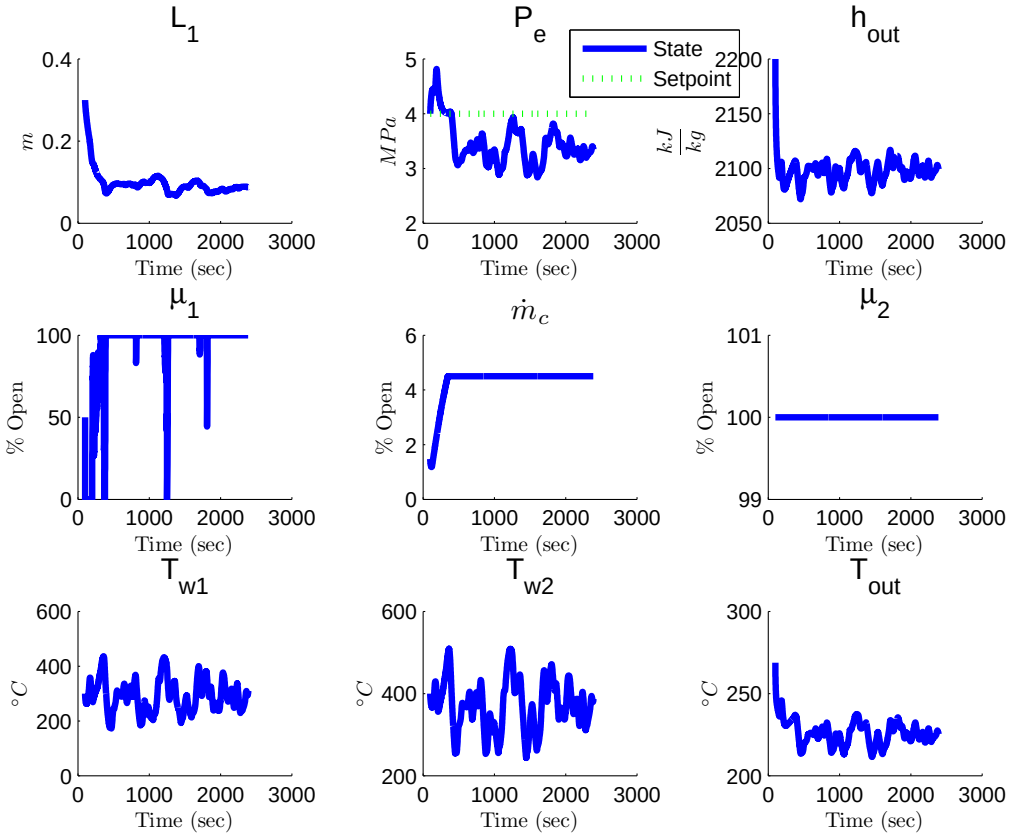

Figure 7.56: Base Load Following [$N_{exp} = 10$] for Nonlinear RC under Rolling Hills Driving Cycle: Evaporator

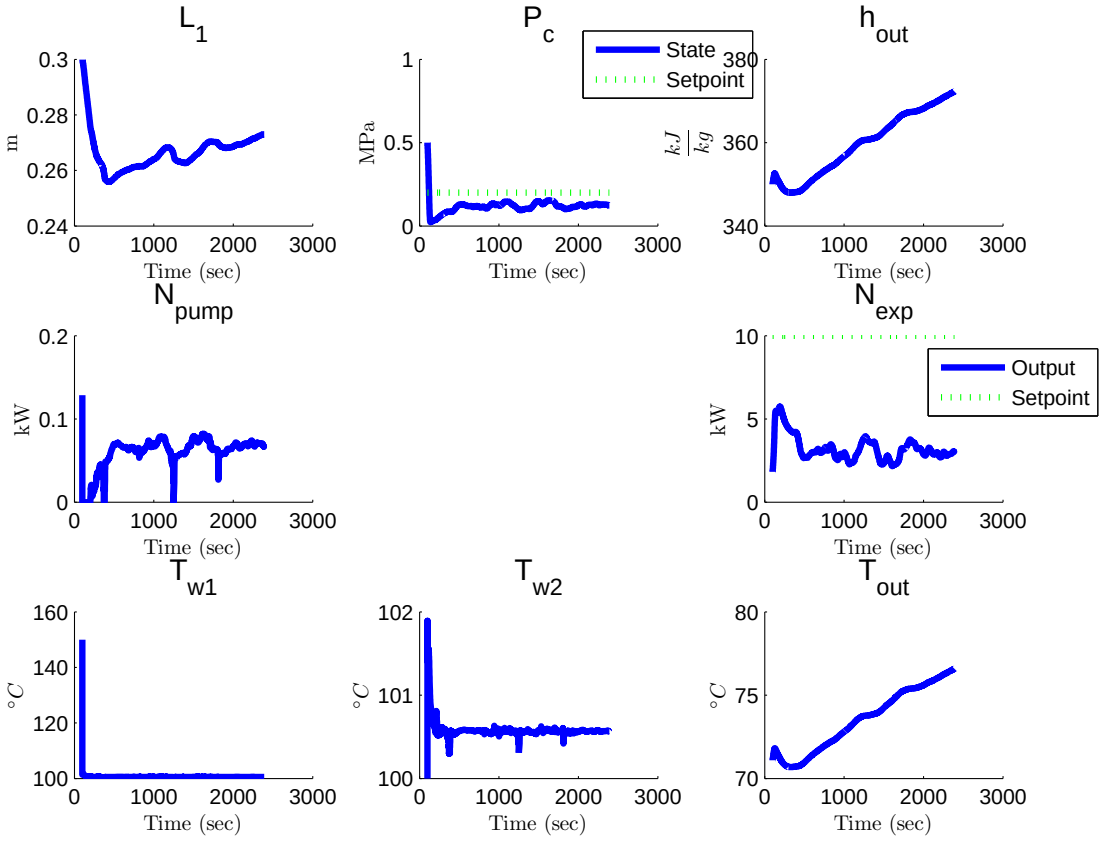

Figure 7.57: Base Load Following [$N_{exp} = 10$] for Nonlinear RC under Rolling Hills Driving Cycle: Condenser

7.6.2.3 Power Load Following

Square-wave and sinusoidal power demands are tracked in this section. Both simulations reveal a stronger coupling to the condensing pressure than to the evaporating pressure. In Figures 7.58 and 7.60, the evaporating pressure reaches its setpoint. Square-wave and sinusoidal features are evident in the condensing pressure around its setpoint in Figures 7.59 and 7.61 and suggest that power tracking affects condensing pressure tracking. For large enough amplitudes in

power demand, the condensing pressure may fall below atmospheric pressure and experience undesirable vacuum conditions.

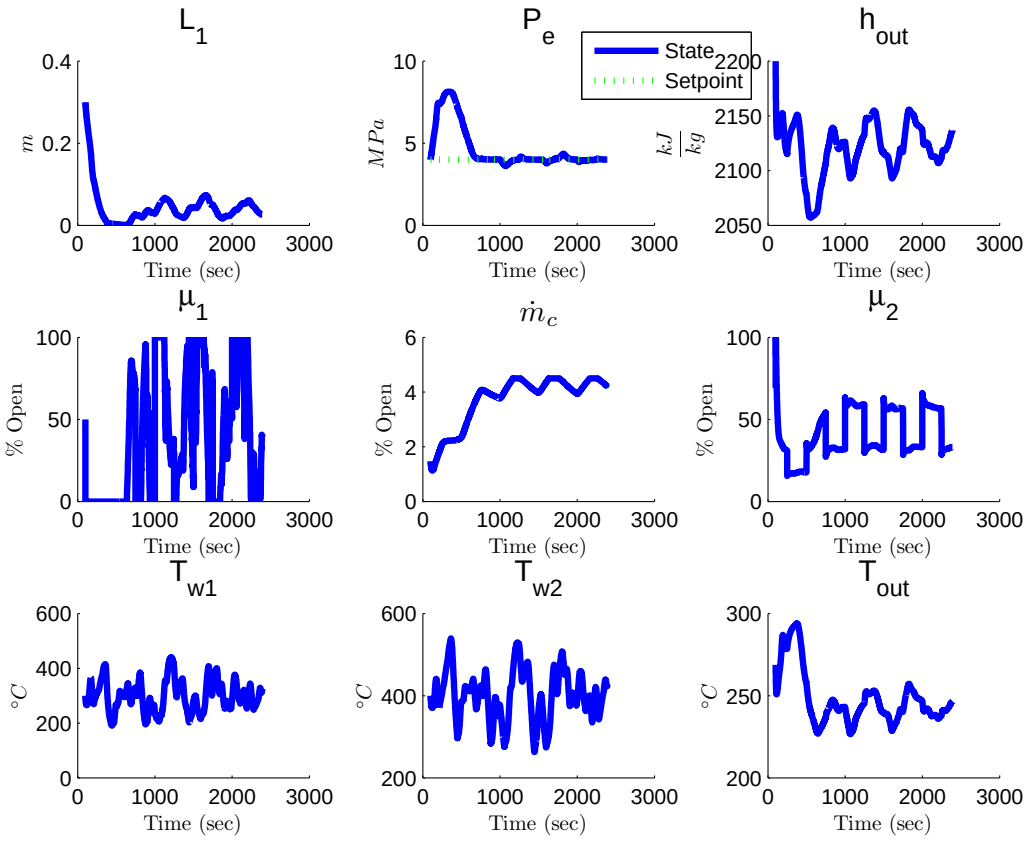

Figure 7.58: Power Load Following [Square-waveN_{exp}] for Nonlinear RC under Rolling Hills Driving Cycle: Evaporator

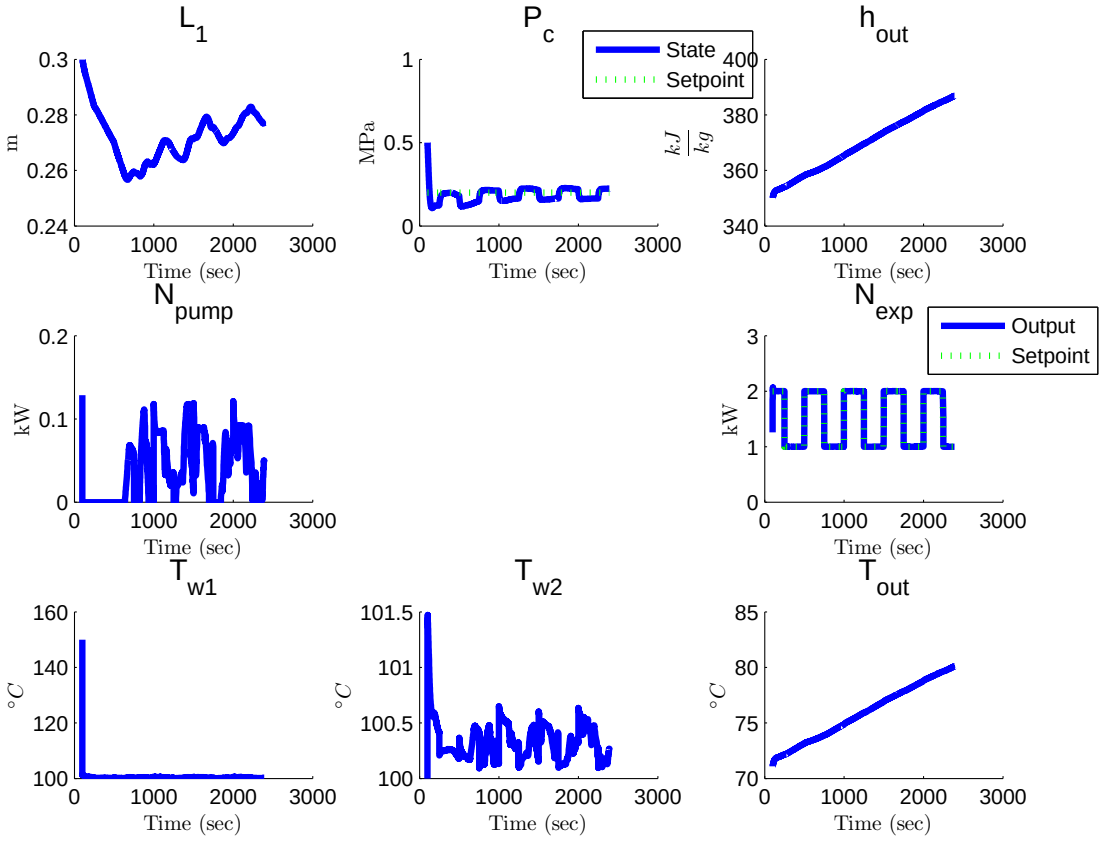

Figure 7.59: Power Load Following [Square-waveN_{exp}] for Nonlinear RC under Rolling Hills Driving Cycle: Condenser

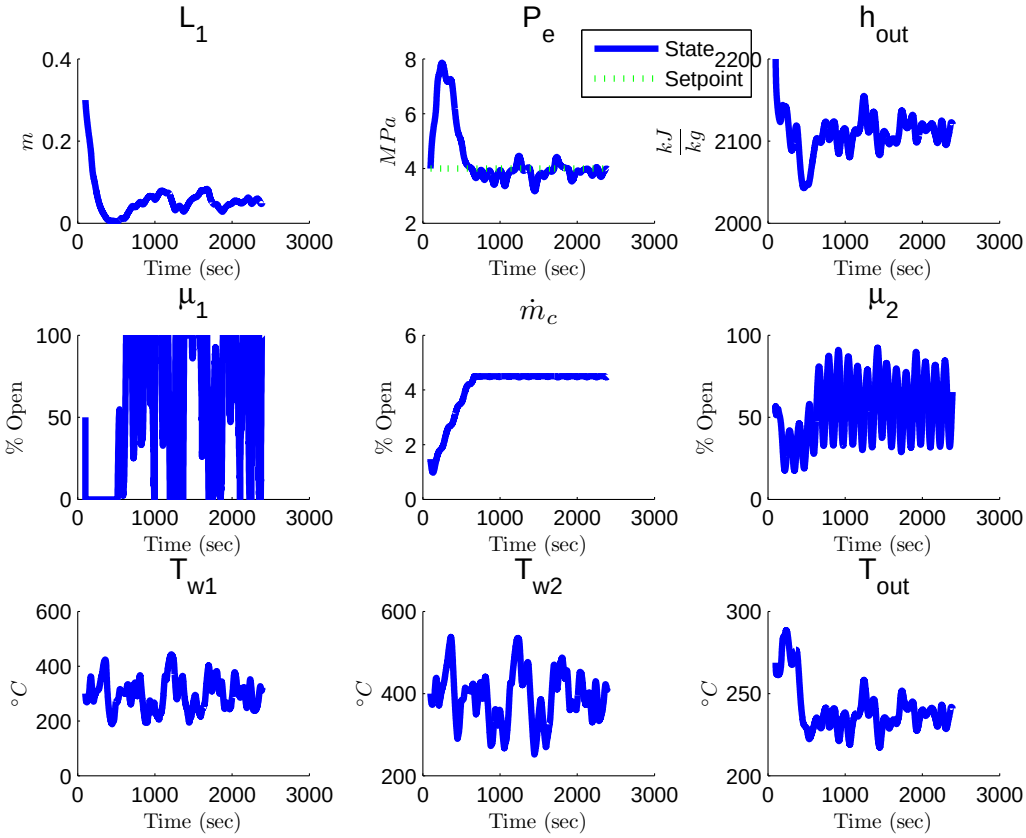

Figure 7.60: Power Load Following [SinusoidalN_{exp}] for Nonlinear RC under Rolling Hills Driving Cycle: Evaporator

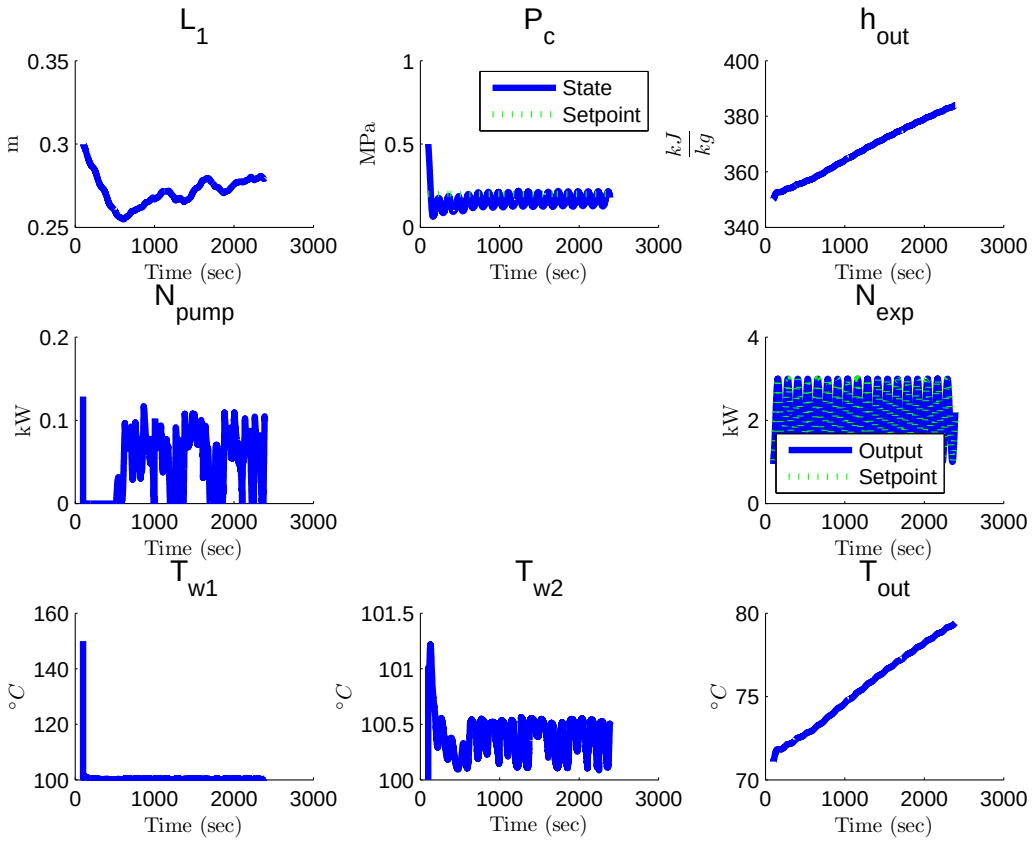

Figure 7.61: Power Load Following [SinusoidalN_{exp}] for Nonlinear RC under Rolling Hills Driving Cycle: Condenser

Similar to the case without power tracking, the evaporating pressure cannot be controlled in the beginning of each simulation. The pump throttle position is in the closed position during this time. The absence of working fluid flow in the evaporator leads to its pressure increasing significantly.

7.6.3 Remarks

Proportional Integral (PI) control regulates heat exchanger pressures and expander power fairly well under base and power load following. Both constant and

time-varying power load demands are successfully tracked while meeting pressure setpoints.

In power load following, the pressure regulation performance slightly degrades at the expense of the expander tracking a load power demand. Power regulation seems to affect condensing pressure regulation more significantly than evaporating pressure. This is attributed to the expander throttle valve influencing both power and condensing pressure.

While the previous section showed improved tracking performance using advanced controllers for the same RC architecture, the PI controller performs fairly well for the specified operating and heat source/sink conditions presented in this section. The results suggest that advanced control may be a requirement for general operating conditions where PI may not perform well. Additionally, higher regulation performance may be needed for advanced controllers to meet although PI may be sufficient.

CHAPTER 8

Thermodynamic and Component Library

A library of the component models used in this research has been created for the purpose of simulating power cycle systems. The components can be used as-is for 52% Ethanol and 48% Water mixture, though the user can simulate for other working fluids as long as thermodynamic and transport properties are available. A fitting function routine is provided to least squares fit tabular properties to polynomial functions compatible with the component models. The following sections document the MATLAB functions and Simulink files for these components.

8.1 build_components.m

This file builds example models including evaporators, condensers, and expanders in MATLAB and loads the workspace to run the associating Simulink block models.

8.2 Evaporator Models

8.2.1 Three-Zone

8.2.1.1 Z3MBevapMain.m

This calculates and loads the required variables to the workspace to simulate the 3-zone evaporator model. The results are also loaded and displayed. Be sure to first load the heat source data and determine the equilibrium points prior to running the simulation model in `EGRevaporatorSim.mdl`.

8.2.1.2 Z3MBevap.m

This file generates the derivatives for the 3-zone nonlinear evaporator model for `EGRevaporatorSim.mdl`.

8.2.1.3 Z3MBevapReduced.m

This file generates the derivatives for the 3-zone nonlinear evaporator reduced model for `EGRevaporatorSimReduced.mdl`.

8.2.1.4 EGRevaporatorSim.mdl

This file simulates the 3-zone nonlinear evaporator model. Be sure to use `Z3MBevapMain.m` to generate the heat source and equilibrium point. Load the simulation data to plot the results afterwards.

8.2.1.5 EGRevaporatorSimReduced.mdl

This file simulates the 3-zone nonlinear evaporator reduced model. Be sure to use `Z3MBevapMain.m` to generate the heat source and equilibrium point. Load the simulation data to plot the results afterwards.

8.2.1.6 Z3MBevapLinear.m

Z3MBevapLinear.m is a MATLAB function that creates a 3-zone Moving Boundary Evaporator Linear Model for 52% Ethanol 48% Water mixture given user-defined geometry parameters. The function has the following syntax:

```
[A B Aevaplqr Bevaplqr xe ue u_t_evap u_evap ulqr_evap K Lobsv] =
Z3MBevapLinear(L, nT, Di, Do, wall_thickness,roadcycle)
```

The function inputs are:

1. length of heat exchanger, **L** (in meter)
2. number of tube bundles, **nT**
3. diameter of inner tube, **Di** (in meter)
4. diameter of outer tube (shell), **Do** (in meter)
5. thickness of inner tube wall, **wall_thickness** (in meter)
6. driving cycle heat source to test model, **roadcycle**

The function outputs are:

1. linear model `A` matrix

2. linear model `B` matrix
3. closed-loop linear model `A` matrix, `Aevaplqr`
4. closed-loop linear model `B` matrix, `Bevaplqr`
5. equilibrium state vector `xe`
6. equilibrium input vector `ue`
7. time vector of input vector for simulation plots, `u_t_evap`
8. input vector for simulation plots, `u_evap`
9. LQR input vector for simulation plots, `ulqr_evap`
10. LQR feedback gain matrix, `K`
11. observer gain matrix, `Lobsv`

This function calculates the linearized model of the 3-zone Moving Boundary model for evaporators described by

$$Z(x,u)\dot{x} = f(x,u) \tag{8.1}$$

where

$$x = \begin{bmatrix} L_1 \\ L_2 \\ P \\ h_{out} \\ T_{w1} \\ T_{w2} \\ T_{w3} \end{bmatrix} \quad u = \begin{bmatrix} \dot{m}_{in} \\ \dot{m}_{out} \\ h_{in} \\ \dot{h}_{in} \\ T_h \\ \dot{m}_h \end{bmatrix}$$

The linear model is described by

$$\delta\dot{x} = A\delta x + B\delta u \tag{8.2}$$

where

$$A = Z^{-1}\frac{\delta f}{\delta x}\Big|_{x_e,u_e} \tag{8.3}$$

and

$$B = Z^{-1}\frac{\delta f}{\delta u}\Big|_{x_e,u_e} \tag{8.4}$$

and x_e,u_e is an equilibrium point that satisfy $f(x_e, u_e) = 0$. The working fluid is 52% Ethanol, 48% Water mixture.

Note: The `A` matrix may be unstable for specified geometry, use `eig(A)` to check stability.

A LQR control law `K` is designed for an evaporator model without uncontrollable states to minimize the pressure state. The controllable system is defined by matrices `Ac,Bc` with states

$$x_c = \begin{bmatrix} L_1 \\ L_2 \\ P \\ T_{w1} \\ T_{w2} \\ T_{w3} \end{bmatrix}$$

The LQR outputs are:

1. `Aevap` $= A_c - B_cK$, Bevap: the closed-loop matrices

2. K: the feedback gain matrix

3. `ulqr_evap` $= -Kx_c$, `u_t_evap`: the LQR control signal and its time series

An observer gain Lobsv is designed to estimate evaporator states using pole-placement with δP as measurement.

Plot(s) of the LQR controller and observer are displayed for a driving cycle simulation with EGR exhaust as the heat source.

Specify the variable `roadcycle` as a string from the following:

1. rolling

2. flat

3. hilly

8.2.1.7 MB3ZSS.m

This MATLAB function uses a nonlinear equation solver `fsolve` to calculate equilibrium points for 3-zone evaporator model with 52% ethanol 48% water mixture as the working fluid. `fsolve` interatively finds the state and input vector pair (x, u) such that $f(x, u) = 0$. Users can choose the geometry and initial conditions by editing the m-file.

The user should be cautious of no solutions using `fsolve`, indicating an equilibrium solution may not exist for the specified conditions and/or working fluid.

8.2.2 Temperature Dynamics Model

8.2.2.1 HXdTempSimSetup.m

This file loads the variables to the workspace for `HXdTempSim.mdl` to simulate a 3-zone evaporator model using transient data. Choose between Ricardo or Hagerstown experimental data. The file also plots the results of the simulation once it is completed.

8.2.2.2 dTemp.m

This file is used by `HXdTempSim.mdl` to generate the derivatives in the 3-zone temperature dynamics evaporator model.

8.2.2.3 HXdTempSim.mdl

This file simulates the 3-zone temperature dynamics evaporator model. Use `HXdTempSimSetup.m` to load the required variables to the workspace prior to simulation. Use the switches to select constant or transient inputs for the model.

8.3 Condenser Models

8.3.1 Three-Zone

8.3.1.1 MBCondSS.m

This file generates equilibrium solutions for the 3-zone nonlinear condenser model. Can also be used to generate initial conditions for `MB3ZCondenserSim.mdl`.

8.3.1.2 Z3MBcond.m

This file generates the derivatives for the 3-zone nonlinear condenser model for `MB3ZCondenserSim.mdl`.

8.3.1.3 MB3ZCondenserSim.mdl

This file simulates the 3-zone nonlinear condenser model based on `Z3MBcond.m` generating the derivatives. You may use `MBCondSS.m` to generate initial condition *xc*.

8.3.2 Two-Zone

8.3.2.1 Z2MBcondLinear.m

Z2MBcondLinear.m is a MATLAB function that creates a 2-zone Moving Boundary Condenser Linear Model for 52% Ethanol 48% Water mixture given user-defined geometry parameters. The function has the following syntax:

```
[A B xc uc u_t u] = Z2MBcondLinear(L, nT, Di, Do, thickness_wall)
```

The function inputs are:

1. length of heat exchanger, **L** (in meter)
2. number of tube bundles, **nT**
3. diameter of inner tube, **Di** (in meter)
4. diameter of outer tube (shell), **Do** (in meter)
5. thickness of inner tube wall, **wall_thickness** (in meter)

The function outputs are:

1. linear model `A` matrix
2. linear model `B` matrix
3. equilibrium state vector `xc`
4. equilibrium input vector `uc`
5. time vector of input vector for simulation plots, `u_t`
6. input vector for simulation plots, `u`

This function calculates the linearized model of the 2-zone Moving Boundary model for condensers described by

$$Z(x,u)\dot{x} = f(x,u) \tag{8.5}$$

where

$$x = \begin{bmatrix} L_1 \\ P \\ h_{out} \\ T_{w1} \\ T_{w2} \end{bmatrix} \quad u = \begin{bmatrix} \dot{m}_{in} \\ \dot{m}_{out} \\ h_{in} \\ T_c \\ \dot{m}_c \end{bmatrix}$$

The linear model is described by

$$\delta\dot{x} = A\delta x + B\delta u \tag{8.6}$$

where

$$A = Z^{-1}\frac{\delta f}{\delta x}\Big|_{x_c,u_c} \tag{8.7}$$

and

$$B = Z^{-1}\frac{\delta f}{\delta u}\Big|_{x_c,u_c} \tag{8.8}$$

and x_c, u_c is an equilibrium point that satisfies $f(x_c, u_c) = 0$. The working fluid is 52% Ethanol, 48% Water mixture.

Note: The A matrix may be unstable for specified geometry and/or nominal operating condition, use `eig(A)` to check stability.

Plot(s) of model is displayed for a sinusoidal disturbance of amplitude 0.025 kg/s in coolant flow rate.

8.3.2.2 Z2MBcondLinearTPSC.mdl

This Simulink file runs the 2-zone condenser linear model built using `Z2MBcondLinear.m`.

8.3.2.3 MB2ZSScond.m

This MATLAB function calculates equilibrium points for 2-zone condenser models.

8.4 Expander Models

8.4.1 Static

8.4.1.1 expander_static.mdl

This Simulink file runs an example static expander model described in Chapter 4 and [BM09].

8.4.2 Dynamic

8.4.2.1 expander_dynamic.mdl

This Simulink file runs an example dynamic 2-cylinder reciprocating piston expander model based on the ThermoBox MATLAB toolbox [Lim11].

The model inputs are:

1. engine speed, in revolutions per minute (RPM)
2. intake pressure conditions, in MPa
3. intake enthalpy conditions, in $\frac{kJ}{kg}$
4. exhaust pressure conditions, in MPa
5. exhaust enthalpy conditions, in $\frac{kJ}{kg}$

The function outputs are:

1. temperature of cylinder 1 `T1`, in K
2. mass of cylinder 1 `m1`, in kg
3. volume displacement of cylinder 1 `V1`, in m^3
4. crank angle of cylinder 1 `V1`, in degrees
5. temperature of cylinder 2 `T2`, in K
6. mass of cylinder 2 `m2`, in kg
7. volume displacement of cylinder 2 `V2`, in m^3

8. crank angle of cylinder 2 `V2`, in degrees

These variables are:

1. `Bore` diameter , in m
2. `Stroke`, in m
3. rod length `b`, in m
4. crank radius `c`, in m
5. connecting rod ratio, `Rod`, $\frac{c}{b}$
6. displaced volume `Vd`, in liters
7. dead volume `Vc`, in liters
8. compression ratio, `rc`
9. area of intake port, `Aintake`, in m^2
10. area of exhaust port, `Aexhaust`, in m^2
11. valve diameter for intake, `Vd_intake1`, in mm
12. valve diameter for exhaust, `Vd_exhaust1`, in mm
13. valve diamter for intake, `Vd_intake2`, in mm
14. valve diameter for exhaust, `Vd_exhaust2`, in
15. initial density in cylinder 1, `rho_i1`, in $\frac{kg}{m^3}$
16. initial density in cylinder 2, `rho_i2`, in $\frac{kg}{m^3}$
17. initial crank angle of cylinder 1, `theta_i1`, in degrees

18. initial crank angle of cylinder 2, `theta_i2`, in degrees
19. initial volume of cylinder 1, `V_i1`, in m^3
20. initial volume of cylinder 2, `V_i2`, in m^3
21. initial mass of cylinder 1, `m_i1`, in kg
22. initial mass of cylinder 2, `m_i2`, in kg
23. initial temperature of cylinder 1, `T_i1`, in K
24. initial temperature of cylinder 2, `T_i2`, in K
25. theta1, calculated from `invVcrank.m`, in
26. theta2, calculated from `invVcrank.m`, in
27. lift profile data file, `liftCyl#.mat`, generated by Cyl#lift.m

Use `building_components.m` to load designed values to the workspace prior to simulation and plot figures for the work, power, torque, and engine improvement (based on average engine power and torque from selected driving cycle).

8.4.2.2 Cyl#lift.m

This function generates a lift profile for intake and exhaust valves as a function of crank angle. # denotes the cylinder number e.g. 1, 2, etc.

The function inputs are:

1. Area of intake valve opening `Ai`, in m^2
2. Area of exhaust valve opening `Ae`, in m^2

The function outputs are:

1. valve diameter for intake `Vd_intake`, in mm
2. valve diameter for exhaust `Vd_exhaust`, in mm
3. file of valve lift profile (mm) as a function of crank angle θ, in .mat file

8.4.2.3 Vcrank.m

This function returns the cylinder volume as a function of crank position in the same units as `Vd`.

The function inputs are:

1. crank position θ, in degrees
2. displaced volume `Vd`, in m^3
3. compression ratio, `rc`
4. connecting rod length, `R`, in m

The function outputs are:

1. cylinder volume `V`, in m^3

8.4.2.4 invVcrank.m

This function returns the two crank angle positions for a given displaced volume.

The function inputs are:

1. length of piston cylinder `L`, in m

2. bore diameter `B`, in m

3. stroke `S`, in m

4. compression ratio `rc`

5. connecting rod ratio `R`

The function outputs are:

1. first crank angle position θ_1, in degrees

2. second crank angle position θ_2, in degrees

8.5 Thermodynamic Properties

8.5.0.5 thermoProp2.m

This function determines thermodynamic properties for air at different states given independent properties of pressure and temperature. The function is designed for use in MATLAB.

The function input is the following:

1. pressure `p`, in Pa

2. temperature `T`, in K

The function output is a vector of the following in the same order:

1. density `rho`, in $\frac{kg}{m^3}$

2. internal energy `u`, in $\frac{J}{kg}$

3. enthalpy `h`, in $\frac{J}{kg}$
4. entropy `s`, in $\frac{J}{kgK}$
5. isochoric heat capacity `cv`, in $\frac{J}{kgK}$
6. isobaric heat capacity `cp`, in $\frac{J}{kgK}$
7. first derivative of pressure with respect to density `dp_drho`, in $\frac{Pa}{\frac{kg}{m^3}}$
8. first derivative of pressure with respect to temperature `dp_dT`, in $\frac{Pa}{K}$
9. speed of sound `w`, in $\frac{m}{s}$

8.5.0.6 Ethanol_H2O_52_48_thermoprop_Ph_simulink.m

This function determines thermodynamic properties for 52% Ethanol, 48% Water mixture at different states given independent properties of pressure and enthalpy. The function is designed for use in Simulink.

The function input is a vector of the following in the same order:

1. pressure `P`, in MPa
2. enthalpy `h`, in $\frac{kJ}{kg}$
3. `phase`, either 1 (subcooled), 2 (two-phase), or 3 (superheat)

The function output is a vector of the following in the same order:

1. density `rho`, in $\frac{kg}{m^3}$
2. temperature `T`, in K

8.5.0.7 Ethanol_H2O_52_48_thermoprop.m

This function determines thermodynamic properties for 52% Ethanol, 48% Water mixture at different states given independent properties of pressure and temperature. The function is designed for use in MATLAB.

The function inputs are the following in the same order:

1. temperature `T`, in K
2. pressure `P`, in MPa
3. `phase`, either 1 (subcooled), 2 (two-phase), or 3 (superheat)

The function outputs are the following in the same order:

1. density `rho`, in $\frac{kg}{m^3}$
2. enthalpy `h`, in $\frac{kJ}{kg}$
3. partial derivative of density with respect to pressure, in `dp_dP` $\frac{\frac{kg}{m^3}}{MPa}$
4. partial derivative of density with respect to enthalpy `dp_dh`, in $\frac{\frac{kg}{m^3}}{\frac{kJ}{kg}}$
5. internal energy `u`, in $\frac{kJ}{kg}$
6. partial derivative of internal energy with respect to pressure `du_dP`, in $\frac{\frac{kJ}{kg}}{MPa}$
7. partial derivative of temperature with respect to pressure `dT_dP`, in $\frac{K}{MPa}$
8. entropy `s`, in $\frac{kJ}{kgK}$
9. speed of sound `w`, in $\frac{m}{s}$
10. specific heat capacity, constant pressure `Cp`, in $\frac{kJ}{kgK}$

11. specific heat capacity, constant volume `Cv`, in $\frac{kJ}{kgK}$

12. liquid saturation temperature `Tsatf`, in K

13. vapor saturation temperature `Tsatg`, in K

8.5.0.8 Ethanol_H2O_52_48_thermoprop_simulink.m

This function determines thermodynamic properties for 52% Ethanol, 48% Water mixture at different states given independent properties of pressure and temperature. The function is designed for use in Simulink.

The function input is a vector of the following in the same order:

1. temperature `T`, in K

2. pressure `P`, in MPa

3. `phase,` either 1 (subcooled), 2 (two-phase), or 3 (superheat)

The function output is a vector of the following in the same order:

1. density `rho`, in $\frac{kg}{m^3}$

2. enthalpy `h`, in $\frac{kJ}{kg}$

3. partial derivative of density with respect to pressure $\frac{\frac{kg}{m^3}}{MPa}$

4. partial derivative of density with respect to enthalpy $\frac{\frac{kg}{m^3}}{\frac{kJ}{kg}}$

5. internal energy `u`, in $\frac{kJ}{kg}$

6. partial derivative of internal energy with respect to pressure $\frac{\frac{kJ}{kg}}{MPa}$

7. partial derivative of temperature with respect to pressure $\frac{K}{MPa}$

8. entropy `s`, in $\frac{kJ}{kgK}$
9. speed of sound `w`, in $\frac{m}{s}$
10. specific heat capacity, constant pressure `Cp`, in $\frac{kJ}{kgK}$
11. specific heat capacity, constant volume `Cv`, in $\frac{kJ}{kgK}$

8.5.0.9 Ethanol_H2O_52_48_thermoprop_Trho.m

This function determines thermodynamic properties for 52% Ethanol, 48% Water mixture either in superheat or subcooled states given independent properties of density and temperature. The function is designed for use in Simulink in conjuction with ThermoBox models.

The function input is a vector of the following in the same order:

1. density `rho`, in $\frac{kg}{m^3}$
2. temperature `T`, in K
3. phase, either 1 (subcooled) or 0 (superheat)

The function output is a vector of the following in the same order:

1. pressure `p`, in Pa
2. internal energy `u`, in $\frac{J}{kg}$
3. enthalpy `h`, in $\frac{J}{kg}$
4. entropy `s`, in $\frac{J}{kgK}$
5. isochoric heat capacity `Cv`, in $\frac{J}{kgK}$

6. isobaric heat capacity `Cp`, in $\frac{J}{kgK}$
7. partial derivative of pressure with respect to density at constant temperature `dP_dp`, in $\frac{Pam^3}{kg}$
8. partial derivative of pressure with respect to temperature at constant density `dP_dT`, in $\frac{Pa}{K}$
9. speed of sound `W`, in $\frac{m}{s}$

8.5.0.10 Ethanol_H2O_52_48_thermoprop_Ph.m

This function determines thermodynamic properties for 52% Ethanol, 48% Water mixture at different states given independent properties of pressure and enthalpy. The function is designed for use in MATLAB.

The function inputs are the following in the same order:

1. enthalpy `h`, in $\frac{kJ}{kg}$
2. pressure `P`, in MPa
3. `phase,` either 1 (subcooled), 2 (two-phase saturated liquid), 3 (two-phase saturated vapor), or 4 (superheat)

The function outputs is are the following in the same order:

1. density `rho`, in $\frac{kg}{m^3}$
2. entropy `s`, in $\frac{kJ}{kgK}$
3. partial derivative of density with respect to pressure `dp_dP` $\frac{\frac{kg}{m^3}}{MPa}$
4. partial derivative of density with respect to enthalpy `dp_dh` $\frac{\frac{kg}{m^3}}{\frac{kJ}{kg}}$

5. partial derivative of enthalpy with respect to pressure `dh_dP` $\frac{\frac{kJ}{kg}}{MPa}$
6. internal energy `u`, in $\frac{kJ}{kg}$
7. partial derivative of internal energy with respect to pressure `du_dP` $\frac{\frac{kJ}{kg}}{MPa}$
8. partial derivative of temperature with respect to pressure `dT_dP` $\frac{K}{MPa}$
9. temperature `T`, in K
10. speed of sound `w`, in $\frac{m}{s}$
11. specific heat capacity, constant pressure `Cp`, in $\frac{kJ}{kgK}$
12. specific heat capacity, constant volume `Cv`, in $\frac{kJ}{kgK}$
13. liquid saturation temperature `Tsatf`, in K
14. vapor saturation temperature `Tsatg`, in K

8.5.0.11 makeA.m

This function makes the A matrix in the least squares problem $Aq = z$.

The function inputs are:

1. first independent variable `x`
2. second independent variable `y`
3. maximum desired order `N`

The function output is:

1. matrix `A`

The entries of A are polynomial functions of x and y of the form $x^{n_x}y^{n_y}$ where n_x and n_y are exponent coefficients less than N. The size of A depends on the desired maximum order N.

8.5.0.12 thermoProp3_tank.m

This function determines thermodynamic properties for air (treated as an ideal gas) given independent properties of density and temperature. The function is designed for use in Simulink in conjuction with Thermobox models.

The function inputs are the following in the same order:

1. density `rho`, in $\frac{kmol}{m^3}$
2. temperature `T`, in K

The function output is a vector of the following in the same order:

1. pressure `p`, in MPa
2. isobaric heat capacity `Cp`, in $\frac{kJ}{kmolK}$
3. partial derivative of pressure with respect to density `dp_drho`, in $\frac{kPa}{\frac{kmol}{m^3}}$
4. partial derivative of pressure with respect to temperature `dp_dT`, in $\frac{kPa}{K}$
5. enthalpy `h`, in $\frac{kJ}{kmol}$
6. isochoric heat capacity `Cv`, in $\frac{kJ}{kmolK}$
7. internal energy `u`, in $\frac{kJ}{kmol}$
8. entropy `s`, in $\frac{kJ}{kmolK}$

8.5.1 Least Squares Fit Coefficients

8.5.1.1 flow_fit_param_ethanol_water_52_48_vapor_expanded_TP_Trho.mat

This MATLAB file contains the least squares fit coefficients q of thermodynamic properties for 52% Ethanol, 48% Water vapor mixture with temperature and pressure as independent properties. The properties are valid in the range of 20 to 240 $\frac{kg}{m^3}$ and 500 to 600 Kelvin.

Generate the A matrix using `makeA.m` to find other thermodynamic properties z by computing $z = Aq$.

8.5.1.2 flow_fit_param_ethanol_water_52_48_subcooled_expanded_TP_Trho.mat

This MATLAB file contains the least squares fit coefficients q of thermodynamic properties for 52% Ethanol, 48% Water subcooled mixture with temperature and pressure as independent properties. The properties are valid in the range of 420 to 1000 $\frac{kg}{m^3}$ and 280 to 600 Kelvin.

Generate the A matrix using `makeA.m` to find other thermodynamic properties z by computing $z = Aq$.

8.5.1.3 flow_fit_param_ethanol_water_52_48_vapor_Trho.mat

This MATLAB file contains the least squares fit coefficients q of thermodynamic properties for 52% Ethanol, 48% Water vapor mixture with temperature and pressure as independent properties. The properties are valid in the range of 20 to 40 $\frac{kg}{m^3}$ and 500 to 580 Kelvin.

Generate the A matrix using `makeA.m` to find other thermodynamic properties z by computing $z = Aq$.

8.5.1.4 flow_fit_param_ethanol_water_52_48_vapor_expanded_TP.mat

This MATLAB file contains the least squares fit coefficients q of thermodynamic properties for 52% Ethanol, 48% Water vapor mixture with temperature and pressure as independent properties. The properties are valid in the range of 0.01 to 10 MPa and 320 to 1200 Kelvin.

Generate the A matrix using `makeA.m` to find other thermodynamic properties z by computing $z = Aq$.

8.5.1.5 flow_fit_param_ethanol_water_52_48_subcooled_expanded_TP.mat

This MATLAB file contains the least squares fit coefficients q of thermodynamic properties for 52% Ethanol, 48% Water subcooled mixture with temperature and pressure as independent properties. The properties are valid in the range of 0.01 to 10 MPa and 250 to 550 Kelvin.

Generate the A matrix using `makeA.m` to find other thermodynamic properties z by computing $z = Aq$.

8.5.1.6 flow_fit_param_ethanol_water_52_48_twophase_f_expanded_TP.mat

This MATLAB file contains the least squares fit coefficients q of thermodynamic properties for 52% Ethanol, 48% Water saturated liquid mixture with temperature

and pressure as independent properties. The properties are valid in the range of 0.01 to 10 MPa and 305 to 552 Kelvin.

Generate the A matrix using `makeA.m` to find other thermodynamic properties z by computing $z = Aq$.

8.5.1.7 flow_fit_param_ethanol_water_52_48_twophase_g_expanded_TP.mat

This MATLAB file contains the least squares fit coefficients q of thermodynamic properties for 52% Ethanol, 48% Water saturated vapor mixture with temperature and pressure as independent properties. The properties are valid in the range of 0.01 to 10 MPa and 312 to 560 Kelvin.

Generate the A matrix using `makeA.m` to find other thermodynamic properties z by computing $z = Aq$.

8.5.1.8 flow_fit_param_ethanol_water_52_48_vapor_expanded_TP_Ph.mat

This MATLAB file contains the least squares fit coefficients q of thermodynamic properties for 52% Ethanol, 48% Water vapor mixture with enthalpy and pressure as independent properties. The properties are valid in the range of 0.01 to 10 MPa and 1874.9 to 4004.6 $\frac{kJ}{kg}$.

Generate the A matrix using `makeA.m` to find other thermodynamic properties z by computing $z = Aq$.

8.5.1.9 flow_fit_param_ethanol_water_52_48_subcooled_expanded_TP_Ph.mat

This MATLAB file contains the least squares fit coefficients q of thermodynamic properties for 52% Ethanol, 48% Water subcooled mixture with enthalpy and pressure as independent properties. The properties are valid in the range of 0.01 to 10 MPa and -14.496 to 1296.1 $\frac{kJ}{kg}$.

Generate the A matrix using `makeA.m` to find other thermodynamic properties z by computing $z = Aq$.

8.5.1.10 flow_fit_param_ethanol_water_52_48_twophase_f_expanded_TP_Ph.mat

This MATLAB file contains the least squares fit coefficients q of thermodynamic properties for 52% Ethanol, 48% Water saturated liquid mixture with enthalpy and pressure as independent properties. The properties are valid in the range of 0.01 to 10 MPa and 191.98 to 1312.8 $\frac{kJ}{kg}$.

Generate the A matrix using `makeA.m` to find other thermodynamic properties z by computing $z = Aq$.

8.5.1.11 flow_fit_param_ethanol_water_52_48_twophase_g_expanded_TP_Ph.mat

This MATLAB file contains the least squares fit coefficients q of thermodynamic properties for 52% Ethanol, 48% Water saturated vapor mixture with enthalpy and pressure as independent properties. The properties are valid in the range of 0.01 to 10 MPa and 1862.3 to 2081.6 $\frac{kJ}{kg}$.

Generate the A matrix using `makeA.m` to find other thermodynamic properties z by computing $z = Aq$.

8.5.1.12 flow_fit_param_ethanol_water_52_48_vapor_Ph.mat

This MATLAB file contains the least squares fit coefficients q of thermodynamic properties for 52% Ethanol, 48% Water vapor mixture with enthalpy and pressure as independent properties. The properties are valid in the range of 0.01 to 6 MPa and 1874.9 to 4004.6 $\frac{kJ}{kg}$.

Generate the A matrix using `makeA.m` to find other thermodynamic properties z by computing $z = Aq$.

8.5.1.13 flow_fit_param_ethanol_water_52_48_subcooled_Ph.mat

This MATLAB file contains the least squares fit coefficients q of thermodynamic properties for 52% Ethanol, 48% Water subcooled mixture with enthalpy and pressure as independent properties. The properties are valid in the range of 0.01 to 10 MPa and 20.759 to 1081.9 $\frac{kJ}{kg}$.

8.6 Heat Transfer

8.6.1 Transport Properties

8.6.1.1 AirthermoProp.m

This function calculates the transport properties for air.

The function inputs are the following:

1. density `rho`, in $\frac{kmol}{m^3}$
2. temperature `T`, in K
3. isobaric heat capacity `Cp`, in $\frac{J}{kgK}$

The function outputs are the following:

1. dynamic viscosity `mu`, in $\frac{Ns}{m^2}$
2. thermoconductivity `k`, in $\frac{W}{mK}$
3. Prandtl number `Pr`

8.6.1.2 H2OtransportProp.m

This function calculates transport properties for water.

The function inputs are the following:

1. temperature `T`, in K
2. density `rho`, in $\frac{kg}{m^3}$
3. isobaric heat capacity, `Cp`, in $\frac{J}{kgK}$

The function outputs are the following:

1. viscosity `mu`, in $Pa - s$
2. thermoconductivity `k`, in $\frac{W}{mK}$
3. Prandtl number, `Pr`

8.6.2 Correlations

8.6.2.1 MB2ZHTC.m

This function determines the heat transfer coefficients for the 2-zone Moving Boundary model with the first region being two-phase and the second superheat. This function can be used for either evaporators or condensers. The function inputs are the following:

1. mass flow rate of outer tube or shell `mdots`, in $\frac{kg}{s}$
2. mass flow rate of inner tube `mdott`, in $\frac{kg}{s}$
3. diameter of shell `ds`, in meters
4. diameter of tube `dt`, in meters
5. wall thickness `wall_thickness`, in meters
6. saturated liquid density `rhof`, in $\frac{kg}{m^3}$
7. saturated vapor density `rhog`, in $\frac{kg}{m^3}$
8. number of tubes in bundle `nT`
9. length of heat exchanger `L`, in meters
10. average temperature of heat source `Th`, in K
11. average temperature of working fluid in region 1 `Tr1`, in K
12. average temperature of working fluid in region 2 `Tr2`, in K
13. average isobaric heat capacity in region 1 `Cp1`, in $\frac{kJ}{kgK}$
14. average isobaric heat capacity in region 2 `Cp2`, in $\frac{kJ}{kgK}$

The function outputs are the following:

1. tube-side heat transfer coefficient in region 1 `alpha_i1`, in $\frac{kW}{m^2K}$
2. tube-side heat transfer coefficient in region 2 `alpha_i2`, in $\frac{kW}{m^2K}$
3. shell-side heat transfer coefficient `alpha_o`, in $\frac{kW}{m^2K}$

8.6.2.2 MB3ZHTC.m

This function determines the heat transfer coefficients for the 3-zone Moving Boundary model with the first region being subcooled, second as two-phase, and the third as superheat. This function can be used for either evaporators or condensers. The function inputs are the following:

1. mass flow rate of outer tube or shell `mdots`, in $\frac{kg}{s}$
2. mass flow rate of inner tube `mdott`, in $\frac{kg}{s}$
3. diameter of shell `ds`, in meters
4. diameter of tube `dt`, in meters
5. wall thickness `wall_thickness`, in meters
6. saturated liquid density `rhof`, in $\frac{kg}{m^3}$
7. saturated vapor density `rhog`, in $\frac{kg}{m^3}$
8. length of heat exchanger `L`, in meters
9. length of two-phase region `L2`, in meters
10. average temperature of heat source `Th`, in K

11. average temperature of working fluid in region 1 `Tr1`, in K
12. average temperature of working fluid in region 2 `Tr2`, in K
13. average temperature of working fluid in region 3 `Tr3`, in K
14. average isobaric heat capacity in region 1 `Cp1`, in $\frac{kJ}{kgK}$
15. average isobaric heat capacity in region 2 `Cp2`, in $\frac{kJ}{kgK}$
16. average isobaric heat capacity in region 3 `Cp3`, in $\frac{kJ}{kgK}$
17. saturated liquid enthalpy `hf`, in $\frac{kJ}{kg}$
18. saturated vapor enthalpy `hg`, in $\frac{kJ}{kg}$

The function outputs are the following:

1. tube-side heat transfer coefficient in region 1 `alpha_i1`, in $\frac{kW}{m^2K}$
2. tube-side heat transfer coefficient in region 2 `alpha_i2`, in $\frac{kW}{m^2K}$
3. tube-side heat transfer coefficient in region 3 `alpha_i3`, in $\frac{kW}{m^2K}$
4. shell-side heat transfer coefficient `alpha_o`, in $\frac{kW}{m^2K}$

8.7 Road Cycles

8.7.1 roadcycles110415.m

This function loads pre-processed road cycle data `roadcycles110415.mat` and generates a structure and plots of several engine characteristics. The `movingaverage.m` function smooths out some of the undesired/questionable data points.

The function input is:

1. choice of road cycle entered as a string, either 'flat', 'rolling,' or 'hilly'

The function output is a struct `cycle` with the following fields:

1. `time`, in seconds
2. engine throttle position `throttlepos`, in percent
3. engine speed `engine_spd`, in revolutions per minute
4. engine brake torque `engine_brake_torque`, in Newton-meters
5. engine brake power `engine_brake_power`, in kW
6. EGR exhaust mass flow rate `mdotegr`, in $\frac{kg}{s}$
7. tailpipe heat exchanger exhaust mass flow rate `mdotexhaust`, in $\frac{kg}{s}$
8. inlet working fluid pressure in EGR heat exchanger `Pegrin`, in MPa
9. outlet working fluid pressure in EGR heat exchanger `Pegrout`, in MPa
10. temperature of tailpipe heat exchanger exhaust `Texhaustin`, in Celcius
11. inlet temperature of EGR exhaust `Tegrin`, in Celcius
12. outlet temperature of EGR exhaust `Tegrout`, in Celcius

8.7.2 roadcycles110415.mat

This mat data file contains driving cycle data for flat, rolling, and hilly conditions. Use `roadcycles110415.m` to load the data.

8.7.3 movingaverage.m

This function computes a moving average of a vector of data `x` with window size `M`.

The function inputs are:

1. original data `x`
2. window size `M`

The function outputs are:

1. averaged data y

CHAPTER 9

Conclusion

Important challenges of increasing energy demand and improving the reliance on alternative energy sources characterize our world today. Recovering and converting heat energy from either exisiting or sustainable energy sources can improve energy efficiency and reduce energy consumption. To aid in this effort, this dissertation has contributed to the development of waste heat recovery (WHR) systems through techniques in modeling, estimation, and control. Static Rankine (RC) models use traditional steady-state assumptions to describe the power cycle with fixed heat sources. With waste and alternative heat sources typically being low- to medium-grade quality and often highly transient, dynamical models for the RC components are presented to describe the complex WHR dynamics. The static RC model based on thermodynamic energy balance provide design optimization of the cycle based on heat source/sink and working fluid flow conditions. The Moving Boundary method for heat exchangers provide control-oriented and low-order mathematical models of multi-phase evaporators and condensers. Static pump, valve, and piston expander models are applicable for applications where the heat exchange dynamics are relatively slower. A dynamic, reciprocating piston expander based on energy balance in a control-volume is presented for more accurate modeling. The static and dynamic models together provide a physics-based mathematical framework for understanding power recovery and a foundation for the estimation and control methods presented in this dissertation.

Facilitating the growing interest for organic RC (ORC) for low-grade heat source WHR, this dissertation considers an organic working fluid mixture in ethanol and water. A least-squares fitting routine performed off-line for thermodynamic and transport properties provides accurate equations of state for arbitrary fluids. The procedure improves computational efficiency over intensive on-line table look-up methods. Thermoproperties for water and steam are also presented for higher-grade heat sources.

To monitor RC performance and incorporate model-based control design, an Extended Kalman Filter (EKF) provides superior state estimates of the nonlinear Moving Boundary heat exchanger models. The results show that either pressure or temperature measurements effectively construct state estimates in the presence of heat exchanger fouling as well as measurement and process noises. Relative observability based on the empirical gramian for nonlinear systems show the highest relative observability when using both measurements. An Approximated, analytical Jacobian linearization for the process proves nearly as effective as the Full, numerical Jacobian and can avoid the latter's numerical challenges.

To ensure high and proper operational WHR performance in the presence of transient heat sources, several model-based control methods are presented for different RC architectures and actuator configurations. The single valve architecture together with Proportional Integral (PI) control show successful flooding avoidance while regulating heat exchanger pressures. The pressure and phase-change tracking controllers satisfy constraints while open-loop operation does not. Control of an automotive WHR system applied on the dual valve architecture show superior tracking performance for a Linear Quadratic Integral (LQI) and Model Predictive Controller (MPC) over a Proportional Integral controller. For the advanced LQI and MPC controllers, perfect state as well as EKF state estimation feedback

are considered. The state estimation feedback also show improved performance over PI control. Finally, control for power load following address the need for base loading and power load following power plant modes that WHR systems can operate in depending on the application.

Finally, this dissertation provides a library of RC components, thermodynamic, and transport property models useful for constructing WHR system models and for performing studies not limited to trade-off, sensitivity, and "what-if." The estimation and control methods in this dissertation provide possibilities for constrained operation.

To summarize, this dissertation applies modeling, estimation, and control methods for a 13-liter heavy-duty diesel truck powertrain whose exhaust is used as the transient heat source to an ORC WHR system. The results indicate up to 10 kW of power can be generated from the driving cycle heat source transients. The magnitude of the power differs depending on the set of operating conditions chosen. Nonetheless, the power generated represents a significant portion of the overall engine's brake power. The engine power improvement provided by the ORC can be as high as 7%, which agrees with the road testing performed by Volvo Powertrain on its WHR system. However, a note must be given to the reader regarding the accuracy and validity of the simulation results this dissertation provides. The complex geometry of the evaporator pose challenges in modeling, specifically in determining the proper flow configurations for the internal and external flows. The reader should be aware that the results in this dissertation reflect significant simplification of the heat exchanger as a single tube in cross flow. As a result, the heat transfer correlations used for this simpler geometry may not accurately represent the actual geometry. Improvements to this modeling limitation remain as future research.

References

[Adm11] U.S. Energy Information Administration. "History of Energy Consumption in the United States, 1775-2009.", 2011. Tables 1.3, 2.1b-2.1f , 10.3, and 10.4.

[BB02] S. Bendapudi and J.E. Braun. "A Review of Literature on Dynamic Models of Vapor Compression Equipment." ASHRAE REPORT, No. 4036-5, 2002.

[BM09] M. Badami and M. Mura. "Preliminary design and controlling strategies of a small-scale wood waste Rankine Cycle (RC) with a reciprocating steam engine (SE)." *Energy*, **34**:1315–1324, 2009.

[BMR13] A. Bemporad, M. Morari, and N.L. Ricker. "Model Predictive Control Toolbox User's Guide.", March 2013. Natick, Massachusetts, United States.

[BW81] B.T. Beck and G.L. Wedekind. "A Generalization of the System Mean Void Fraction Model for Transient Two-Phase Evaporating Flows." *ASME J. Heat Transfer*, **103**(1):81–85, February 1981.

[CG08] A. Chaibakhsh and A. Ghaffari. "Steam Turbine Model." *Simulation Modelling Practice and Theory*, **16**:1145–1162, 2008.

[CHA04] T. Cheng, X.D. He, and H. Asada, editors. *Nonlinear Observer Design for Two-Phase Flow Heat Exchangers of Air Conditioning Systems.* ASME Proceedings of the 2004 American Control Conference, 2004.

[Cra11] K. Craig. "Mechatronic Modeling Reins in HVAC Power Consumption." On the WWW, September 2011. URL `http://www.designnews.com`.

[DOE09] DOE. "Research and Development Opportunities for Heavy Trucks.", June 2009. URL `http://www1.eere.energy.gov/vehiclesandfuels/pdfs/ truck_efficiency_paper_v2.pdf`.

[DOE10] DOE. "Secretary Chu Announces $187 Million to Improve Vehicle Efficiency for Heavy-Duty Trucks and Passenger Vehicles.", January 2010. URL `http://energy.gov/articles/secretary-chu-announces-187-million-improve-vehicle-efficiency-heavy- duty-trucks-and`.

[ERA08] B.D. Eldredge, B.P. Rasmussen, and A.G. Alleyne. "Moving-Boundary Heat Exchanger Models with Variable Outlet Phase." *Journal of Dynamic Systems, Measurement, and Control*, **130**, November 2008.

[Him] C. Himpe. "emgr - Empirical Gramian Framework." "See also URL `http://gramian.de`".

[HLA97] X.D. He, S. Liu, and H.H. Asada. "Modeling of Vapor Compression Cycles for Multivariable Feedback Control of HVAC Systems." *Journal of Dynamic Systems, Measurement, and Control*, **119**:183–191, June 1997.

[HLI98] X.D. He, S. Liu, H. Itoh, and H.H. Asada. "Multivariable Control of Vapor Compression Systems." *HVAC&R Research*, **4**:205–230, July 1998.

[Ibr12] H. Ibrahim. "Fouling in Heat Exchangers." On the WWW, September 2012. URL `http://www.intechopen.com`.

[IDB06] F.P. Incropera, D.P. DeWitt, T.L. Bergman, and A.S. Lavine. *Fundamentals of Heat and Mass Transfer*. John Wiley & Sons Inc., 2006.

[Inc] The MathWorks Inc. "MATLAB and Control Systems Toolbox Release 2009b." Natick, Massachusetts, United States.

[Int07] The International Association for the Properties of Water and Steam, Lucerne, Switzerland. *Revised Release on the IAPWS Industrial Formulation 1997 for the Thermodynamic Properties of Water and Steam*, 2007. See also URL `http://www.iapws.org`.

[Int08a] The International Association for the Properties of Water and Steam, Lucerne, Switzerland. *Revised Release on the IAPWS Industrial Formulation 1985 for the Thermal Conductivity of Ordinary Water Substance*, 2008. See also URL `http://www.iapws.org`.

[Int08b] The International Association for the Properties of Water and Steam, Lucerne, Switzerland. *Revised Release on the IAPWS Industrial Formulation 2008 for the Viscosity of Ordinary Water Substance*, 2008. See also URL `http://www.iapws.org`.

[Ise03] R. Isermann. *Mechatronic Systems: Fundamentals, 1st Edition*. Springer., 2003.

[JLP07] G.R. Jonsson, S. Lalot, O.P. Palsson, and B. Desmet. "Use of Extended Kalman Filtering in Detecting Fouling in Heat Exchangers." *International Journal of Heat and Mass Transfer*, **50**:2643–2655, February 2007.

[JT02] J.M. Jensen and H. Timmescheit, editors. *Moving Boundary Models for Dynamic Simulations of Two-Phase Flows*, Oberpfaffenhofen, Germany, March 2002. Second International Modelica Conference Proceedings.

[Kan08] S.G. Kandlikar. "A General Correlation for Saturated Two-Phase Flow Boiling Heat Transfer Inside Horizontal and Vertical Tubes." *Applied Thermal Engineering*, **28**:219–228, 2008.

[LCW04] B-T Liu, K-H Chien, and C-C Wang. "Effect of working fluids on organic Rankine cycle for waste heat recovery." *Energy*, **29**:1207–1217, 2004.

[LHM07] E.W. Lemmon, M.L. Huber, and M.O. McLinden. "Reference fluid thermodynamic and transport properties database 8.0, National Institute of Standards and Technology." Boulder, CO, 2007.

[Lim11] C. Lim. *Modeling and Analysis of Cam-based and Camless Air Hybrid Vehicles*. PhD dissertation, University of California, Los Angeles, Los Angeles, CA, USA, 2011.

[MA08] T.L. MicKinley and A.G. Alleyne. "An Advanced Nonlinear Switched Heat Exchanger Model for Vapor Compression Cycles using Moving-Boundary Method." *International Journal of Refrigeration*, **31**:1253–1264, February 2008.

[NGL78] R.E. Niggerman, W.J. Greenlee, and P.D. Lacey. "Fluid selection and optimization of an organic Rankine cycle waste heat power conversion system." *ASME 78-WA/Ener-6*, 1978.

[PJ77] N.H. Proctor and J.P. Jughes. "Chemical hazards of the work place." Technical report, Lippincott JB Co, 1977.

[PPO01] B.E. Poling, J.M. Prausnitz, and J.P. O'Connell. *The Properties of Gases and Liquids, 5th Edition*. McGraw-Hill, New York, New York, 2001.

[QAG11] S. Quoilin, R. Aumann, A. Grill, A. Schuster, V. Lemort, and H. Spliethoff. "Dynamic Modeling and Optimal Control Strategy of Waste Heat Recovery Organic Rankine Cycles." *Applied Energy*, **88**:2183–2190, January 2011.

[QD08] Q. Qi and S. Deng. "Multivariable Control-oriented Modeling of a Direct Expansion (DX) Air Conditioning (A/C) System." *International Journal of Refrigeration*, **31**:841–849, July 2008.

[QLL10] S. Quoilin, V. Lemort, and J. Lebrun. "Experimental Study and Modeling of an Organic Rankine Cycle using Scroll Expander." *Applied Energy*, **87**:1260–1268, 2010.

[RA04] B.P. Rasmussen and A.G. Alleyne. "Control-oriented Modeling of Transcritical Vapor Compression Systems." *Transactions of the ASME*, **126**:54–64, March 2004.

[Ras02] B.P. Rasmussen. *"Control-Oriented Modeling of Transcritical Vapor Compression Systems."*. MS Thesis, University of Illinois, Urbana, IL, October 2002.

[Ros08] J. Rosebro. "Honda Researching Advanced Hybrid Drive with Rankine Cycle Co-Generation.", February 2008. URL `http://www.greencarcongress.com/2008/02/honda-researchi.html`.

[SH04] A.K. Singh and J. Hahn, editors. *Optimal Sensor Location for Nonlinear Dynamic Systems via Empirical Gramians*. Proceedings of the DYCOPS 2004, 2004.

[SM78] P.H. Snyder and W.C. Moreland. "The selection of working fluid candidates for use in high temperature industrial heat pumps." Doe ec-77-c01-5026, Westinghouse Electric Corporation, 1978.

[WLL90] D. Wei, X. Lu, Z. Lu, and J. Gu. "Dynamic Modeling and Simulation of an Organic Rankine Cycle (ORC) System for Waste Heat Recovery." *Journal of Heat Transfer*, **112**:219–1224, February 1990.

[ZZH12] J. Zhang, W. Zhang, G. Hou, and F. Fang. "Dynamic Modeling and Multivariable Control of Organic Rankine Cycles in Waste Heat Utilizing Processes." *Computers and Mathematics*, **64**:908–921, February 2012.